Technical Report Documentation Page

1. Report No.	2. Government Accession No.	3. Recipient's Catalog No.
FHWA/TX-14/5-5253-03-1		

4. Title and Subtitle	5. Report Date
Structural Monitoring of the World's First Precast Network Arch Bridge during Construction	April 2014; Published November 2014
	6. Performing Organization Code
7. Author(s)	8. Performing Organization Report No.
Hossein Yousefpour, Todd Helwig, Oguzhan Bayrak	5-5253-03-1
9. Performing Organization Name and Address	10. Work Unit No. (TRAIS)
Center for Transportation Research The University of Texas at Austin 1616 Guadalupe St., Suite 4.202 Austin, TX 78701	11. Contract or Grant No. 5-5253-03
12. Sponsoring Agency Name and Address	13. Type of Report and Period Covered
Texas Department of Transportation Research and Technology Implementation Office P.O. Box 5080 Austin, TX 78763-5080	Technical Report December 2010–February 2014
	14. Sponsoring Agency Code

15. Supplementary Notes
Project performed in cooperation with the Texas Department of Transportation and the Federal Highway Administration.

16. Abstract

This report provides an overview of a monitoring study on the West 7th Street Bridge in Ft Worth, Texas that was carried out by The University of Texas at Austin (UT). The West 7th Street Bridge was designed by the Texas Department of Transportation (TxDOT) and is believed to be the first precast concrete network arch bridge in the world. The bridge consists of a series of prestressed concrete arches that were precast and post-tensioned at a staging area before they were transported to the bridge site and erected. Due to the innovative construction of this bridge, some of the most critical stresses in the life of the arches happened during construction. Therefore, an instrumentation program was conducted to make sure that the arches were not damaged during the fabrication, transport, and erection procedures. The researchers from UT embedded a series of Vibrating Wire Gages (VWGs) in the critical sections of arches and monitored the sensors throughout construction to ensure the safety of the arches. The recorded data also allowed the researchers to evaluate the accuracy of some of the assumptions that were necessary during the design of the arches. An overview of the monitoring effort and the major findings from instrumentation are provided in this document.

17. Key Words	18. Distribution Statement
Arch bridge, Network arch, Concrete, Precast, Prestressed, Post-tensioned, Monitoring, Accelerated bridge construction	No restrictions. This document is available to the public through the National Technical Information Service, Springfield, Virginia 22161; www.ntis.gov.

19. Security Classif. (of report)	20. Security Classif. (of this page)	21. No. of pages	22. Price
Unclassified	Unclassified	181	

Form DOT F 1700.7 (8-72) Reproduction of completed page authorized

THE UNIVERSITY OF TEXAS AT AUSTIN
CENTER FOR TRANSPORTATION RESEARCH

Structural Monitoring of the World's First Precast Network Arch Bridge during Construction

Hossein Yousefpour
Todd Helwig
Oguzhan Bayrak

CTR Technical Report:	5-5253-03-1
Report Date:	April 2014
Project:	5-5253-03
Project Title:	Monitoring Stresses and Placing Sweep Control System in Innovative Prestressed, Precast Concrete Arches
Sponsoring Agency:	Texas Department of Transportation
Performing Agency:	Center for Transportation Research at The University of Texas at Austin

Project performed in cooperation with the Texas Department of Transportation and the Federal Highway Administration.

Center for Transportation Research
The University of Texas at Austin
1616 Guadalupe St, Suite 4.202
Austin, TX 78701

http://ctr.utexas.edu/

Disclaimers

Author's Disclaimer: The contents of this report reflect the views of the authors, who are responsible for the facts and the accuracy of the data presented herein. The contents do not necessarily reflect the official view or policies of the Federal Highway Administration or the Texas Department of Transportation (TxDOT). This report does not constitute a standard, specification, or regulation.

Patent Disclaimer: There was no invention or discovery conceived or first actually reduced to practice in the course of or under this contract, including any art, method, process, machine manufacture, design or composition of matter, or any new useful improvement thereof, or any variety of plant, which is or may be patentable under the patent laws of the United States of America or any foreign country.

Notice: The United States Government and the State of Texas do not endorse products or manufacturers. If trade or manufacturers' names appear herein, it is solely because they are considered essential to the object of this report.

Engineering Disclaimer

NOT INTENDED FOR CONSTRUCTION, BIDDING, OR PERMIT PURPOSES.

Project Engineer: Todd A. Helwig
Professional Engineer License State and Number: Texas No. 94280
P. E. Designation: Research Supervisor

Acknowledgments

The authors gratefully acknowledge the Texas Department of Transportation (TxDOT) for providing financial support for this implementation study. In particular, the authors would like to thank Dean Van Landuyt and Courtney Holle for their substantial guidance on the project. In addition, there were numerous engineers and representatives from TxDOT and the contractor, Sundt Construction, who provided significant assistance throughout the investigation. Many thanks are also due to Jose Gallardo, Ali Morovat, David Garber, Kostas Belivanis, Vasilis Samaras, and Hemal Patel, current and former graduate students at The University of Texas at Austin, for assisting with the instrumentation.

TABLE OF CONTENTS

List of Figures ..... **x**

List of Tables ..... **xiv**

CHAPTER 1: Introduction **1**
1.1 Introduction 1
1.2 The West 7th Street Bridge 1
1.3 Project Objectives 3
1.4 Implementation Tasks 3
1.5 Report Organization 4
Chapter Bibliography 5

CHAPTER 2: Background **7**
2.1 Introduction 7
2.2 The West 7th Street Bridge Replacement Project 7
2.2.1 Structural Design of the New Bridge 8
2.2.2 Construction Sequence 11
2.2.3 Construction timeline 26
2.3 Motivation for Instrumentation 26
2.4 Roles of Instrumentation 28
2.4.1 Monitoring the Stresses during Construction 28
2.4.2 Monitoring the Hydration Temperatures in the Concrete 29
2.4.3 Monitoring the Lateral Stability during Post Tensioning 29
2.4.4 Sweep Control 29
2.4.5 Monitoring the Long-Term Changes 29
2.5 Summary 30
Chapter Bibliography 30

CHAPTER 3: Material Studies **31**
3.1 Introduction 31
3.2 The Mix 31
3.3 The Specimens 33
3.4 Testing Procedure 33
3.5 Test Results 34
3.6 Analysis 36
3.6.1 Modulus-Compressive Strength Correlation 36
3.6.2 Splitting Tensile Strength 37
3.6.3 Estimating the In-Situ Mechanical Properties of Concrete 39
3.6.4 Consistency between FSEL Tests and Tests by Sundt Construction 45
3.7 Summary 46
Chapter Bibliography 46

CHAPTER 4: Field Instrumentation 49
4.1 Introduction 49
4.2 Instrumentation Procedure 49
4.2.1 Identifying Measurement Requirements 49
4.2.2 Selecting the Sensor Type: Vibrating Wire Gages 50
4.2.3 Assessing the Instrumentation Capabilities 53
4.2.4 Selecting the Instrumentation Locations 54
4.2.5 Designing the Data Acquisition Network 60
4.2.6 Programming the data loggers 63
4.2.7 Assembling the DAQ Units 64
4.2.8 Installing the VWGs 67
4.3 Monitoring the Instrumentation 71
4.4 Live Load Test 78
4.5 Observed Durability of the VWGs 82
4.6 Practical Considerations 83
4.6.1 Coordination Requirements 83
4.6.2 Workforce for VWG Installation 83
4.6.3 Travel 83
4.6.4 Encountered Problems 83
4.7 Summary 85
Chapter Bibliography 86

CHAPTER 5: Data Processing 87
5.1 Introduction 87
5.2 Estimating the In-Situ Strength of the Concrete 87
5.3 Calculating Strain Changes at the Locations of VWGs 90
5.4 Sectional Strain Calculations 90
5.4.1 Sections with Two VWGs 91
5.4.2 Sections with Three or Four VWGs 92
5.5 Estimating the Coefficient of Thermal Expansion of Concrete 93
5.6 Stress Calculations 96
5.6.1 Calculating Elastic Stress Changes 98
5.6.2 Calculating Total Stresses 103
5.7 Calculating Prestress Losses 106
5.8 Summary 108
Chapter Bibliography 108

CHAPTER 6: Results and Discussion 109
6.1 Introduction 109
6.2 Concrete Hydration Temperatures 109
6.3 Arch Stresses 111
6.3.1 Stage 1 Post-Tensioning 111
6.3.2 Rotation 116
6.3.3 Stage 2 PT 120
6.3.4 Sliding 125
6.3.5 Upward Jacking 126

6.3.6 Arch Transportation 131
6.3.7 Floor Beam Installation and Deck Construction 134
6.1 Prestress Losses 137
6.2 Live Load Test Results 141
6.3 Summary 148

CHAPTER 7: Conclusion 149

APPENDIX A: As-Built Locations of the VWGs 151
A.1 Introduction 151
A.2 The Instrumented Sections 151
A.3 Sectional Locations of the VWGS 164

LIST OF FIGURES

Figure 1.1- The location of the West 7th Street Bridge 1
Figure 1.2- The new West 7th Street Bridge 2
Figure 2.1- The old West 7th Street Bridge. 8
Figure 2.2- A typical span in the new West 7th Street Bridge. 9
Figure 2.3- Geometry of a typical network arch in the West 7th Street Bridge 10
Figure 2.4- Arch details in the knuckle region 12
Figure 2.5- Arch formwork. 12
Figure 2.6- Concrete casting operations 13
Figure 2.7- General paths of the tendons in the arches 14
Figure 2.8- The multi-strand jack. 15
Figure 2.9- Anchorage of rib tendons in Stage 1 PT 16
Figure 2.10- Rotation details 17
Figure 2.11- Arch rotation. 18
Figure 2.12- Intentional curves in the duct paths. 19
Figure 2.13- Sliding operation on one of the arches. 20
Figure 2.14- Upward Jacking 21
Figure 2.15- The transportation path 22
Figure 2.16-Arch transportation 23
Figure 2.17- Temporary bracing of the arches 24
Figure 2.18- Initial hanging of the floor beams. 24
Figure 2.19- Post tensioning the floor beam bars. 25
Figure 2.20- Installation of the precast panels 25
Figure 2.21- Construction timeline for the West 7th Street Bridge project. 26
Figure 2.22- Models of the arches in LUSAS 27
Figure 2.23- Effect of casting direction on variability in material properties 28
Figure 3.1- Modulus of elasticity of concrete according to ASTM C469. 33
Figure 3.2- Testing equipment 34
Figure 3.3- Testing for splitting tensile strength. 34
Figure 3.4- Results of concrete cylinder tests. 35
Figure 3.5- The mix-specific correlation between $\boldsymbol{E}$ and $\boldsymbol{f'_c}$ 37
Figure 3.6- Comparison between the proposed $\boldsymbol{E}$ vs. $\boldsymbol{f'_c}$ equation and some commonly used equations. 38
Figure 3.7- The mix-specific correlation between $\boldsymbol{f_{ct}}$ and $\boldsymbol{f'_c}$ 38
Figure 3.8- Temperature-time factor, $\boldsymbol{M(t)}$ 39
Figure 3.9- The procedure for estimating the in-situ values of $\boldsymbol{E}$ and $\boldsymbol{f'_c}$. 40

Figure 3.10- Strength-maturity relationship for arches 1-4. 42
Figure 3.11- Strength-maturity relationship for arches 5-8. 43
Figure 3.12- Strength-maturity relationship for arches 9-12 44
Figure 3.13- Comparison between FSEL test results and the contractor's results 45
Figure 4.1- Geokon Model 4200 VWG. 51
Figure 4.2- Locations of critical sections in the structure, as predicted in design. 55
Figure 4.3- Locations of the instrumented sections with respect to D- and B- regions. 57
Figure 4.4- Arrangement of VWGs in different sections of the arches. 58
Figure 4.5- Instrumented sections in different arches. 59
Figure 4.6- DAQ network configuration. 61
Figure 4.7- A GK-404 Readout box 63
Figure 4.8- DL and DC boxes. 65
Figure 4.9- DL box details 66
Figure 4.10- A VWG attached to the reinforcing bar. 67
Figure 4.11- VWG installation process 68
Figure 4.12-VWG installation process(continued). 70
Figure 4.13- VWG installation process(continued). 71
Figure 4.14- The situation of the DC boxes during different arch movement operations 73
Figure 4.15- Disconnecting a DC box after the transportation of Arch 3 73
Figure 4.16- Timeline for monitoring Arches 1-4 during construction. 74
Figure 4.17- Timeline for monitoring Arches 5-8 during construction. 75
Figure 4.18- Timeline for monitoring Arches 9-12 during construction. 76
Figure 4.19- The Control panel for the post-processing module. 77
Figure 4.20- Using a smart phone to track stress changes in the structure. 77
Figure 4.21- The dimensions of the trucks used for live load test 78
Figure 4.22- Eastbound truck positions. 79
Figure 4.23- Westbound truck positions. 80
Figure 4.24- The live load test 81
Figure 5.1- Procedure for calculating the maturity-based compressive strength 88
Figure 5.2- Difference between the strength gain of Arch 6 and other arches. 88
Figure 5.3- Correlation equations for estimating f_c', as compared to the maturity-based strength values. 89
Figure 5.4- General layout of sections with two VWGs. 91
Figure 5.5- General layout of sections in B-regions. 92
Figure 5.6- Strain-temperature correlation for Arch 9. 95
Figure 5.7- Coefficient of thermal expansion in the arches. 96
Figure 5.8- The components of the recorded strain from the structure. 97
Figure 5.9- Approximate stress levels at the bottom of the rib and bottom of the tie at the midspan of Arch 2 during Stage 1 PT 99

Figure 5.10- Strain change at the bottom of the tie and the bottom of the rib at the midspan of Arch 1, before and during rotation operations. 100
Figure 5.11- Stress increments at the midspan of Arch 2 during Stage 1 PT. 101
Figure 5.12- Cumulative sum of the stress increments during Stage 1 PT on Arch2. 101
Figure 5.13- The criteria for selecting the data points for calculating the stresses. 102
Figure 5.14- Arch deformations under Stage 1 PT. 104
Figure 6.1- Concrete temperatures in Arch 2 during the first week after concrete pour 110
Figure 6.2- Maximum recorded temperatures in the arches during the first 48 hours after the concrete pour. 110
Figure 6.3- Compressive stresses acting on the arch rib due to post-tensioning. 112
Figure 6.4- Stresses in Arch 2 during Stage 1 PT operations 113
Figure 6.5- Stresses in Arch 2 during Stage 1 PT operations (continued). 114
Figure 6.6- Arch stresses at the end of Stage 1 PT. 115
Figure 6.7- Stresses during rotation of Arch 2 at midspan-rib 117
Figure 6.8- Stresses during rotation of Arch 2 at midspan-tie 118
Figure 6.9- Critical stresses during supported rotation of the arches 119
Figure 6.10- Arch stresses at the end of rotation. 121
Figure 6.11- Stresses in Arch 2 during Stage 2 PT operations on the tie. 122
Figure 6.12- Stresses in Arch 2 during Stage 2 PT operations on the tie (continued). 123
Figure 6.13- Arch stresses at the end of Stage 2 PT. 124
Figure 6.14- Typical stress changes in Arch 2 during sliding operations. 125
Figure 6.15- Stresses in Arch 2 during upward jacking operations. 127
Figure 6.16- Stresses in Arch 2 during upward jacking operations (continued). 128
Figure 6.17- Arch stresses during upward jacking (rams active). 129
Figure 6.18- Arch stresses after upward jacking (after removal of the rams). 130
Figure 6.19- Change in the support conditions during arch transportation. 131
Figure 6.20- Stresses in Arch 4 during transportation. 132
Figure 6.21- Stresses in Arch 4 during transportation (continued). 133
Figure 6.22- Strain changes in the knuckle region of Arch 2 during transportation. 133
Figure 6.23- Arch stresses after floor beam installation 135
Figure 6.24- Arch stresses after casting the topping slab 136
Figure 6.25- The stresses in PT tendons following Stage 2 PT 138
Figure 6.26- PT stresses in the arch tendons at different stages of construction. 139
Figure 6.27- PT stresses in the arch tendons at different stages of construction(continued). 140
Figure 6.28- Stress changes in Arch 1 during live load test 142
Figure 6.29- Stress changes in Arch 1 during live load test (continued). 143
Figure 6.30- Stress changes in Arch 1 during live load test (continued). 144
Figure 6.31- Stress changes in Arch 2 during live load test. 145
Figure 6.32- Stress changes in Arch 2 during live load test (continued). 146

Figure 6.33- Stress changes in Arch 2 during live load test (continued). 147
Figure A.1- The instrumented sections in Arch 1. 152
Figure A.2- The instrumented sections in Arch 2. 153
Figure A.3- The instrumented sections in Arch 3. 154
Figure A.4- The instrumented sections in Arch 4. 155
Figure A.5- The instrumented sections in Arch 5. 156
Figure A.6- The instrumented sections in Arch 6. 157
Figure A.7- The instrumented sections in Arch 7. 158
Figure A.8- The instrumented sections in Arch 8. 159
Figure A.9- The instrumented sections in Arch 9. 160
Figure A.10- The instrumented sections in Arch 10. 161
Figure A.11- The instrumented sections in Arch 11. 162
Figure A.12- The instrumented sections in Arch 12. 163
Figure A.13- The coordinate system for the locations of the VWGs. 164

LIST OF TABLES

Table 2.1- Stressing sequence for Stage 1 PT. 15
Table 2.2- Stressing sequence for Stage 2 PT on the tie. 19
Table 3.1- Concrete mix ingredients (as designed). 32
Table 3.2- Concrete mix parameters. 32
Table 3.3- Results of the material test program. 36
Table 3.4- Strength-maturity results reported by Sundt Construction. 41
Table 4.1-Requirements for the sensors 50
Table 4.2- Geokon Model 4200 VWG Specifications 52
Table 4.3- Description of the critical sections as predicted in design. 55
Table 4.4-Number of VWGs in different arches. 57
Table 4.5- The schedule of VWG installation and concrete pour for the arches. 71
Table 4.6- Measured axle weights from the trucks. 79
Table 4.7- Durability of embedded VWGs. 82
Table A.1- Coordinates of the VWGs in Arch 1 164
Table A.2- Coordinates of the VWGs in Arch 2 165
Table A.3- Coordinates of the VWGs in Arch 3 165
Table A.4- Coordinates of the VWGs in Arch 4 166
Table A.5- Coordinates of the VWGs in Arch 5. 166
Table A.6- Coordinates of the VWGs in Arch 6. 166
Table A.7- Coordinates of the VWGs in Arch 7. 167
Table A.8- Coordinates of the VWGs in Arch 8. 167
Table A.9- Coordinates of the VWGs in Arch 9. 167
Table A.10- Coordinates of the VWGs in Arch 10. 167
Table A.11- Coordinates of the VWGs in Arch 11. 167
Table A.12- Coordinates of the VWGs in Arch 12. 167

CHAPTER 1
Introduction

1.1 INTRODUCTION

This report provides an overview of a monitoring study on the West 7th Street Bridge in Fort Worth, Texas that was carried out by The University of Texas at Austin (UT). The West 7th Street Bridge was designed by the Texas Department of Transportation (TxDOT) and is believed to be the first precast concrete network arch bridge in the world. The bridge consists of a series of prestressed concrete arches that were precast and post-tensioned at a staging area before they were transported to the bridge site and erected. Due to the innovative construction of this bridge, some of the most critical stresses in the life of the arches happened during construction. Therefore, an instrumentation program was conducted to make sure that the arches were not damaged during the fabrication, transport, and erection procedures. The researchers from UT embedded a series of Vibrating Wire Gages (VWGs) in the critical sections of arches and monitored the sensors throughout construction to ensure the safety of the arches. The recorded data also allowed the researchers to evaluate the accuracy of some of the assumptions that were necessary during the design of the arches. An overview of the monitoring effort and the major findings from instrumentation are reported in this document.

1.2 THE WEST 7TH STREET BRIDGE

The West 7th Street Bridge was designed to replace a century-old city bridge that connected downtown Fort Worth to the Cultural District. As can be seen in Figure 1.1, the bridge spanned over four lanes of traffic, the Clear Fork of the Trinity River, and a number of recreational trails.

Figure 1.1- The location of the West 7th Street Bridge [1].

The site conditions allowed the use of six uniform spans. Therefore, the designers conceived an innovative solution, which consisted of 12 identical precast, prestressed concrete network arches. Each arch has a span of 163.5 ft and a rise of 23.5 ft.

The procedure used in the construction of the West 7th Street Bridge allowed the construction team to minimize the time of street closure. The precast arches were constructed in a yard, less than one mile away from the bridge location. The arches were cast on their sides in precision-made formwork. Following a first stage of post tensioning and installation of hand-tightened hangers, the arches were rotated into a vertical position. After rotation, a second stage of post tensioning was carried out on the arches. The hangers were also prestressed using an upward jacking operation. Each arch then remained in a storage area until all arches were constructed and new piers were built adjacent to the existing bridge. Once all 12 of the arches were constructed, each of the arches was individually transported from the staging area to its final location, where it was lifted and installed on bearings. The old bridge was demolished only after all 12 arches were installed in their final locations and were properly braced. The construction of the deck for the new bridge was then started. A photo of finished bridge is shown in Figure 1.2.

Since the 280-ton arches experienced several post tensioning and handling operations, concerns were raised regarding potential damage of arches during construction, especially against cracking. The design methodology for the arches had utilized strut and tie modeling techniques that were recommended on a research study 0-5253 (D-Region Strength and Serviceability Design). In addition, due to the complex structural behavior of the arches, TxDOT had used sophisticated nonlinear finite element models of the bridge for design calculations. Since this bridge was the first of its kind, there was an interest in verifying the design calculations. Therefore, TxDOT initiated an implementation study (project 5-5253-3) to evaluate the implementation of the previous research study and to obtain performance data to ensure that the arches were not damaged during construction.

Figure 1.2- The new West 7th Street Bridge.

1.3 PROJECT OBJECTIVES

The main objectives of the instrumentation under Project 5-5253-3 were to verify the calculated stresses in the arches and to ensure that the arches were not damaged during construction. While some of the most critical stresses in the life of the arches happened during construction, the work plan for arch handling operations was primarily developed by the contractor and was out of direct control of the design team. Potential cracking of the arches during construction could be detrimental to the performance and stability of the arches in the finished bridge and therefore, measures to reduce the likelihood of damage were important to the success of the bridge. The instrumentation was to be used to provide a real-time measure of stresses and deformations to ensure that the arches were not damaged. The measured stresses also provided data for verifying the design assumptions. Since it was the first time a precast arch of this size was built, a validation of the predicted stresses in this project provides valuable insights into modeling of such complicated structural elements in future projects.

Instrumentation on the bridge also provides the contractor with a clear picture of the stress distribution in the arches during post-tensioning operations and a measure of the out-of-plane deformations of the arches (sweep). The embedded sensors also have the ability to provide an indication of the internal temperature in the concrete, which is useful during early hydration. Such measurements provide an indication of the in-situ maturity of the concrete and ensure that elements do not experience undesirably high temperatures.

1.4 IMPLEMENTATION TASKS

The objectives of this project were achieved through significant field activity, a series of material studies, and a substantial calculation and post-processing effort. The work completed under the major project tasks is summarized in the following paragraphs. The material study and the live load test were not parts of the originally proposed implementation plan, but were considered necessary for supporting the instrumentation effort.

1. Obtaining and configuring data loggers and instruments

The researchers provided a list of necessary equipment and instrumentation, which was included in the contract for the construction project. The equipment was purchased by the contractor, Sundt Construction, and was delivered to Ferguson Structural Engineering Laboratory (FSEL).

The researchers designed a flexible Data Acquisition (DAQ) system with wireless communication and remote monitoring capabilities for collecting the data with minimal interference with construction activities. The components of the DAQ system were assembled in FSEL according to the design.

A preliminary study was conducted in FSEL to evaluate the capabilities of the instrumentation in controlled laboratory tests and to identify the resolution and limitations of the sensors. The results of this study helped the researchers gain confidence in the measurements from the instrumentation.

2. The material study

Prior to casting the first arch, the researchers conducted a material study in FSEL to evaluate the rate of strength and stiffness gain in the concrete mix that was to be used in the

arches. These tests provided critical information that was necessary for post-processing the data. Forty-eight concrete cylinders were made from the same concrete mix that was used in the arches and were tested to measure the mix strength and modulus of elasticity. The results of these tests were the basis for converting the strains measured by the instrumentation to stresses.

3. Installing the instrumentation

A total of 224 vibrating wire gages were installed in the arches of the West 7th Street Bridge at sections that were identified as critical by the design team. For each arch, the instrumentation was installed after the reinforcing cage was completed and before concrete placement.

4. Monitoring the instrumentation after placement of the concrete

Monitoring of the instrumentation was started before concrete placement. Prior to post tensioning, all strains and temperatures were recorded once per hour to enable evaluation of concrete hydration temperatures and shrinkage strains. The gages were also monitored once every 150 seconds during all post-tensioning and upward jacking operations on the arches to evaluate the stress levels in the structure. During these operations, the researchers continuously evaluated the stresses in the arches and relayed their observations to the construction team.

5. Monitoring the instrumentation during arch lifting, transportation, and deck construction

The researchers closely monitored the instrumentation during all arch handling operations including arch rotation and transportation. The continuous monitoring of the sensors provided an alert of stress conditions that might lead to damage to the arches. In addition to protecting the arches from damage, the instrumentation also provided a safer work environment since dangerous conditions were avoided. Following the construction of the arches, the gages on select arches were also monitored during deck construction to verify the stresses predicted in design.

6. Tracking Prestress Losses

Measurements of strain and temperature during the life of the project were used to obtain the changes in the prestressing force in the tendons due to time-dependent deformations of concrete.

7. Live load testing on the finished bridge

After the bridge was opened to traffic, a static live load test was conducted on the bridge. Four 50-*kip* trucks were positioned on one of the spans of the bridge at different locations and the structure's response was recorded. As a result, the baseline performance of the bridge immediately after opening could be documented.

1.5 REPORT ORGANIZATION

This report is divided into seven chapters, including this introduction. Chapter 2 provides a background on the innovative design of the West 7th Street Bridge and the

motivation for the instrumentation effort. The material study to obtain the mechanical properties of the concrete used in the arches is explained in Chapter 3. Chapter 4 presents an overview of the field instrumentation program, including the detailed procedure for designing and installing the instrumentation. The post-processing procedures for interpreting the data obtained from the instrumentation are described in Chapter 5. The post-processed results from the instrumentation are presented and discussed in Chapter 6. Finally, Chapter 7 provides a summary of the scope of the study and the major findings.

Chapter Bibliography

[1] Bing Maps, [Online]. Available: http://www.bing.com/maps/. [Accessed 8 April 2014].

This page is intentionally left blank

CHAPTER 2
Background

2.1 INTRODUCTION

The West 7th Street Bridge in Fort Worth, Texas is believed to be the first precast network arch bridge in the world. This bridge consists of twelve 280-ton network arches that were built on their sides as precast elements, then rotated into a vertical position, and later installed in their final location. To make the substantial stresses induced by rotation tolerable, the arches were prestressed in both the tie and the rib. Utilizing precast structural elements for this bridge minimized the time necessary for street closures at the bridge site. However, the precast arches were subjected to large demands during construction, which had the potential to damage the arches and affect the behavior of the bridge under service conditions. The design team developed detailed finite element models of the bridge to simulate different construction stages to minimize the likelihood of damaging the arches during construction. However, although the analysis provides insight into the expected behavior of the arch, the accuracy of the analysis is contingent on several assumptions that may not accurately reflect the actual conditions in the field. Therefore, the arches were instrumented to provide an accurate picture of their behavior.

This chapter presents an overview of the West 7th Street Bridge project and the specific roles of the instrumentation in supporting the construction of the bridge.

2.2 THE WEST 7TH STREET BRIDGE REPLACEMENT PROJECT

The West 7th Street Bridge connects downtown Fort Worth to the Cultural District. With an estimated average traffic of 12,000 motorists per day [1], this structure plays an important role in the city's transportation network. As shown in Figure 2.1, the bridge spans over four lanes of traffic, the Clear Fork of the Trinity River, and a number of recreational trails.

Figure 2.1 also shows that the old West 7th Street Bridge consisted of two parts: (1) an original bridge, built in 1913 with a total length of $437ft$, including a $138ft$ arch span and girder approach spans, and (2) an expansion built in 1953, which consisted of concrete girder spans and increased the total length of the bridge to $981ft$ [2].

The old bridge had experienced significant deterioration, including carbonation, contamination with chlorides, and concrete spalling. The original decision was to rehabilitate the bridge and widen the sidewalks. However, in 2007, the city council decided to replace the bridge completely because the repairs would be very expensive, and the strengthened bridge would not probably withstand future demands and would be architecturally unpleasant [2].

The new bridge needed to carry four lanes of traffic, accommodate $10ft$-wide sidewalks, and support possible future rails for streetcars. The city council also wanted the bridge to be aesthetically elegant, consistent with the architectural setting of the Cultural District. Therefore, among several options proposed by TxDOT engineers, the council embraced a unique concrete network arch, which is introduced in this section.

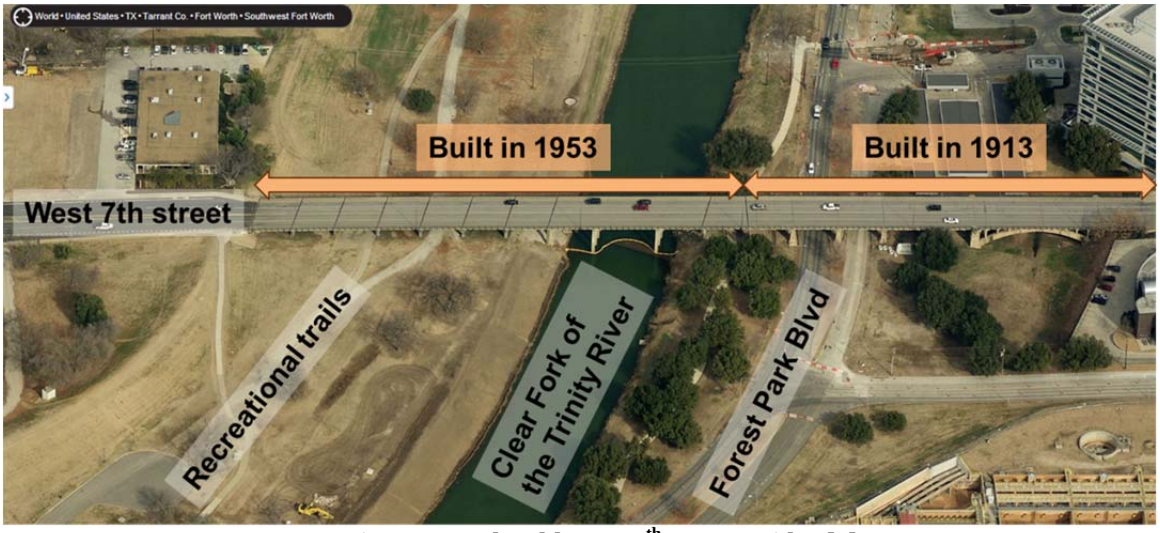

Figure 2.1- The old West 7th Street Bridge [3].

2.2.1 Structural Design of the New Bridge

The new West 7th Street Bridge has a total length of $981ft$ and a total deck width of $88ft$ and consists of six uniform spans of $163.5ft$. As can be seen in Figure 2.2, each span is supported by two concrete arches, which are located on both sides of the roadway. The deck is constructed using precast panels and a cast-in place deck and is supported by 17 transverse floor beams. The floor beams are suspended from the arches using post-tensioned bars.

The geometry and the nomenclature of the components of the arches are illustrated in Figure 2.3. The curved element on the top is called the rib, whereas the horizontal element at the bottom is called the tie. These two elements are connected to each other at both ends at a region referred to as the knuckle. All along the arch length, stainless steel rods, called the hangers, connect the tie and the rib and transfer the loads between these elements.

By definition, a network arch is a tied arch bridge with inclined hangers, in which most hangers cross at least two other hangers in the plane of the arch [4]. Due to significant material savings, steel network arches have gained popularity. However, the West 7th Street Bridge is believed to be the first precast concrete network arch bridge in the world [2].

Each concrete arch in the West 7th Street Bridge includes 52 hangers, which are located in two parallel planes, spaced $2ft$ apart from each other. The 26 hangers in each plane are parallel to each other, all with an angle of 35° from the vertical orientation. However, the hangers in two planes are inclined in opposite directions, resulting in a mesh that is typical of a network arch.

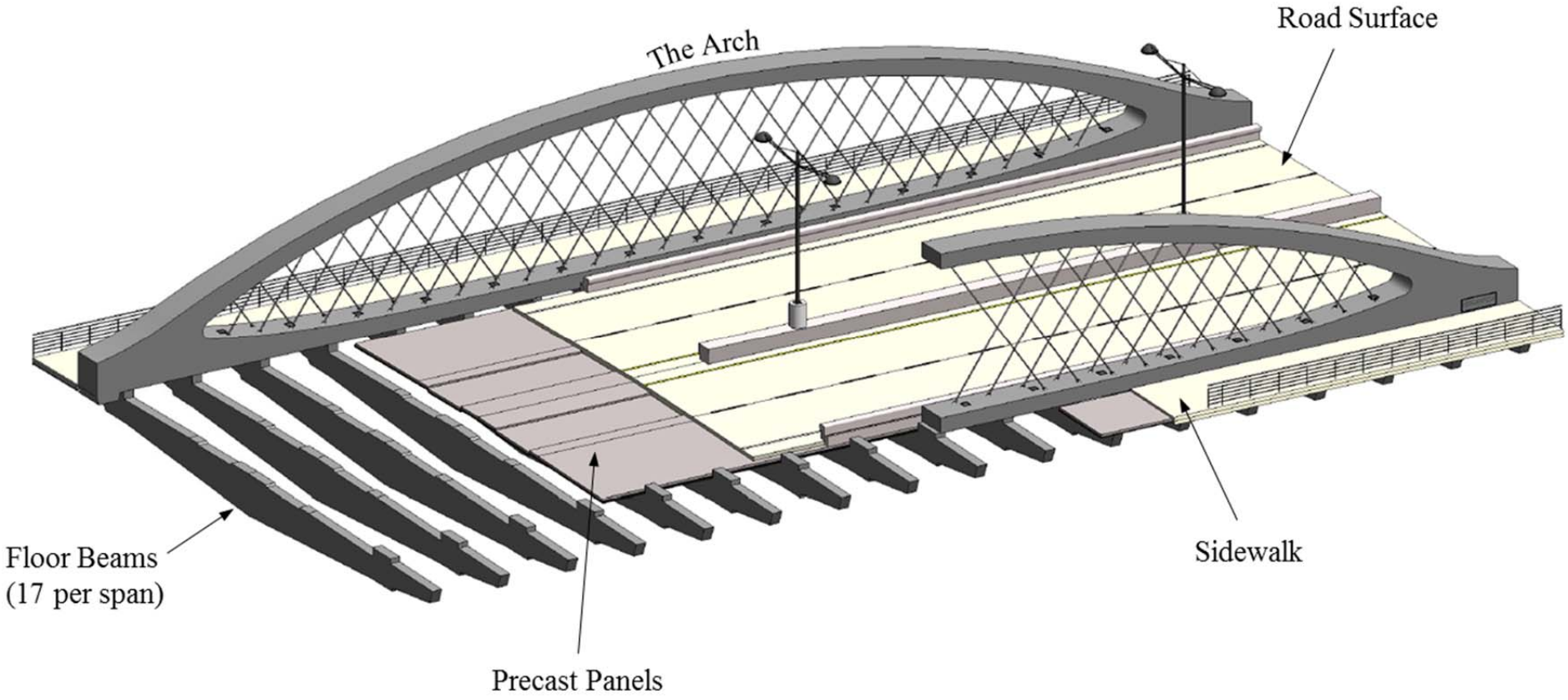

Figure 2.2-A typical span in the new West 7th Street Bridge [1].

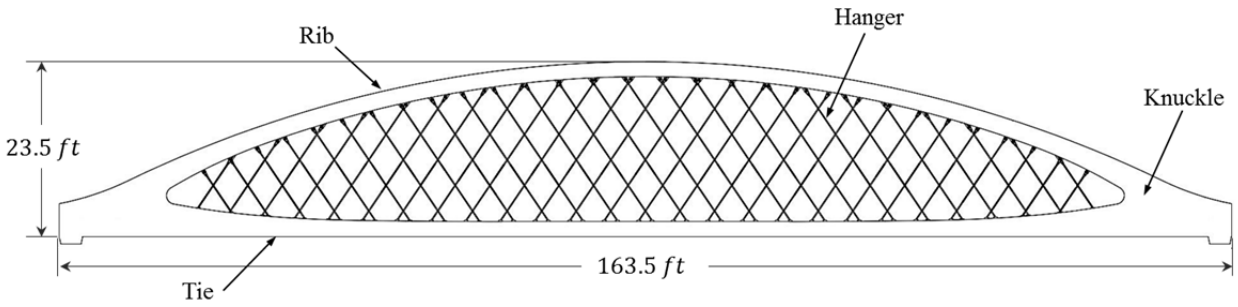

(a)

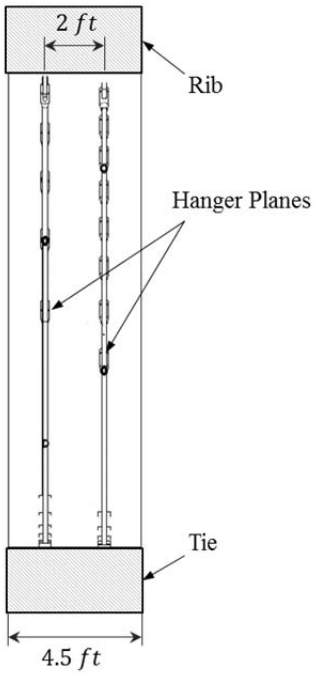

(b)

Figure 2.3- Geometry of a typical network arch in the West 7th Street Bridge [1].
(a) Elevation view. (b)Sectional view.

The vertical loads from the deck are first transferred to the floor beams and then to the tie. The tie resists vertical loads in bending between the hangers, which transfer the loads to the rib. The rib then transfers the loads to piers through compressive action. The primary structural role of the tie is not bending between hangers, but transferring tension. The tie transfers the horizontal thrust between the ends of the rib, and as such, converts the arch to a self-reacting system, which relieves the supports from horizontal reaction forces. While both rib and tie are subject to bending due to non-uniform live loads on the bridge, the lattice of inclined hangers provide a nearly continuous shear transfer between rib and tie, and therefore greatly reduce the bending moments and deflections in these elements. Moreover, the small

distance between the hanger connection points, called the nodal points, limit the unbraced length of the rib and significantly increase the in-plane buckling capacity of the arch.

Unlike most arches, the lateral stability of the West 7th Street Bridge is provided by the floor beams. For economic and aesthetic reasons, no rib cross bracing was considered in the design of this bridge. Even if desired, the relatively low rise of the arches would allow few bracing elements to be added. However, overturning moments on the arch rib are resisted by the frame action that is created by moment connections between the two arches and the floor beams. TxDOT checked the stability of this system using a three-dimensional finite element model and concluded that the *uncracked* ribs would be sufficiently stable against lateral buckling.

The floor beams in the West 7th Street Bridge are pretensioned elements with a nominal depth of 5'-6" at midspan, which is tapered down to a depth of 3' at the arches and further to a depth of 1'-9" at the ends. These floor beams are 1'-4" wide and are spaced 9'-7 ½" apart from each other. The arches sit on High-Load, Multi-Rotational (HLMR) disc bearings that are located on top of 7'-3" by 5'-6"oval piers.

2.2.2 Construction Sequence

The construction of the precast arches was carried out in a yard, less than one mile from the bridge location. The steps for constructing the arches are explained in this section.

2.2.2.1 Casting

Each arch was cast on its side in precision-made steel formwork. As can be seen in Figure 2.5 (a and b), the formwork included a fixed bottom soffit and a series of inside and outside forms, which could be attached or detached when needed. After the inside forms were installed, a variety of components, shown in Figure 2.4, were placed in the formwork, including mild steel reinforcement, Post Tensioning (PT) ducts, block-outs for floor beams and hangers, and light fixtures. Figure 2.5 (c) shows how hanger tubes and floor beam block-outs were installed in the formwork in the tie. Stainless steel plates were also placed in the rib, which were later connected to hanger clevises. The outside forms were installed last, after all of these components were in place. The contractor used two sets of formwork to facilitate work on two arches in parallel and maximize the productive time on the precasting yard.

A high performance concrete mix was used for the arches, which satisfied a variety of criteria, including low shrinkage, high strength, low heat of hydration, high slump, and low permeability. More details about the mix design are discussed in Chapter 3.

In order to reduce the undesirable effects due to excessive temperatures and thermal gradients in the concrete, several measures were taken. For arches that were cast in the summer heat, liquid nitrogen was added to the mix to reduce the temperature of the fresh concrete. Moreover, as shown in Figure 2.6(a), cooling pipes were installed in the knuckle region to reduce the internal temperatures of the concrete. Most arches were cast overnight to provide better thermal conditions in the concrete and avoid potential delays in concrete delivery due to increased traffic during daytime hours.

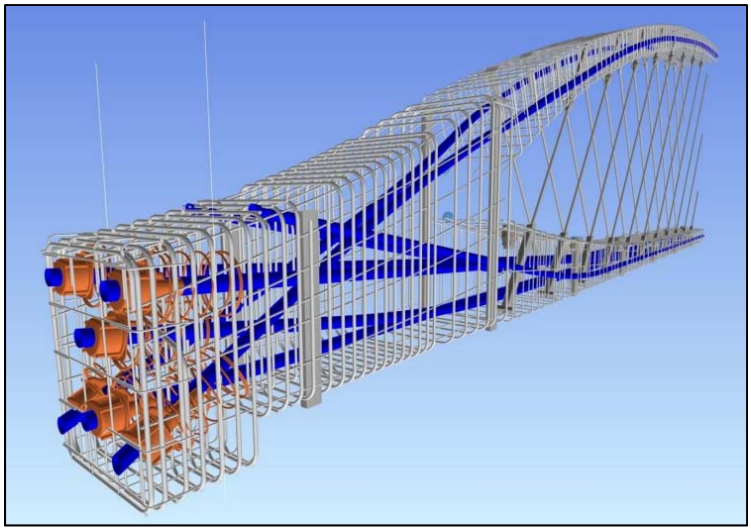

Figure 2.4- Arch details in the knuckle region. (Image courtesy of Sundt Construction)

(a)

(b)

(c)

Figure 2.5- Arch formwork. (a) The soffit and inside forms. (b) The completed formwork prior to concrete pour. (c) Hanger tubes and block-outs in the tie.

Casting of the concrete in the arches was performed continuously from one end to the other. As shown in Figure 2.6 (b and c), two concrete pumps were used to cast the rib and the tie simultaneously so that no cold joints were present in the arch, and the arch was a monolithic unit.

After 24 hours, the side forms were removed to minimize the potential for restrained shrinkage cracking. Each arch was wet cured for at least 5 days before PT operations.

(a)

(b)

(c)

Figure 2.6- Concrete casting operations. (a) Cooling pipes in the knuckle region. (b) The two concrete pumps used for casting the arch. (c) Simultaneous casting of the rib and the tie.

2.2.2.2 Stage 1 Post Tensioning

Each arch contained six PT tendons, the approximate paths of which are sketched in Figure 2.7. As can be seen in this figure, two tendons were located in the rib and four were located in the tie. Each of these tendons consisted of nineteen 0.62-inch strands. As previously mentioned, ducts that housed these tendons were installed in the formwork prior to the concrete pour. In addition to six primary ducts required for accommodating these tendons, two supplemental ducts, each capable of housing 12 strands, were placed in the tie. These ducts provided the possibility of additional post tensioning of the tie in the future, if necessary.

Stage 1 PT was carried out once the concrete reached a specified strength of 5 ksi. The main purpose of Stage 1 PT was to minimize the risk of cracking in the arch during rotation. In this stage, the rib tendons were stressed to a level of 208 ksi, which corresponded to a jacking stress of $0.77f_{pu}$. The tie tendons were also stressed to 104 ksi.

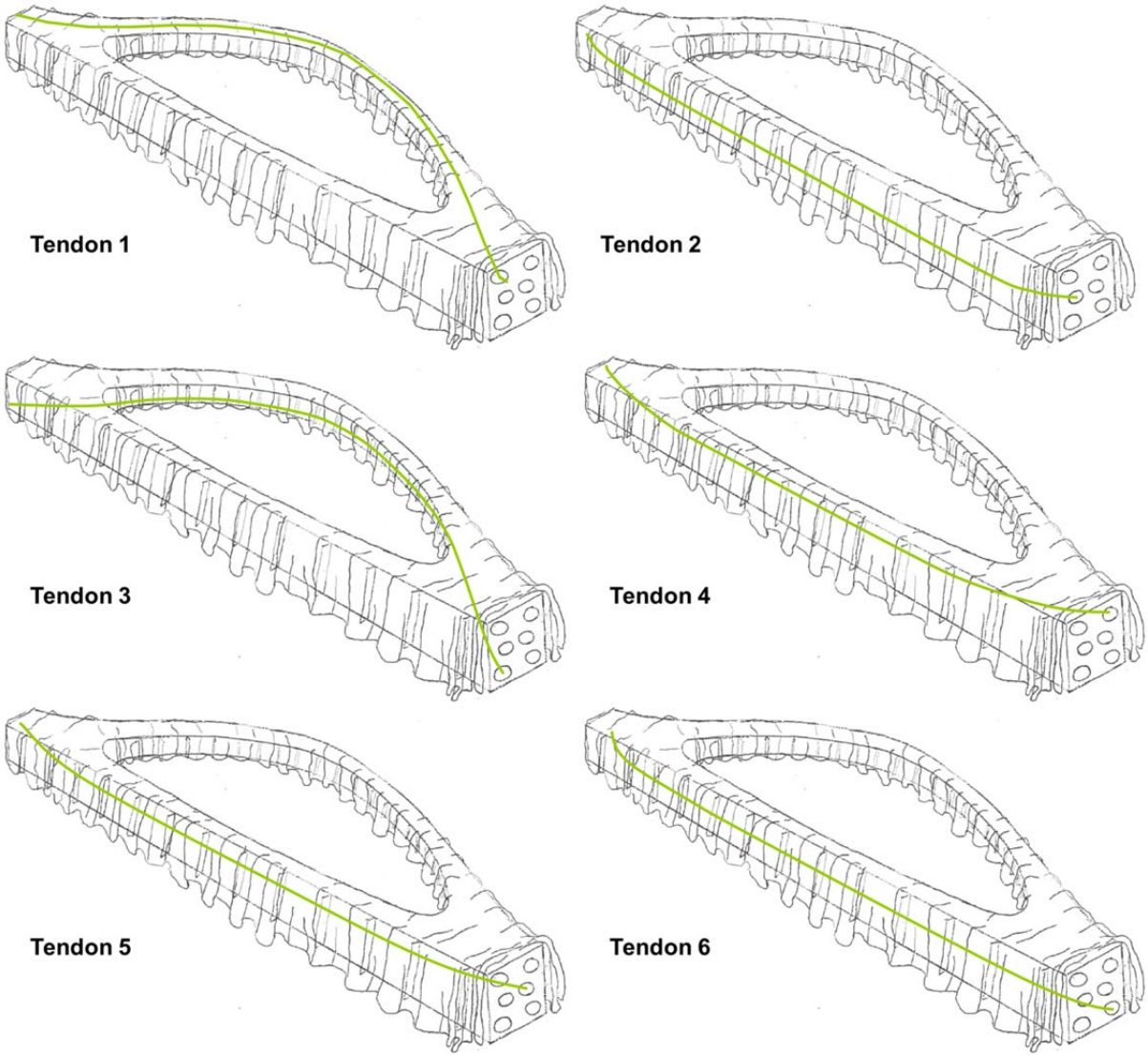

Figure 2.7- General paths of the tendons in the arches. (Drawing courtesy of TxDOT)

The tendons were post tensioned according to a sequence specified by the design team. In the first arch, the post tensioning was carried out in 26-ksi increments, which were equal to one-eighth of the final stress level. However, after the first arch, the design team allowed 52-ksi increments for stressing the tendons. The sequence of post tensioning in Stage 1 PT in the subsequent arches is presented in Table 2.1. All strands in each tendon were stressed simultaneously using a multi-strand jack, which is shown in Figure 2.8.

Since the rib tendons needed to be de-tensioned at a later stage to a level of 104ksi, the anchorage for the rib tendons was supported by a series of shims that could be removed later. The details of the anchorage for a rib tendon are shown in Figure 2.9.

Table 2.1- Stressing sequence for Stage 1 PT.

Increment No.	Tendon	Jacking stress(ksi)
1	Tendon 1	52
2	Tendon 3	52
3	Tendon 2	52
4	Tendon 4	52
5	Tendon 5	52
6	Tendon 6	52
7	Tendon 1	104
8	Tendon 3	104

Increment No.	Tendon	Jacking stress(ksi)
9	Tendon 2	104
10	Tendon 4	104
11	Tendon 5	104
12	Tendon 6	104
13	Tendon 1	156
14	Tendon 3	208
15	Tendon 1	208

Figure 2.8- The multi-strand jack.

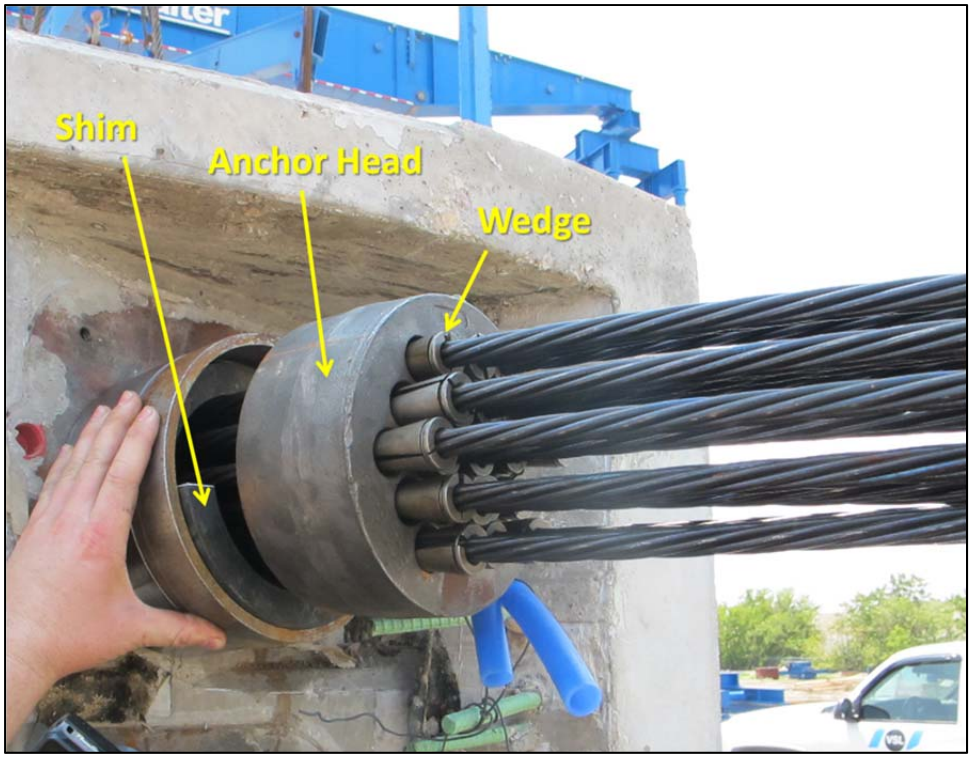

Figure 2.9- Anchorage of rib tendons in Stage 1 PT.

2.2.2.3 Rotation

Prior to rotation, the hanger elements were installed, as can be seen in Figure 2.10 (b). Each hanger was passed through a hanger tube in the tie and was threaded into a clevis at the rib. A nut was put at the other end of the hanger and was hand-tightened before rotation.

The rotation operation was accomplished through a lifting assembly in which six lifting frames, shown in Figure 2.10 (a), engaged the sides and bottom surface of the rib and the tie. The lifting frames were supported by a gantry system through a series of equalizer beams and lifting ropes above the rib and below the tie. The gantry system was equipped with strand jacks, which were installed on spreader beams capable of moving laterally for proper rotation and positioning of the arches.

According to the lifting sequence, all lifting points were first raised equally (Figure 2.11 (a)). As can be seen in Figure 2.10 (c), the arch formwork was constructed in a way that parts of the soffit could be lifted with the arch. Once clear of the formwork, only the back lifting points (at the rib) were raised, allowing the arch to pivot to its final vertical orientation, as can be seen in Figure 2.11 (b). After completing the 90° rotation, the arch was moved laterally and positioned on temporary supports, each at a distance of approximately $7ft$ from the end of the arch.

The rotation operation was performed slowly to minimize any dynamic or impact effects on the arches. Rotation of the first arch was carried out over a 6-hour period. The subsequent arches were rotated in approximately 3 hours.

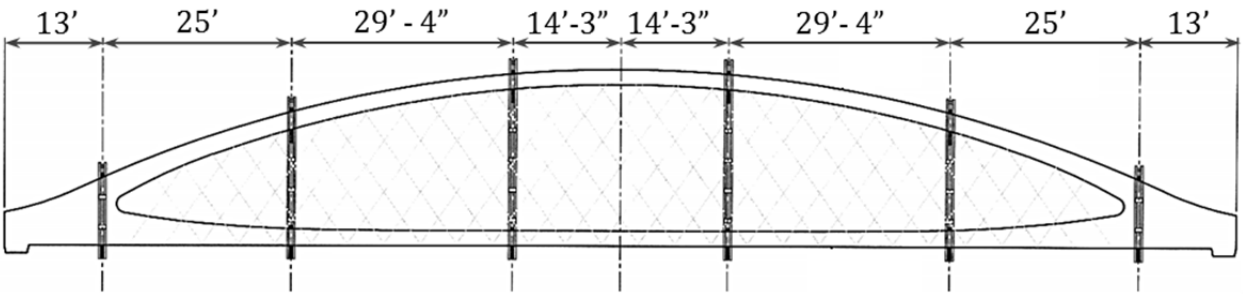

(a)

(b)

(c)

Figure 2.10- Rotation details. (a) Lifting frame spacing. (b) The hangers and lifting frames installed before rotation. (c) A part of the soffit lifted together with the arch.

2.2.2.4 Stage 2 Post Tensioning

After rotation, a second stage of post tensioning was carried out to provide the final prestressing forces in the arches. In the Stage 2 PT, the tie tendons were stressed to 208 ksi and the rib tendons were de-tensioned to 104 ksi. All of the tie tendons were stressed first, in the order shown in Table 2.2. De-tensioning of the rib tendons was performed later, after the arch sliding operation, and was accomplished by removing the shims and stressing the tendons to 104ksi. If neded, the designers allowed the construction team to de-stress the rib tendons by different amounts to adjust the out-of-plane deformations of the rib.

(a)

(b)

Figure 2.11- Arch rotation. (a) Vertical lifting. (b) Arch pivoting to the vertical orientation.

Table 2.2- Stressing sequence for Stage 2 PT on the tie.

Increment No.	Tendon	Jacking stress(ksi)
1	Tendon 2	156
2	Tendon 4	156
3	Tendon 5	156
4	Tendon 6	156
5	Tendon 2	208
6	Tendon 4	208
7	Tendon 5	208
8	Tendon 6	208

Since a significant compressive force was applied to the tie during the second stage post tensioning, there was a possibility of second order deformations under the post-tensioning force. To avoid potential instability in the tie element, the design included a series of small curves, in the duct paths so that the tendons would be in contact with the wall of the ducts after a very small lateral displacement. As a result, the second order displacement of the tie element was minimized.

After the Stage 2 PT, the extra lengths of the strands were cut, and the ducts were grouted.

Figure 2.12- Intentional curves in the duct paths.

2.2.2.5 Sliding

After the Stage 2 PT on the tie, the arches were transported to a storage area. For arches 1 to 8, this transportation was accomplished through lateral sliding of the arches, as shown in Figure 2.13. The arches were first braced for lateral stability, and then a pair of synchronized hydraulic rams was used to push the temporary supports underneath the arches incrementally. The supports moved over temporary rails until the arch arrived in its storage position. Arches 9-12 did not need any sliding operations and were set at their storage locations by the gantry system.

Figure 2.13- Sliding operation on one of the arches.

2.2.2.6 Upward Jacking

The stressing of the hangers in the West 7th Street Bridge was carried out through an upward jacking operation. As can be seen in Figure 2.14 (c), 13 hydraulic rams were positioned under the tie at the locations of future floor beams. The hydraulic rams were simultaneously activated to push the tie upward with a force of 17 $kips$. While the rams were actively engaged, sag in the hangers was manually removed, and the nuts on the hangers were re-tightened as shown in Figure 2.14 (b). The rams were then deactivated. As a result, the self-weight of the tie induced a prestress in the hangers. The design documents allowed the construction team to increase the jacking force to 20 kip if the desired camber was not achieved. However, jacking forces in excess of 17 kip was not necessary throughout the arch construction.

This method of stressing the hangers produced significant tensile stresses at the rib in the knuckle region, which could not be compensated by the prestressing forces. In the finished bridge, the weight of the floor beams and deck would compensate for the hanger stresses. However, until that stage, temporary strengthening was necessary to avoid cracking at the top of the knuckle region. Therefore, prestressed strong-backs were clamped to the rib in the knuckle region before upward jacking to strengthen the arches and prevent excessive tensile stresses. These strong-backs remained attached to the arches until the arches were moved to their final locations and all floor beams were installed in each span. Installation of the strong backs on one of the arches is shown in Figure 2.14 (a).

(a)

(b)

(c)

Figure 2.14- Upward Jacking. (a) Strong-back installation. (b) Re- tightening the hangers. (c) Arrangement of the hydraulic rams.

2.2.2.1 Arch Transportation

Once all the arches were fabricated and the piers for the new bridge were constructed on the sides of the existing bridge, the transportation and erection of the arches began. As illustrated in Figure 2.15, the arches were transported over an average distance of approximately 0.5 miles from the precasting yard to the existing bridge. Two Self Propelled Modular Transporters (SPMTs), which are shown in Figure 2.16 (a), carried each arch from the precast yard to the destination, where two cranes lifted the arch and installed it on bearings (Figure 2.16 (c)). During transportation, the arches were supported at their knuckle regions, as can be seen in Figure 2.16 (b).

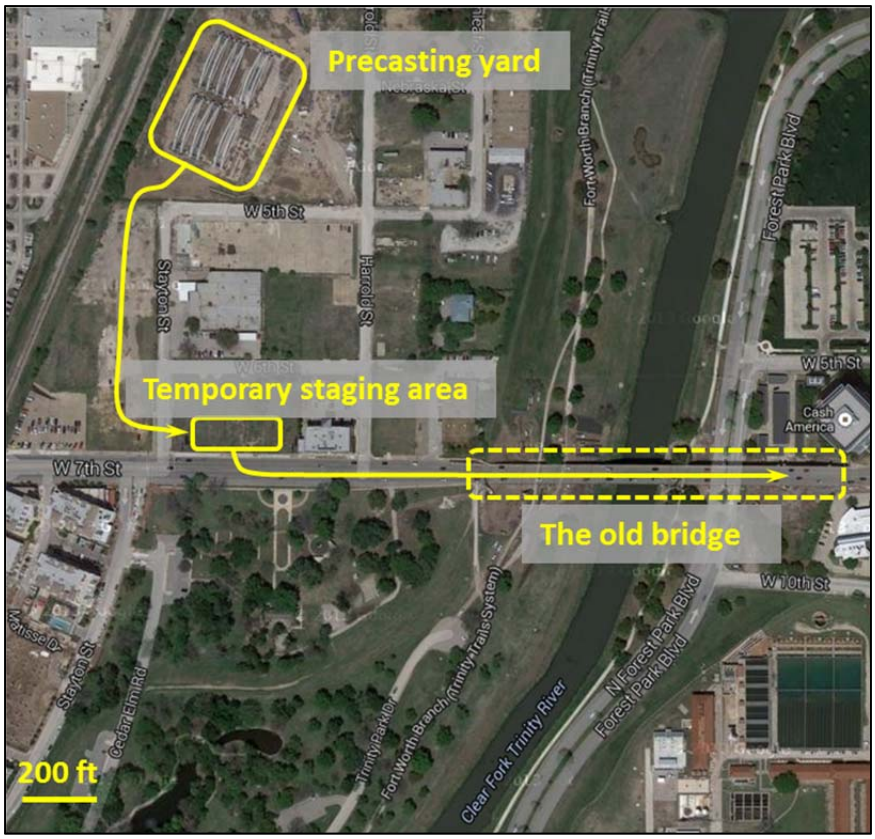

Figure 2.15- The transportation path [5].

After installation on bearings, the arches were braced for lateral stability using steel members. For each span, the first arch was stabilized using diagonal bracing members. However, once the second arch was installed in that span, top lateral braces were added between the two arches and the diagonal members were removed. The bracing members on the arches are visible in Figure 2.17.

(a)

(b)

(c)

Figure 2.16-Arch transportation. (a) The arch leaving the precasting yard on SPMTs. (b) The location of arch support on the SPMTs. (3) Installation of the arch on the bearings.

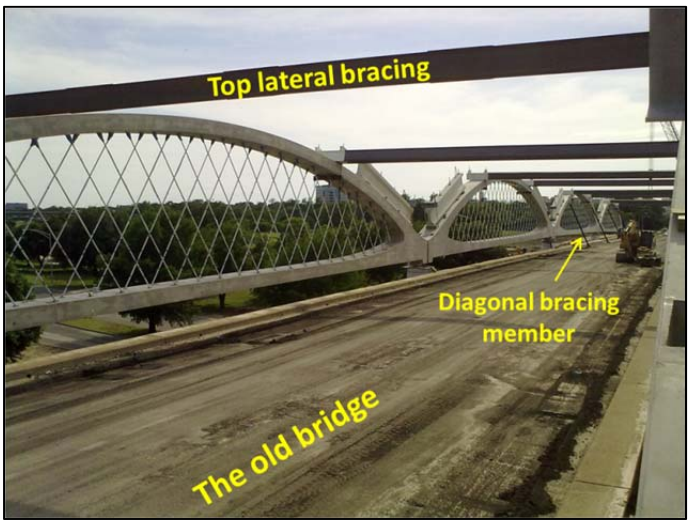

Figure 2.17- Temporary bracing of the arches.

2.2.2.2 Deck Construction

Once all the arches were installed on bearings and properly braced, the demolition of the old bridge began. For each span, soon after demolition of the old bridge, the floor beams were installed.

The floor beams were first simply hung from the arches using two post tensioning bars, as can be seen in Figure 2.18. A bed of epoxy grout, with a thickness of approximately 0.5” and plan dimensions of 1’-4” by 4’-2”, was then placed on top of the floor beams under the arch ties. The floor beams were then raised until they were in contact with the arches. When the grout reached the specified strength, the post tensioning bars were stressed, as shown in Figure 2.19, and the floor beam block-outs were grouted.

Figure 2.18- Initial hanging of the floor beams.

Figure 2.19- Post tensioning the floor beam bars.

After the floor beams were installed, precast deck panels were positioned above bedding strips on the floor beams, as shown in Figure 2.20. A final topping slab with a nominal thickness of 4.5 inches was then placed over the precast panels.

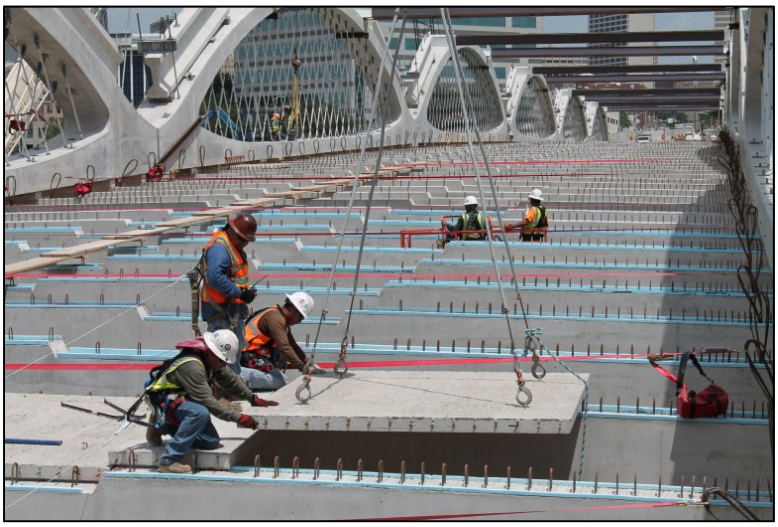

Figure 2.20- Installation of the precast panels. (Photo courtesy of TxDOT)

2.2.3 Construction timeline

Figure 2.21 shows the construction timeline for the new West 7th Street Bridge. The project was awarded to Sundt Construction in June 2011 at a cost of $209 per square foot [2]. The first arch was cast in July 2012 and the last arch was cast in February 2013. The old bridge was closed on June 7, 2013, and the new bridge was opened to traffic ahead of schedule, on October 9, 2013.

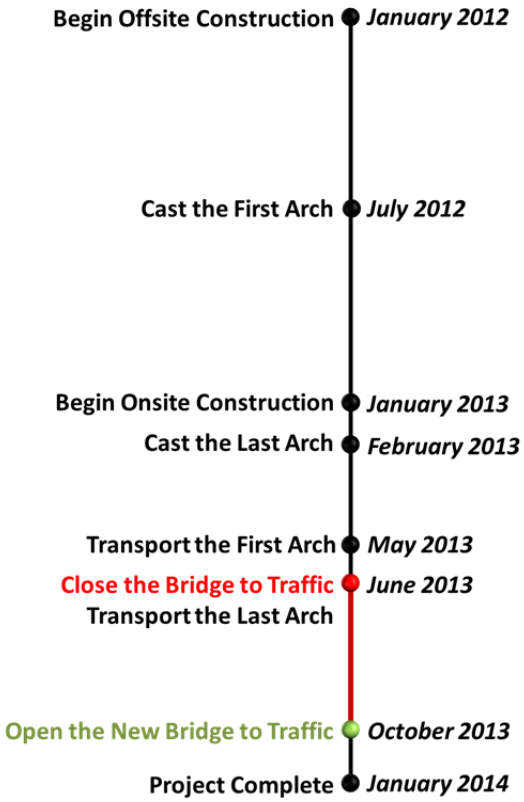

Figure 2.21-Construction timeline for the West 7th Street Bridge project.

2.3 MOTIVATION FOR INSTRUMENTATION

The innovative construction procedure for the West 7th Street Bridge minimized the onsite construction and limited the street closure time to 120 days. However, several concerns were raised regarding the performance of the arches, mainly because some of the most critical stresses throughout the life of the structure happened during construction.

All the design calculations for the West 7th Street Bridge were based on the assumption that the arches were crack-free. Cracking is generally a serviceability concern in most structures. However, potential cracking of the arches during construction could significantly reduce the stiffness of the rib element and result in potential out-of-plane instability of the arches in the finished bridge, especially because no top lateral bracing was used. Therefore, several measures were taken during design to make sure the arches did not experience excessive tensile stresses so that the behavior of the arches would follow the uncracked section assumptions.

To calculate the structural stresses, TxDOT developed sophisticated nonlinear finite element models of the bridge in LUSAS, shown in Figure 2.22. The models included time-dependent behavior of concrete and staged construction. However, uncertainties existed about the modelling assumptions, especially because the structure was the first of its kind. On the other hand, the work plan for the arch handling operations was primarily developed by the contractor and was out of direct control of the design team.

Another concern about the construction process was the potential effect of variable through-thickness material properties on the arch performance. The aggregates in the concrete have a tendency to settle while bleed water moves in the upward direction. As a result, since the arches were cast in a horizontal position, the modulus of elasticity of the concrete could vary through the width of the arch, as shown in Figure 2.23. The variable stiffness of the material could result in out-of-plane deformations of the arches, known as "sweep". As mentioned in Section 2.2.2.4, the designers allowed the construction team to de-tension the rib tendons by different amounts in the second stage post tensioning so that the sweep could be removed from the arch ribs. The design team preferred to have accurate measurements of the strain through the width of the arch to be able to control the sweep more effectively.

There were also concerns regarding the stability of the arches during post tensioning. As previously mentioned, the arch elements were subjected to large prestressing forces. In particular, the relatively slender tie element had to tolerate a compressive force of approximately 3500 $kips$ after the second stage of post tensioning. The designers provided the intentional curves in the duct paths, introduced in Section 2.2.2.4, to limit the second-order deformations of the tie element. However, if this method was not effective, the tie element could experience excessive lateral deformations and potentially buckle. Therefore, it was desirable to have an indicator of the second-order deformations and make sure of the stability of the arches during post tensioning.

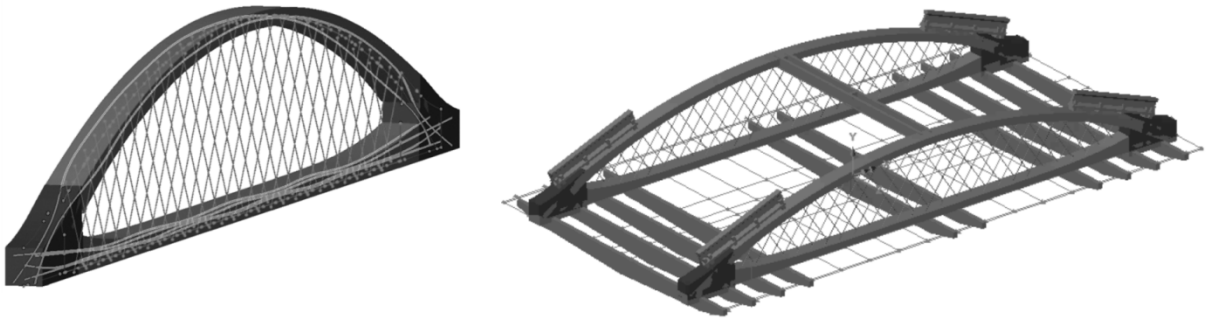

Figure 2.22- Models of the arches in LUSAS [6].

In response to these concerns, TxDOT decided to initiate this field monitoring study to instrument the arches and make sure that they were not damaged during construction. As part of field monitoring, the researchers from UT instrumented and monitored the arches during casting, post tensioning, handling operations, and deck construction to evaluate the structural behavior. As a result, the researchers could detect impending problems and inform the design engineers and the construction team. The instrumentation was therefore a valuable tool that could assist with making decisions about modifying the construction procedure when needed. Moreover, the measured stresses in the structure could be used to verify the

design calculations and assess the validity of the assumptions made in the modeling of the structure.

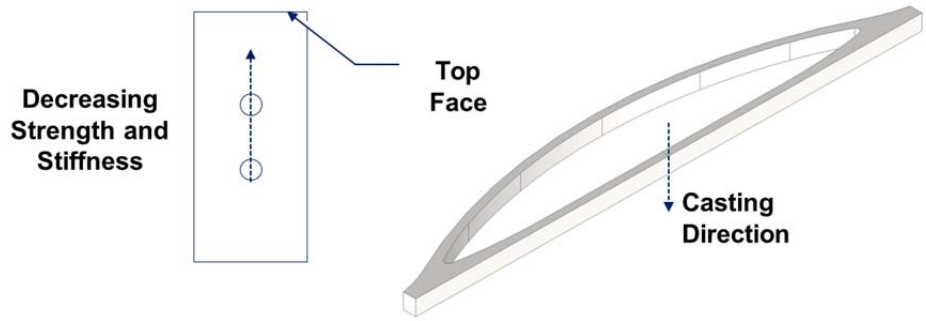

Figure 2.23- Effect of casting direction on variability in material properties

2.4 ROLES OF INSTRUMENTATION

The instrumentation in the West 7th Street Bridge had the specific roles described in this section.

2.4.1 Monitoring the Stresses during Construction

Monitoring the stresses was the primary role of the instrumentation and had two major objectives: (1) to make sure the arches were not damaged during construction operations (2) to verify the design assumptions.

Ensuring the safety of the arches required continuous monitoring of the installed sensors during construction operations to make sure that the arches did not experience excessive stresses. The researchers carefully evaluated the structure's response and informed the designers and the construction team of potentially alarming conditions or critical stresses that were not anticipated in design.

Concrete is generally strong in compression but weak in tension. If tensile stresses in excess of the tensile strength of concrete were developed in the arches, cracking would occur. Therefore, it was essential to observe potential tensile stresses in the arches and make sure that they were below the tensile strength of concrete. The allowable tensile stress in the concrete was conservatively estimated by Equation (2.1). The allowable compressive stress was also assumed to be 50% of the estimated compressive strength of the concrete at any time.

$$f_t(t) = 4\sqrt{f_c'(t)} \tag{2.1}$$

Where,

f_t = Allowable tensile stress in the concrete at time t, psi

f_c' = Compressive strength of the concrete at time t, psi

The stresses could also be used during post tensioning operations to evaluate the axial load distribution in the structure. The researchers could use this information to detect inconsistent force distribution along the arches, which could indicate a jammed tendon.

To verify the design assumptions, the measured stresses were compared with the design calculations only at certain times, which corresponded to the end of specific construction operations.

2.4.2 Monitoring the Hydration Temperatures in the Concrete

Concrete hydration is an exothermic reaction. As a result, the temperatures increase in the concrete early in the hydration process. Knuckle regions of the structure consist of large masses of concrete. Consequently, the heat of hydration is diffused slowly in these regions, and there is a potential for excessive temperatures, or excessive thermal gradients between the depth and the surface of the concrete. Undesirably high temperatures early in the hydration process can affect the long-term durability of concrete. Moreover, large thermal gradients might lead to thermal cracks in the recently cast concrete. While several measures such as using liquid nitrogen and cooling pipes were taken to reduce the temperatures in the knuckle region, the temperatures recorded by the instrumentation could verify the effectiveness of those measures and ensure that the arches did not experience undesirably high temperatures.

Monitoring the hydration temperatures could also indicate the in-situ maturity of the concrete. The recorded thermal history could be used to estimate the realistic mechanical properties of the concrete such as compressive strength and modulus of elasticity.

2.4.3 Monitoring the Lateral Stability during Post Tensioning

The data from the instrumentation were used as an indicator of the stability of the arch elements during post tensioning. The strains measured in the cross sections were used to find the internal axial loads and curvatures. The plots of axial load versus in-plane and out-of-plane curvatures were qualitatively assessed during post tensioning to detect any nonlinear lateral deformations under axial load increments, which could indicate impending buckling.

2.4.4 Sweep Control

If necessary, the design team intended to control the sweep by using different forces in the rib tendons. The instrumentation provided accurate measurements of the out-of-plane curvatures, which could potentially be used to verify the satisfactory removal of the sweep. Therefore, the designers could potentially set a limit on the out-of-plane curvature of the arches as the acceptance criteria for sweep control. However, this capability of the instrumentation was not used in the project. The contractor checked the out-of-plane deformations through surveying and measured a total sweep smaller than 1” in the arch ribs. Therefore, no sweep control operations were carried out, and the rib tendons were de-tensioned to the same amount in all arches.

2.4.5 Monitoring the Long-Term Changes

The strains measured by the instrumentation provided valuable data on the thermal response of the arches and time-dependent changes due to concrete creep and shrinkage. The data was also used to evaluate the prestress losses throughout construction.

The focus of the instrumentation effort was on assisting with the construction of the arches in the West 7th Street Bridge. However, as discussed in Chapter 4, the sensors that were used in this project can be used to provide reliable data from the arches for decades to

come. The embedded gages can be used to evaluate the long-term changes in the structure and to make decisions regarding the maintenance of the bridge in the future.

2.5 SUMMARY

The new West 7th Street Bridge was built with an innovative construction method, which was described in this chapter. The precast arches were constructed in a casting yard less than one mile away from the bridge location and were later transported to their final locations. As a result, the time of street closure was limited to 120 days and the interruption to traffic was minimized. However, several post tensioning and handling operations were needed, which posed a cracking risk to the arches. Cracking during construction could be detrimental to the stability of the arches in the finished bridge. Therefore, TxDOT initiated this field instrumentation study to ensure that the arches were not damaged during construction and to verify the design assumptions. The instrumentation was a valuable tool during construction to measure the stresses and internal temperatures as well as in-plane and out-of-plane curvatures of structural elements. The embedded gages can also be used for long-term evaluations of the bridge in the future.

The information presented in this chapter provides a valuable background for the remainder of this report. The material study, which was a prerequisite for interpreting the instrumentation data from the West 7th Street Bridge, is discussed in the next chapter, followed by a comprehensive description of the field instrumentation program in Chapter 4.

Chapter Bibliography

[1] J. Blok, "Stress Monitoring and Sweep Control Studies for Innovative Prestressed Precast Arches," Master's Thesis, The University of Texas at Austin, Austin, TX, 2012.

[2] D. Van Landuyt, C. Holle and J. Aparicio, "Precast Network Arch Bridge," in *PCI Convention and National Bridge Conference*, Grapevine, TX, 2013.

[3] Bing Maps, [Online]. Available: http://www.bing.com/maps/. [Accessed 8 April 2014].

[4] P. Tveit, "Considerations for Design of Network Arches," *ASCE Journal of Structural Engineering*, vol. 113, no. 10, pp. 2189-2207, 1987.

[5] Google Maps, [Online]. Available: www.maps.google.com. [Accessed 12 July 2013].

[6] Lusas, "West 7th Street Bridge," [Online]. Available: http://www.lusas.com/case/bridge/west_7th_street_bridge.html. [Accessed 26 April 2014].

CHAPTER 3
Material Studies

3.1 INTRODUCTION

Accurate information on the mechanical properties of concrete is essential in calculating the stresses in the structure from measured strain data and also in identifying the allowable stress limits during each stage of construction. Among the parameters representing the mechanical behavior of concrete, the two most important are the elastic modulus (E) and the compressive strength (f_c') of the concrete, both of which are time dependent.

In the West 7th Street Bridge project, compressive strength testing at different ages was a regular quality control procedure. However, the quality control process did not include any tests for modulus of elasticity. Although many equations are available in the literature for estimating E from f_c' values, the scatter in the databases used for calibrating each of those equations might result in large errors for a particular concrete mix. Therefore, prior to the beginning of the construction, a mix-specific material study was conducted in Ferguson Structural Engineering Laboratory (FSEL) to provide E and f_c' values at different concrete ages.

Since the arches in the West 7th Street Bridge are indeterminate, time-dependent properties of the concrete, namely creep and shrinkage, are also critical in converting the measured strain history to a reliable stress history. While it would have been ideal to have an extensive material study for time-dependent parameters, it was beyond the scope of this project and also impractical considering the available resources. As a result, the test program was limited to instantaneous parameters, but reliable time-dependent models that are available in the literature were used to represent the time-dependent behavior. The results obtained from the models were later verified using the data obtained from the instrumentation.

This chapter describes the measurement process and the results of the material test program. An overview is also provided of the methodology that was applied in the combination of the material test results, maturity studies conducted by the construction team, and the recorded temperature history to obtain more realistic estimates of the in-situ parameters in the structure.

3.2 THE MIX

A high performance concrete (HPC) mix was designed by the ready mix supplier, TXI Inc., to meet several criteria, including:

- low shrinkage, to minimize the risk of cracking during curing,
- low heat of hydration, to reduce the risk of cracking due to thermal gradients,
- high slump, to eliminate concerns regarding proper consolidation of concrete,
- high strength
- low permeability [1]

The ingredients and important parameters of the mix design are introduced in Table 3.1 and Table 3.2, respectively.

Table 3.1- Concrete mix ingredients (as designed).

Component	Type	Description/Source	Units	Quantity
Water	-	City water	lb/cy	250
Cement	Type I/II	TXI Cement(Midlothian, TX)	lb/cy	525
Aggregate	Coarse Aggregate(3/4")	Crushed Limestone (TXI Bridgeport Grade 5)	lb/cy	1500
	Intermediate Aggregate(3/8")	Crushed Limestone (TXI Bridgeport Grade 8)	lb/cy	200
	Fine aggregate 1	Siliceous Sand (TXI Tin Top Sand)	lb/cy	692
	Fine aggregate 2	Crushed limestone (TXI Bridgeport manufactured sand)	lb/cy	692
Admixtures	Set Retarder(B)	Delvo Stabilizer (BASF Master Builders)	oz/cy	14
	Water Reducer(A)	Pozzolith 200N (BASF Mater Builders)	oz/cy	21
	High Range Water Reducer(F)	PS 1466 (BASF Mater Builders)	oz/cy	32
	Shrinkage Reducer	Tetraguard AS20 (BASF Mater Builders)	oz/cy	128
SCM	Class F Fly ash	Headwater Resources(Jewett, TX)	lb/cy	175

Table 3.2- Concrete mix parameters.

Parameter	Units	Quantity
Slump	in	9
Target 28 days Compressive Strength	psi	7900
Cementitious Material Content	lb/(cu ft)	25.9
Fly ash replacement ratio	%	25
Water/Cementitious Material Ratio	lb/lb	0.36
Aggregate/Cement Ratio	lb/lb	4.4
Typical air content	%	1.4

3.3 THE SPECIMENS

In order to confirm the satisfactory placement of concrete in the arches, the contractor constructed a mock-up piece of the arch at the site in Ft Worth on May 24, 2012 at 5:00 AM. Using the mock-up concrete, TxDOT personnel prepared forty-eight 4-inch by 8-inch concrete cylinders in plastic molds and delivered them to FSEL the following day. The plastic molds were then removed and the cylinders were stored in a water tank. Prior to testing each specimen, the cylinder's top and bottom faces were ground using a cylinder grinder to provide a smooth surface for the test. Therefore, neoprene pads or sulphur capping were not used at the ends of the cylinders during the tests.

3.4 TESTING PROCEDURE

All of the 48 concrete cylinders were tested for modulus of elasticity. Since the specimens are loaded only up to 40% of their compressive strength in the modulus test, they are assumed to remain in the elastic range and can be used for compressive strength or split cylinder tests. A total of 40 out of the 48 cylinders were tested for compressive strength while eight cylinders were used for split-cylinder testing.

The modulus of elasticity tests were conducted according to ASTM C469 [2]. As shown in Figure 3.1, this standard defines the modulus as the slope of the chord between two points: (1) a point corresponding to a very small strain of 50 με and (2) a point corresponding to a stress of $0.4f'_c$. The compressive load was applied and measured using a 400-kip testing machine and the deformations were measured using a compressometer, as shown in Figure 3.2. The compressometer was fixed to the cylinder using screw pins and the displacements were measured using a spring-loaded dial gage.

The compressive strength tests and split cylinder tests were conducted according to ASTM C39 [3] and ASTM C496 [4], respectively. The same 400-kip testing machine was used for the splitting tensile strength tests. The splitting test on one of the specimens is shown in Figure 3.3.

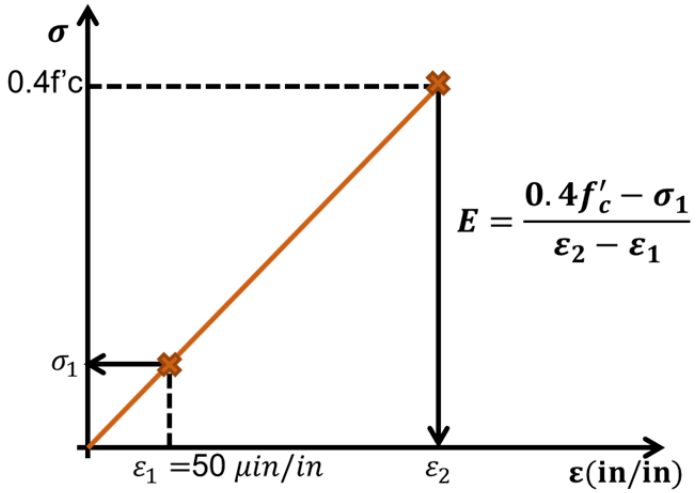

Figure 3.1- Modulus of elasticity of concrete according to ASTM C469.

(a)

(b)

Figure 3.2- Testing equipment: (a) compressometer (b) 400-kip testing machine.

Figure 3.3- Testing for splitting tensile strength.

3.5 TEST RESULTS

The results from the modulus of elasticity tests, compressive strength tests, and split cylinder tests are shown in Figure 3.4 and Table 3.3. As can be seen in Figure 3.4, the data points from the cylinders tested at the ages of 35 and 56 days are inconsistent with the trend observed in other data points. As a result, these points were considered as outliers and were not used in any further analysis of the data. The inconsistency may be due to errors during testing or to different level of compaction in making those particular specimens.

The results show that modulus of elasticity develops much faster than the compressive strength. For example, at the age of 1.5 days, the modulus is 80% of the modulus at the age of 49 days while the compressive strength is only 45% of the 49-day strength.

(a)

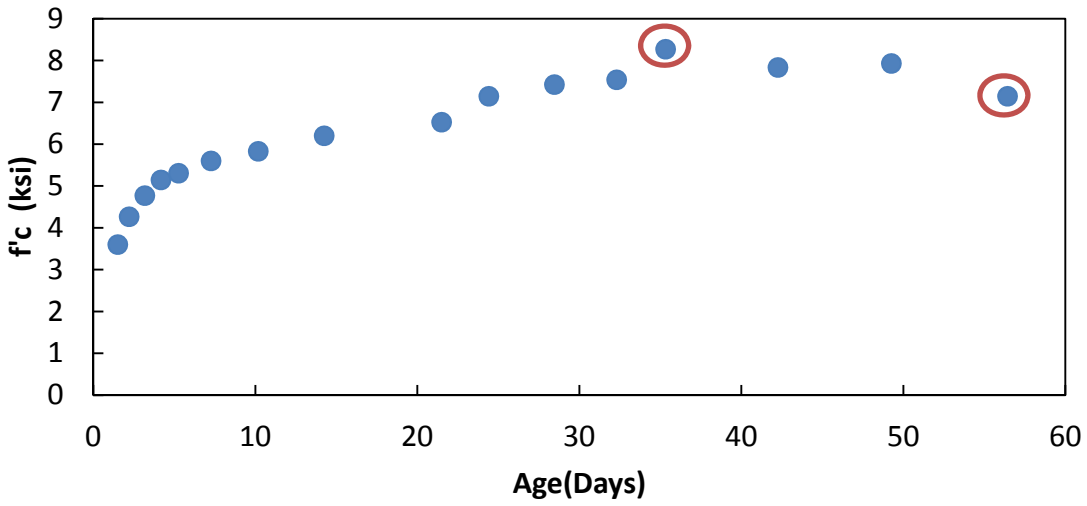

(b)

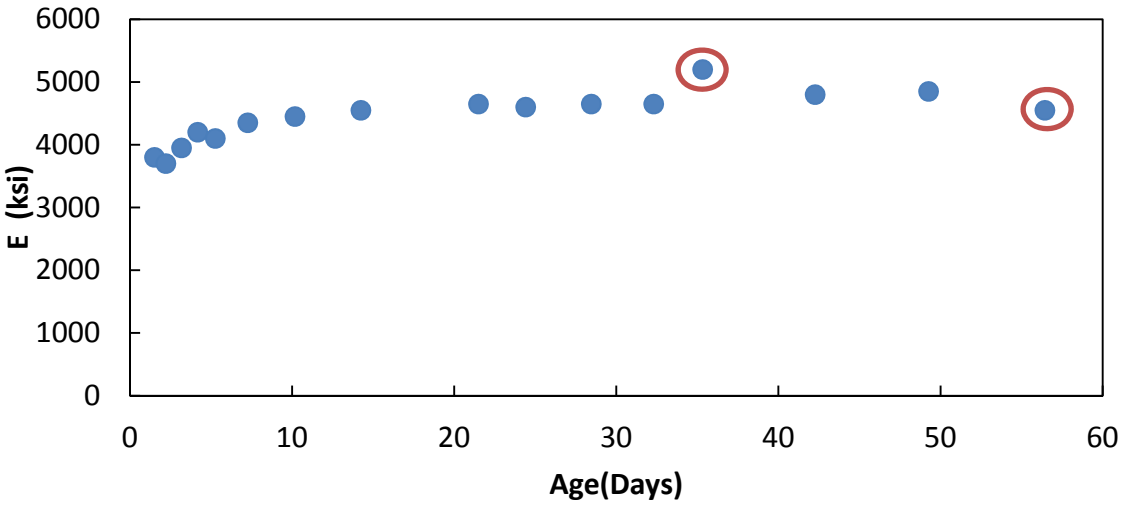

(c)

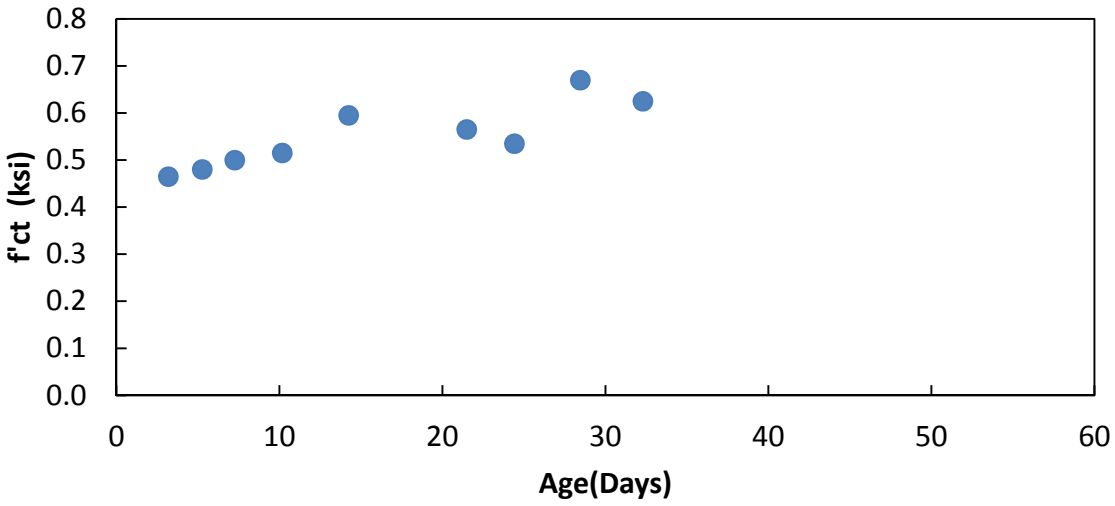

Figure 3.4-Results of concrete cylinder tests.
(a) Compressive strength (b) Modulus of elasticity (c) Splitting tensile strength

Table 3.3- Results of the material test program.

Age(Days)	$E_{ave}(ksi)$	$f'_{c_{ave}}(ksi)$	$f'_{ct}(ksi)$
1.5	3800	3.6	-
2.2	3700	4.3	-
3.2	3950	4.8	0.47
4.2	4200	5.1	-
5.3	4100	5.3	0.48
7.3	4350	5.6	0.50
10.2	4450	5.8	0.52
14.2	4550	6.2	0.60
21	4650	6.5	0.57
24	4600	7.1	0.54
28	4650	7.4	0.67
32	4650	7.5	0.63
35	5200	8.3	-
42	4800	7.8	-
49	4850	7.9	-
56	4550	7.1	-

3.6 ANALYSIS

3.6.1 Modulus-Compressive Strength Correlation

The age-dependent compressive strength and modulus results were combined to obtain a mix-specific correlation equation between E and f'_c values. This equation makes it possible to estimate E values from the f'_c values reported at each stage of construction by the quality control team. Moreover, the equation plays an important role in the procedure for estimating the in-situ E values, as explained in Section 3.6.3.

The first step in developing the correlation was to select an appropriate format for the equation. The equations in ACI318 [5] and AASHTO LRFD [6] for E have the general form of Equation (3.1).

$$E = C_1\sqrt{f'_c} \tag{3.1}$$

In this equation, C_1 is a constant, which is dependent on the density of the concrete. In AASHTO LRFD, the constant is also dependent on the aggregate type. This form of equation is generally less satisfactory in representing higher strength concretes and was not consistent with the results obtained in this study. On the other hand, ACI363 [7] introduces several E vs. f'_c equations for high strength concrete, which are in the form of either Equation (3.2) or Equation (3.3).

$$E = C_1\sqrt{f'_c} + C_2 \tag{3.2}$$

$$E = C_1(f_c')^{\alpha} \tag{3.3}$$

In these equations, C_1 and C_2 are constants and α is a number between 0.3 and 0.33.

As shown in Figure 3.5, the form of Equation (3.2) provides a suitable fit to the data obtained from the FSEL tests conducted as part of this project. For simplicity, the coefficients from the regression analysis were rounded, and Equation (3.4) was obtained. This equation is used throughout this project to correlate E and f_c' values in the arches.

$$E_{ksi} = 39\sqrt{f_{c\,psi}'} + 1350 \tag{3.4}$$

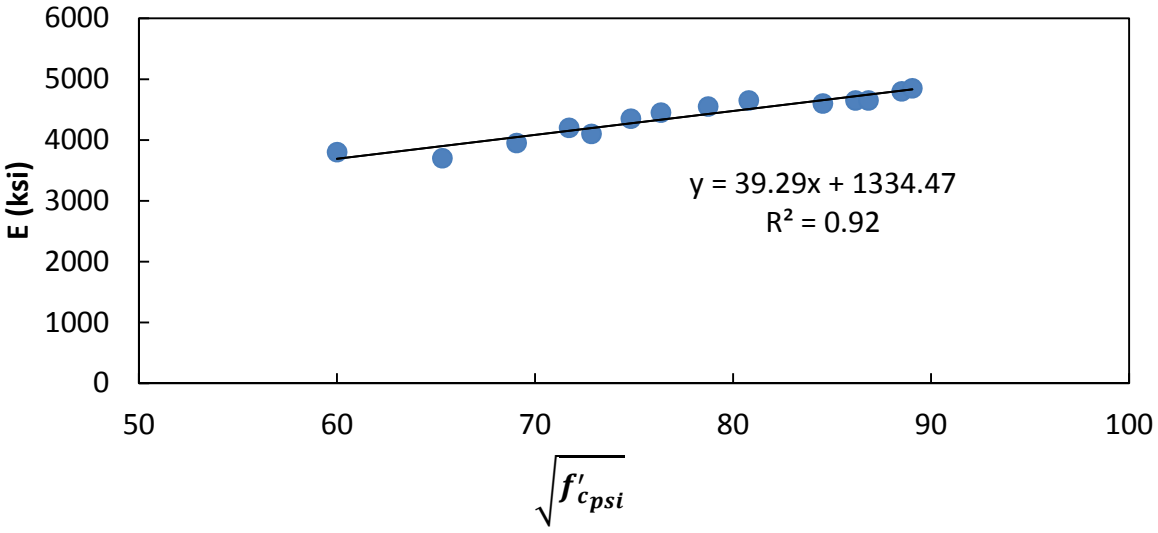

Figure 3.5- The mix-specific correlation between *E* and $\sqrt{f_c'}$.

Figure 3.6 compares the results of Equation (3.4) with ACI318, Eurocode 2 (for limestone concrete) [8], and NCHRP 496 [9] equations. Although Eurocode 2 equation has a format dissimilar to that of Equation 3.4, Figure 3.6 shows a very good agreement between the results from Equation 3.4 and Eurocode 2.

3.6.2 Splitting Tensile Strength

Only eight concrete specimens were tested for splitting tensile strength (f_{ct}). Although there was significant scatter in the data, and few data points were available, an attempt was made to correlate the obtained f_{ct} values with $\sqrt{f_c'}$.

As can be seen in Figure 3.7, Equation (3.5) provides a reasonable estimate of the splitting tensile strength of the concrete used in the arches. This equation is consistent with $6.7\sqrt{f_c'}$, which is recommended in ACI 318 commentary for the average splitting tensile strength of normal weight concrete. [5]

$$f_{ct_{psi}} = 7\sqrt{f'_{c\,psi}} \tag{3.5}$$

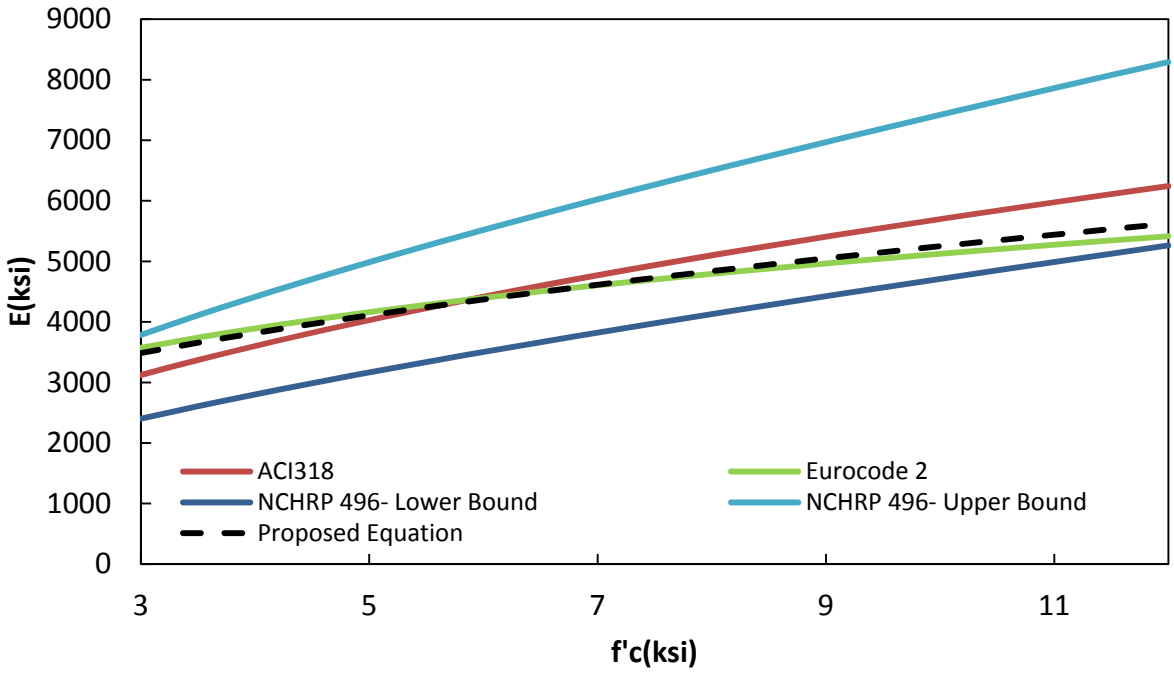

Figure 3.6- Comparison between the proposed *E* vs. f'_c equation and some commonly used equations.

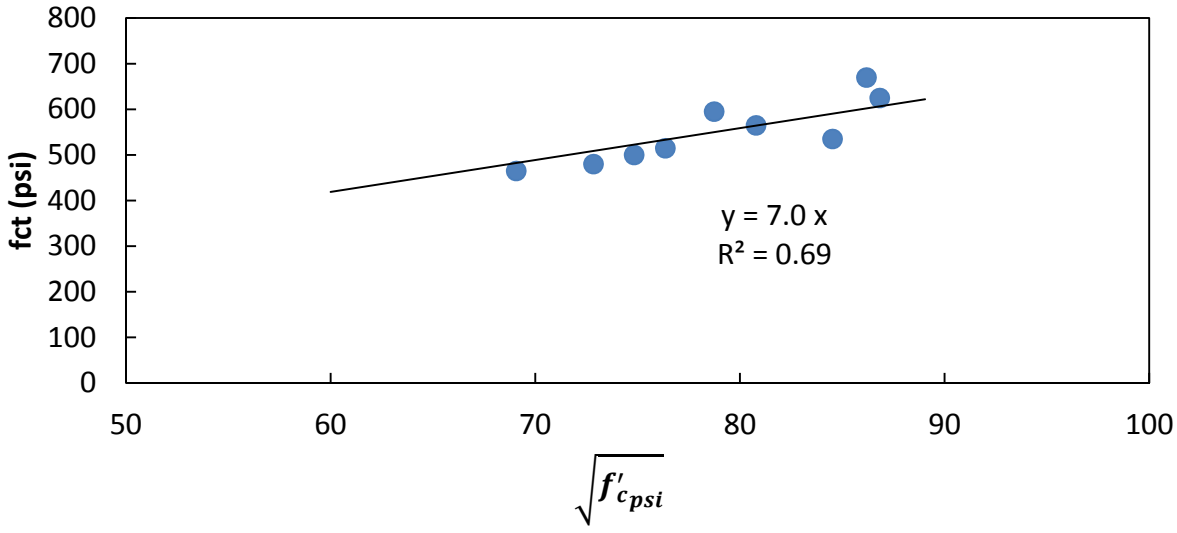

Figure 3.7- The mix-specific correlation between f_{ct} and $\sqrt{f'_c}$.

3.6.3 Estimating the In-Situ Mechanical Properties of Concrete

The rate of strength and stiffness development in concrete depends on its thermal history, which is a function of the concrete mix design, geometry of the concrete element, ambient temperatures and placing temperatures, the type of formwork, and curing method [10]. Therefore, accurate measurements of concrete mechanical parameters should be taken from the concrete that has experienced the same thermal history as the concrete in the real structure. Although quality control (QC) concrete cylinders are usually cured next to the concrete member, they experience different temperature histories due to their different geometry and rate of heat diffusion. In most cases, the cylinders experience lower temperatures than the concrete members, and as a result, the in-situ compressive strength may be underestimated from cylinder tests. However, the difference is most noticeable at early concrete ages and typically diminishes over time [10].

In order to obtain a more realistic estimate of concrete strength at early ages, maturity measurements and match-curing techniques have become popular in the precast industry, where early removal of the forms or early prestress transfer is of financial benefit. In match curing, the temperature profile is measured in the real structure, and concrete cylinders are cured using the actual temperature profiles before being tested for compressive strength.

By definition, maturity is the extent to which a property of the mixture is developed. One commonly used indicator of maturity is the temperature-time factor, M(t), which is determined from Equation (3.6) [11]. If the datum temperature is chosen to be 0 ℃, M(t) is equal to the area under the temperature vs. time plot, as shown in Figure 3.8.

$$M(t) = \Sigma(T_a - T_0) \times \Delta t \tag{3.6}$$

where:

$M(t)$ = the temperature-time factor at age t, $°C - hours$
Δt = time interval, $hours$
T_a = average concrete temperatures during time interval Δt, $°C$
T_0 = datum temperature, $°C$

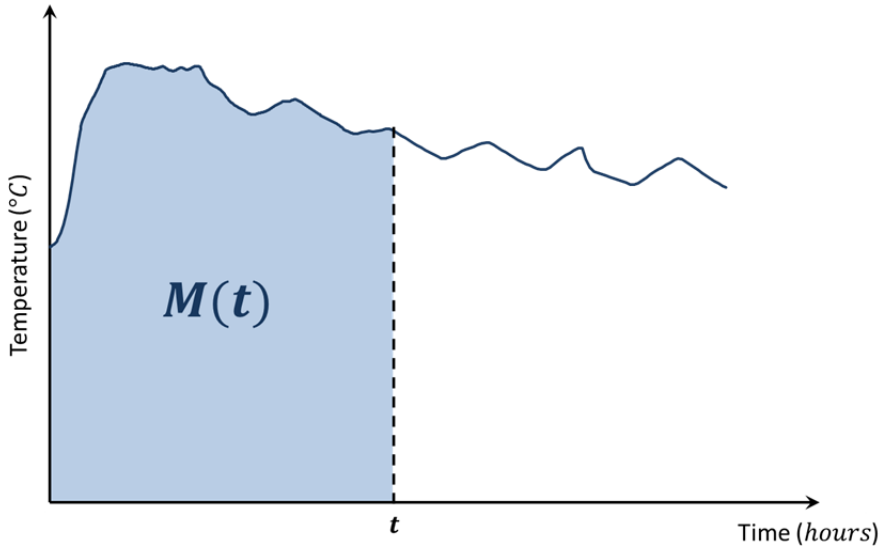

Figure 3.8- Temperature-time factor, $M(t)$.

Since realistic values of E and f'_c were needed on this project instead of lower bound estimates, the parameters obtained from the material study could not directly be used for the arches. The cylinders tested in FSEL were not match cured and could have a different rate of stiffness and strength gain from the full-scale mock-up. Moreover, the arches were cast over a period of 7 months and as a result, different arches experienced significant variations in the thermal histories, not only because of different ambient temperatures, but also because of the intentional changes in the temperature of the fresh concrete to minimize the risk of thermal cracking. Therefore, even the mock-up itself could not necessarily be a precise representative of all 12 arches.

To obtain more realistic estimates of E and f'_c, the data obtained from three sources were combined to estimate the in-situ parameters of concrete in the arches, as shown in Figure 3.9.

1) **Material tests in FSEL:** Equation (3.4) is the main output of the tests that was used in this procedure.
2) **Maturity tests by the contractor:** Sundt construction performed a maturity study on the concrete from the arches and developed a strength-maturity relationship for the concrete from each arch. The strength-maturity results as reported by Sundt are shown in Table 3.4.
3) **Temperature history of the arches:** The instrumentation embedded in the arches provided records of temperatures, which could be used to develop the maturity of concrete as function of time.

Based on the maturity test results reported by Sundt, a logarithmic strength-maturity regression curve was developed for each arch, as shown in Figures 3.10 to 3.12. The recorded temperature histories from the arches were later used as the input to these regression equations to find the compressive strength as a continuous function of time. The details of this calculation procedure are explained in Chapter 5.

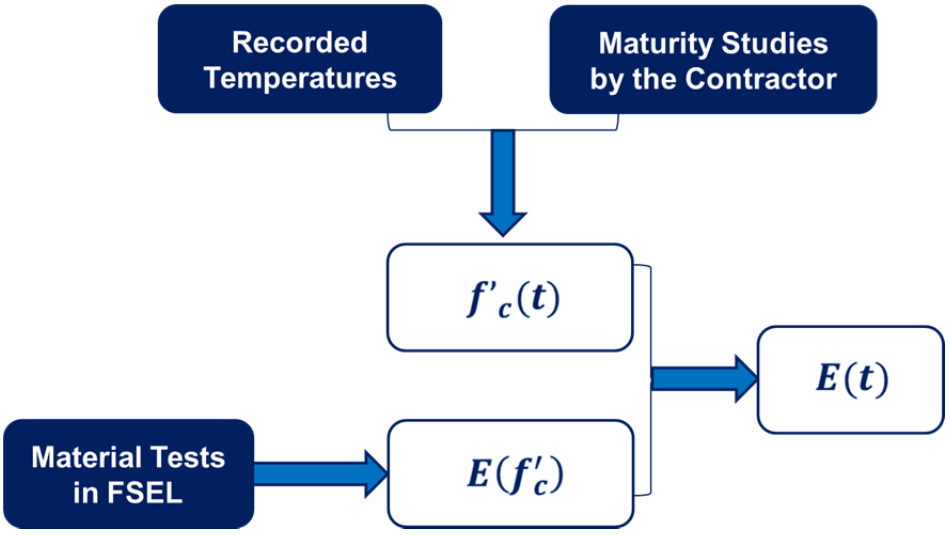

Figure 3.9- The procedure for estimating the in-situ values of E and f'_c.

Table 3.4- Strength-maturity results reported by Sundt Construction.

Arch1		
t(days)	*M*(°C-hrs)	f_c'(psi)
1	942	2653
3	2495	3959
7	5600	5292
14	11035	5758
21	16470	7138
28	21905	7443
38	29668	7829
56	44420	8388

Arch2		
t(days)	*M*(°C-hrs)	f_c'(psi)
1	967	3719
3	2415	4686
7	5311	5298
15	11103	6483
21	20515	7007
37	27031	7273
49	36464	7560

Arch3		
t(days)	*M*(°C-hrs)	f_c'(psi)
1	1141	3199
3	2299	5050
7	4615	5698
9	5773	5729
10	6352	5989
14	8668	6062
15	9247	6928
28	16774	7318
37	21985	7659

Arch4		
t(days)	*M*(°C-hrs)	f_c'(psi)
1	1185	3675
3	2185	5288
7	4185	6245
9	5185	6591
14	7685	6834
28	14685	7203
56	29186	8313

Arch5		
t(days)	*M*(°C-hrs)	f_c'(psi)
1	636	2554
3	1524	5103
7	3300	5715
10	4632	6773
14	6408	6955
28	12624	7513
56	25524	8864

Arch6		
t(days)	*M*(°C-hrs)	f_c'(psi)
1	250	2057
4	1000	6426
7	1750	6910
21	5250	8353
31	7750	9151
56	13986	10234

Arch7		
t(days)	*M*(°C-hrs)	f_c'(psi)
1	-	1776
4	1452	4908
5	1936	5155
7	2904	5852
14	6292	6724
28	13545	7230

Arch8		
t(days)	*M*(°C-hrs)	f_c'(psi)
1	501	2834
3	1177	5518
7	2529	6368
8	2867	6553
14	4895	6930
28	9952	7793

Arch9		
t(days)	*M*(°C-hrs)	f_c'(psi)
1	781	2617
8	2993	6101
14	4889	6573
28	9313	7307
56	18463	9074

Arch10		
t(days)	*M*(°C-hrs)	f_c'(psi)
1	360	2656
7	2016	6284
14	3948	6878
28	7812	8002
56	15812	9338

Arch11		
t(days)	*M*(°C-hrs)	f_c'(psi)
1	-	2138
5	1396	5915
7	2094	6034
14	4537	6342
28	9423	7911

Arch12		
t(days)	*M*(°C-hrs)	f_c'(psi)
1	354	3359
4	1428	5637
7	2502	6392
14	5008	6898
28	10378	7619

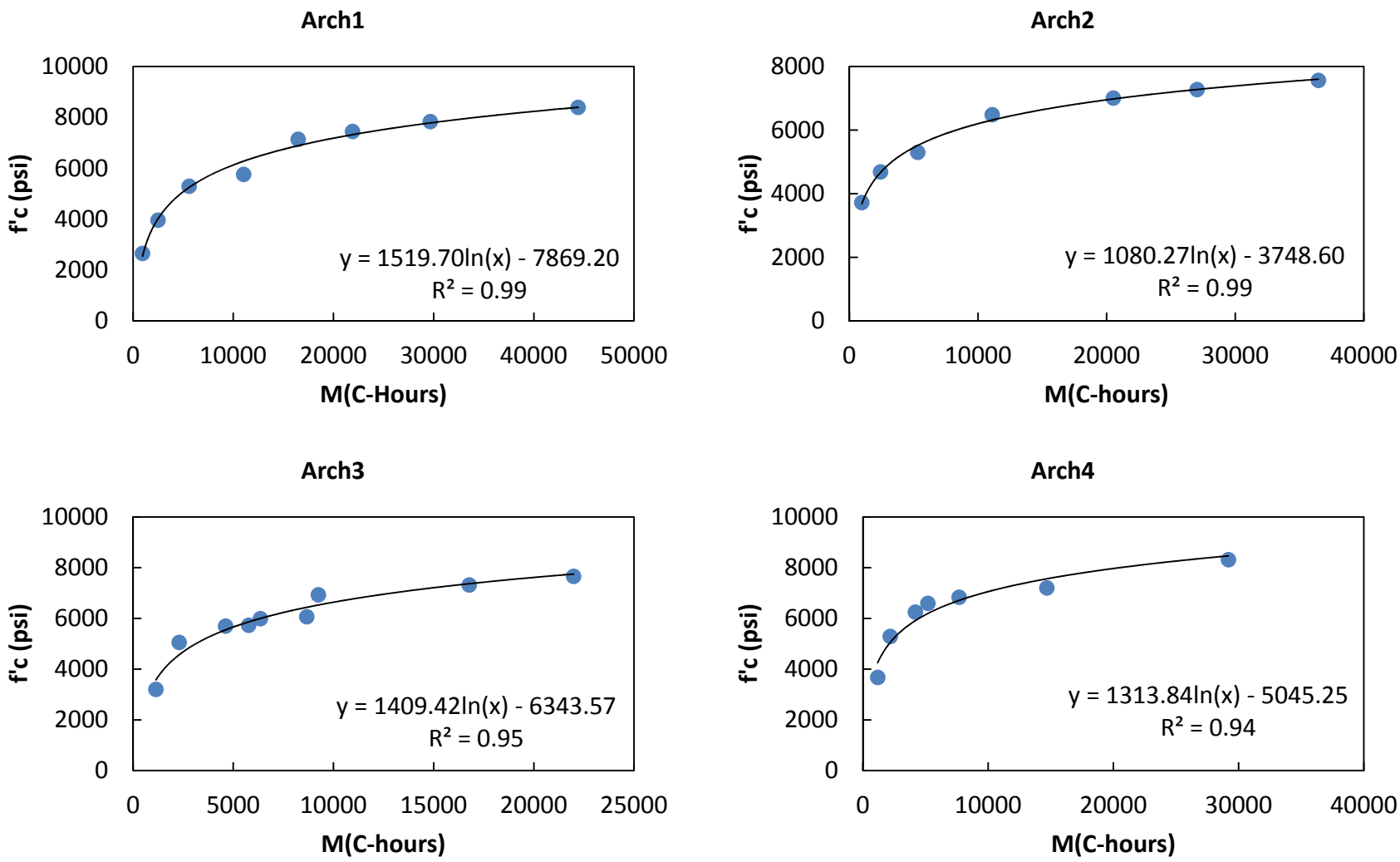

Figure 3.10-Strength-maturity relationship for arches 1-4.

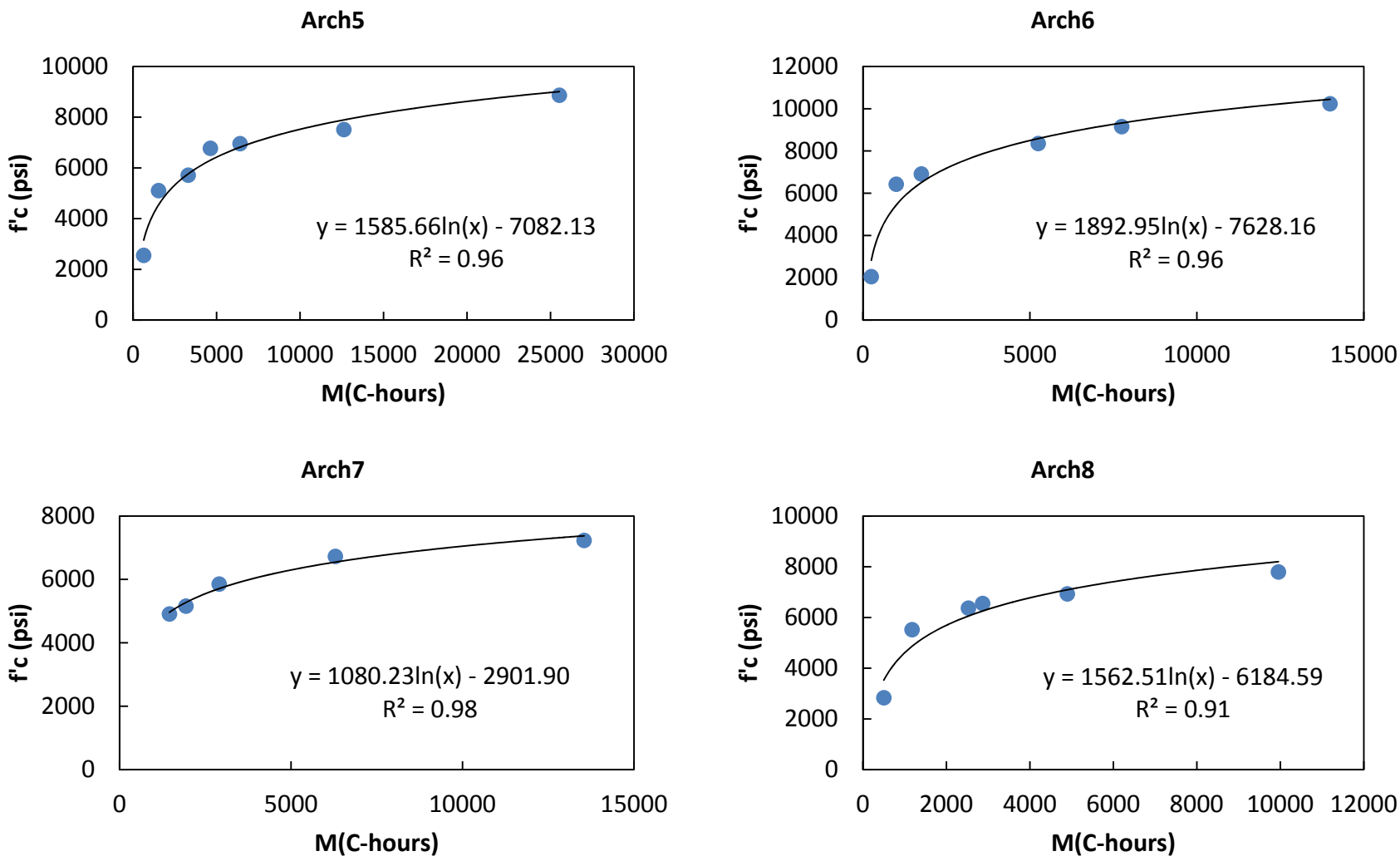

Figure 3.11-Strength-maturity relationship for arches 5-8.

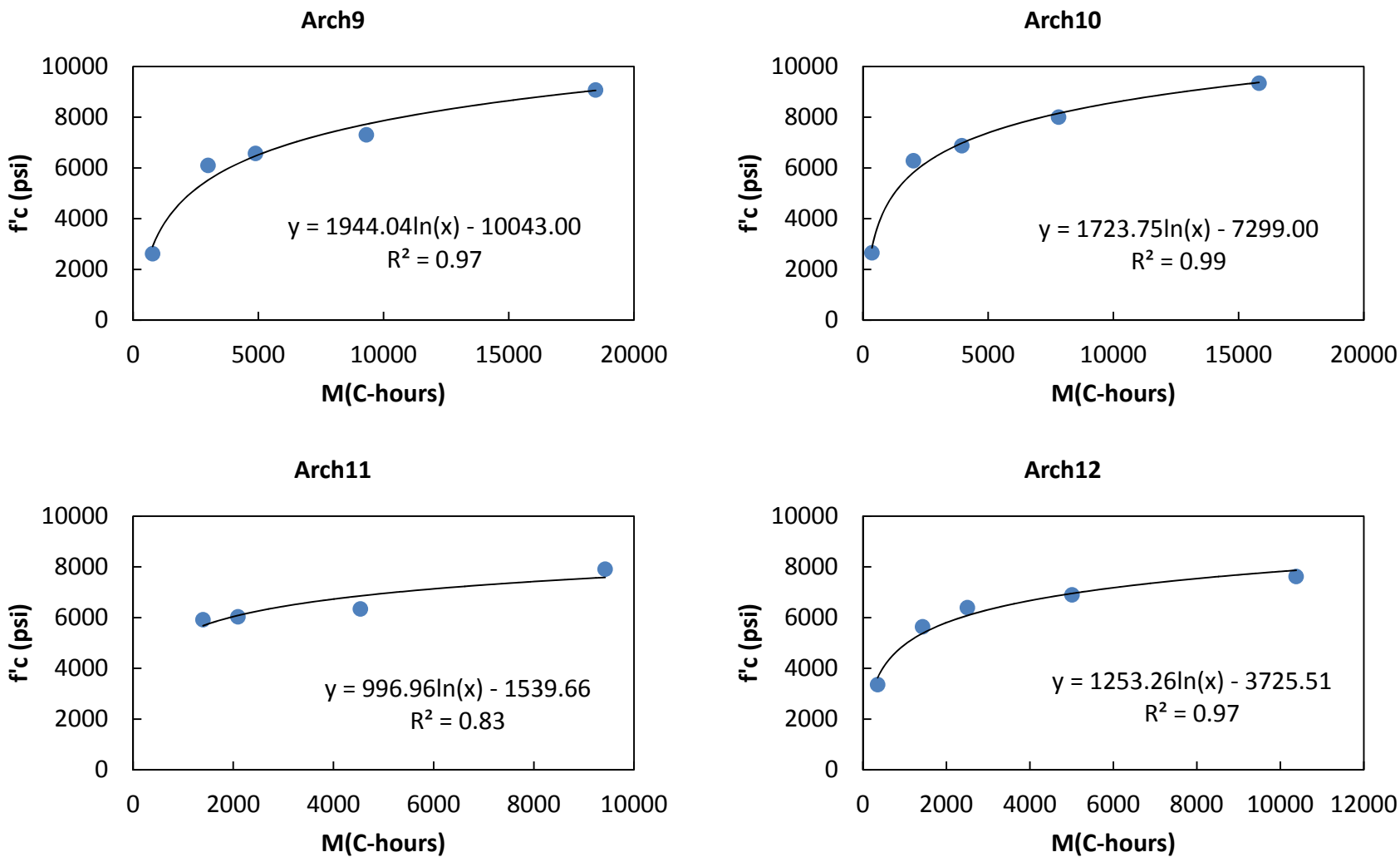

Figure 3.12- Strength-maturity relationship for arches 9-12

3.6.4 Consistency between FSEL Tests and Tests by Sundt Construction

Since the contractor used different testing equipment and a different method for preparing cylinder ends, the results reported by the contractor could not be directly combined with those from the FSEL tests without checking for consistency of the two sets of data.

In order to control the consistency, the mock-up concrete was used as the reference and the compressive strength values reported by the contractor were compared with results obtained in the FSEL tests. Figure 3.13 shows such a comparison. The figure shows that the compressive strength of the 6-inch cylinders reported by Sundt is very close to 90% of the compressive strength of the 4-inch cylinders tested at FSEL.

Several studies have tried to find a ratio between the compressive strength obtained from 4-inch cylinders to that obtained from 6-inch cylinders. While no correlation has been globally accepted, the ratio is known to be affected by aggregate gradation, age at testing, and strength range and is reported between 0.85 and 1.15 in different studies [12], [13]. Therefore, considering the variability in cylinder preparation method and testing equipment, the results from Sundt are in good agreement with the FSEL results. Consequently, it was possible to combine these two sets of data to calculate the parameters needed at each time during construction.

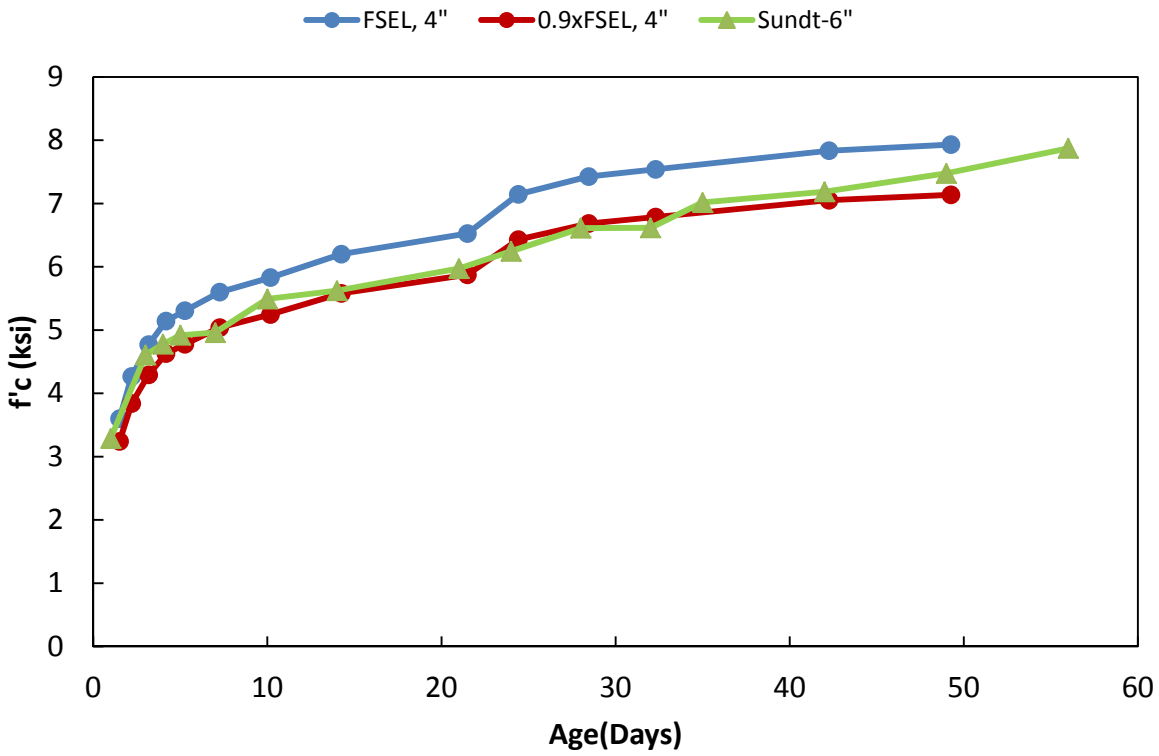

Figure 3.13- Comparison between FSEL test results and the contractor's results

3.7 SUMMARY

The FSEL material test program included testing 48 concrete cylinders for modulus of elasticity, forty of which were also tested for compressive strength. The eight remaining cylinders were tested for splitting tensile strength. The cylinders were constructed using the concrete from a mock-up element that was cast before the beginning of construction. In order to include the effects of thermal history of the concrete in the instrumented arches, the results of this study were to be combined with the temperature profile recorded by the instrumentation and the results of a maturity study by Sundt Construction. As a result, the most important output of the material test program was Equation (3.4), which was a mix-specific E vs. f_c' equation

It should be mentioned that the coefficient of thermal expansion of the concrete, α_c, was also important in post-processing of the data. However, α_c was not obtained from the material tests. The in-situ values of α were determined by investigating the measured response of the structure to temperature changes, as discussed in Chapter 5.

Chapter Bibliography

[1] D. Van Landuyt, C. Holle and J. Aparicio, "Precast Network Arch Bridge," in *PCI Convention and National Bridge Conference*, Grapevine, TX, 2013.

[2] ASTM International, "ASTM C469: Standard Test Method for Static Modulus of Elasticity and Poisson's Ratio of Concrete in Compression," ASTM International, West Conshohocken, PA, 2010.

[3] ASTM International, "ASTM C39: Standard Test Method for Compressive Strength of Cylindrical Concrete Specimens," ASTM International, West Conshohocken, PA, 2012.

[4] ASTM International, "ASTM C496: Standard Test Method for Splitting Tensile Strength of Cylindrical Concrete Specimens," ASTM International, West Conshohocken, PA, 2011.

[5] ACI Committee 318, "Building Code Requirements for Structural Concrete (ACI 318-11) and Commentary," American Concrete Institute, Farmington Hills, MI, 2011.

[6] AASHTO, AASHTO LRFD Bridge Design Specifications - Sixth Edition, Washington, DC: American Association of State Highway and Transportation Officials, 2012.

[7] ACI Committee 363, "Report on High-Strength Concrete," American Concrete Institute, Farmington Hills, MI, 2010.

[8] British Standards Institution, Eurocode 2 : design of concrete structures: British standard, London: BSi, 2008.

[9] M. Tadros, N. Al-Omaishi, S. Seguirant and J. Gallt, "NCHRP REPORT 496: Prestress Losses in Pretensioned High-Strength Concrete Bridge Girders," Transportation Research Board, Washington, DC, 2003.

[10] R. Kehl and R. Carrasquillo, "Investigation of the Use of Match Cure Technology in the Precast Concrete Industry," Center for Transportation Research, The University of Texas at Austin, Austin, TX, 1998.

[11] ASTM International, "ASTM C1074: Standard Practice for Estimating Concrete Strength by the Maturity Method," ASTM International, West Conshohocken, PA, 2011.

[12] R. L. Day and M. N. Haque, "Correlation between Strength of Small and Standard Concrete Cylinders," *ACI Materials Journal*, vol. 90, no. 5, pp. 452-462, 1993.

[13] D. Vandegrift and A. Schindler, "The Effect of Test Cylinder Size on the Compressive Strength of Sulfur Capped Concrete Specimens," Highway Research Center, Auburn Univeristy, Auburn, AL, 2005.

This page is intentionally left blank

CHAPTER 4
Field Instrumentation

4.1 INTRODUCTION

An extensive field instrumentation program was conducted to monitor the West 7th Street Bridge. A total of 224 Vibrating Wire Gages (VWGs) were embedded in the arches in critical sections that were identified by the design team. The VWGs were monitored over the 17-month period of construction to enable a comprehensive assessment of the short-term and time-dependent behavior of the structure. The gages were also monitored during a static live load test after the bridge was opened to traffic to establish a performance baseline for the bridge.

The instrumentation layout that was developed for the field monitoring resulted in high-precision data from a system that provided a good deal of flexibility. The embedded VWGs allowed for both strain and temperature measurements with excellent precision. Moreover, the configured data acquisition system was capable of wireless communication to minimize the interference with the construction activities. It also provided remote monitoring capability and enabled variable scan rates that were adjustable to the speed of ongoing construction operations.

This chapter provides an overview of the field instrumentation program, including the detailed procedure for designing and executing the instrumentation and a discussion of some practical considerations involved. Post-processing of the data obtained from the instrumentation is discussed in Chapter 5.

4.2 INSTRUMENTATION PROCEDURE

The following sub-section describes the systematic procedure used in instrumenting the West 7th Street Bridge. A comprehensive explanation of the instrumentation efforts are given herein so that the experiences of the project team on this study can potentially provide guidance for other field monitoring projects.

4.2.1 Identifying Measurement Requirements

The measurements of interest in this project included concrete strains and temperatures. Concrete strains were the most important outputs of the instrumentation, which enabled the UT researchers to evaluate the structure's response to different loading conditions in terms of stresses, curvatures, time-dependent strain changes, and prestress losses. On the other hand, concrete temperatures at the time of strain measurement were essential in correcting the strain values for thermal effects. Moreover, as discussed in Chapter 3, concrete hydration temperatures were needed for calculating the maturity index of the concrete in the structure and hence the in-situ mechanical parameters. Therefore, any instrumentation plan for this structure should have accommodated both strain and temperature measurements.

Another important consideration was the necessary scan rates for the instrumentation. The researchers needed to determine how frequently strain and temperature data were needed

from the sensors. As discussed in Chapter 2, the measurements from the arches in the field were based upon the major objectives of (1) verifying the design assumptions, and (2) ensuring the safety of the arches during construction. For the purpose of design verification, frequent scans were not necessary. A few measurements per day were usually adequate for distinguishing between the changes due to different construction stages and comparing the stresses at the end of each stage with design predictions. However, ensuring the safety of the structure during construction operations needed almost real-time output from the sensors. Fortunately, the construction operations were performed relatively slowly, and a high scan frequency was not needed for ensuring that the arches were not damaged. Post-tensioning operations caused the fastest stress changes in the structure, and therefore governed the scanning frequency. Considering the speed of post-tensioning operations, a scan rate of once every 3 minutes was sufficient to detect potentially alarming conditions in the structure after post-tensioning of each tendon. As a result, the instrumentation used in this project required the ability to make static measurements with a minimum frequency of once every 3 minutes.

4.2.2 Selecting the Sensor Type: Vibrating Wire Gages

The sensors for the West 7th Street Bridge should have satisfied a variety of requirements in addition to those discussed above. These requirements, which are listed in Table 4.1, resulted in selecting Vibrating Wire Strain Gages (VWGs), as the optimal sensor type for this project. The following paragraphs provide an overview of the VWGs and their benefits and disadvantages.

Table 4.1-Requirements for the sensors.

Requirement	Description
Accuracy	Providing accurate measurements of strains
Precision	Capable of making repeatable measurements of the expected strain levels
Resolution	Capable of making fine measurements and detecting small changes [1]
Durability	Capable of surviving the construction operations and long-term environmental effects
Time stability	Possessing a stable “zero reading” that does not drift so that readings can always be referred to a fixed datum [2]
Economy	Economically feasible
Ease of installation	Easy to install in field in a timely fashion

Vibrating wire transducers were first developed in Europe in the early 1930s [2] and have been used in a wide variety of instruments including strain gages, load cells, and earth pressure cells. Various types of structures including dams, tunnels, bridges, buildings, and piles have been instrumented using vibrating wire transducers.

A vibrating wire strain gage consists of a steel wire that is tensioned between two end blocks. The end blocks are attached to or embedded inside the member under study. The wire can vibrate freely at its natural frequency, which depends on the tensile force in the wire. Any relative displacement between the two end blocks will change the tension in the wire and hence its natural frequency. Therefore, by measuring the natural frequency of the wire, the strain can be calculated. In addition to measuring strain, VWGs usually include a thermistor to provide a simultaneous measure of temperature at the gage location.

Whenever a frequency measurement is needed, an electrical current is run through a magnetic coil adjacent to the tensioned wire to “pluck” the wire. The magnetic field in the

coil displaces the wire from its original position. When the current is turned off, the plucked wire starts to vibrate at its natural frequency. The vibrations cause an alternating current in a pick-up sensor, which can be the same coil that was used to pluck the wire. The frequency of the alternating current will be the same as that of the wire and is measured by a frequency counter [3], [4].

Figure 4.1 shows a Geokon Model 4200 vibrating wire strain gage, which is the sensor that was selected for use in this project. This model is designed for direct embedment in concrete. As can be seen in the figure, the vibrating wire is protected inside a steel tube and is attached to a mechanism that comprises pluck and read coils and a resistance-based thermistor. The specifications for this model of VWG are listed in Table 4.2.

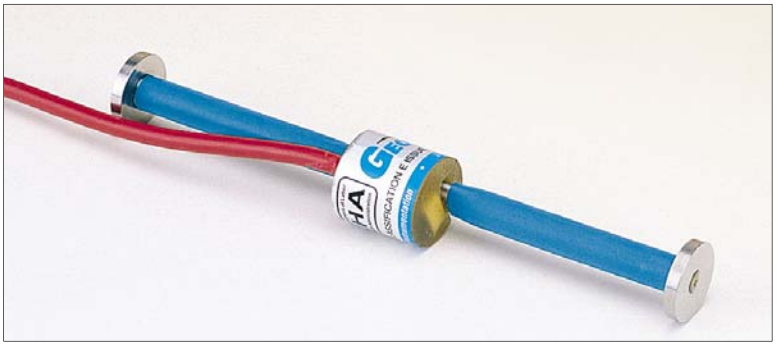

(a)

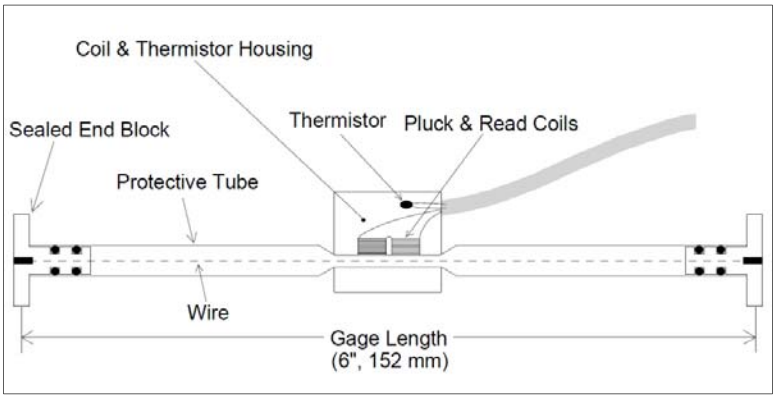

(b)

Figure 4.1-Geokon Model 4200 VWG. (a) A VWG with the plucking coil and lead wire [5]. (b) schematic diagram of the gage components [6].

Table 4.2- Geokon Model 4200 VWG Specifications [6].

Parameter	Units	Quantity
Strain Range	$Microstrain$	3000
Strain Resolution	$Microstrain$	1
Operational Temperature	$°C$	$-20\ to + 80$
Thermistor Resolution	$°C$	± 0.5
Gage Dimensions(Length×Diameter)	in	6.125×0.75
Coefficient of Thermal Expansion	$1/°C$	12.2×10^{-6}

Vibrating wire gages offer a variety of benefits that make them desirable for field instrumentation, especially if long-term monitoring is intended. Some of their most important benefits highlighted in the following paragraphs.

Superior durability

There is global agreement that VWGs are very durable, both in surviving the construction operations and in remaining serviceable for extended periods. In an article in 1985, Bordes and Deberuille investigated statistics from Telemac VWGs in France, which were in service for 40 years and reported an average loss of 0.004 gages per year, not counting the first-year failures. The most common cause of instrumentation failure was reported to be cable damage during gage installation. They predicted that at least 80% of the VWGs installed in 1985 were expected to remain operational for more than 50 years [2]. The excellent durability of the VWGs under construction operations was also observed in several previous research projects at the University of Texas at Austin [7], [8], [9], and [10].

Excellent long-term stability

An instrument is said to have "time-stability" or "no zero-drift" if under constant input, its calibrated output does not change over time [11]. The stability of the instruments is of paramount importance in applications that involve long-term monitoring, especially if periodic, rather than continuous monitoring, is intended. The readings at any time can be compared to the same initial datum only if the sensor output has long-term stability.

The manufacturing procedure for VWGs relieves them from any residual stresses that could affect the long-term output [11]. As a result, VWGs possess outstanding long-term stability. In studies by McRae, negligible changes were observed in the calibrated output of Geokon VWGs after 15 years [12]. In another study by Choquet et al., VWGs were evaluated for approximately four years and revealed minimal changes in their calibration slope [4]. DiBiagio studied the long-term stability of 10 VWGs, from which eight were continuously vibrating at their natural frequency. Over a period of 27 years, the average drift of the zero reading was only 0.2% Full Scale (FS) [13]. These studies demonstrate that VWG outputs are very reliable for long-term and periodic monitoring applications.

Insensitivity to wire length

Since the measurement output from a VWG is a frequency, the readings are not affected by the length of the lead wire. As a result, VWGs are more precise than foil strain gages, which work based on electrical resistance and are affected by lead wire lengths. In

field instrumentation, the lead wires can be cut to desired lengths up to 200' without any concerns regarding increased errors in strain measurements [12].

Ease of Installation

The main components of the VWGs are well protected from environmental effects, especially water infiltration, so their installation is relatively easy. The only consideration for the embedment of VWGs is to make sure that during the concrete pour, the location and orientation of the gages do not change and the coil housings are not detached from the gages. For example, as described in Section 4.2.8, VWGs can be installed quickly using plastic zip ties. Easy and quick installation of VWGs is one of their main advantages over foil strain gages, which require time-consuming preparation steps, including grinding, sanding, cleaning, bonding, and waterproofing.

While VWGs provide the aforementioned benefits to field instrumentation applications, they have some setbacks, which are discussed below.

Scan Rate Limitations

Single-coil VWGs such as Geokon Model 4200 have been categorized as static instruments because measuring the natural frequency of the wire takes some time. With the available technology at the time of the West 7th Street Bridge instrumentation, the maximum possible measurement rate for VWGs was slightly more than once every 2 seconds. Moreover, the monitoring system that was used in this project necessitated the use of sequential relay terminals called multiplexers, which further limited the available scan rates. As a result, the instrumentation on the West 7th Street Bridge was not capable of monitoring dynamic effects including those due to traffic loading. However, the objective of the instrumentation was monitoring the construction operations and time-dependent changes, and as mentioned in Section 4.2.1, a scan rate of once every 3 minutes was sufficient for this project. Therefore, limited scan rate was not a concern in this project.

A new technology for exciting single-coil VWGs was introduced in 2013. With this technology, scan rates up to 300 times per second has become possible for standard VWGs similar to those embedded in the arches. Thus, the same embedded instruments can potentially be used for monitoring the traffic effects on the West 7th Street Bridge in the future.

Cost

Compared to foil strain gages, VWGs are relatively expensive. At the time of instrumenting the West 7th Street Bridge, a Geokon Model 4200 VWG was approximately 10 times more expensive than a regular foil gage. However, due to their long-term reliability and remarkable survival rate in field conditions, VWGs are still considered economically feasible.

4.2.3 Assessing the Instrumentation Capabilities

The instrumentation was expected to play a key role in ensuring the safety of the arches. Therefore, gaining confidence in VWG readings was essential. A preliminary study was conducted in FSEL to evaluate the capabilities of VWGs in controlled laboratory tests and to identify their limitations. Three slender post-tensioned concrete elements with relatively small cross-sections were constructed and tested under several combinations of post-tensioning and

external axial load. The specimens were instrumented using embedded Geokon Model 4200 VWGs in addition to linear potentiometers and load cells.

This study, details of which are reported by Blok [14], showed that VWGs were an effective means to ensure the safety of the arches. The lab studies showed that the gages are capable of providing a reliable picture of the behavior of a post-tensioned element and can be used for detecting impending distress such as cracking or buckling. The VWG readings were stable, precise, and consistent with linear potentiometer and load cell measurements. As a result, the research team was confident that the selected type of instrument was an effective choice for monitoring the West 7th Street Bridge.

4.2.4 Selecting the Instrumentation Locations

Selecting the locations of the VWGs in the West 7th Street Bridge was based on the following decisions, which were made in coordination with the design team:

4.2.4.1 Instrumented sections in each arch

Design calculations had identified sections with the largest stresses during construction operations and service load conditions. These sections, which are shown in Figure 4.2 and listed in Table 4.1, were selected as the primary locations of the instrumentation. Among these sections, Section 1 was the most vulnerable section to cracking, with a minimum compressive stress of approximately 100 psi during upward jacking. Therefore, monitoring Section 1 was particularly important for ensuring the safety of the arches.

The exact locations of Section 1 and Section 8 could not be instrumented, because block-outs for the floor beam connections were located at the same sections. Therefore, the instrumented Section 1 and Section 8 were typically 2 ft and 3 ft apart from the most critical sections, respectively.

4.2.4.2 Arrangement of VWGs at instrumented sections

The sectional arrangement of VWGs required knowledge of the expected strain distribution in each cross section. While VWGs were located inside the cross sections, the largest strains and stresses occurred at the corners. Therefore, the most critical strains and stresses could not be directly found through measurement and needed to be calculated. This calculation was dependent on the distribution of the strains within each cross section.

According to St. Venant's principle, disturbed regions or D-regions ("D" representing discontinuity or disturbed) are assumed to exist within one member depth from the location of any discontinuity in load or geometry, and other parts of the structure are assumed to be B-regions("B" representing beam or Bernoulli). In B-regions, the distribution of the strains is linear. In other words, plane sections remain plane and linear interpolation or extrapolation can be used to calculate the strains and stresses at any point in the cross section. On the other hand, in D-regions, the distribution of strains is nonlinear, and interpolation or extrapolation of strains is invalid [15].

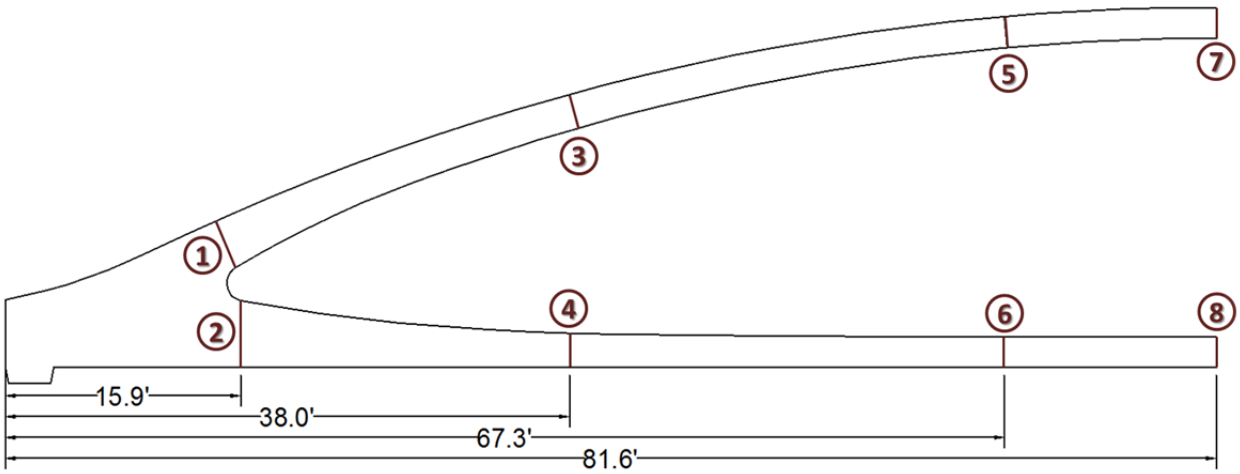

Figure 4.2- Locations of critical sections in the structure, as predicted in design.
(The critical sections are symmetric about the midspan, so only half of the arch is shown).

Table 4.3- Description of the critical sections as predicted in design.

Section No.	Location	Critical Loading Conditions
1	Knuckle- Rib	Upward jacking, Service load
2	Knuckle- Tie	Stage 1 PT, Service load
3	Lifting frames 2 and 5-Rib	Rotation
4	Lifting frames 2 and 5-Tie	Rotation
5	Lifting frames 3 and 4-Rib	Rotation
6	Lifting frames 3 and 4-Tie	Rotation
7	Midspan-Rib	Slab cast, Service load
8	Midspan-Tie	Service load

The arches were divided into B- and D-regions that are shown in Figure 4.3. The geometric discontinuity at the knuckle regions and concentrated forces at the locations of floor beams were the main sources of disturbance to strains. The arches also included 52 hangers, which crossed the rib and the tie many times. However, each hanger carried a small force, which was not expected to disturb the linear strain profile significantly. Therefore, the hangers were not considered in separating the B- and D-regions that are shown in Figure 4.3. As can be seen in this figure, sections 1 and 2 were located in D regions whereas other instrumented sections were located in B-regions.

Different numbers of VWGs were used for instrumenting the sections in B- and D-regions of the arches. For the sections located in B-regions, (sections 3 through 8), three non-collinear VWGs were used because a unique plane could be passed through every three non-collinear points. In contrast, determining the strain distribution in D-regions would have required many VWGs within the depth of the section. However, using numerous VWGs in

the D-regions of the arches (sections 1 and 2) would have been impractical. Therefore, it was decided to rely on the design team's predictions for sections 1 and 2. In these sections, two VWGs were installed near the top surface, which was anticipated to experience the maximum strains.

Figure 4.4 shows the final arrangement of the VWGs in different sections of the structure. As can be seen in this figure, sections in D- and B-regions are instrumented using two and three VWGs, respectively. For the first four arches, the midspan sections were instrumented using four VWGs in order to provide some redundancy and a reference for comparison. For subsequent arches, the midspan sections were instrumented using three gages.

4.2.4.3 Variation of the instrumentation between arches

If the arches had been identical, instrumenting only one arch would have been sufficient for making sure that none of the arches would get damaged during construction. However, due to the following reasons, different construction stresses were expected in subsequent arches.

> ***Unanticipated Incidents***: There was a possibility of unanticipated incidents during construction, especially during post-tensioning. For example, in two arches, anchorage failures occurred during post tensioning, resulting in sudden changes in the prestressing forces and concrete stresses.
>
> ***Hand-tightened elements***: The construction procedure required the hangers to be hand-tightened before arch rotation. Due to the high level of indeterminacy in the structural system, the forces in the hangers were generally unknown before the upward jacking operations and could be significantly variable between arches.
>
> ***Different locked-in stresses:*** As noted above, the arches were highly indeterminate. Therefore, time-dependent and thermal deformations of the concrete in the arches induced substantial stresses in the structure. On the other hand, each arch experienced a different thermal history and had a different age at final erection into the bridge. As a result, even if the construction was perfectly consistent, different locked-in stresses would be expected in apparently identical arches.

Considering the expected general uniformity of the construction together with sources of variability mentioned above, it was decided to instrument the first four arches extensively to evaluate their structural response during construction and make sure of the suitability of the construction procedure. Once these arches were constructed successfully, the other arches could be instrumented only at the midspan and the most vulnerable sections during construction.

Figure 4.5 shows the instrumented sections in different arches. As can be seen in this figure, all of the sections shown in Figure 4.4 were instrumented in arches 1 and 2 so that the safety of these arches could be ensured. Since construction operations were successful for these two arches, sections 5 and 6 were not instrumented in arches 3 and 4. After successful construction of Arch 4, the subsequent arches were instrumented only at the midspan and

Section 1, which was the most vulnerable section during construction. The number of VWGs in each arch is shown in Table 4.4.

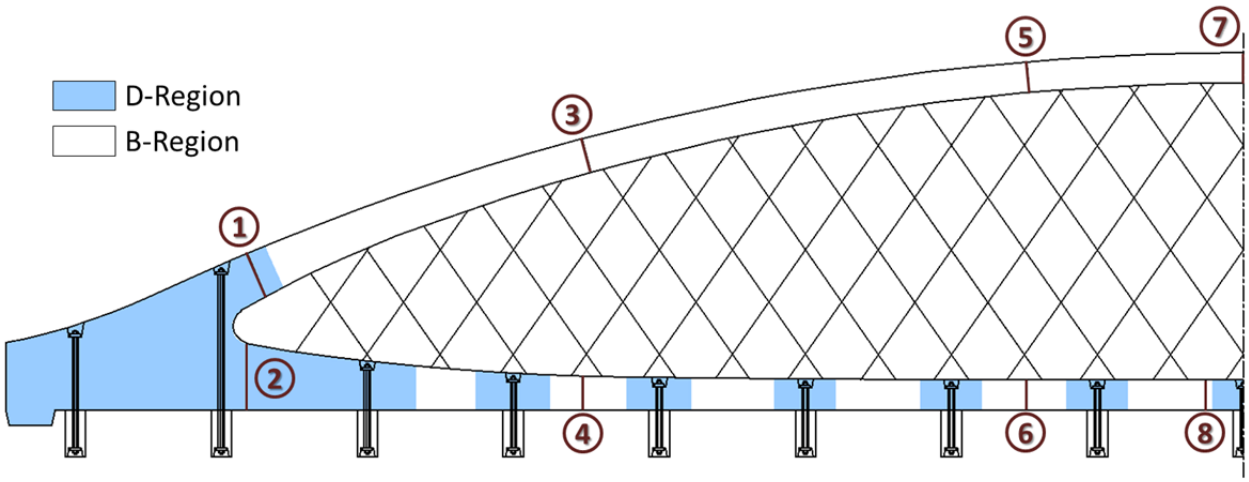

Figure 4.3- Locations of the instrumented sections with respect to D- and B- regions.

Table 4.4-Number of VWGs in different arches.

Arch No.	Instrumented Sections	Number of VWGs
1-2	1,2,3,4,5,6,7,8	40
3-4	1,2,3,4,7,8	28
5-12	1,7,8	10
Sum		224*

* Eight VWGs, used for assessing local effects in arches 11 and 12, are taken into account.

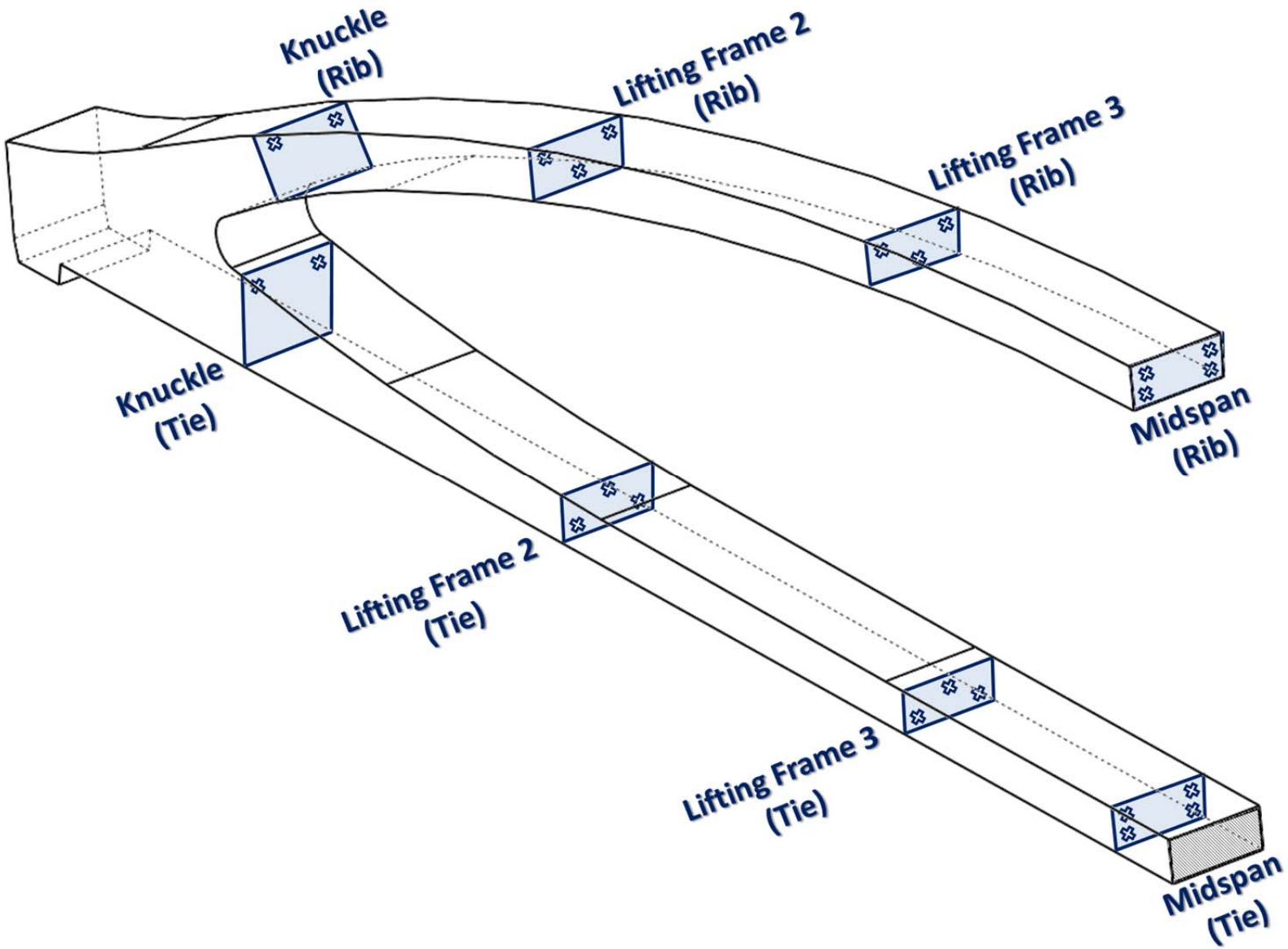

Figure 4.4- Arrangement of VWGs in different sections of the arches.
(Each × signs represent the location of a VWG.)

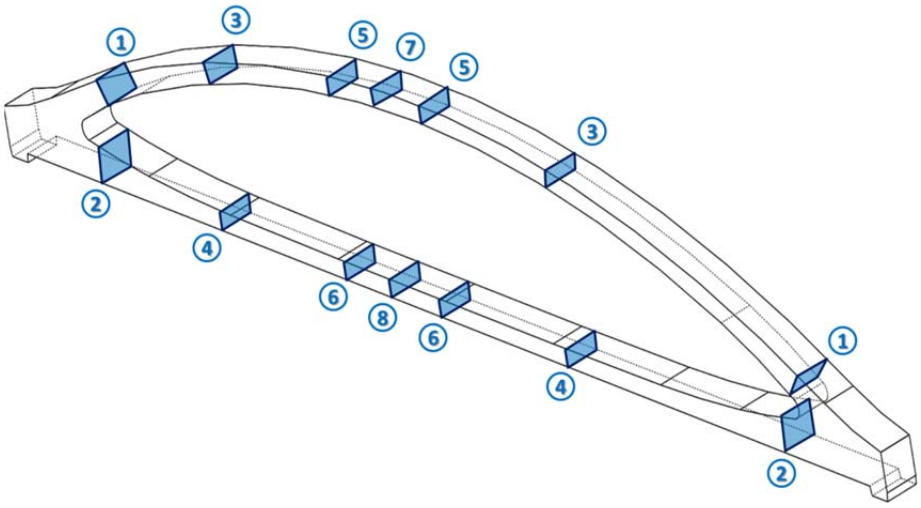

(a) Instrumented sections in arches 1 and 2.

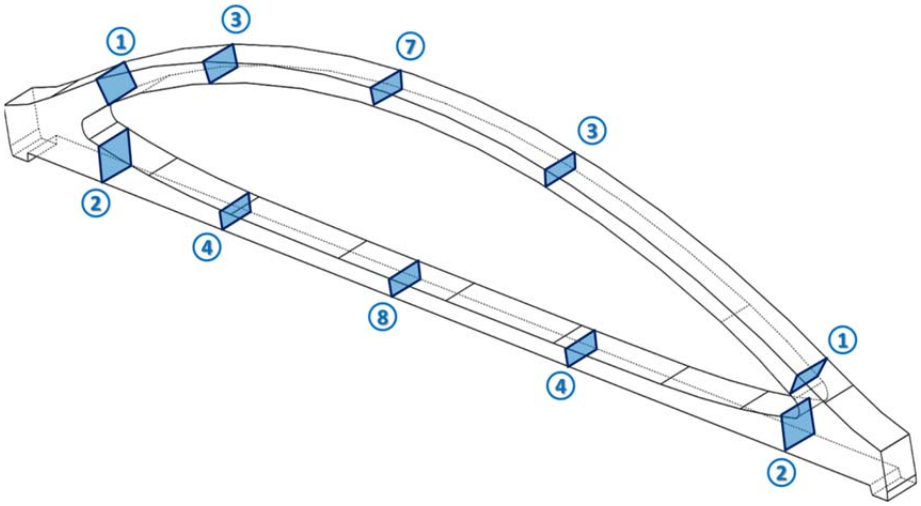

(b) Instrumented sections in arches 3 and 4.

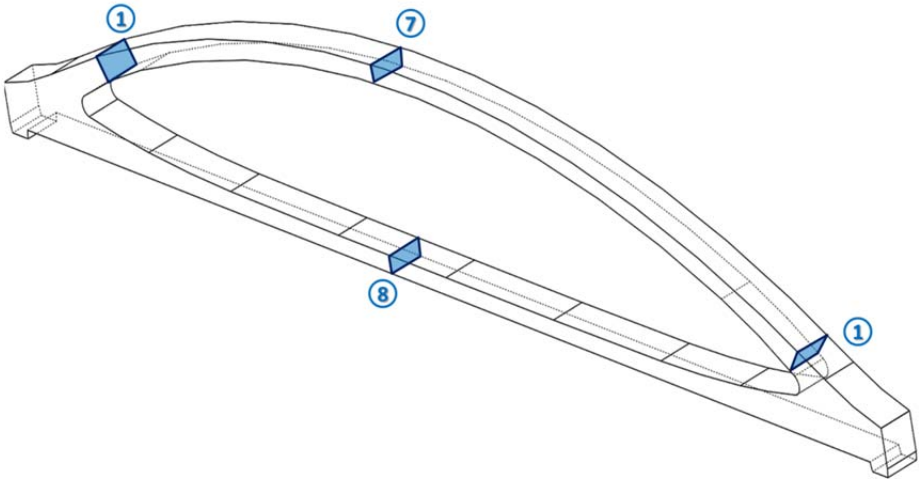

(c) Instrumented sections in arches 5-12.

Figure 4.5-Instrumented sections in different arches.

4.2.5 Designing the Data Acquisition Network

Monitoring the instrumentation in the arches was accomplished through several Data Acquisition (DAQ) units that formed a network. The function of this DAQ network was to excite the instruments, acquire and process the response signals, and store the data. The demands on the network necessitated several requirements, including those listed below:

1) Being compatible with VWGs
2) Providing enough channels for VWGs so that at least two arches could be monitored simultaneously
3) Producing minimized interference to the construction activities on the site
4) Providing flexibility for arch rotation and transportation operations
5) Being capable of remote and on-site monitoring

A wireless DAQ network, which is shown in Figure 4.6, was designed to satisfy these requirements. The following paragraphs describe the main components of the DAQ network.

4.2.5.1 Data logger

The primary function of a data logger is to make the measurements from the instrumentation at certain times and then, collect and store the data. In essence, the data logger is the command and control center for the DAQ network.

The data loggers used in this project were Campbell Scientific CR3000 Microloggers, which were able to connect to a variety of instruments and interface devices. These data loggers were programmable to execute scans at variable rates as well as performing initial post-processing calculations. To make measurements from VWGs, the data loggers were used together with VWG analyzers. In this configuration, the DAQ network had a decentralized control fashion, and data acquisition was distributed between the data logger and the analyzer, as explained in Section 4.2.5.2. Each data logger controlled multiple analyzers through wireless communication, and each analyzer made measurements from as many as 32 VWGs through multiplexers.

Since all measurements were made by the analyzers, no instrument was wired to the measurement ports of the data loggers. However, as shown in Figure 4.6, two important communication devices were connected to each CR3000: (1) an RF401 spread spectrum radio, which enabled communication with wireless analyzers, and (2) an Airlink RavenXTV cellular network modem, which made the data loggers controllable via internet connection so that the DAQ programs could be changed and the collected data could be retrieved remotely. The RF401 radios were manufactured by Campbell Scientific while the modems were manufactured by Sierra Wireless.

Three data loggers were used for instrumenting the arches. Wireless connectivity and the decentralized style of the network enabled each data logger to connect to a practically unlimited number of analyzers. However, scanning a large number of VWGs was time consuming, and using a single data logger would have resulted in long delays between measurements. Therefore, the number of data loggers was increased to three to keep the maximum scan delay below 3 minutes. Each data logger worked independently, making measurements from certain VWGs.

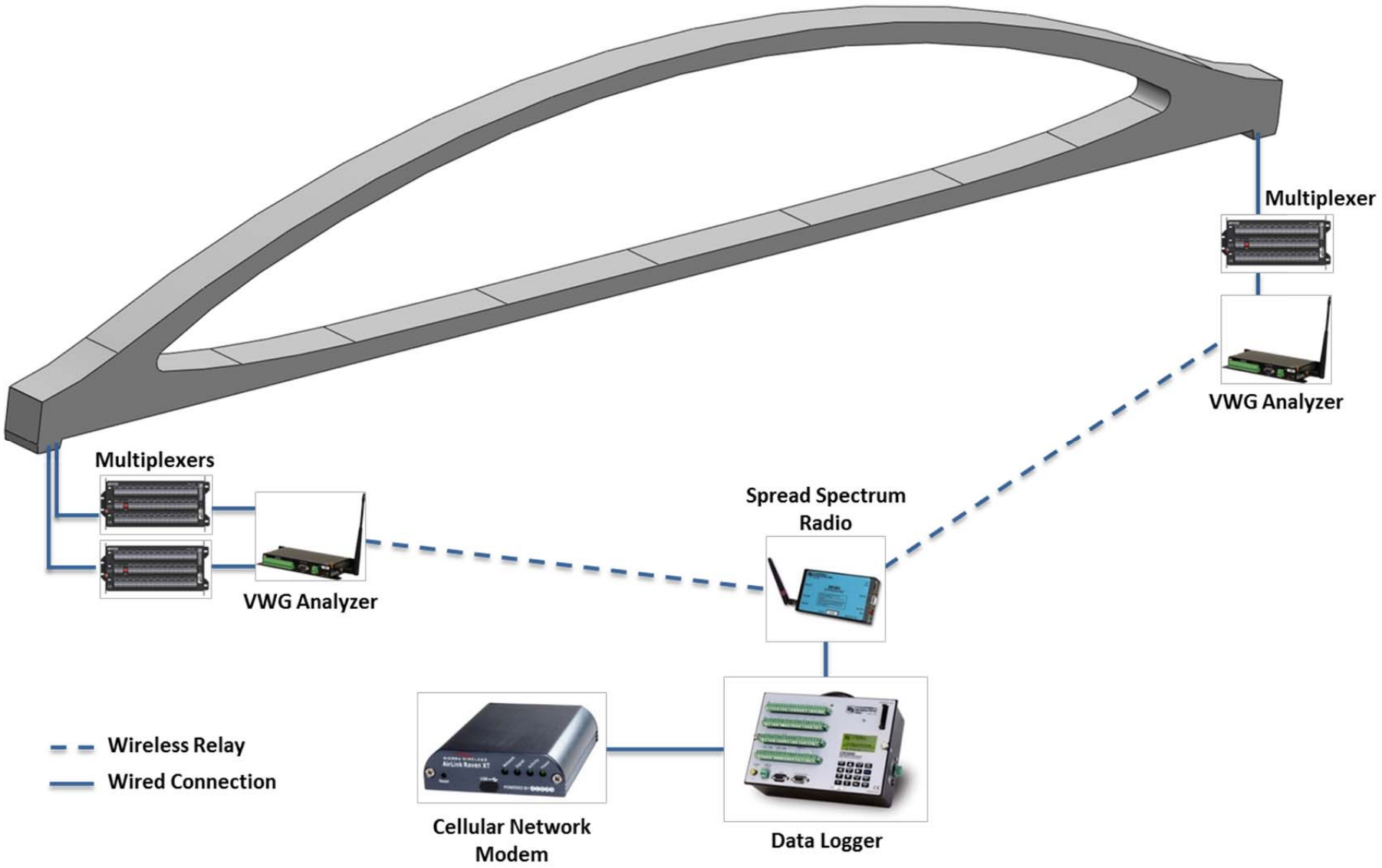

Figure 4.6- DAQ network configuration.

4.2.5.2 VWG Analyzer

The vibrating wire spectrum analyzer, herein referred to as "the analyzer", functions as a local command center in the network and makes the DAQ compatible with VWGs. This device measures the natural frequency of the VWG and the electrical resistance of its thermistor. For each VWG measurement, the data logger contacts the analyzer through wireless communication and requests for data. In response, the analyzer makes the measurements and transmits the data back to the data logger. Each analyzer has a unique network address so that the data logger can contact a particular analyzer when needed.

Five Campbell Scientific AVW206 analyzers were used in instrumenting the West 7th Street Bridge. This model had only two channels for connecting to VWGs. Since more gages needed to be scanned by each analyzer, multiplexers were connected to the analyzer channels, as explained below.

4.2.5.3 Multiplexer

The main function of a multiplexer is to increase the number of instruments that can be connected to a limited number of channels on DAQ units. The multiplexer is connected to multiple gages at one end and a single communication channel at the other end. When needed, this device goes through the gages and connects them to the communication channel one after another.

In this project, Campbell Scientific AM16/32B multiplexers were positioned between the analyzers and the VWGs. Whenever the data logger ordered a scan, the analyzer turned on the multiplexer. The multiplexer then progressed through the VWGs and connected them one by one to the analyzer channel to read and store data from the sensors. Once all the VWGs were scanned, the analyzer relayed the data to the data logger and then turned off the multiplexer. Each AM16/32B multiplexer can be connected to a maximum of 16 VWGs. Therefore, with two multiplexers, the reading capability of each analyzer was increased from 2 to 32 gages.

This combination of multiplexers and analyzers introduced more limitations to the available scan rates. As mentioned in Section 4.2.2, reading a single VWG takes slightly less than 2 seconds. When the VWG was connected to a multiplexer, switching between the channels of the multiplexer increased this delay time to 2 seconds. Therefore, in order to satisfy the scan rate limits in this project, the maximum number of VWGs that could be handled by one data logger was limited to 90.

4.2.5.4 Hand-held Readout Box

All arches were monitored during the main construction operations. However, keeping all arches connected to network at all times was not possible due to limitations on the number of channels available on the DAQ network. Therefore, when the arches were in storage, many of them were not continuously monitored.

In order to keep track of time-dependent changes in the arches that were disconnected from the DAQ network, a Geokon GK-404 readout box, which is shown in Figure 4.7, was used. This palm-sized readout device enabled the researchers to measure the strains and temperatures from the VWGs. The reader was also used during the VWG installation phase to make sure of the functionality of the gages.

Figure 4.7- A GK-404 Readout box [16].

4.2.6 Programming the data loggers

The CR3000 data loggers were programmed using Loggernet 4, the software package produced by Campbell Scientific. The most important instrumentation parameters in the program were as follows.

Scan rate

The data loggers were programmed to be able to make measurements in three modes: fast (one scan every 150 seconds), slow (one scan per hour), and intermediate (one scan every 10 minutes). The researchers could choose any of these scan rates when needed, without changing the program. The fast mode was used during construction operations while the slow mode was used throughout the idle periods of construction such as nights. The intermediate scan mode was primarily used when the DAQ system was on standby for a construction operation.

VWG Measurement Parameters

The program determined which analyzers should be contacted by each data logger at each time. Moreover, VWG measurement parameters were defined in the program, which included excitation voltage and frequency range for the VWGs and the number of multiplexer channels that needed to be scanned by the analyzer.

Data Processing and Storage

After each measurement, the analyzers report the natural frequency and thermistor resistance obtained from each VWG to the data logger. The reported data also included a set of diagnostic parameters that describe the quality of the VWG signal. The data loggers were programmed to store all measurements and diagnostic parameters and conduct basic calculations to convert the measurements to strain and temperature data, according to Equations (4.1) and (4.2).

$$\varepsilon_{VWG} = G \times B_1 \times f^2 \tag{4.1}$$

$$T = 1.8 \times \left(\frac{1}{A + B \times Ln(R) + C \times \left(Ln(R)\right)^3} - 273.2 \right) + 32 \tag{4.2}$$

In which,

ε_{VWG} = strain in the vibrating wire, $Microstain$
T = temperature, $°F$
f = frequency in the vibrating wire, Hz
R = thermistor resistance, Ω
G = gage factor = 3.304×10^{-3}
B_1 = batch calibration factor = 0.97
A =1.026×10^{-3}
B =2.478×10^{-3}
C =1.289×10^{-7}

4.2.7 Assembling the DAQ Units

To provide protection from rain and dust on the field, all DAQ units were installed in weather resistant boxes. The analyzers and multiplexers were installed in small boxes, herein referred to as Data Collection (DC) boxes, which were attached to the arches. Each data logger, together with its cellular network modem and spread spectrum radio was installed in larger boxes, herein referred to as Data Logger (DL) boxes. All DC and DL boxes were corrosion resistant PVC enclosures in which the DAQ equipment was mounted on metal back panels. The DC and DL boxes measured $12"\times12"\times6"$ and $19"\times17"\times9"$, respectively.

One of the assembled DL boxes is shown in Figure 4.8 (a and b). The data loggers in these boxes were powered by $20w$ solar panels during daytime hours and $12V$, 12 Ah backup batteries during nighttime hours. During the initial stages of construction, the DL boxes were located inside a trailer belonging to UT on the construction site. Figure 4.9 (a) shows the solar panels that provided power for the DL boxes in the trailer. At later stages, the boxes were mounted on solar panel stands in the field, as shown in Figure 4.9 (c). The DL boxes were designed for portability. Therefore, as shown in Figure 4.9 (b), during the half-mile transportation of the first two arches, one of the DL boxes could be positioned in a car and be moved together with the arches to make sure the data logger was within the communication range of the analyzers. For later arches, two stationary DL boxes were used together to monitor the whole transportation process; one of the DL boxes, which is shown in Figure 4.9 (d), was positioned on the roof of a parking garage near the bridge site and the other one remained on the precast yard.

Figure 4.8(c and d) shows one of the assembled DC boxes. Each DC box was powered by a 12V, 12-Ahr sealed rechargeable battery, which maintained sufficient power for approximately one month. The discharged batteries were regularly replaced by recharged batteries during site visits.

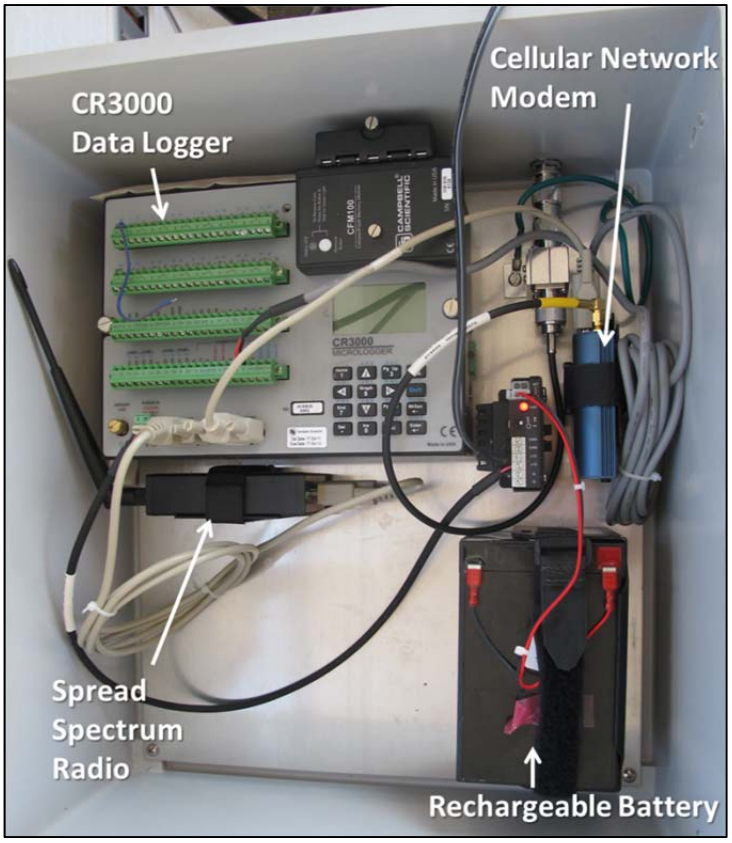

(a)

(b)

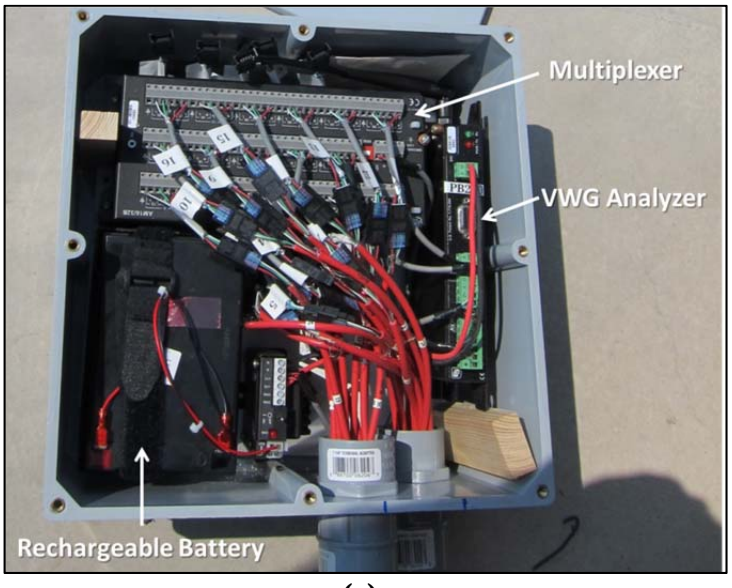

(c)

(d)

Figure 4.8- DL and DC boxes.
(a) The components inside a DL box (b) The outside appearance of a DL box. (c) The components inside a DC box. (d) The outside appearance of a DC box.

(a)

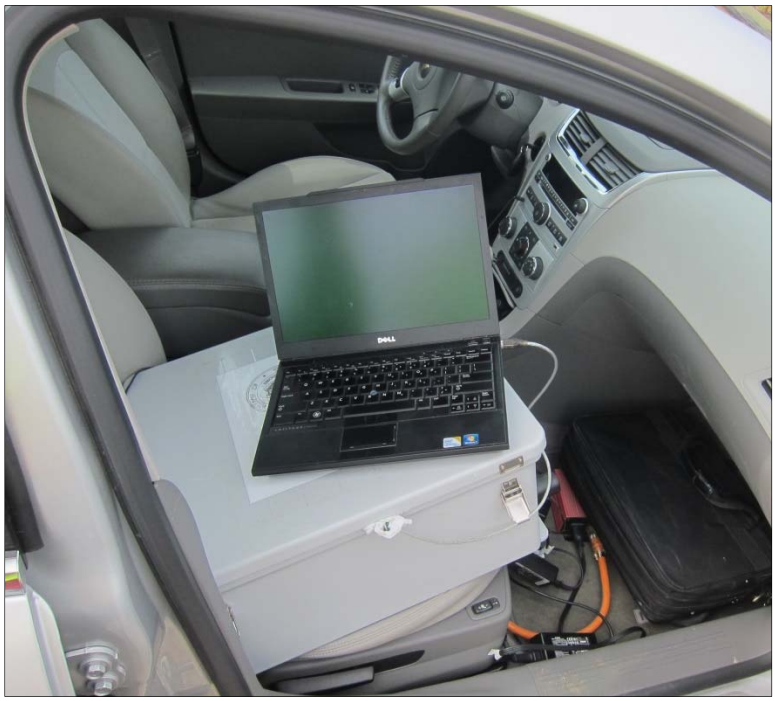

(b)

(c)

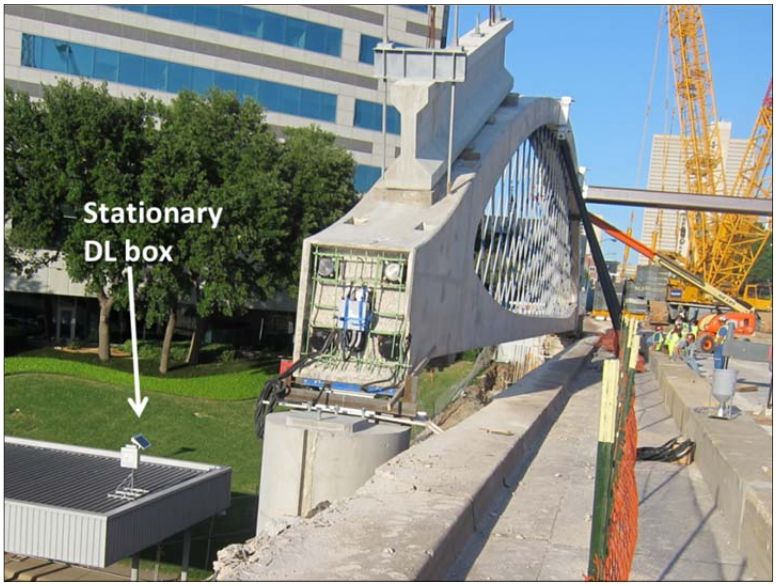

(d)

Figure 4.9- DL box details. (a) Solar panels for powering up the DL boxes in the trailer. (b) The portable DL box during arch transportation. (c) A stationary DL box mounted on the solar panel stand. (d) The stationary DL box near the transported arches.

4.2.8 Installing the VWGs

Field installation of the VWGs started in June 2012 and was finished in February 2013. For each arch, the VWGs were installed immediately prior to installing the outside forms.

The VWGs used in this project were attached to 18-inch number 3 reinforcing bars that were tied to the transverse reinforcement of the arches. As shown in Figure 4.10, machined plastic blocks were used to provide the spacing between the gage and the rebar. Two pairs of plastic zip ties were also used to attach the VWGs to the blocks and the blocks to the rebars. Prior to field instrumentation, the VWGs were mounted on the rebars in FSEL to facilitate the installation process on the field. However, the zip ties that attached the plastic blocks to the rebars were not completely tightened to allow for some flexibility in the field. All VWGs were also tested in the laboratory to confirm their functionality.

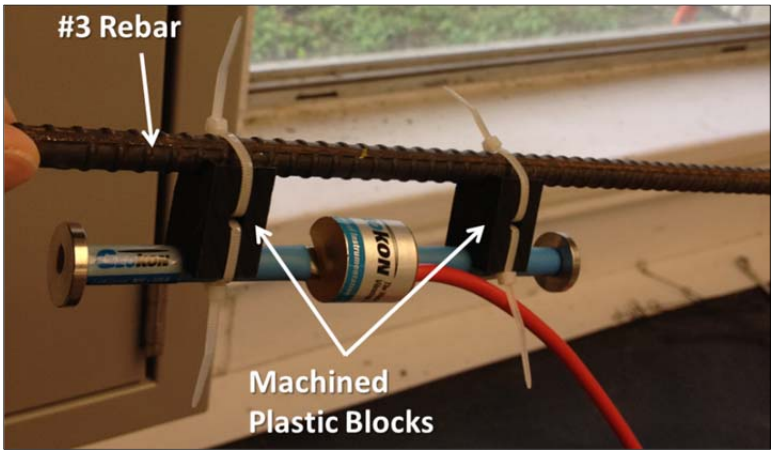

Figure 4.10-A VWG attached to the reinforcing bar.

Installation of the VWGs in the field included the following steps:

1- The longitudinal location of each gage was marked on the arch reinforcement. Since the soffit of the arch formwork was constructed with excellent precision, all measurements were taken from the corners or edges of the soffit. To make sure that all the VWGs at the instrumented sections were located in the same plane, a rotary laser level was used, as shown in Figure 4.11 (a). A square was also used to make sure that the all instrumented sections were exactly perpendicular to the longitudinal axis of the tie or the rib so that only normal strains and stresses could affect the VWGs.

2- The number 3 rebars were tied to the transverse reinforcement of the arches using plastic zip ties, as shown in Figure 4.11 (b). Once the mounting rebar was fixed in the desired location, the VWG was moved along the mounting rebar if needed, and then all the zip ties were tightened.

3- The VWG cables were pulled through the reinforcing cage, as shown in Figure 4.11(c and d). The cables were labeled in FSEL, so each cable was assigned to a certain VWG. All the cables were routed to the locations approved by the design team and the contractor. For the first three arches, the cables entered the

(a)

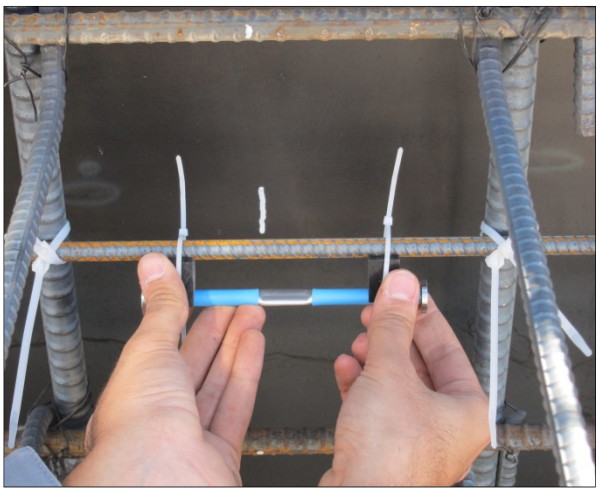

(b)

(c)

(d)

Figure 4.11- VWG installation process. (a) Using the rotary laser level. (b) Installing the VWG in the marked position. (c) Cable spools at the end of the arch. (d) Pulling the cables through the cage.

cage from both arch ends. For other arches, all the cables entered the cage from one end, which became the eastern end of the arches in the finished bridge.

5- The VWG pluckers were attached to the gages. To make sure the pluckers would not get detached from the VWGs, two zip ties were used to fix the plucker to the gage, as shown in Figure 4.12 (a). Moreover, a relief loop was provided in the cable path, so that if the cables were pulled for any reason, they would not get detached or disconnected.
6- Using plastic zip ties, the cables were fixed to the longitudinal reinforcement of the arches for protection during the casting and concrete consolidation operations. (Figure 4.12 (b))
7- The cables were cut outside of the reinforcing cage. To allow for flexibility and safety of the DC boxes, an extra cable length of $20ft$ was provided outside the arches, as shown in Figure 4.12(c). The cables outside the arch were also covered with UV resistant conduit for protection from exposure to the sunlight.
8- The ends of the VWG cables were attached to special connectors shown in Figure 4.12 (d). These connectors enabled quick attachment to or detachment from multiplexer channels.
9- All VWGs were checked using a GK-404 readout box to confirm their functionality. (Figure 4.12(e))
10- The gages were connected to appropriate channels on the multiplexers in the DC boxes. (Figure 4.12 (f)). The first three arches were connected to two DC boxes whereas other arches were connected to only one DC box.
11- The final as-built locations of the VWGs were measured and recorded to provide the coordinates of each gage critical for calculations.
12- Once the outside forms were installed, the locations of all gages were labeled on top of the formwork, as shown in Figure 4.13 (a), to make sure construction personnel were aware of the gage locations. Therefore, the potential for damage during concrete placement and consolidation was minimized.
13- After the concrete pour was completed and before the end of finishing operations, a temporary wood assembly was constructed at the arch plinths, as shown in Figure 4.13 (b), to ensure that the cables exited the arch at the selected locations and remained perpendicular to the surface of the arch.

UT researchers were present on the site for casting of all 12 arches of the West 7th Street Bridge to make sure that the VWGs remained operational before they were embedded in the concrete. The researchers also ensured the suitability of the cable arrangement at the exit locations in the final concrete finish so that the instrumentation could be maintained in the final bridge following the end of construction. Table 4.5 provides the schedule of VWG installation and concrete pour for the arches.

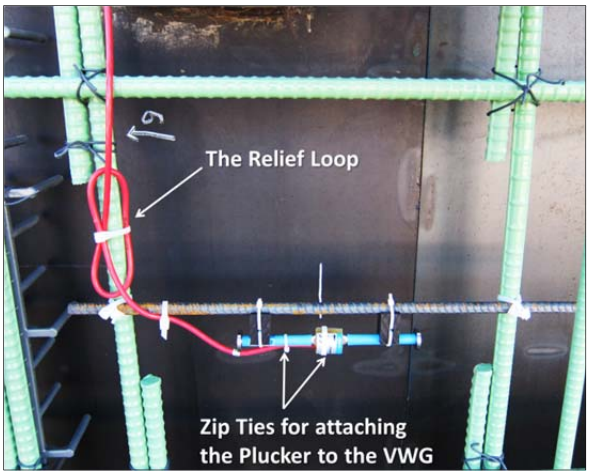

(a)

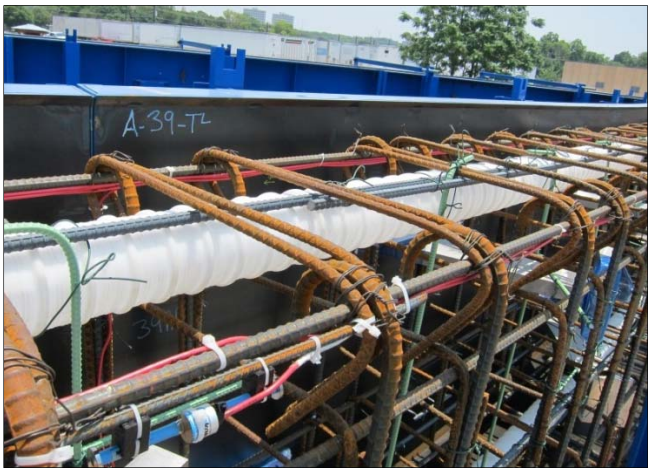

(b)

(c)

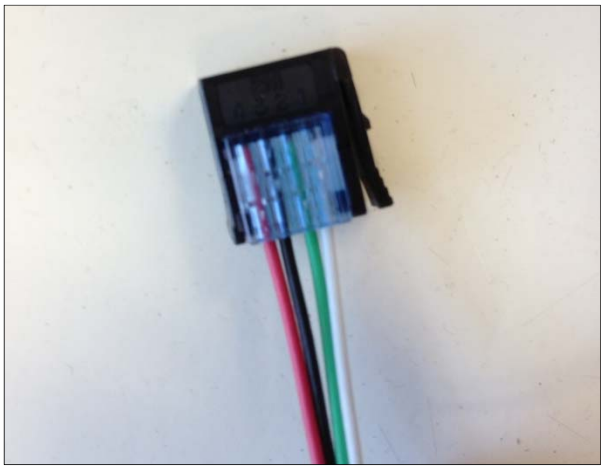

(d)

(e)

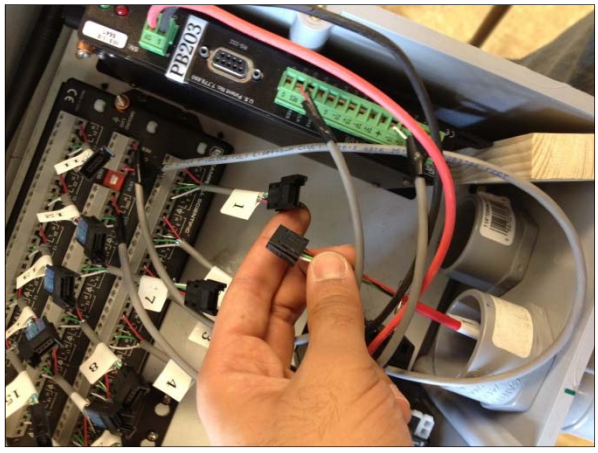

(f)

Figure 4.12-VWG installation process (continued).
(a) Attachment of the plucker to a VWG. (b) VWG cables fixed to the longitudinal reinforcement. (c) Providing extra length for VWG cables outside the arches. (d) VWG end connectors. (e) Checking VWGs using a GK-404. (f) connecting the VWGs to the multiplexers.

(a) **(b)**

Figure 4.13- VWG installation process (continued).
(a) Labeling the locations of the VWGs on the formwork. (b) Fixing the gage cables at the exit location.

Table 4.5- The schedule of VWG installation and concrete pour for the arches.

Arch No.	Number of VWGs	VWG Installation Date	Concrete Pour Date
1	40	June 20, 2012	July 10, 2012
2	40	July 20, 2012 and July 24, 2012	August 7, 2012
3	28	August 27, 2012	September 11, 2012
4	28	September 14, 2012 and September 15, 2012	September 25, 2012
5	10	October 6, 2012	October 16, 2012
6	10	October 13, 2012	October 26, 2012
7	10	November 6, 2012	November 13, 2012
8	10	November 24, 2012	December 4, 2012
9	10	December 8, 2012	December 19, 2012
10	10	December 24, 2012	January 7, 2013
11	12	January 17, 2013	January 22, 2013
12	16	Feb 1, 2012 and February 2, 2012	February 5, 2013
Total	224		

4.3 MONITORING THE INSTRUMENTATION

For each arch, monitoring the strains and temperatures began before the concrete pour was started and continued throughout the construction operations until the end of Stage 2 post tensioning. Following the end of Stage 2 post tensioning, the DC boxes could be transferred to subsequent arches if needed, and periodic readings could be used to track the time-dependent changes in the arches that were in storage. For later stages of construction, such as upward jacking and transportation operations, the continuous monitoring was reinstated by moving the DC boxes from one arch to another. In order to get a better picture of time-dependent changes in the arches, attempts were made to maintain continuous monitoring for as long as possible, even when no construction activity was in progress. In particular, Arch 2 was continuously monitored throughout the construction. The data

collected during the idle stages of construction also played an important role in understanding the thermal behavior of the structure.

The designed components of the instrumentation network proved to be efficient and flexible during construction. When the arches were moved over relatively large distances, for example during arch rotation, sliding and transportation, the DC boxes were moved together with the arches and the DL boxes could communicate with the DC boxes, manage the instrumentation process, and provide the researchers with the measured data. Figure 4.14 shows the situation of the DC boxes during different arch movement operations.

After the arches were installed in their final locations, moving the DC boxes from one arch to another and doing routine battery replacement became much more challenging. As shown in Figure 4.15, accessing the DC boxes on transported arches required using a manlift. When the original bridge was demolished, the situation worsened, and some of the arches became practically inaccessible for monitoring purposes. As a result, although all arches were monitored for the transportation operations and during erection onto the final bearings, only two spans of the bridge were monitored for floor beam installation and deck construction. A third span was monitored for floor beam installation, but not for deck construction.

Figures 4.16 to 4.18 provide a summary of the monitoring timeline for the arches during a 16-month period that starts at the end of concrete pour for Arch 1 and finishes at the end of construction. As can be seen in these figures, Arch 2 and Arch 4 were the only arches that were continuously monitored during deck construction. For Arch 1, during most of the storage time and also during deck construction, only half of the VWGs were connected to the DC boxes. However, as mentioned earlier, when the arches were not connected to the DC boxes, periodic monitoring was still in progress, and strains and temperatures were measured using the hand-held reader on each site visit.

For the first two arches, monitoring was conducted on site. UT researchers were present in the field for all construction operations so that they could ensure proper functioning of the monitoring system and immediately inform the construction team of any potentially alarming conditions. For subsequent arches, remote monitoring was used; however, the researchers were in close communication with the construction team to get informed of ongoing activities on the field and to relay the observations from the structure’s response.

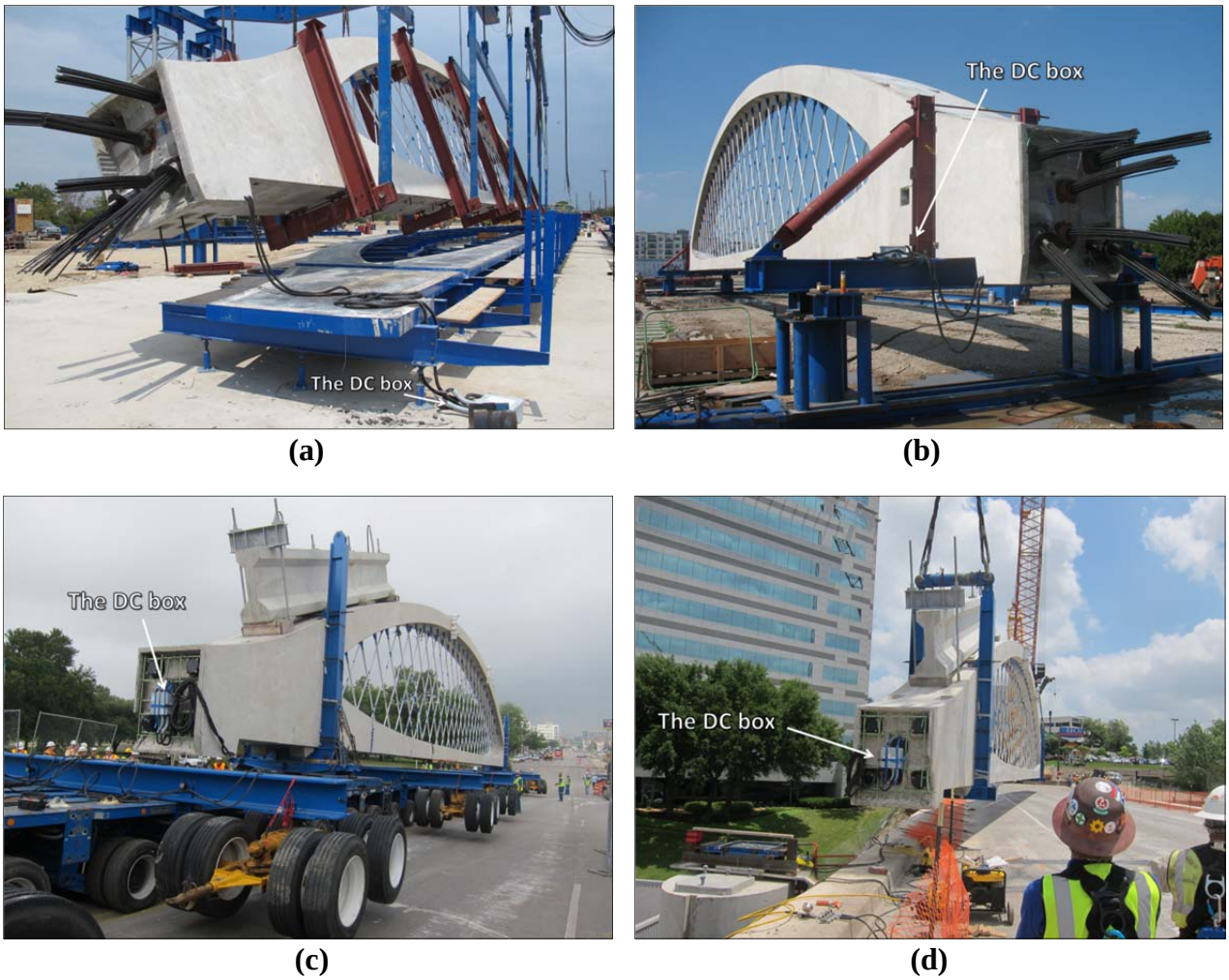

(a) **(b)**

(c) **(d)**

Figure 4.14- The situation of the DC boxes during different arch movement operations. (a) Rotation. (b) Sliding. (c) Transportation. (d)Final lifting.

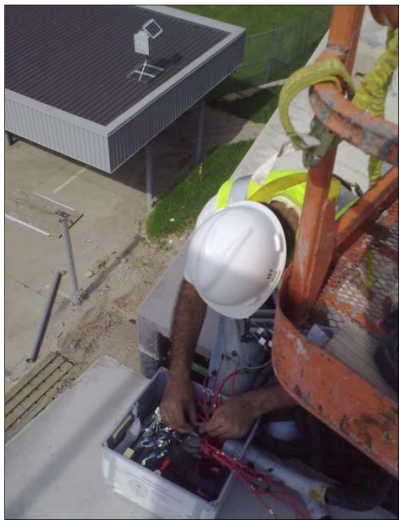

Figure 4.15- Disconnecting a DC box after the transportation of Arch 3.

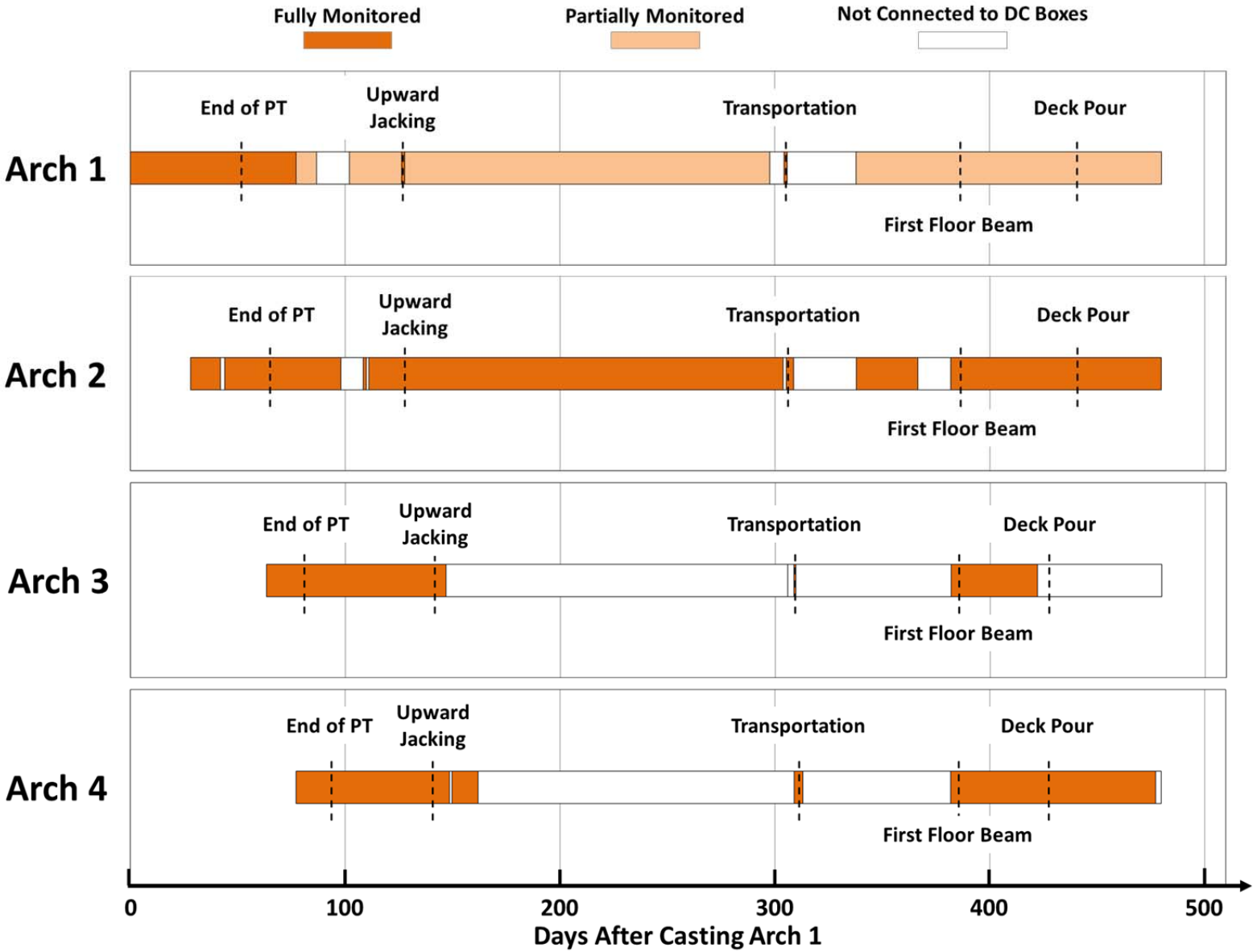

Figure 4.16- Timeline for monitoring Arches 1-4 during construction.

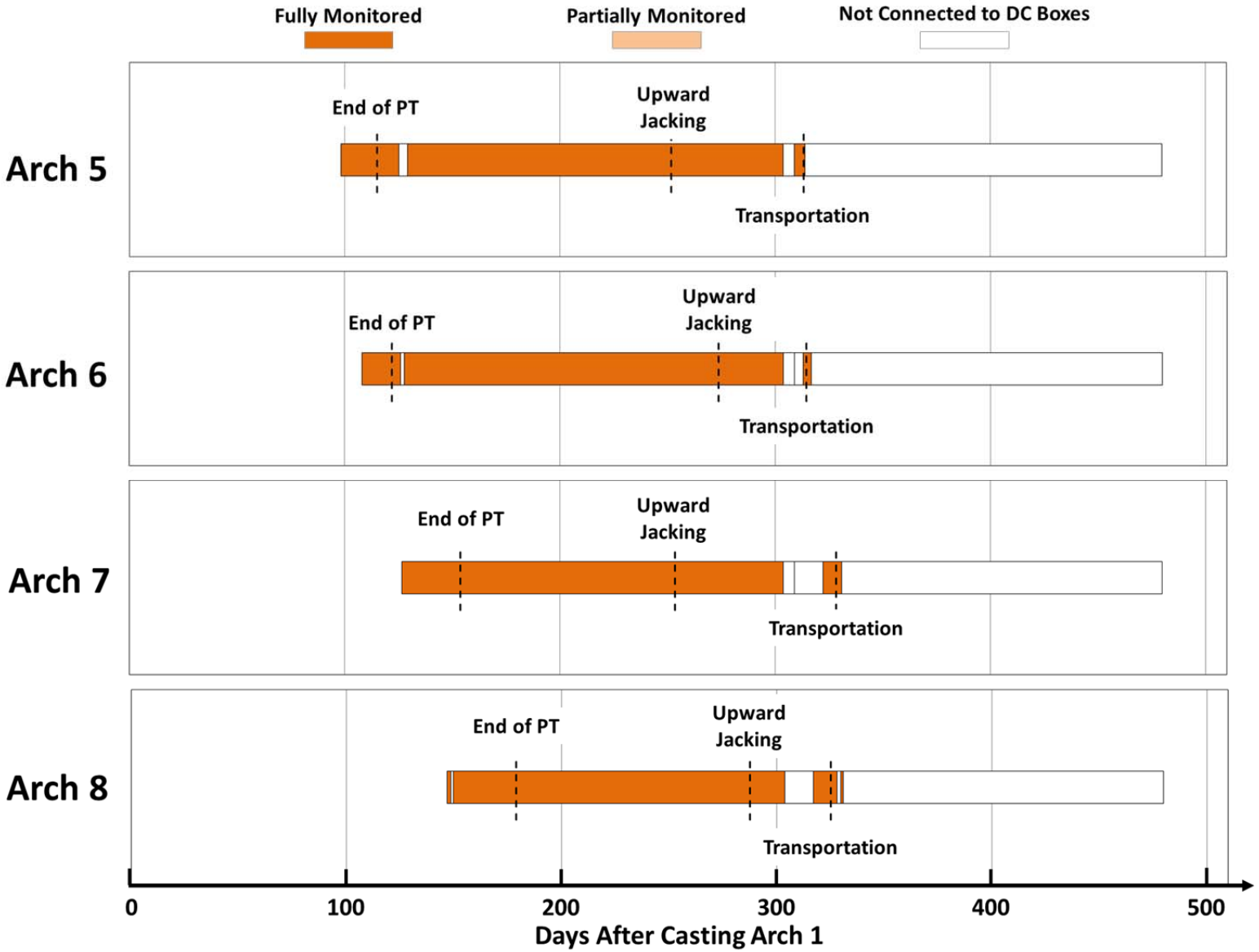

Figure 4.17- Timeline for monitoring Arches 5-8 during construction.

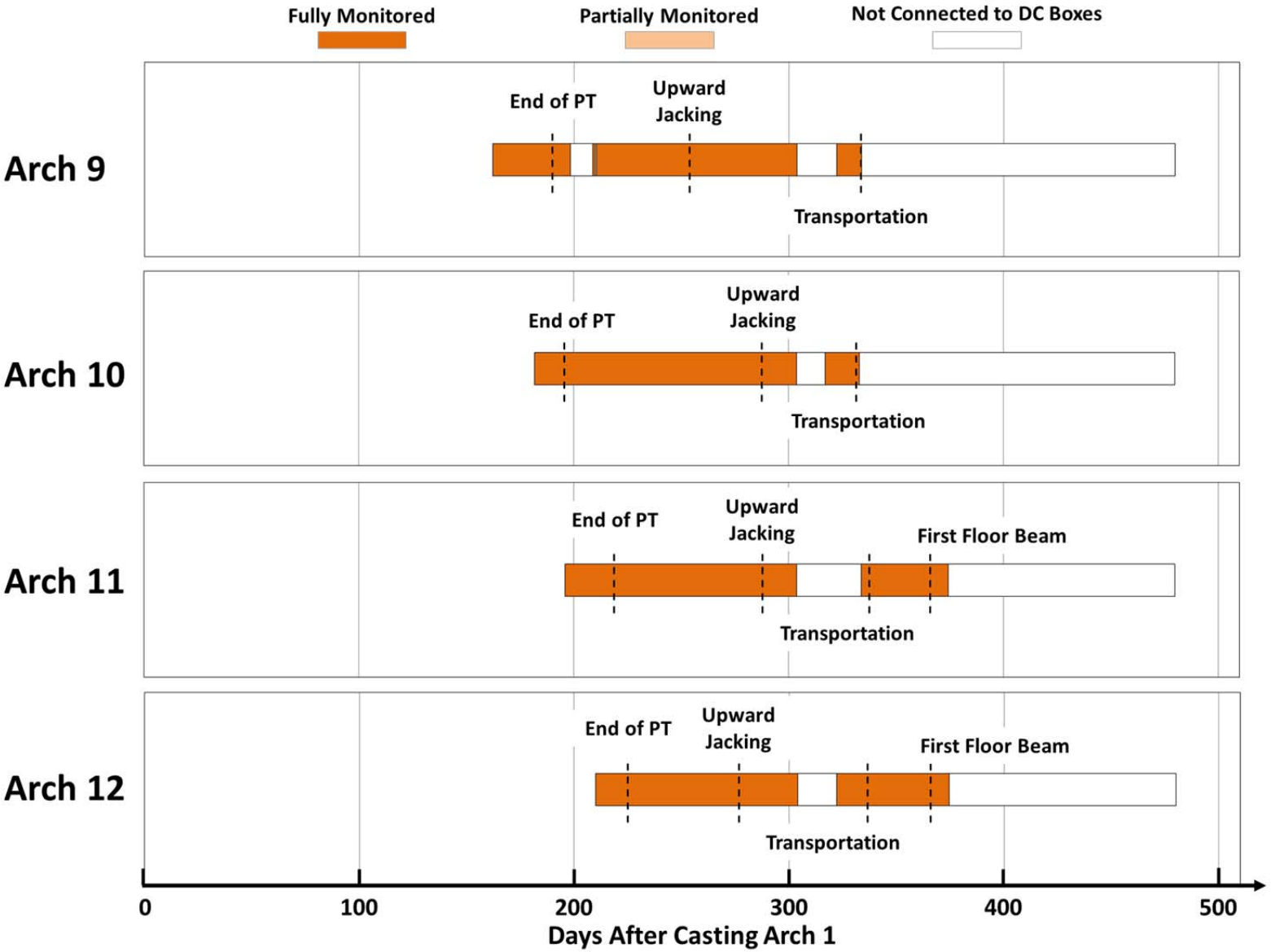

Figure 4.18- Timeline for monitoring Arches 9-12 during construction.

In order to ensure the safety of the arches during construction, an immediate picture of the structural behavior of the arches was necessary. Therefore, a post-processing module was programmed to calculate the stresses, curvatures, and internal actions in the critical sections of the arches in a real-time fashion. The basis for the calculations in this module is explained in Chapter 5. This module is also able to show structural parameters in appropriate graphs to give insight to UT researchers on the behavior of the arches and make the results easier to communicate with the design team. The control panel for this post-processing module is shown in Figure 4.19. When monitoring was performed on site, the graphs were also relayed to a smartphone, as shown in Figure 4.20, so that UT researchers could be aware of the structural behavior as well as the ongoing construction activity, without interfering with the construction personnel.

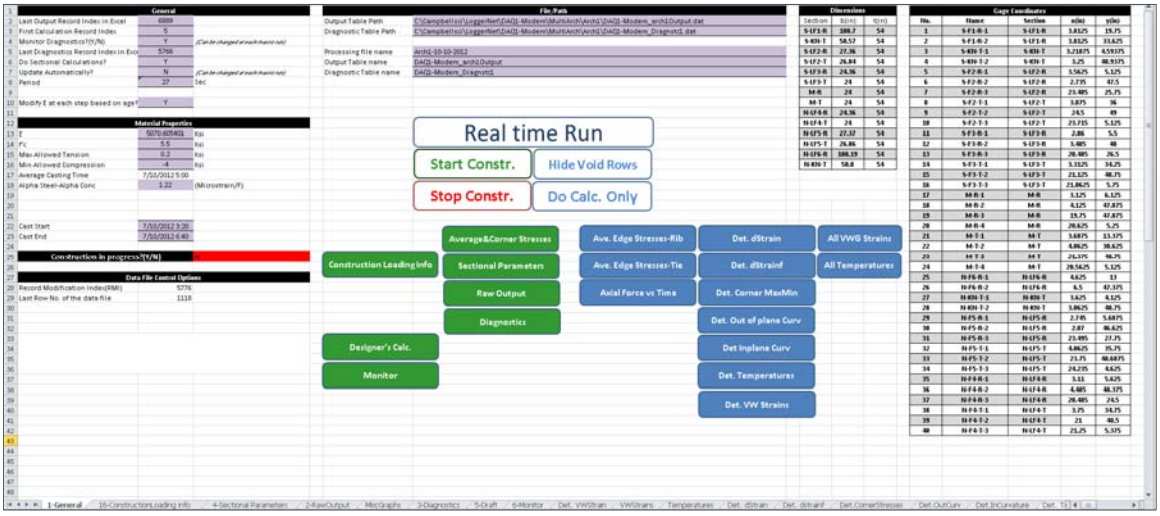

Figure 4.19- The Control panel for the post-processing module.

Figure 4.20- Using a smart phone to track stress changes in the structure.

4.4 LIVE LOAD TEST

After the bridge was opened to traffic, a static live load test was conducted on the bridge. The goal of the live load test was to measure the response of the arches under known live load conditions in the finished bridge, which included the non-instrumented deck and floor beams. The results from this test were used to produce a calibrated base-line finite element of the as-built bridge. Moreover, the documented response of the bridge immediately after opening would be a valuable reference for decisions regarding management and maintenance of the bridge in the future.

The live load test was conducted on December 18, 2013 between 10 AM and 11:30 AM. Performing the test overnight was preferable for minimizing thermal effects during the test. However, traffic control was only available for daytime testing. Since the structure had been monitored for thermal effects over an extended time, the thermal effects could be calculated and later excluded from the measured response of the structure. Only one span of the bridge, which was the easternmost span, was monitored during the live load tests. The tested span was supported by Arches 1 and 2, which were the most heavily instrumented arches. To obtain a static measurement, the trucks were positioned at desired locations on the span and after waiting for approximately 30 seconds, the measurements were made. For each position, at least three readings were taken to make sure of the repeatability of data.

The trucks used in the tests consisted of four sand trucks weighing approximately 50 , which were provided by the city of Fort Worth. Three of these trucks (Trucks A, B, and C) were identical. However, the fourth truck (Truck D) was of a different model and had slightly different axle dimensions. All trucks were weighed and measured for their dimensions before the test. Typical dimensions and axle weights of the trucks are presented in Figure 4.21 and Table 4.1, respectively.

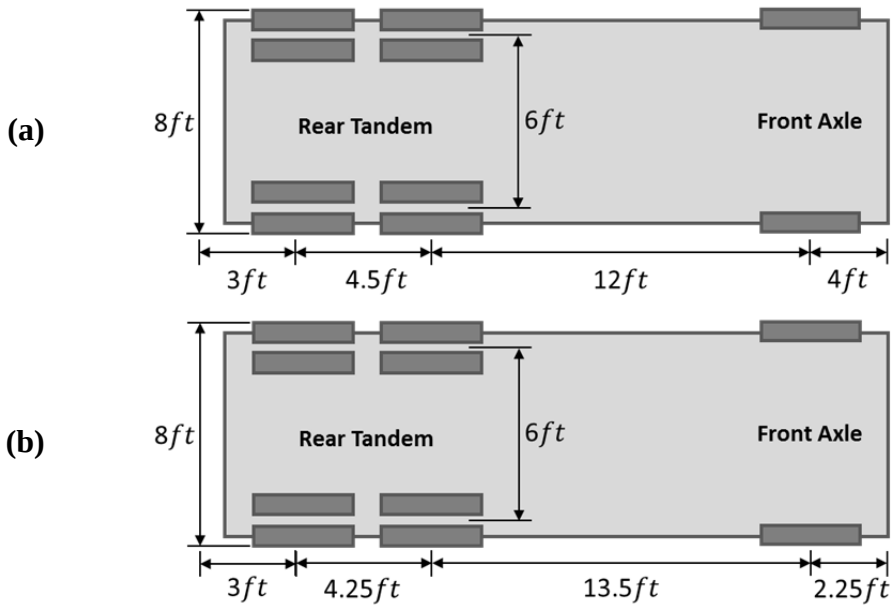

Figure 4.21- The dimensions of the trucks used for live load test. (a) Trucks A, B, and C. (b) Truck D.

Table 4.6- Measured axle weights from the trucks.

Truck	Front Axle Weight(lbs)	Rear Tandem Weight(lbs)
A	12960	36600
B	14440	42120
C	13240	38640
D	11880	39480

The trucks were positioned at four locations on the tested span, as shown in Figures 4.22 and 4.23. For positions 1 and 2, the trucks were located as close as possible to Arch 2. However, for positions 3 and 4, the trucks were positioned as close to the median as possible. As a result, the response of the arches to different longitudinal and transverse positions of the loads was recorded.

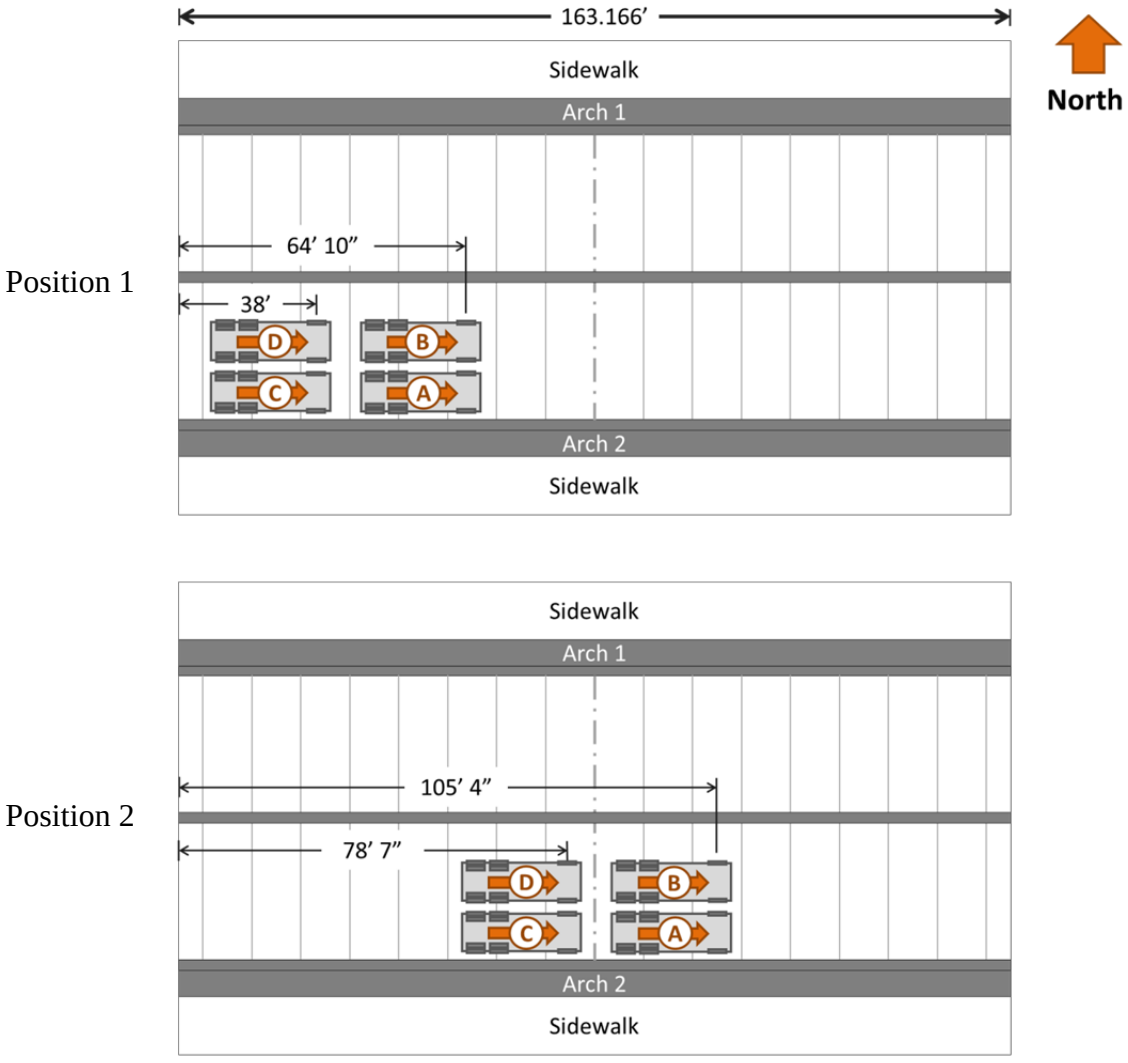

Figure 4.22-Eastbound truck positions.

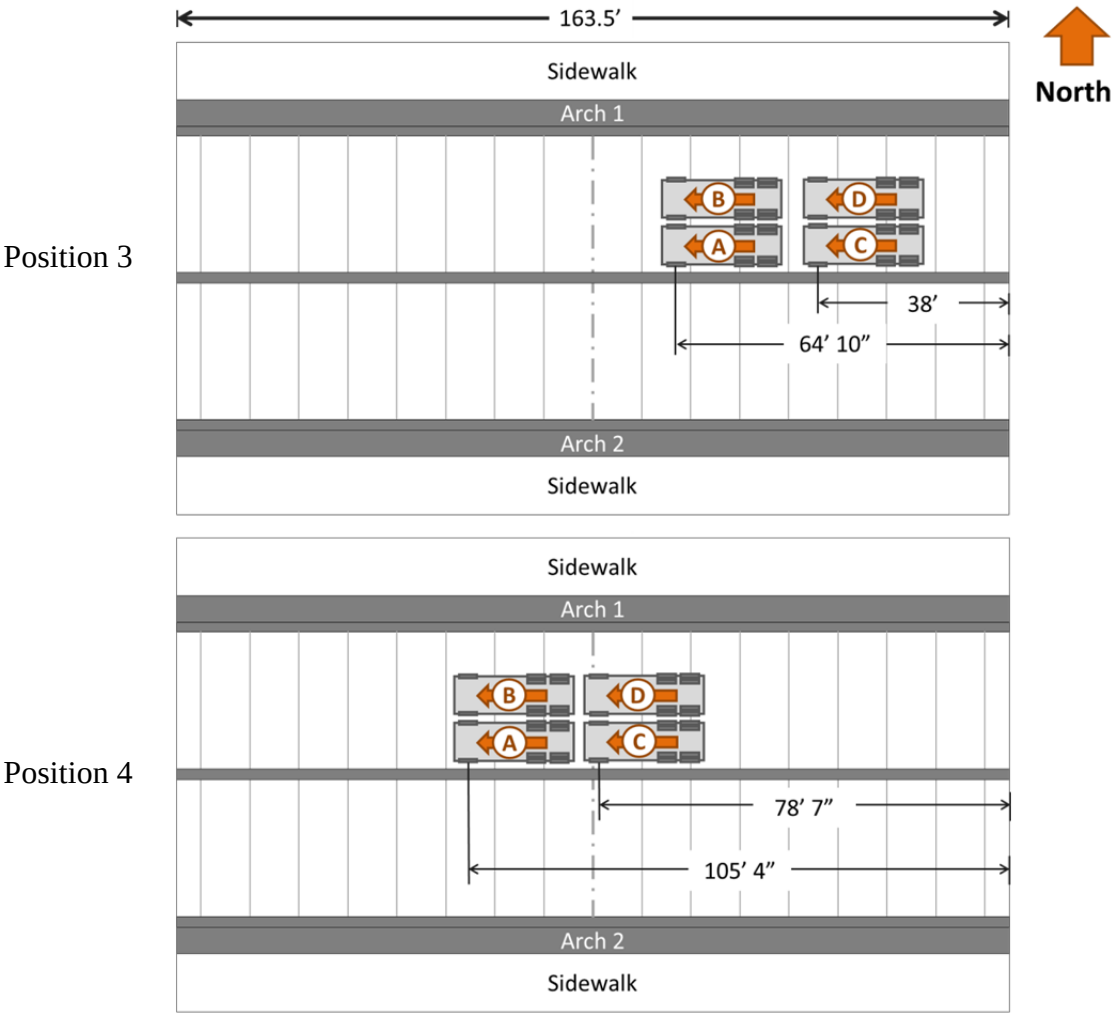

Figure 4.23-Westbound truck positions.

In order to reduce the disruption to traffic, the live load tests were conducted with a minimized time of full bridge closure. One day before the test, the desired longitudinal positions of the trucks were labeled on the arches. On testing day, first, one traffic lane of the bridge was closed so that the anticipated locations of the front axles of the trucks could be marked on the roadway, as shown in Figure 4.24 (a). Trucks A and C used the same closed lane to move to the marked locations, as shown in Figure 4.24 (b). Next, the traffic was completely blocked in one direction so that trucks B and D could move to position. It was only when all trucks were in position that both directions of traffic were closed, as shown in Figure 4.24(c), to make the measurements. When the sensor measurements were being made, the exact locations of the trucks were also recorded. The same steps were repeated for positioning the trucks in the other direction of traffic.

The results of the live load test are discussed in Chapter 6.

(a)

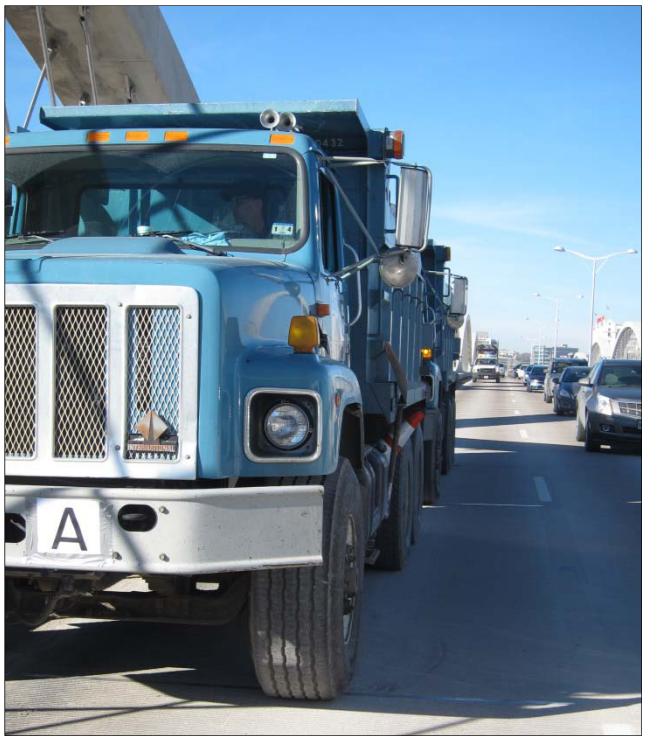

(b)

(c)

Figure 4.24- The live load test. (a) Marking the locations of the trucks on the road way (b) Moving the first two trucks to their positions (c) Complete bridge closure for making measurements.

4.5 OBSERVED DURABILITY OF THE VWGS

During the 17-month period of construction, the performance of the VWGs was carefully evaluated. As can be seen in Table 4.7, from the 224 VWGs installed in the arches, only one gage was lost during the concrete placement. The loss of this gage was attributed to a disconnected cable inside the cage, and not to the VWG itself. In total, only nine out of the 224 installed VWGs, or 4% of the VWGs, were lost over time in the instrumentation of the West 7th Street Bridge.

The outstanding performance of the VWGs in this project satisfied the researchers' expectation of the instrument durability and confirmed the observations from previous bridge monitoring studies. The 96% survival rate of the VWGs in this project provided justification for the extra cost for the VWGs as compared to foil gages, which have a typical survival rate of less than 40% after one year when embedded in concrete [8].

Table 4.7- Durability of embedded VWGs.

		Arch No.											
		1	**2**	**3**	**4**	**5**	**6**	**7**	**8**	**9**	**10**	**11**	**12**
No. of functional VWGS	Installed	40	40	28	28	10	10	10	10	10	10	12	16
	After Concrete Pour	40	40	27	28	10	10	10	10	10	10	12	16
	Upward Jacking	40	40	27	28	10	10	10	10	10	10	12	16
	Transportation	40	40	27	28	10	10	10	10	10	10	12	16
	End of Construction	40	39	26	26	10	10	10	10	9	10	12	16
	Live Load Test	38	38	N/A	N/A	N/A	N/A	N/A	N/A	N/A	N/A	N/A	N/A
Total Lost VWGs		2	2	2	2	0	0	0	0	1	0	0	0

Total Installed	224
Total Lost	9
Percent Loss	4%

4.6 PRACTICAL CONSIDERATIONS

4.6.1 Coordination Requirements

The relatively long distance between Austin and the job site in Fort Worth made coordination between the researchers and the construction team extremely important. The researchers needed to be informed of the updated construction schedule for planning the trips for installing the VWGs, attending the concrete pours, conducting on-site monitoring of the first two arches, and making the changes in the DAQ network as necessary. When remote monitoring was being used, the communication with the construction team was even more critical because the researchers needed to be continuously informed of ongoing activities on the site.

Fortunately, a successful cooperation was established in this project between the UT personnel and the construction team. The QC engineer from Sundt Construction and the TxDOT field engineer communicated the most recent progress on the site with the UT personnel, especially before the arches were transported to their final locations. Sundt personnel were also supportive of the instrumentation effort significantly by providing the researchers with continuous access to the site and providing construction equipment such as manlifts when needed.

4.6.2 Workforce for VWG Installation

Since only a limited time was available to UT personnel for instrumenting each arch, the VWGs had to be installed quickly. To accelerate the instrumentation, a team of UT graduate students was formed for installing the VWGs. The team included Hossein Yousefpour, Jose Gallardo, Ali Morovat, Kostas Belivanis, Vasilis Samaras, David Garber, and Hemal Patel.

Instrumenting the first two arches was especially challenging because of the large number of VWGs. While five members of the team participated in instrumenting these two arches, instrumentation took approximately 14 hours for each arch. However, for the last arches with only 10 VWGs, two members of the team could finish the instrumentation in 6 hours. The VWGs in most of the arches were installed over the weekends to minimize the interference with construction work.

4.6.3 Travel

One of the major difficulties in this project was the distance between Austin and the bridge location in Fort Worth and the significant number of visits necessary throughout construction. To accomplish the instrumentation plan, UT researchers had 48 trips to Fort Worth and spent more than 260 travel hours commuting back and forth to the jobsite. The substantial travel requirements greatly increased the demand on the research team and made planning of the instrumentation a remarkable endeavor.

4.6.4 Encountered Problems

While the instrumentation program was a success, there were isolated problems with the instrumentation that were encountered during the construction. These problems had two main reasons: first, the exposure of the instrumentation components to an uncontrolled environment, and second, the speed of construction activity, which was the main priority of

the construction team. These problems, which were not surprising in a field instrumentation study of this magnitude, are briefly described in the following paragraphs.

4.6.4.1 Misplacement of VWGs

Isolated misplacement of the VWGs occurred only in three sections of the first arch, mainly because of a miscommunication between UT researchers and the design team. In this arch, the instrumented knuckle sections at the rib were not located where the largest stresses were predicted, but at a distance of approximately $18\,in$ from the most critical sections. Moreover, the instrumented tie section at midspan was located exactly at the midspan, where large floor beam block-outs were also present. As a result, the observed strains at this section were highly influenced by the local effects and could not be a representative of the global behavior of the tie. UT researchers realized this mistake soon after casting the first arch. Other instrumented sections in this arch and all sections in other arches were instrumented correctly, according to the plan described in Section 4.2.4.

4.6.4.2 Displacement of the VWG Mounting Rebars

In the knuckle region of some of the first few arches, the construction workers untied and slightly moved the number 3 rebar to which the VWGs were attached. The reason was some last-minute changes in the reinforcement arrangement in that region. Fortunately, the instrumented sections were not changed because the rebars were not moved in longitudinal direction. When UT researchers were on the site before the concrete pour, they measured the new locations of these gages and updated the as-built records.

4.6.4.3 Damaged Equipment in the DC Boxes

In two instances, the analyzers and multiplexers in the DC boxes were severely damaged by water. Since the DC boxes had to remain attached to the arches, they were left exposed to the environment. Several precautionary measures, including the use of weather-resistant enclosures, had been implemented to protect the components of the instrumentation in these boxes from rain damage. However, the boxes could not stop water seepage if submerged. While the arches were monitored remotely, the construction personnel were responsible for moving the boxes with the arches as needed. However, on two occasions, the boxes were positioned in improper positions and were eventually submerged in rainwater. As a result, water seeped into the boxes and damaged the analyzers and multiplexers, which required costly repairs.

4.7 SUMMARY

The field instrumentation program included installing 224 VWGs in the arches of the West 7th Street Bridge and monitoring the strain and temperature changes in the structure during the construction. All components of the instrumentation were carefully selected to match the requirements of this project. The selected type of instrument, the vibrating wire strain gage could provide precision in measuring temperatures and strains together with long-term stability and durability in field conditions. Moreover, a flexible data acquisition network, which was capable of wireless communication and remote monitoring, was designed and configured for this project.

The instrumented sections in the structure were selected in coordination with the design team. Depending on the sectional strain distribution, two or three VWGs were used for instrumenting each section. The first arches were heavily instrumented to ensure their safety during construction operations, but subsequent arches were instrumented only at their midspan and most vulnerable sections.

All arches were monitored during construction operations on the precast yard and during transportation. However, only few arches were monitored for the deck construction stages. For the first two arches, UT researchers were present on the site for all construction operations. However, remote monitoring was used for evaluating later arches. After the bridge was opened to traffic, a static live load test was conducted on the bridge. Four 50-kip trucks were positioned on one of the spans of the bridge at different locations to measure the structure's response to live load conditions and provide more calibration data for a baseline finite element model of the bridge. The recorded as-built response of the bridge is believed to be a valuable tool for assisting with making future decisions regarding the maintenance of the bridge.

Due to careful planning and positive collaboration of the parties involved, the instrumentation program was very successful. All arches were instrumented as planned, and a significant amount of valuable data was collected. The results from this instrumentation program are used in the post-processing procedures of Chapter 5 to obtain the results that are discussed in Chapter 6.

Chapter Bibliography

[1] Campbell Scientific, Inc., "CR3000 Micrologger: Operator's Manual," Campbell Scientific, Inc., Logan, UT, 2011.

[2] J. L. Bordes and P. J. Debreuille, "Some Facts about Long-Term Reliability of Vibrating Wire Instruments," *Transportation Research Record*, no. 1004, pp. 20-27, 1985.

[3] L. E. Jacobsen, D. L. Israelsen and J. A. Swenson, "Vibrating Wire Sensor Using Spectral Analysis". US Patent US 7779690 B2, 24 August 2010.

[4] P. Choquet, F. Juneau, P. Debreuille and J. Bessette, "Reliability, Long-term Stability, and Gage Performance of Vibrating Wire Sensors with Reference to Case Histories," in *Field Measurements in Geomechanics: Proceedings of the Fifth International Symposium on Field Measurements in Geomechanics*, Singapore, 1999.

[5] Geokon, Inc., "Concrete Embedment," Geokon, Inc., [Online]. Available: http://www.geokon.com/4200-Series. [Accessed 21 3 2014].

[6] Geokon, Inc., Instruction Manual: Model 4200 Series Vibrating Wire Strain Gages, Lebanon, NH: Geokon, Inc., 2012.

[7] C. Oswald and R. Furlong, "Observed Behavior of a Concrete Arch Culvert," Center for Transportation Research at The University of Texas at Austin, Austin, TX, 1993.

[8] S. P. Gross, "Field Performance of Prestressed High Performance Concrete Highway Bridges in Texas," PhD Dissertation, The University of Texas at Austin, Austin, TX, 1998.

[9] K. Y. Kwon, "Design Recommendations for CIP-PCP Bridge Decks," PhD Dissertation, The University of Texas at Austin, Austin, TX, 2012.

[10] D. Garber, J. Gallardo, D. Deschenes, D. Dunkman and O. Bayrak, "Effect of New Prestress Loss Estimates on Pretensioned Concrete Bridge Girder Design," Center for Transportation Research at The University of Texas at Austin, Austin, TX, 2013.

[11] J. B. McRae and T. Simmonds, "Long-Term Stability of Vibrating Wire Instruments: One Manufacturer's Perspective," in *Proceedings of the 3rd International Symposium on Field Measurements in Geomechanics*, Oslo, Norway, 1991.

[12] M. K. Larson, D. R. Tesarik, J. B. Seymour and R. L. Rains, "Instruments for Monitoring Stability of Underground Openings," *Proceedings: New Technology for Coal Mine Roof Support*, pp. 259-269, 2000.

[13] E. DiBiagio, "A Case Study of Vibrating-Wire Sensors That Have Vibrated Continuously for 27 Years," in *Proceedings of the 6th International Symposium on Field Measurements in Geomechanics*, Oslo, Norway, 2003.

[14] J. Blok, "Stress Monitoring and Sweep Control Studies for Innovative Prestressed Precast Arches," Master's Thesis, The University of Texas at Austin, Austin, TX, 2012.

[15] D. Birrcher, R. Tuchscherer, M. Huizinga, O. Bayrak, S. Wood and J. Jirsa, "Strength and Serviceability Design of Reinforced Concrete Deep Beams," Center for Transportation Research, The University of Texas at Austin, Austin, TX, 2008.

[16] Geokon, Inc., "Vibrating Wire Readout Box (Hand-held) | Model GK-404," Geokon, Inc., [Online]. Available: http://www.geokon.com/vibrating-wire-readout-box/. [Accessed 3 April 2014].

CHAPTER 5
Data Processing

5.1 INTRODUCTION

A considerable post-processing effort was necessary to interpret the data obtained from the instrumentation. The raw data included the strains in the VWGs and the temperatures at the locations of these sensors. These measurements were converted to parameters related to the structural behavior, namely structural strains and stresses, through the post-processing procedures.

Post-processing of the data from the West 7th Street Bridge was especially intricate due to time-dependent effects, numerous stages of construction, high degree of static indeterminacy and large thermal effects. The calculation procedure was modified several times to obtain stress estimates that did not include thermal and time-dependent effects. The final approved method required a substantial programing effort.

This chapter describes the post-processing procedure for the West 7th Street Bridge. The results obtained from these calculations are discussed in Chapter 6.

5.2 ESTIMATING THE IN-SITU STRENGTH OF THE CONCRETE

As noted in Chapter 3, the in-situ mechanical properties of concrete in the arches were estimated as a function of time by combining the results of the material tests in FSEL with the results of the maturity tests by the contractor and the temperature history of the arches recorded by the instrumentation.

Figure 5.1 illustrates the procedure for calculating the compressive strength for each arch using the recorded temperatures. For each arch, the temperatures of the concrete were monitored from the beginning of the concrete pour. Since most of the temperature records were taken from the rib and the tie, the average temperature from all VWGs would have been biased towards the rib and the tie. To avoid this problem, three average temperatures were calculated: average rib temperature (T_{Ave}^{Rib}), average tie temperature (T_{Ave}^{Tie}), and average knuckle temperature (T_{Ave}^{Kn}). The maturity index was independently calculated for the rib, the tie, and the knuckle using these average values and Equation (3.6). Using the calculated maturity indices and the strength-maturity relationships obtained in Section 3.6.3, the compressive strength of the concrete was calculated for the rib, the tie, and the knuckle region. Finally, these three compressive strength values were averaged to obtain the average compressive strength of the concrete at each time. One important consideration in using the equations of Section 3.6.3 was that the maturity-based strength relationship was considered valid only within its calibration range. In other words, calculating the maturity-based strength was stopped once the recorded maturity index exceeded the maximum maturity that was observed in the maturity studies by Sundt.

Figure 5.1- Procedure for calculating the maturity-based compressive strength of the arches.

With the exception of Arch 6, all arches showed a similar trend for strength gain. As shown in Figure 5.2, Arch 6 showed a significantly higher strength than the other arches. The QC reports from the construction team had also reported higher strength for this particular arch. The higher compressive strength may have resulted from a particular batch of cement that was used for Arch 6.

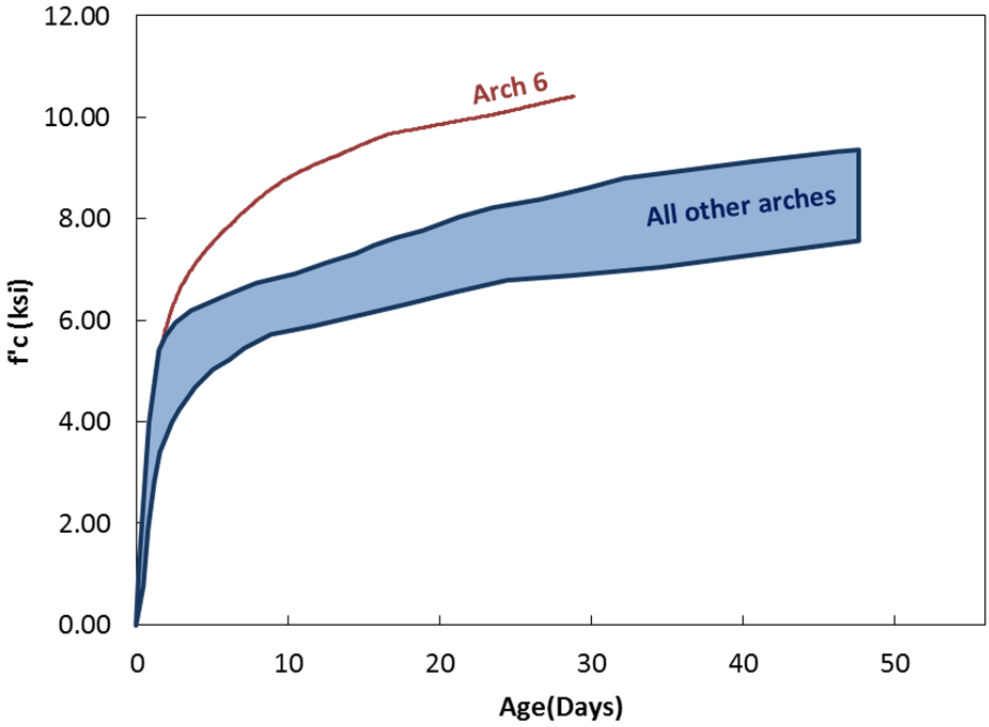

Figure 5.2-Difference between the strength gain of Arch 6 and other arches.

In order to simplify the post-processing calculations, the calculated maturity-based strength values were used to develop a continuous correlation equation for f_c' versus time. Since all arches except Arch 6 had similar strength development over time, a correlation was developed based on average compressive strength from all arches other than Arch 6. A separate correlation was also developed for Arch 6 so that realistic stresses could be calculated for this arch as well. After trying several equation forms, Equation (5.1) provided a good representation of the average calculated f_c' values as a function of time. This equation uses a form similar to what was used in a concrete creep model by Gardner and Lockman,

known as GL2000 [1]. However, the coefficients are calibrated for the values obtained in this project. For Arch 6, the compressive strength at each time was found using Equation (5.2). Figure 5.3 compares the values obtained from the correlation equations with the maturity-based strength of the concrete in the arches.

$$f'_{c\,All}(t) = 7500\left(\frac{t^{0.75}}{1.75 + 0.8t^{0.75}}\right) \tag{5.1}$$

$$f'_{c\,(6)}(t) = 7500\left(\frac{t^{0.75}}{1.15 + 0.65t^{0.75}}\right) \tag{5.2}$$

In which,

$f'_{c\,All}(t)$ = Time-dependent strength of concrete in all arches except Arch 6, psi
$f'_{c\,(6)}(t)$ = Time-dependent strength of concrete in Arch 6, psi
t = Concrete age, $days$

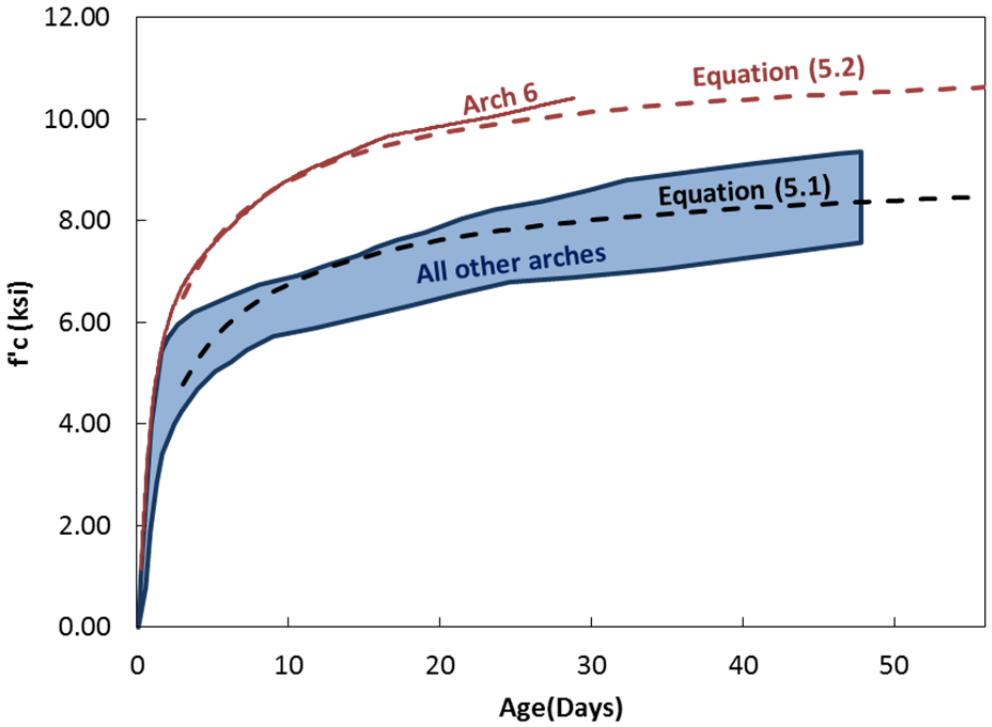

Figure 5.3- Correlation equations for estimating f'_c, as compared to the maturity-based strength values.

The modulus of elasticity of the concrete was calculated at each specific time, using the time-dependent compressive strength from Equation (5.1) or Equation (5.2) as the input to Equation (3.4).

5.3 CALCULATING STRAIN CHANGES AT THE LOCATIONS OF VWGS

As discussed in Chapter 4, the output of the VWGs consisted of the strain indicated by the vibrating wire (ε_{VWG}), and the temperature in the corresponding thermistor (T). These two parameters were first used for calculating strain changes in the concrete at the locations of the VWG.

The strain change calculation requires careful attention to thermal deformations in concrete and in the VWG. Since the end blocks of the VWGs move together with concrete, the total deformation in the VWG is equal to that of its surrounding concrete. However, the strain measured by the VWG does not include the thermal expansion of the sensor itself [2]. If the coefficient of thermal expansion of the gage (α_{VWG}), is equal to that of concrete (α_C), any unrestrained thermal expansion or contraction of concrete would remain undetected by the VWG because the gage would deform by the same magnitude. However, α_{VWG} is generally different from α_C and the strain change as measured by the VWG was corrected using Equation (5.3), to calculate the real total strain change in the gage. This strain change is equal to the total strain change in the surrounding concrete at the location of the gage.

$$\Delta\varepsilon_{Total}^{(i)}(t,t_0) = [\varepsilon_{VWG}^{(i)}(t) - \varepsilon_{VWG}^{(i)}(t_0)] + \alpha_{VWG} \times [T^{(i)}(t) - T^{(i)}(t_0)] \quad (5.3)$$

In which,

$\Delta\varepsilon_{Total}^{(i)}(t,t_0)$ = Total strain change at the location of VWG i, between time t and time t_0, including unrestrained thermal deformation

$\varepsilon_{VWG}^{(i)}(t)$ = Strain in VWG i at time t, as obtained from DAQ

$\varepsilon_{VWG}^{(i)}(t_0)$ = Strain in VWG i at time t_0, as obtained from DAQ

$T^{(i)}(t)$ =Temperature in VWG i at time t

$T^{(i)}(t_0)$ =Temperature in VWG i at time t_0

α_{VWG} =$6.78 \times 10^{-6} \frac{1}{^\circ F}$, Coefficient of thermal expansion of the VWG

In order to calculate the non-thermal part of the concrete strain change ($\Delta\varepsilon_{nth}$), the unrestrained thermal deformation of the concrete was subtracted from $\Delta\varepsilon_{\text{Total}}$, as expressed in Equation (5.4) [2]. However, since the arches were indeterminate, temperature changes induced stresses in the arches, and $\Delta\varepsilon_{nth}$ included elastic strain changes due to restrained thermal deformation.

$$\Delta\varepsilon_{nth}^{(i)}(t,t_0) = [\varepsilon_{VWG}^{(i)}(t) - \varepsilon_{VWG}^{(i)}(t_0)] + (\alpha_{VWG} - \alpha_C) \times [T^{(i)}(t) - T^{(i)}(t_0)] \quad (5.4)$$

In which,

$\Delta\varepsilon_{nth}^{(i)}(t,t_0)$ = Total strain change in the concrete at the location of VWG i, between time t and time t_0,excluding unrestrained thermal deformations

α_C = Coefficient of thermal expansion of the VWG, determined in Section 5.5

5.4 SECTIONAL STRAIN CALCULATIONS

As noted in Chapter 4, the most critical strains are expected to occur at the corners and edges of each cross section. These corner and edge strains were calculated from strain

changes at the location of the VWGs, as explained in the following paragraphs. In this section, terms “top”, “bottom”, and “side” refer to different locations on the arches in their vertical position.

5.4.1 Sections with Two VWGs

Sections in the D-regions of the arches were instrumented using two VWGs that were close to the top edges. For these sections, the strain distribution was assumed linear along the 4.5 ft width of the arches. However, the distribution was expected to be highly nonlinear along the depth of the section. As a result, the strains and therefore the stresses were calculated along the width of the arch, but only at the level of the installed VWGs, as shown by line AB in Figure 5.4.

Using linear extrapolation, the strains at any point along AB can be calculated as follows.

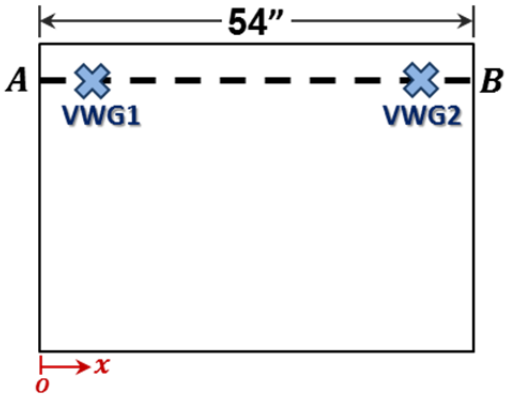

Figure 5.4- General layout of sections with two VWGs.

$$\Delta\varepsilon(x) = \Delta\varepsilon^{(1)} + \frac{\Delta\varepsilon^{(2)} - \Delta\varepsilon^{(1)}}{x_2 - x_1} \times (x - x_1) \tag{5.5}$$

In which,

$\Delta\varepsilon(x)$	= strain change at any location along AB with a distance x from the origin
$\Delta\varepsilon^{(1)}, \Delta\varepsilon^{(2)}$	= concrete strain changes at the locations of the VWGs
x	= horizontal distance from the location under consideration along AB from the origin
x_1, x_2	= horizontal distances between the locations of VWGs and the origin

The origin for the coordinate system can be selected on any arbitrary side of the arches. The maximum strains occur either at A or B and are calculated as follows.

$$\Delta\varepsilon^{(A)} = \Delta\varepsilon(0) = \Delta\varepsilon^{(1)} - \frac{\Delta\varepsilon^{(2)} - \Delta\varepsilon^{(1)}}{x_2 - x_1} \times (x_1) \tag{5.6}$$

$$\Delta\varepsilon^{(B)} = \Delta\varepsilon(54") = \Delta\varepsilon^{(1)} + \frac{\Delta\varepsilon^{(2)} - \Delta\varepsilon^{(1)}}{x_2 - x_1} \times (54" - x_1) \tag{5.7}$$

When the arches are treated as 2D structures, the average strain along AB is of interest and is calculated by averaging the strains at points A and B. It should be noted that this average is different from the result of simply averaging $\Delta\varepsilon^{(1)}$ and $\Delta\varepsilon^{(2)}$.

$$\Delta\varepsilon^{(Ave)} = \frac{\Delta\varepsilon^{(A)} + \Delta\varepsilon^{(A')}}{2} \tag{5.8}$$

5.4.2 Sections with Three or Four VWGs

Most of the monitored sections in the B-regions of the arches were instrumented using three or four VWGs. Strains at any point in these sections can be calculated using Equations (5.9) to (5.17). These equations were derived using analytic geometry, assuming arbitrary locations for the VWGs. Therefore, the equations are valid for all VWG arrangements shown in Figure 5.5.

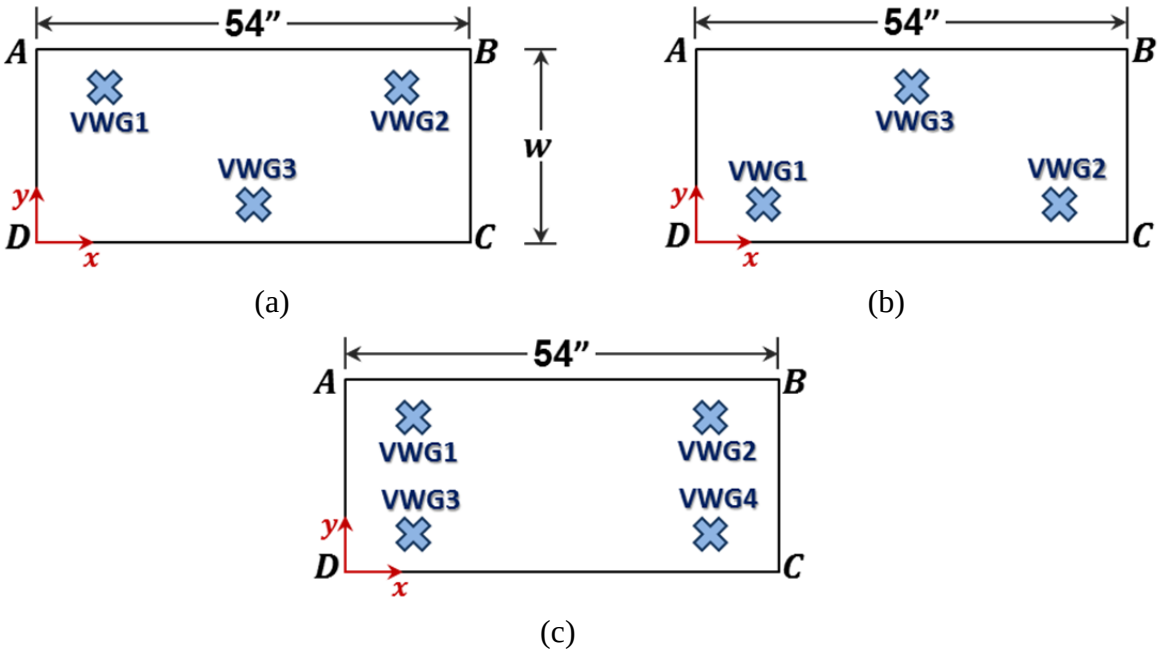

Figure 5.5- General layout of sections in B-regions.
(a) Rib sections with three VWGs (b) Tie sections with three VWGs (c) Sections with four VWGs.

Strain changes at any point in the instrumented cross section can be found using Equation (5.9).

$$\Delta\varepsilon(x, y) = a \times x + b \times y + c \tag{5.9}$$

In which,

$\Delta\varepsilon(x, y)$ = strain change at any arbitrary point in the section with coordinates x and y
a, b, c = plane equation coefficients.

The plane equation coefficients, a, b, and c are calculated using Equation (5.10). For sections with three VWGs, the equation describes the unique plane that passes through the instrumented points. For sections with four VWGs, the equation represents the best fit for the deformed section.

$$\begin{bmatrix} a \\ b \\ c \end{bmatrix} = \begin{bmatrix} K_1 & K_2 & n \\ K_4 & K_6 & K_1 \\ K_6 & K_5 & K_2 \end{bmatrix}^{-1} \times \begin{bmatrix} K_3 \\ K_7 \\ K_8 \end{bmatrix} \tag{5.10}$$

$$K_1 = \sum_{i=1}^{n} x_i \qquad K_2 = \sum_{i=1}^{n} y_i \qquad K_3 = \sum_{i=1}^{n} \Delta\varepsilon^{(i)} \qquad K_4 = \sum_{i=1}^{n} x_i^2$$

$$K_5 = \sum_{i=1}^{n} y_i^2 \qquad K_6 = \sum_{i=1}^{n} x_i \times y_i \qquad K_7 = \sum_{i=1}^{n} x_i \times \Delta\varepsilon^{(i)} \qquad K_8 = \sum_{i=1}^{n} y_i \times \Delta\varepsilon^{(i)}$$

In Equation (5.10),

n = number of VWGs in the cross section
x_i = horizontal distances from the location of each VWG to the origin
y_i = horizontal distances from the location of each VWG to the origin
$\Delta\varepsilon^{(i)}$ = concrete strain changes at the locations of each VWG

The strains at the corners are calculated by substituting the coordinates of the corners for x and y in Equation (5.9).

$$\Delta\varepsilon^{(A)} = b \times (w) + c \tag{5.11}$$
$$\Delta\varepsilon^{(B)} = a \times (54") + b \times (w) + c \tag{5.12}$$
$$\Delta\varepsilon^{(C)} = a \times (54") + c \tag{5.13}$$
$$\Delta\varepsilon^{(D)} = c \tag{5.14}$$

The strains at the center of gravity of each section and the average strains at top and bottom edges of the cross section can be calculated as follows.

$$\Delta\varepsilon^{(C.G.)} = a \times (27") + b \times (\frac{w}{2}) + c \tag{5.15}$$
$$\Delta\varepsilon^{(top)} = \frac{\Delta\varepsilon^{(A)} + \Delta\varepsilon^{(B)}}{2} \tag{5.16}$$
$$\Delta\varepsilon^{(bot)} = \frac{\Delta\varepsilon^{(C)} + \Delta\varepsilon^{(D)}}{2} \tag{5.17}$$

5.5 Estimating the Coefficient of Thermal Expansion of Concrete

As discussed in Section 5.3, calculating the non-thermal component of the concrete strain required knowledge of the coefficient of thermal expansion of concrete (α_c).

Moreover, α_c is an important parameter for simulating the response of the arches to thermal changes.

The coefficient of thermal expansion can be highly variable between different concrete mixes. While a value of 5.5 microstrain per degree Fahrenheit is usually used for design, thermal expansion tests reported in literature have revealed α_c values between 3 and 8 microstrain per degree Fahrenheit [3]. The aggregate type and volume is known to have a dominating effect, with limestone concrete generally expanding less than river gravel concrete. In a relatively recent study by TxDOT, 94 concrete mixes from Texas were evaluated for their coefficient of thermal expansion. Concrete mixes made with limestone were found to possess α_c values up to 30% lower than similar mixes made with siliceous gravel, and α_c values for limestone mixes were reported to be between 4 and 4.7 microstrain per degree Fahrenheit [4].

The values of α_c for the concrete in the West 7th Street Bridge were calculated based on the recorded response of the arches to thermal changes. This method is believed to be more reliable in providing representative values of the structure as compared to cylinder-level tests. If no elastic or time-dependent strain occurs in the arches, their recorded response is governed by unrestrained thermal expansion. More specifically, the strain change between two data points recorded from the arches can be considered as thermal strain if the following conditions are met:

(1) No loads are applied to the arches between the two recorded data points.
(2) The arch elements can freely expand or contract under temperature change so that no stresses are produced due to restrained thermal deformations.
(3) All temperatures in the structure are changed by the same amount, so no stresses are induced in the structure due to thermal gradients.
(4) Other time-dependent concrete deformations, namely creep and shrinkage, are zero or negligible.

Since significant creep strains affect the data after post tensioning, the useful data for calculating α were limited to what was collected before Stage 1 PT. Moreover, all data points from the first 24 hours after the concrete pour, all of the daytime records, and all of the nighttime records in which the total temperature range was larger than $7.5°F$ were filtered out. The strain change between the remaining data points was governed by thermal strains. During the period represented by these records, the arches were positioned on their sides on the soffit of the formwork, and no hangers were installed. Therefore, no significant internal or external restraint prevented expansion or contraction of the arches. Moreover, since the structure was compared between different states of uniform temperature, no thermal stresses were expected to affect the strain changes between the data points. The only remaining concern was shrinkage. However, the arches were more sensitive to thermal changes than to shrinkage, and the effects of shrinkage were neglected when using the filtered records. The concrete used in the arches was a low-shrinkage mix, and the arches had relatively large volume to surface ratios. As a result, the drying shrinkage was relatively small during the calibration period. In most arches, the first filtered record was obtained several days after concrete pour. Therefore, the autogeneous shrinkage was also not expected to be significant. Moreover, if significant shrinkage had happened between the filtered data points, a strong correlation would not have existed between strains and temperatures. Nevertheless, a linear correlation with a large coefficient of determination, R^2, existed between strains and temperatures, and the validity of neglecting the shrinkage strains was reaffirmed.

The filtered data were first used to calculate the total strain change at the location of each VWG, using Equation (5.3). These strain changes were then used as the input to the equations of Section 5.4.2 to find the total strain changes at the center of gravity of all instrumented sections of each arch. Finally, the strain changes at the center of gravity of all sections for the filtered records were plotted versus temperature changes, and a linear regression analysis was used to find α_c for each arch, as shown in Figure 5.6 for one of the arches.

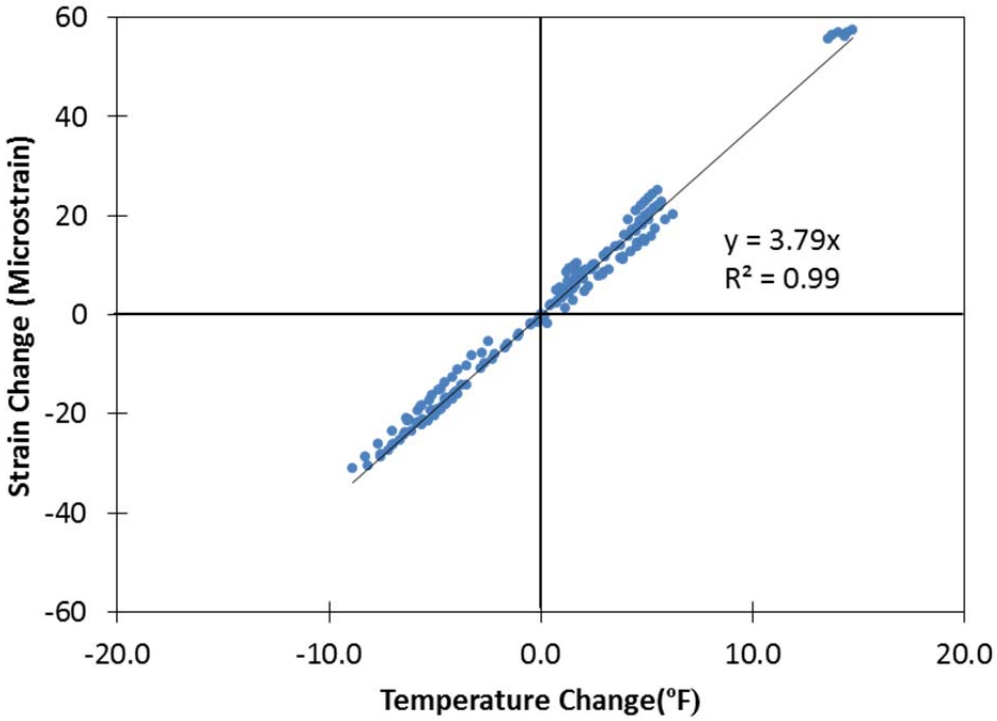

Figure 5.6- Strain-temperature correlation for Arch 9.

Figure 5.7 shows the α_c values that were calculated for the arches. After filtering the data, the number of remaining points was too few for arches 3, 4, 7, and 8. Therefore, α_c was not calculated for these four arches. As can be seen in the figure, the average value of α_c was equal to 4 microstrain per degree Fahrenheit and this value was used throughout the post-processing calculations.

$$\alpha_c = 4 \times 10^{-6} \left(\frac{1}{^\circ F}\right) \tag{5.18}$$

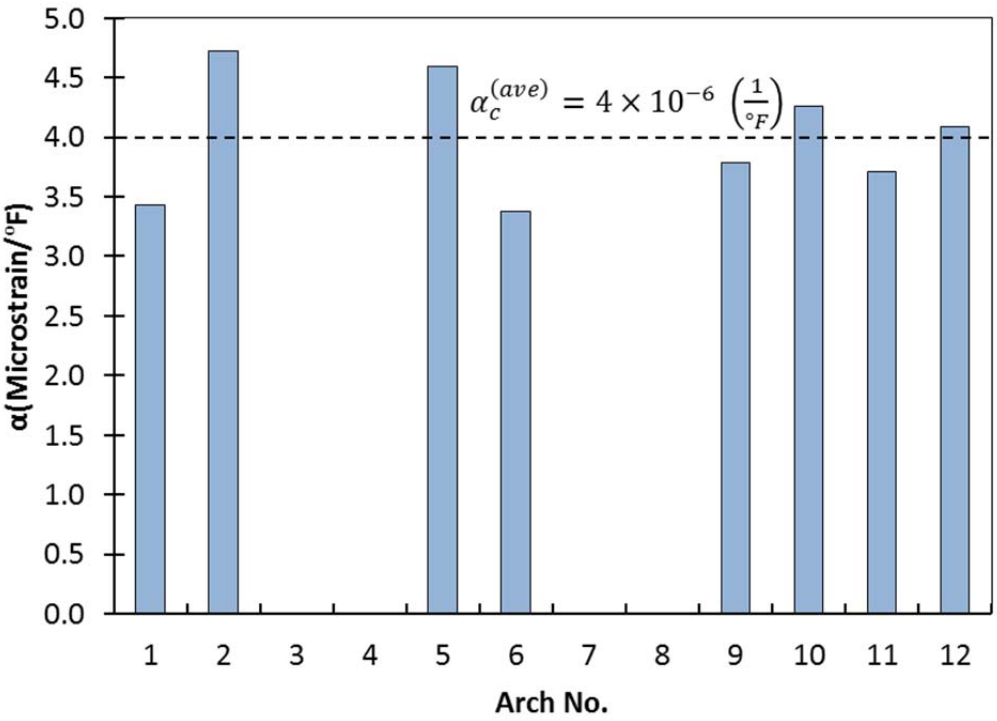

Figure 5.7- Coefficient of thermal expansion in the arches.

5.6 STRESS CALCULATIONS

Calculated strains provided a valuable picture of the elastic and time-dependent response of the arches. However, from a practical perspective, the stresses were more important. Ensuring the safety of arches against cracking was possible only if the total stress level in the structure could be calculated and compared with tensile strength of concrete. Moreover, all design calculations were based on stress values, and the only way to verify those calculations was by calculating the stresses in the structure. Unfortunately, the recorded strains could not be easily converted to stresses because stresses were not the only sources of strain changes in the structure.

When concrete is subjected to sustained loads, its volume tends to change over time. This change is usually divided into two main categories of creep, which is dependent on the stress level, and shrinkage, which is assumed independent of the stress level. Most of creep and shrinkage deformations occur during the early ages of concrete elements and soon after loading. As a result, large creep and shrinkage effects are expected in the construction response of any concrete structure, including the arches of the West 7th Street Bridge.

On the other hand, for exposed structures such as bridges, significant thermal effects are expected in the structure's response. The structure is affected by direct solar radiation, changes in the ambient temperatures, and heat exchange with the surroundings. The thermal changes result in both unrestrained and restrained strains. Unrestrained thermal strains do not correspond to any stress changes in the structure. Therefore, they can be excluded from the measured strain history. However, in a highly indeterminate structure such as the West 7th Street Bridge, thermal strains are highly restrained. As a result, thermal changes result in real

stress changes in the structure, which tend to be redistributed and relieved during subsequent thermal changes.

Considering the thermal and time-dependent changes in the stress calculations was the most challenging aspect of the post-processing effort. Figure 5.8 shows the components of the strain changes that were recorded by the instrumentation. Among several components of the strain that are shown in this figure, those illustrated in red were excluded. The unrestrained thermal strains could be directly excluded by using Equation (5.4). Restrained thermal deformations caused real stress changes, but these stresses were short-lived and needed to be excluded. The strain changes due to creep and shrinkage needed a more in-depth evaluation. While creep and shrinkage strains per se did not correspond to stress changes, the indeterminacy of the structure caused these deformations to induce stress changes. As a result, a well-designed procedure was required to convert the strain history of the structure to a stress history.

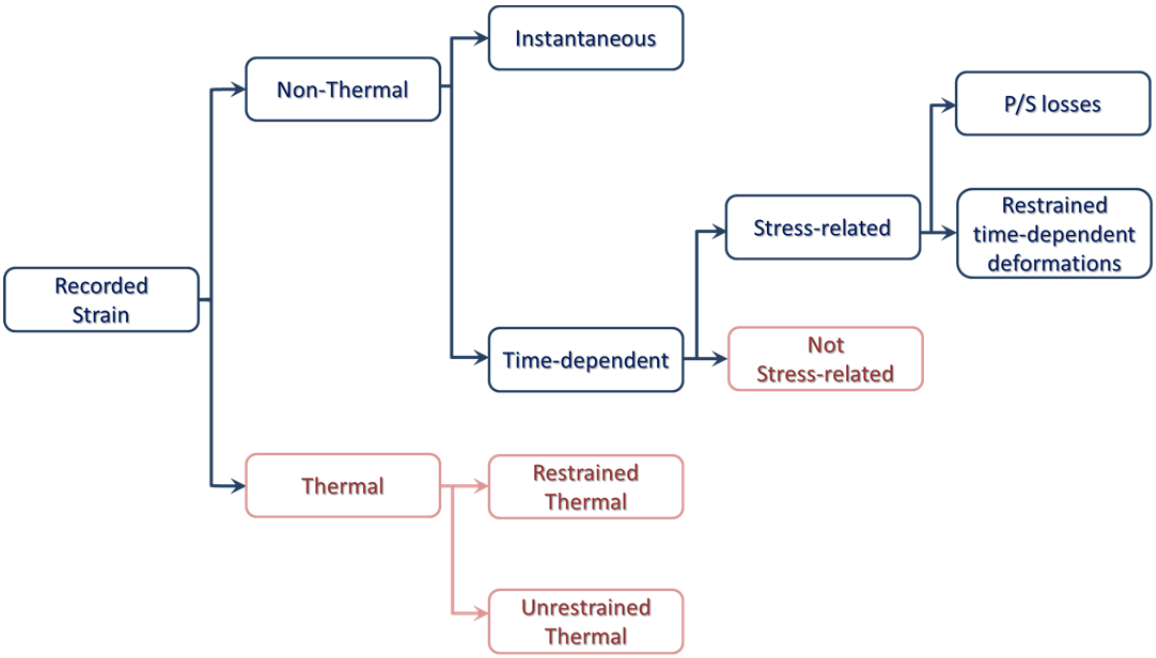

Figure 5.8-The components of the recorded strain from the structure.

The stress calculation procedure is explained in the following paragraphs. Calculating the stress changes, or stress increments due to each construction operation is explained first, and then the procedure for calculating the total stresses is discussed.

5.6.1 Calculating Elastic Stress Changes

5.6.1.1 Approximate Stress Changes during an Ongoing Construction Operation

In order to ensure the safety of the arches during an ongoing construction operation, the stress changes needed to be calculated in a real-time fashion. When a construction operation was carried out on the arches, temperature changes, shrinkage, and creep due to previous construction steps were also in progress. Some of these environmental and time-dependent effects caused strain changes that were larger than the strains induced by construction stresses. Separating the construction loading effects from other sources of strain changes was possible, as explained in later sections of this report; however, the "exact" procedure required collecting data from the arches over an extended period before and after each construction operation to identify the trends of strain and temperature changes. Such data were not available until the construction step under study was finished. Therefore, for monitoring the operation in real time, the approximate stress change was calculated using Equation (5.19).

$$\Delta\sigma'(\tau, \tau_0) = E_i \times \Delta\varepsilon_{nth}(\tau, \tau_0) \tag{5.19}$$

In which,

$\Delta\sigma'(\tau, \tau_0)$ = Approximate stress change at a corner or edge of the structure, between time τ_0 and time τ.

E_i = Average modulus of elasticity of concrete between τ_0 and τ, as found from Equation (3.4) and Section 5.2.

$\Delta\varepsilon_{nth}(\tau, \tau_0)$ = Total strain change at the desired corner or edge of the structure between τ_0 and τ, as found using the equations of Section 5.4.

Figure 5.9 shows an example of the result of this calculation during the first stage of post tensioning on Arch 2. As can be seen in this figure, while the overall stress changes can be easily identified, there are significant time-dependent and thermal effects, which cause the apparent stresses to drift with time.

This method was the only available option in real-time monitoring of the arches, and with some conservatism, the approximate stress levels were used for checking the safety of the arches. However, the approximate stresses from subsequent operations could not be added together because it would have induced very large errors in the stresses and would have made them unrealistic. In other words, for any ongoing operation, the approximate stress change was calculated from the beginning of that operation, but the stresses due to previous steps needed to be corrected before they could be added to this approximate stress change. As a result, the errors in the approximate stress levels were limited to the effects of time-dependent and thermal effects only over a period of only one day.

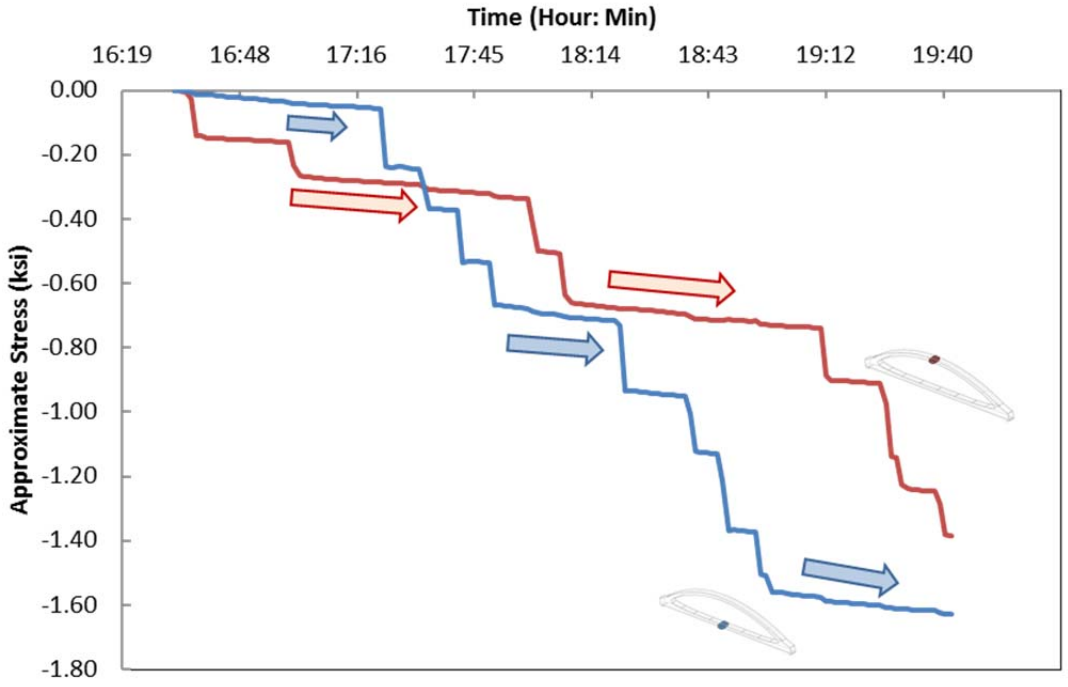

Figure 5.9-Approximate stress levels at the bottom of the rib and bottom of the tie at the midspan of Arch 2 during Stage 1 PT. The arrows show time-dependent and thermal effects.

5.6.1.2 Exact Stress Changes Due to Completed Construction Operations

If the structure is compared before and after a finished construction operation, the stress change can be calculated at the corners and edges of the arches due to each construction step, as expressed in Equation (5.20).

$$\overline{\Delta\sigma_i} = E_i \times \overline{\Delta\varepsilon_i} \tag{5.20}$$

In which,

$\overline{\Delta\sigma_i}$ = Stress change at a corner or edge of the structure due to construction step i.

E_i = Average modulus of elasticity of concrete during the construction step, as found from Equation (3.4) and Section 5.2

$\overline{\Delta\varepsilon_i}$ = Stress-related non-thermal strain change at the desired corner or edge of the structure due to construction step i, as found using the equations of Section 5.4

Based on the speed of construction activity and the rate of stress changes in the arches, the construction steps could be divided into two categories: rapid operations, and slow operations.

Rapid operations such as post tensioning induced significant stress changes in the structure over a short time. These operations usually included several sub steps, and the strain changes due to each of these sub steps was easily distinguished from temperature or time-dependent effects by looking at graphs similar to Figure 5.9.

On the other hand, slow operations such as rotation or arch sliding resulted in a gradual change in the strain and stress levels. The slow nature of these operations made it difficult to distinguish the strain changes due to the construction operation from thermal or time dependent effects. For example, the strain changes during the rotation of Arch 1 are shown in Figure 5.10. As can be seen in this figure, the rotation occurred between 8:00 AM and 7:30 PM. It appears that strain changes due to rotation can be identified in the record. However, the strain record from the day before rotation reveals significant strain changes over the same period, although no construction activity was in progress. It is clear that similar changes have occurred during rotation, but since only total strains are measured, these thermal effects cannot be easily distinguished from the strain changes due to rotation.

In order to calculate the stress changes in the structure due to a rapid construction operation, the strain record was carefully evaluated and the sub steps of each operation were identified and separated from the time dependent changes. Each sub step occurred over a period of typically 3 to 4 minutes. Therefore, the time-dependent and thermal effects during the sub steps were negligible. Once the sub steps were identified and separated, the stress changes due to each sub step were found. The total stress change due to the construction operation was then calculated by adding these stress increments.

As an example, Figure 5.11 shows the sub steps detected during Stage 1 post tensioning of Arch 2. As can be seen in this figure, the post tensioning of individual tendons can be identified by looking at the stress increments. Moreover, the interaction between rib and tie during post tensioning was evaluated using this figure. For example, prestressing the rib tendons had no effect on the stresses at the bottom of the tie at midspan. However, when the tie tendons were stressed, slight changes were observed in the stresses at the bottom of the rib.

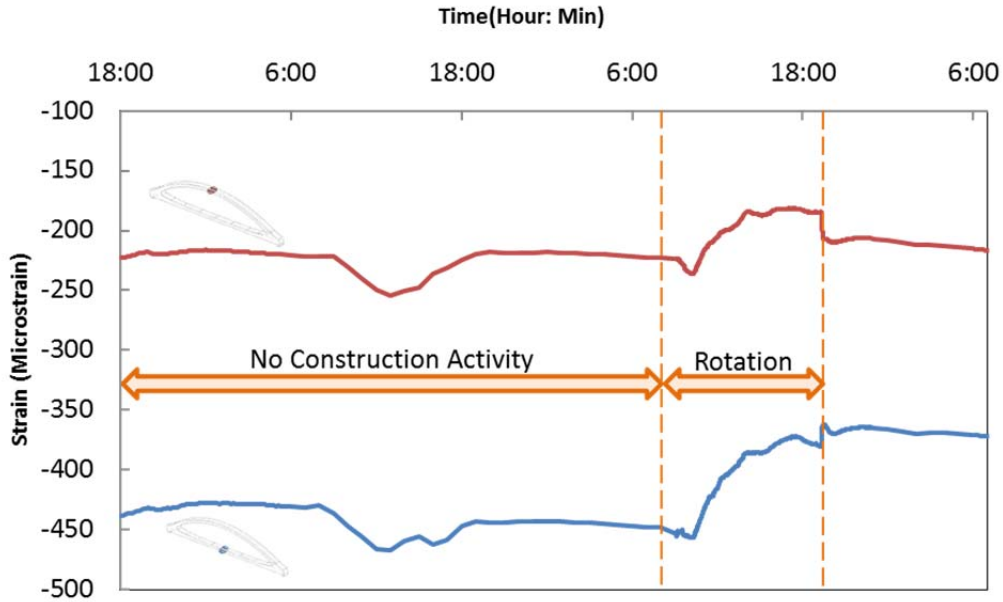

Figure 5.10- Strain change at the bottom of the tie and the bottom of the rib at the midspan of Arch 1, before and during rotation operations.

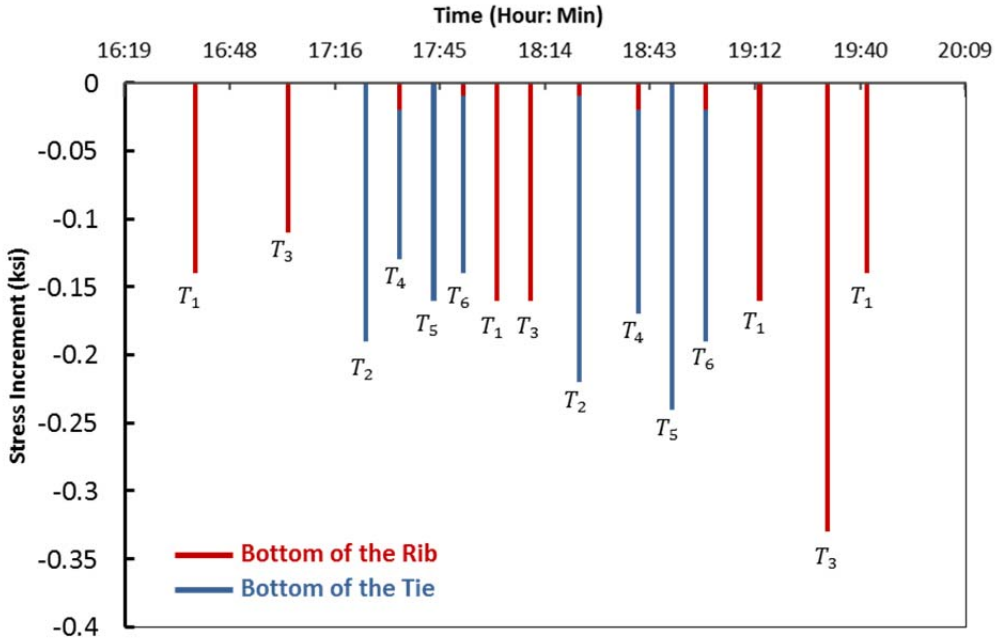

Figure 5.11- Stress increments at the midspan of Arch 2 during Stage 1 PT.

Figure 5.12 shows the cumulative sum of the stress increments obtained above for Arch 2. For comparison, the approximate stress changes according to Section 5.6.1.1 are also shown in this figure by dotted lines.

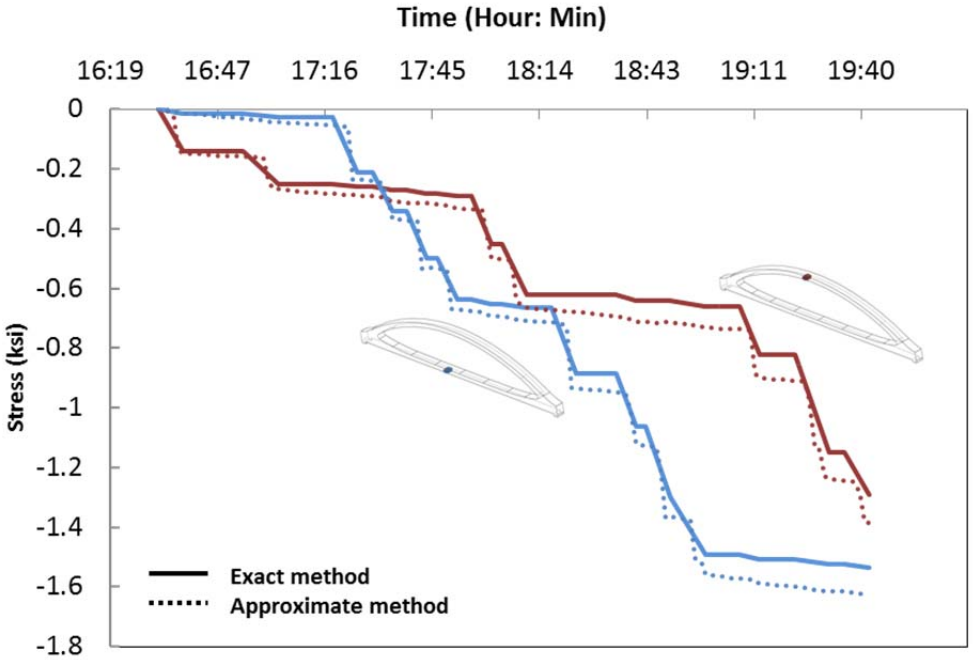

Figure 5.12- Cumulative sum of the stress increments during Stage 1 PT on Arch2.

For slow operations, the stress increments due to construction loading were not easily identifiable. Therefore, the total stress change was calculated by comparing the strains at a point before the operation with a point after the operation.

Since the arches were very sensitive to thermal changes, special care was taken in selecting the pair of data points so that the calculated stress change did not include thermal effects. Finding two data points that included the same temperatures at the locations of all VWG was not practical. However, if the following criteria were satisfied, the thermal effects were assumed negligible between the points:

1- Both points needed to be recorded overnight (after sunset and before sunrise.)
2- The average temperature of the arch was not more than $1°F$ different between the two records.
3- The temperatures at the locations of all VWGs did not differ more than $5\,°F$ between the two records.

These criteria are also shown in Figure 5.13.

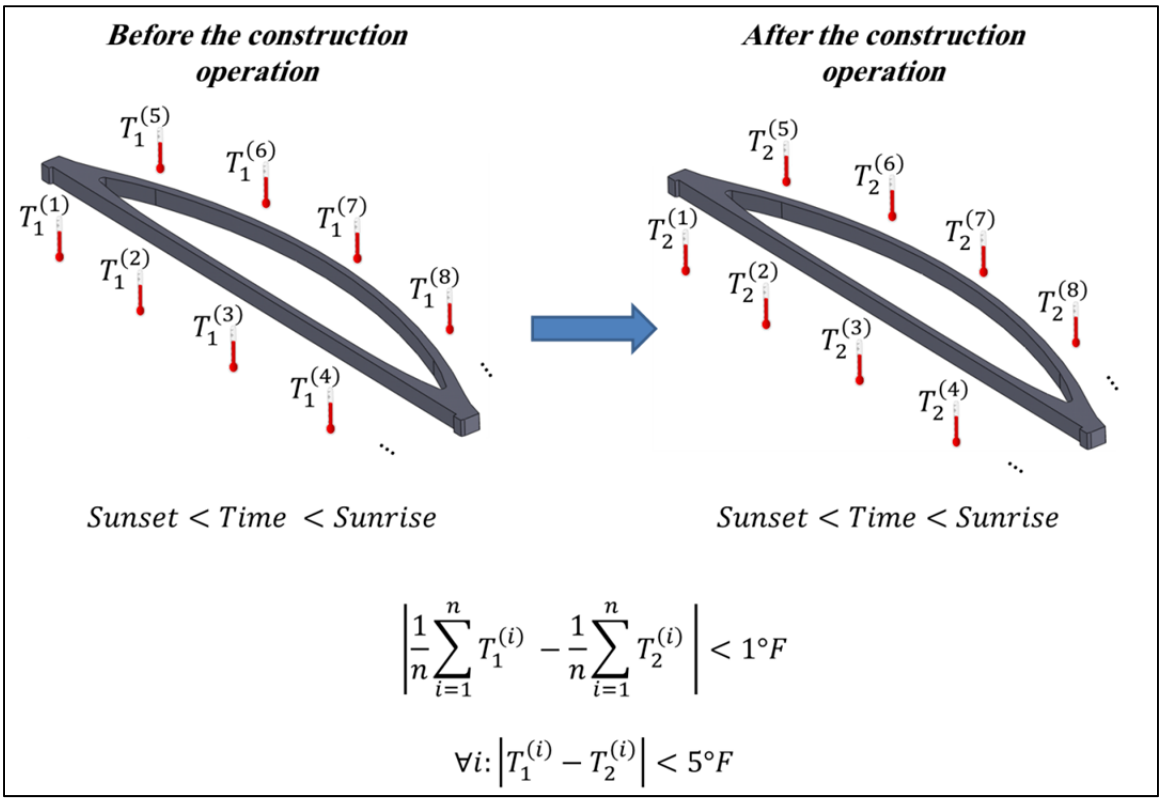

Figure 5.13- The criteria for selecting the data points for calculating the stresses.

Shrinkage and creep were still components of the strain change between the two reference records. Several methods were used to exclude creep and shrinkage from the 24-hour strain changes. However, those methods involved their own approximations and did not yield outputs that were more reliable. After all, the two records were typically 24 hours apart, and the error due to time-dependent effects over this short period was not significant.

Therefore, a decision was made to neglect the creep and shrinkage effects that occurred during the slow operations.

5.6.2 Calculating Total Stresses

The post-processing steps discussed so far have focused on the instantaneous strains induced in the arches during construction operations. However, the arches experience stress changes because of creep and shrinkage during the idle periods of construction. Calculating the exact total stresses should include all instantaneous and time-depend changes in the structure. However, considering all of the aforementioned phenomena might not be necessary for obtaining estimates accurate enough for ensuring the safety of the arches. For example, the time-dependent stresses due to creep and shrinkage are small during the initial stages of construction and might be neglected without large errors. Moreover, a more complicated procedure does not necessarily make the calculated stresses more realistic because the more complex the calculation, the more assumptions need to be made regarding the behavior of concrete over time.

Three calculation methods were used by the researchers at UT to obtain the total stress levels in the arches of the West 7th Street Bridge. These methods are based on different sets of assumptions and are introduced below in the order of their sophistication level. Among these methods, only the results of Method 1 are presented in this report. Methods 2 and 3 will be covered in a later publication.

5.6.2.1 Method 1: Neglecting Time-Dependent Stress Changes

The simplest method of calculating the total stresses was to assume that known construction stages were the only sources of stress changes in the structure. Therefore, the stress increments that were calculated in Section 5.6.1.2 could be added together to find the final stress level at each time. In other words,

$$\sigma_{Total}(\tau_j) = \sum_{i=1}^{j} \overline{\Delta\sigma_i} \tag{5.21}$$

In which,

$\sigma_{Total}(\tau_j)$ = Total stress at a corner or edge of the structure, after j^{th} construction operation

$\overline{\Delta\sigma_i}$ = Stress change at a corner or edge of the structure due to construction step i, found using Equation (5.19).

This method neglects the time-dependent changes in the stresses and is therefore approximate. The other disadvantage of this method is that it requires detailed knowledge of the time of all construction operations. If any load is applied to the arches without notifying the researchers, the stress changes due to that load remain undetected, although recorded by the instrumentation.

Despite these setbacks, this method was extensively used for assessing the stress levels in the structure during construction. The time-dependent changes were not expected to be significant during the initial stages of construction. Moreover, the researchers tried to keep the track of all construction operations so that the possibility of undetected loads on the

structure was minimized. Therefore, Method 1 was selected as the basis for calculations in the post-processing module described in Section 4.3 and all stresses that are reported in Chapter 6.

5.6.2.2 Method 2: "Force in the Tendon" Method

Method 2 was a modified version of Method 1, which included the prestress loss effects. In this method, the stress calculation procedure was similar to Method 1, but the total stresses were modified to include the effects of prestress losses, as expressed in Equation (5.22).

$$\sigma_{Total}(\tau_j) = \sum_{i=1}^{j} \overline{\Delta\sigma_i} - \sum_{k=1}^{m} \delta\sigma_{PT_k} \tag{5.22}$$

In which,

$\delta\sigma_{PT_k}$ = Stress loss at a corner or edge of the structure, due to loss of post-tensioning force that was applied to the arches in k^{th} stage of post tensioning.

m = Number of post-tensioning stages.

Calculating $\delta\sigma_{PT_k}$ requires finding the prestress losses, and then determining the effect of losses on the stresses in the arches. The prestress losses could be found from the instrumentation data, as will be discussed in 106. However, correlating the drop in the prestressing force with the changes in structural stresses required using Finite Element (FE) simulations of the bridge. Each arch experienced changes in the material properties with time. Moreover, the boundary conditions of the structure were being changed with time, for example because of rotation. As a result, several FE models of the arches were developed in ANSYS to evaluate the effect of prestress losses on the structural stresses. Figure 5.14 shows samples of these models, which represent the deformations of the arches under post tensioning of rib and tie tendons before arch rotation.

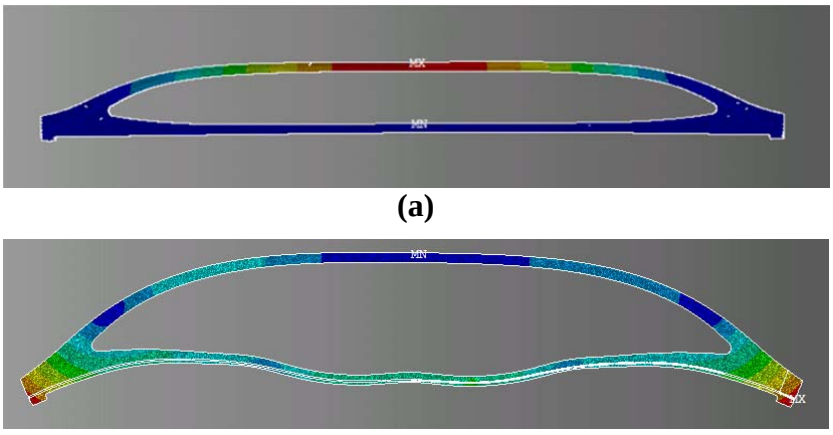

(a)

(b)

Figure 5.14- Arch deformations under Stage 1 PT. (a) Stressing Tendon 1. (b) Stressing Tendon 5.

Due to several setbacks in Method 2, its application in post processing of the data was very limited. First, Method 2 was relatively tedious. The method required several FE models to simulate the effects of prestress losses on the arches in different conditions. For every single corner of the instrumented sections on the structure, a separate time-dependent function needed to be developed for correlating the stress changes with prestress losses in each tendon. Second, the FE models involved significant uncertainties due to presence of hand-tightened hangers, which made many of their results questionable. Finally, the most important disadvantage of this method was discovered after it was used on few of the arches: the results of Method 2 were approximately the same as Method 1, especially after Stage 2 post tensioning. As will be discussed in Chapter 6, the observed prestress losses after Stage 2 post tensioning were generally small. As a result, using Method 2, which was primarily designed to address the effects of prestress losses, was not feasible.

5.6.2.3 Method 3: Developing Continuous Stress-Time Relationship

Method 3 is a method to address all of the stress-related components of the strains, which were illustrated in Figure 5.8. This method is still under development by the researchers at UT and requires an extensive background understanding about the creep and shrinkage behavior of the concrete, as well as considerable numerical calculations. Therefore, it is beyond the scope of this report. However, the basis for this method is briefly introduced in this section.

If the arch elements can deform freely under creep and shrinkage, the shortening of the prestressed elements will result in prestress losses. As a result, the stresses that were induced in the structure due to post-tensioning will diminish over time. On the other hand, if shrinkage and creep deformations are prevented, the stresses will diminish due to another phenomenon, known as stress relaxation. Similar to a prestressing strand that is held at a constant deformation, a concrete element experiences stress loss if it is put under sustained load but is prevented from creep deformations. In simple terms, when concrete is under sustained compressive load, it is expected to continue its creep deformations. If the measurements reveal that the concrete is not deforming, it means that the concrete is being unloaded so that the strain reduction due to unloading is canceling out the increasing strains due to creep, and the net effect is a zero deformation.

Most prestressed concrete bridge girders are relatively free to deform under creep and shrinkage before they are restrained by deck elements. Therefore, concrete relaxation is not common in most bridges. However, in the arches of the West 7th Street Bridge, the stiff network of hangers restrains the time-dependent deformations of the tie and the rib. As mentioned in Section 5.6.2.2 and further discussed in Chapter 6, such a stiff restraint resulted in relatively small prestress losses in the arches. Therefore, there is a possibility that the time-dependent stress changes in the arches of the West 7th Street Bridge are governed by relaxation, rather than prestress losses.

Unfortunately, stress relaxation happens without any change in the strains. Therefore, this phenomenon cannot be detected from strain measurements. However, if sufficient data are available on the mix-specific creep and shrinkage behavior of the concrete, the relaxation effects can be calculated through a numerical procedure.

In Method 3, numerical models are selected for the development of creep and shrinkage over time. Using these numerical models, the strain history is converted to a continuous stress history through numerical step-by-step calculation. The resulting stress history will include all time-dependent effects such as prestress losses and stress relaxation. However, the required numerical creep and shrinkage models can best be obtained through extensive long-term material studies on the concrete that is used in the structure. If such tests are not carried out, large errors might occur in the stresses estimated using Method 3. The researchers at UT are currently trying to calibrate a representative creep and shrinkage model based on the recorded response of the structure so that the accuracy in stress calculations for the West 7th Street Bridge can be improved.

5.7 CALCULATING PRESTRESS LOSSES

The time dependent change in the prestressing force can be divided into two components: relaxation losses and strain-related changes. Relaxation losses happen under constant strain in prestressing tendons. However, strain-related changes happen due to the structure's deformations at the location of prestressing and can be negative (known as prestress losses) or positive (known as stress gains). Since time-dependent deformations of concrete result in larger prestress losses than the stress gains, the overall stress changes in the tendons are referred to as prestress losses.

If the prestressing force is applied at time t_0, the prestress losses at any time t can be found using Equation (5.23).

$$\Delta f_p(t, t_0) = E_p \times \Delta\varepsilon_p(t, t_0) + \Delta f_{pRE}(t, t_0) \tag{5.23}$$

In which,

Δf_p = Total prestress loss, ksi
$\Delta\varepsilon_p$ = strain change in the strands after the end of prestressing
Δf_{pRE} = prestress loss due to relaxation of steel, ksi
E_p = Modulus of elasticity of prestressing steel=29000 ksi

The strain-related prestress losses can be found from the strains measured by the instrumentation. If the coordinates of the tendons are used as the input to Equation (5.9), the strain change in the concrete at the location of the tendons can be determined:

$$\Delta\varepsilon_{nth}^{(i)} = a \times x_p^{(i)} + b \times y_p^{(i)} + c \tag{5.24}$$

Where:

$\Delta\varepsilon_{nth}^{(i)}$ = The non-thermal part of the concrete strain change, at the location of Tendon i
$x_p^{(i)}, y_p^{(i)}$ = Coordinates of Tendon i in the section
a, b, c = Strain plane coefficients, as found in Section 5.4.2

Since prestressing tendons have a different coefficient of thermal expansion from concrete, $\Delta\varepsilon_{nth}^{(i)}$ values needed to be corrected according to Equation (5.25) to find the strain

changes in the tendon. The resulting strains will not include thermal expansion or contraction of the tendons. However, the $\Delta\varepsilon_p$ found from this equation includes all real stress changes in the tendons, including those due to thermal fluctuations.

$$\Delta\varepsilon_p^{(i)}(t,t_0) = \Delta\varepsilon_{nth}^{(i)}(t,t_0) + (\alpha_c - \alpha_{st}) \times [T(t) - T(t_0)] \tag{5.25}$$

In which,

α_c = coefficient of thermal expansion of concrete, as found in Section 5.5
= $4 \times 10^{-6}(\frac{1}{^\circ F})$

α_{st} = coefficient of thermal expansion of the prestressing steel = $6.5 \times 10^{-6}(\frac{1}{^\circ F})$

$T(t) - T(t_0)$ = Temperature change over the period under consideration, $^\circ F$

The relaxation losses cannot be measured using the instrumentation output because relaxation happens without any change in strains. In order to estimate the relaxation losses, Equation (5.26) was used. Equation (5.26) is an empirical equation, which was first developed by Magura et al. in 1964 and was later modified for low-relaxation strands [5].

$$\Delta f_{pRE} = \begin{cases} 0 & \left(\frac{f_{pi}}{f_{py}}\right) \le 0.55 \\ \left(\frac{f_{pi}}{45}\right)\left(\left(\frac{f_{pi}}{f_{py}}\right) - 0.55\right)\log(t) & \left(\frac{f_{pi}}{f_{py}}\right) > 0.55 \end{cases} \tag{5.26}$$

Where:

f_{pi} = initial stress in the strand (ksi)

f_{py} = yield stress of the strand
= 250 ksi as reported by the strand manufacturer in this project

t = time after the end of prestressing (hrs.)

This equation does not consider the beneficial effect of the gradual reduction in the prestressing force on the stress relaxation. Therefore, it tends to overestimate the relaxation losses. However, since prestress losses in this project are small as compared to the total prestressing in the tendons, the error due to this approximation is negligible.

Equations (5.25) and (5.26) were used to calculate the losses at midspan sections of the arches. The initial levels of prestressing for these calculations were assumed based on the friction loss analyses of the arches by VSL.

5.8 SUMMARY

Extensive post-processing calculations were carried out to convert the measurements obtained from the instrumentation to representative structural parameters. These calculations included:

- Estimating realistic material properties of the concrete based on the recorded temperatures from the arches and a maturity-based approach
- Calculating the strains at the corners of the instrumented cross sections from the measurements at the locations of the VWGs, using analytic geometry
- Estimating the coefficient of thermal expansion of the concrete based on the recorded response of the arches to thermal changes
- Calculating stress changes due to each construction operation
- Calculating total stresses
- Calculating the prestress losses

Special care was taken to exclude the undesirable thermal and time-dependent effects from the measured strains in the structure so that only stress-related strains were used in stress calculations.

The stresses obtained from these calculations will be presented in Chapter 6.

Chapter Bibliography

[1] N. J. Gardner and M. Lockman, "Design Provisions for Drying Shrinkage and Creep of Normal-Strength Concrete," *ACI Materials Journal,* vol. 98, no. 2, pp. 159-167, 2001.

[2] Geokon, Inc., Instruction Manual: Model 4200 Series Vibrating Wire Strain Gages, Lebanon, NH: Geokon, Inc., 2012.

[3] T. R. Naik, R. N. Kraus and R. Kumar, "Influence of Types of Coarse Aggregates on the Coefficient of Thermal Expansion of Concrete," *JOURNAL OF MATERIALS IN CIVIL ENGINEERING,* vol. 23, pp. 467-472, 2011.

[4] L. Du and E. Lukefahr, "Coefficient of Thermal Expansion of Concrete with Different Coarse Aggregates," in *15th Annual ICAR Symposium,* Austin, TX, 2007.

[5] M. Collins and D. Mitchel, Prestressed Concrete Structures, Toronto, Canada: Response Publications, 1997.

CHAPTER 6
Results and Discussion

6.1 INTRODUCTION

All 12 arches of the West 7th Street Bridge were instrumented and extensively monitored during construction, as discussed in Chapter 4. The data obtained from the field instrumentation were post-processed using the procedures introduced in Chapter 5 to estimate the stresses in the structure. These stresses were used to assess the safety of the arches against cracking and to evaluate the accuracy of design predictions.

The researchers from UT carefully monitored a variety of structural parameters, including stresses, temperatures, loads, and curvatures in all structures to make sure that none of the arches was damaged during different handling operations. While there was some variation in the magnitude of stresses between different arches, relatively similar behavior was observed among the arches.

This chapter provides an overview of the instrumentation results, including concrete hydration temperatures, stress changes due to each construction operation, prestress losses, and measured stresses in the live load test. For each construction operation, representative stress changes from one of the arches are presented first so that the general response of the arches during that construction operation can be evaluated. Next, the stresses at the end of each construction operation from all arches are presented and compared with the design predictions.

6.2 CONCRETE HYDRATION TEMPERATURES

Figure 6.1 shows the temperatures recorded in Arch 2 during the first week after casting the concrete. This figure also includes the temperatures that were recorded hours before the start of the concrete pour. Arch 2 was cast in hot weather conditions, and, liquid nitrogen was used to reduce the temperature of the fresh concrete. The effect of liquid nitrogen can be seen as a drop in the temperatures during the concrete pour. However, once the hydration is started, the temperatures are increased up to $140°F$. Soon after the peak of hydration, the temperatures are reduced and the daily thermal cycles can be identified in the temperature record of the arch.

As previously discussed in Section 5.2, the thermal records of the arches were extensively used in post-processing of the data to obtain the maturity-based estimates of compressive strength and modulus of elasticity of concrete. The maximum temperatures in the arches were also monitored as a quality control measure for the concrete to make sure that the structural elements did not experience excessive temperatures. As can be seen in Figure 6.2, none of the VWGs in the arches recorded temperatures higher than $150°F$, which is usually used as the limit to prevent long-term durability problems such as Delayed Ettringite Formation (DEF).

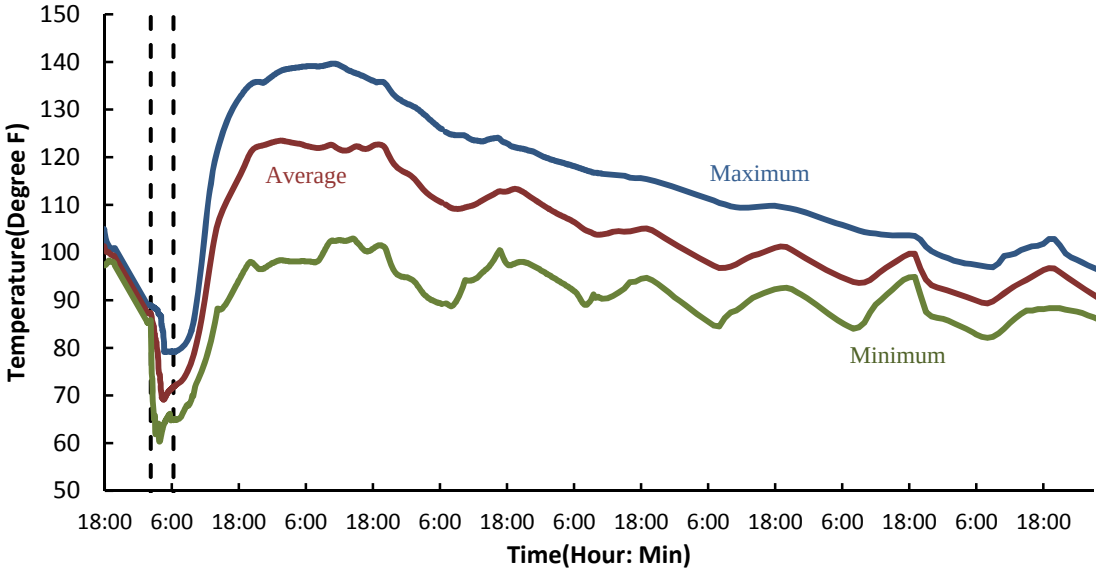

Figure 6.1- Concrete temperatures in Arch 2 during the first week after concrete pour. (The dashed lines represent the start and the end of the concrete pour)

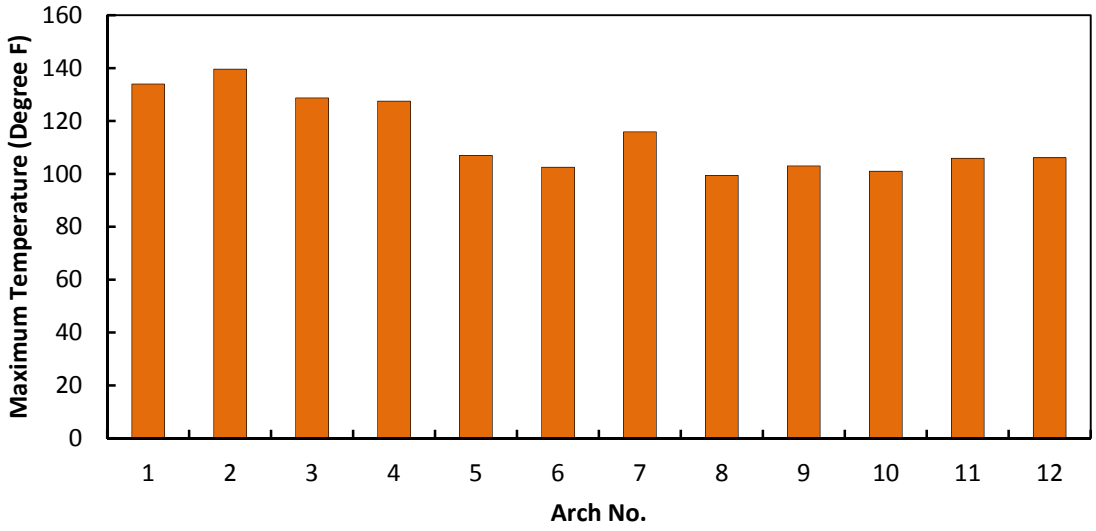

Figure 6.2- Maximum recorded temperatures in the arches during the first 48 hours after the concrete pour.

6.3 ARCH STRESSES

As noted in Chapter 5, the results presented herein are based on Method 1, the simplest method that neglects the stress changes when no construction activity is in progress. The time-dependent stress changes are expected to have a minimal effect on the short-term stress changes, especially until upward jacking. The stresses after upward jacking might be influenced by concrete relaxation, which results in redistribution of concrete stresses over time. To include the effects of long-term changes on stresses in the arches, the more sophisticated Method 3 is being developed by the researchers, which is beyond the scope of this report.

6.3.1 Stage 1 Post-Tensioning

Figures 6.4 and 6.5 show the stress changes in Arch 2 during Stage 1 PT. As can be seen in these figures, the instrumentation was capable of detecting the stressing of individual tendons inside the rib and the tie. As a result, the recorded data provided the opportunity to evaluate the response of the structure and to check the analysis models of the bridge with respect to each tendon separately. Moreover, the interaction of rib and tie elements were evaluated by comparing the stress changes in the rib while the tie was being post-tensioned, and vice versa.

As can be seen in Figures 6.4 and 6.5, the response of the arch rib and the tie element were relatively independent of each other during post-tensioning. During Stage 1 PT, each 52 ksi increment in the rib tendons increased the stresses at the edges of the rib by more than 100 psi, but caused negligible stress changes at the midspan in the tie. The maximum stress change anywhere in the tie when a prestress increment was applied to the rib was smaller than 20 psi.

The centroids of the tendons at the knuckle region were located close to the neutral axis of the tie and the rib. As a result, very small bending moments were exchanged between the rib and the tie elements due to post-tensioning. Moreover, the orientation of post-tensioning anchorage devices for the rib tendons created static equilibrium of the forces without exerting large shear and axial loads on the tie. In other words, the anchorage force remained in line with the internal axial stresses in the rib, providing the equilibrium without mobilizing the tie.

Another important observation was that post-tensioning did not induce bending in the arch rib except for the eccentricity of the tendons from the neutral axis of the rib, i.e., the curved shape of the rib element per se did not result in significant bending in the arch. This behavior is attributed to the circular profile of the arch and careful selection of the tendon paths and anchorage orientation by the designers. As can be seen in Figure 6.3, the response of the arch rib to post-tensioning is similar to a compressive ring, which is in pure compression due to the effect of pressure applied along its radius. This characteristic of the arch design was very important in relieving the arch ribs from long-term bending deformations under sustained post-tensioning forces.

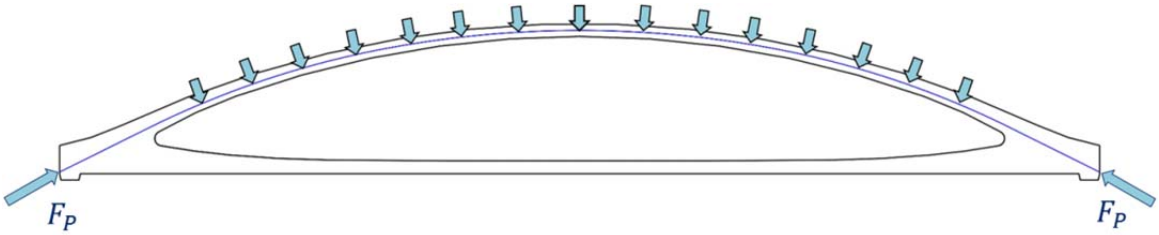

Figure 6.3- Compressive stresses acting on the arch rib due to post-tensioning.

Also visible in Figures 6.4 and 6.5 are the post-tensioning stresses predicted by the design team, which are represented by dotted lines. As can be seen in these figures, the finite element models of the arches used by the designers were largely successful in predicting the structural stresses in the arches, especially in the rib element. For the tie element, the predicted stresses were not as accurate. For example, in the midspan-tie section of Arch 2, the design predicted a bending moment smaller than the measured and in the opposite direction. The total difference between measured and predicted bending moments is approximately $200 kip - ft$. As discussed in Section 4.2.4.1, the instrumented section was not located exactly at the midspan to avoid the local stress concentrations due to the presence of floor beam block-outs. However, the approximately $2.5 ft$ distance between the analysis section and the instrumented section is expected to result in negligible stress changes. Moreover, the same discrepancy can be observed between predicted and measured stresses at the location of Lifting Frame 2 in the tie, where the predicted bending moment is larger than measured and is in the opposite direction.

Since the average stresses are predicted accurately, the difference should be related to a source of bending that was not anticipated in design. Several factors might have generated such bending. The analysis model assumed that the tendons were bonded along the arches. In reality, the tendons could slightly move laterally inside the ducts, resulting in some bending moments. Moreover, there is a possibility of displaced PT ducts, which could result in a different location of the tendons as compared to the design assumptions. Local bending due to friction between the soffit and the arch is also a possibility. On the other hand, the tie is a relatively congested structural element, which includes all the PT ducts, floor beam block-outs, hanger tubes, and light fixtures. The flow of stresses in the tie may have been highly influenced by these sources of stress concentration, which were not considered in the design models of the bridge.

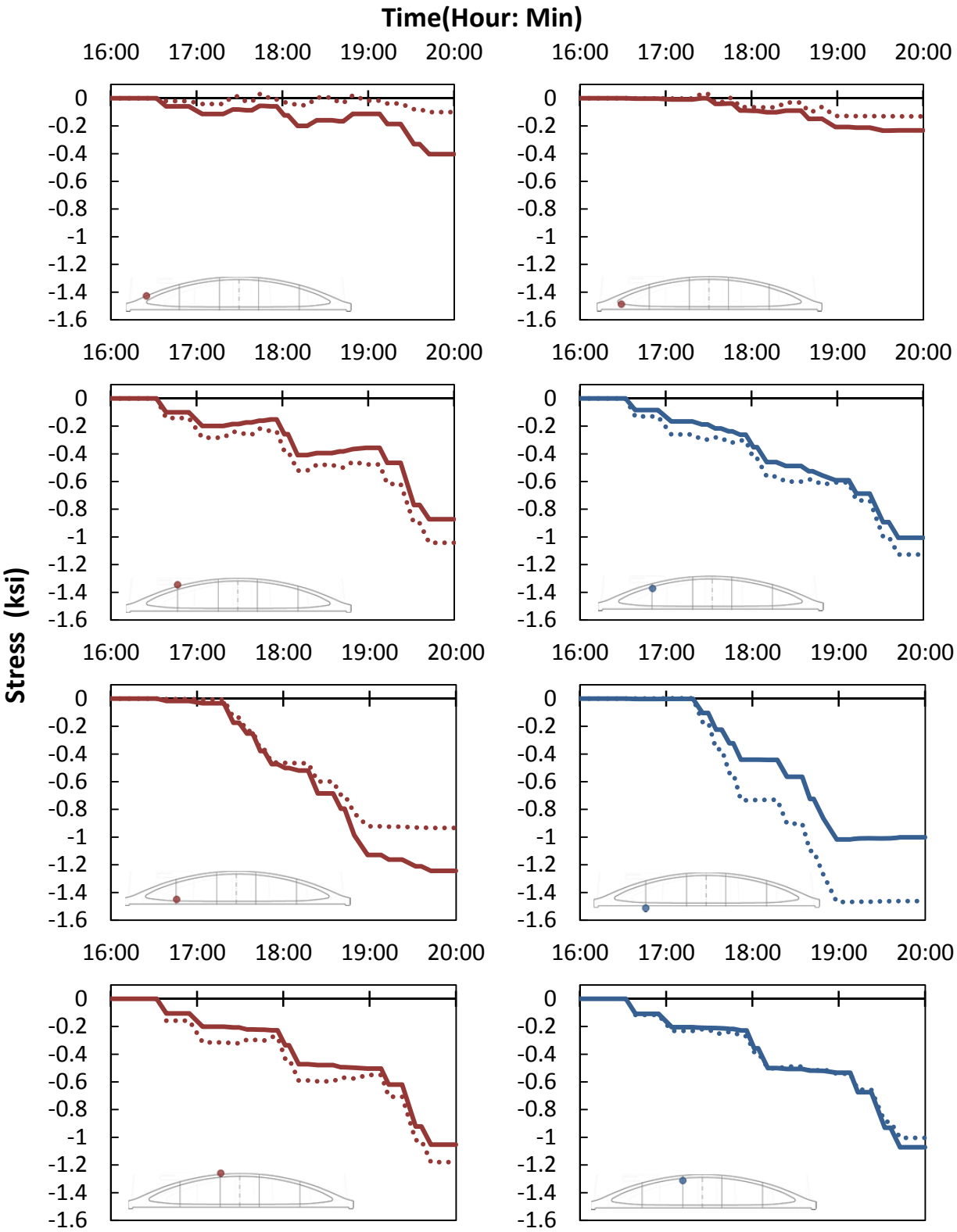

Figure 6.4- Stresses in Arch 2 during Stage 1 PT operations.
The dotted lines show the design predictions.

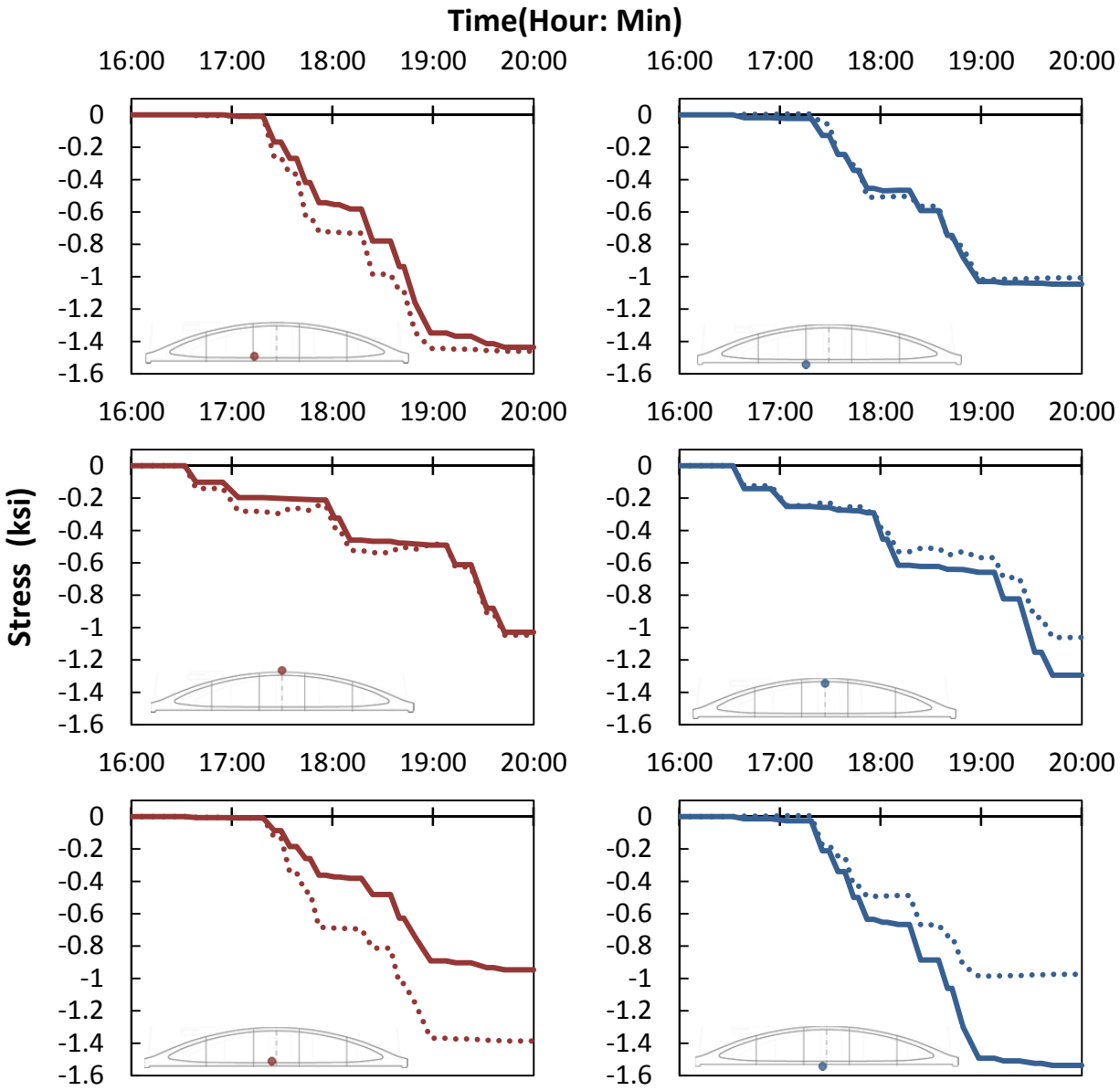

Figure 6.5- Stresses in Arch 2 during Stage 1 PT operations (continued). The dotted lines show the design predictions.

Figure 6.6 shows the stresses at the end of Stage 1 PT in all arches. In this figure, the black lines represent the range of stresses that was observed in different arches of the West 7th Street Bridge. As previously mentioned in Section 4.6.4.1, the VWGs at the midspan-tie section of Arch 1 were located at the same section as the floor beam block-outs. Therefore, the stresses from the midspan-tie section of Arch 1 are excluded from all average stresses and stress ranges that are presented in this chapter.

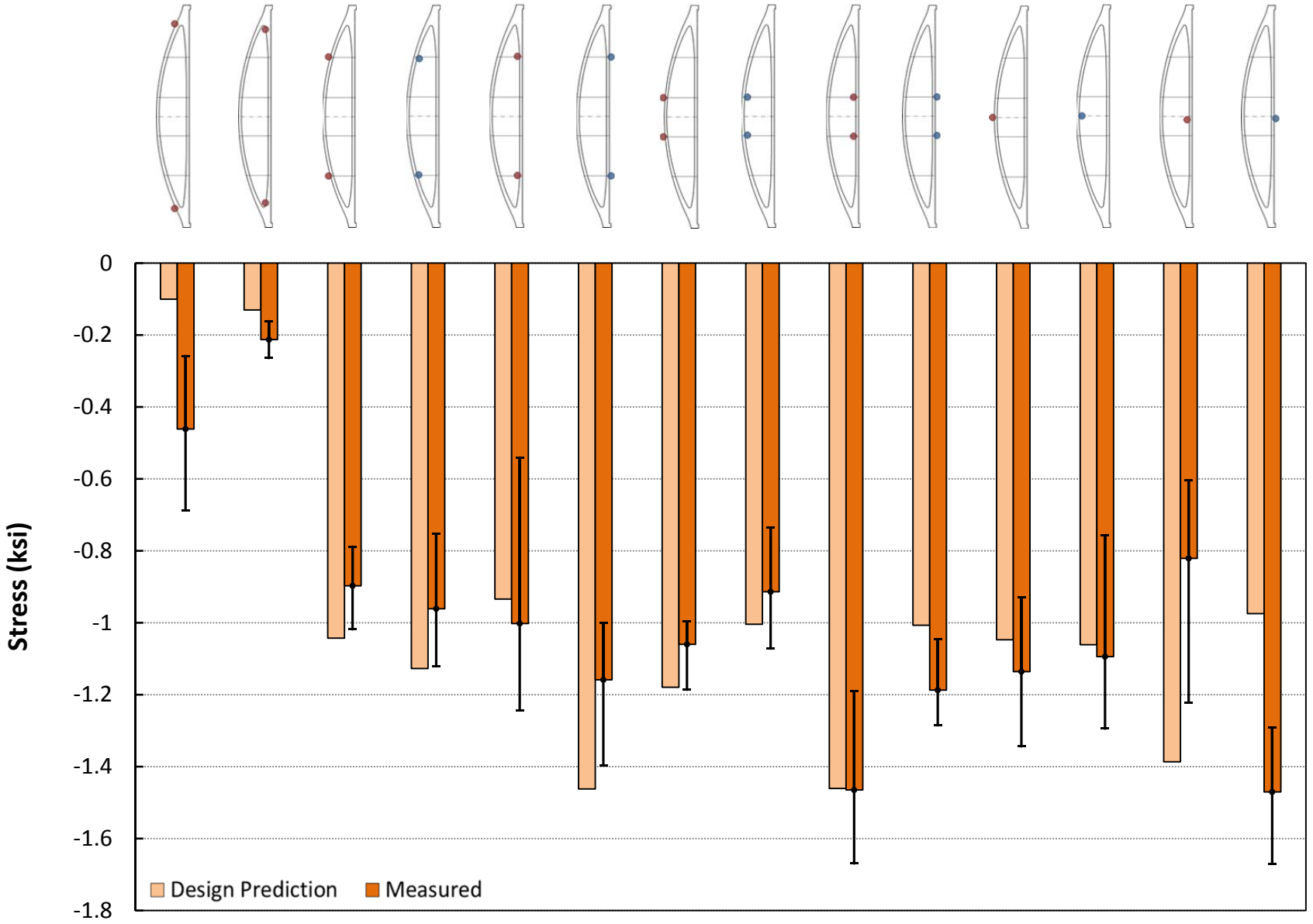

Figure 6.6-Arch stresses at the end of Stage 1 PT.

As can be seen in Figure 6.6, the design models were generally successful in predicting the average stresses in the arches. In the knuckle region, where small compressive stresses were induced by post tensioning, the design underestimated the compressive stresses both in the tie and in the rib. As a result, the stresses in these regions were conservatively estimated. In other regions in the rib, the design provided stress estimates that were in good agreement with the average stress measurements. However, there is some discrepancy between measured and predicted stresses in the tie, especially at the midspan, which is discussed above.

The variability of stresses between arches was also generally larger in the tie than in the rib. For example, the stresses at the top of the tie in midspan in some arches were 50% larger than the average stresses. While this variability was not a source of concern after post tensioning, it was intensified with the progress of the construction, as demonstrated later in this chapter. Fortunately, the midspan in the tie was not a crack-sensitive region in the structure. Otherwise, predicting the risk of cracking in a region with such high variability of stresses would have been very difficult.

6.3.2 Rotation

Figures 6.7 and 6.8 show the stress changes at the midspan of Arch 2 in the rib and the tie during rotation. As can be seen in these figures, the rotation response consists of three stages: vertical lifting, supported rotation, and setting on temporary supports.

The first stage, vertical lifting, occurred when all lifting points were raised equally at the beginning of the rotation process. The self-weight load was applied to the arch during vertical lifting. However, the arch behaved similar to a continuous beam, supported by six lifting frames. As a result, the response of the rib and the tie were governed by bending. As can be seen in the figures, the corners that were located at the top of the rib and the tie before rotation experienced an increase in the compressive stresses while the bottom corners were subjected to a decrease in the compressive stresses. However, the magnitude of stress changes during vertical lifting was generally small.

The second stage, supported rotation, represents the change of the arch from a horizontal position to a vertical position while the arch was supported by the lifting frames. The stress changes during supported rotation were gradual and relatively small. Although the arch was rotated to a vertical orientation, the arch action was not mobilized during the supported rotation. The response of the arch was governed by biaxial bending.

In the third stage, arch setting, the arch was released from the lifting frames and was set on temporary supports. The stress changes during setting of the arch on temporary supports were quick and relatively large. During this stage, the arch action was fully mobilized. Therefore, this stage was associated with a rapid increase in compressive stresses in the rib and a rapid decrease in those in the tie.

As visible in Figures 6.7 and 6.8, the largest stress changes during the rotation process occurred during arch setting. However, the arches were designed to withstand much larger demands due to the loads from the bridge deck and traffic in the finished bridge. As a result, these stresses were easily tolerated by the arches in the vertical orientation. On the other hand, the biaxial state of bending in the arches made supported rotation a more critical time than vertical lifting. Consequently, monitoring the stresses during supported rotation was of particular importance for ensuring the safety of the arches.

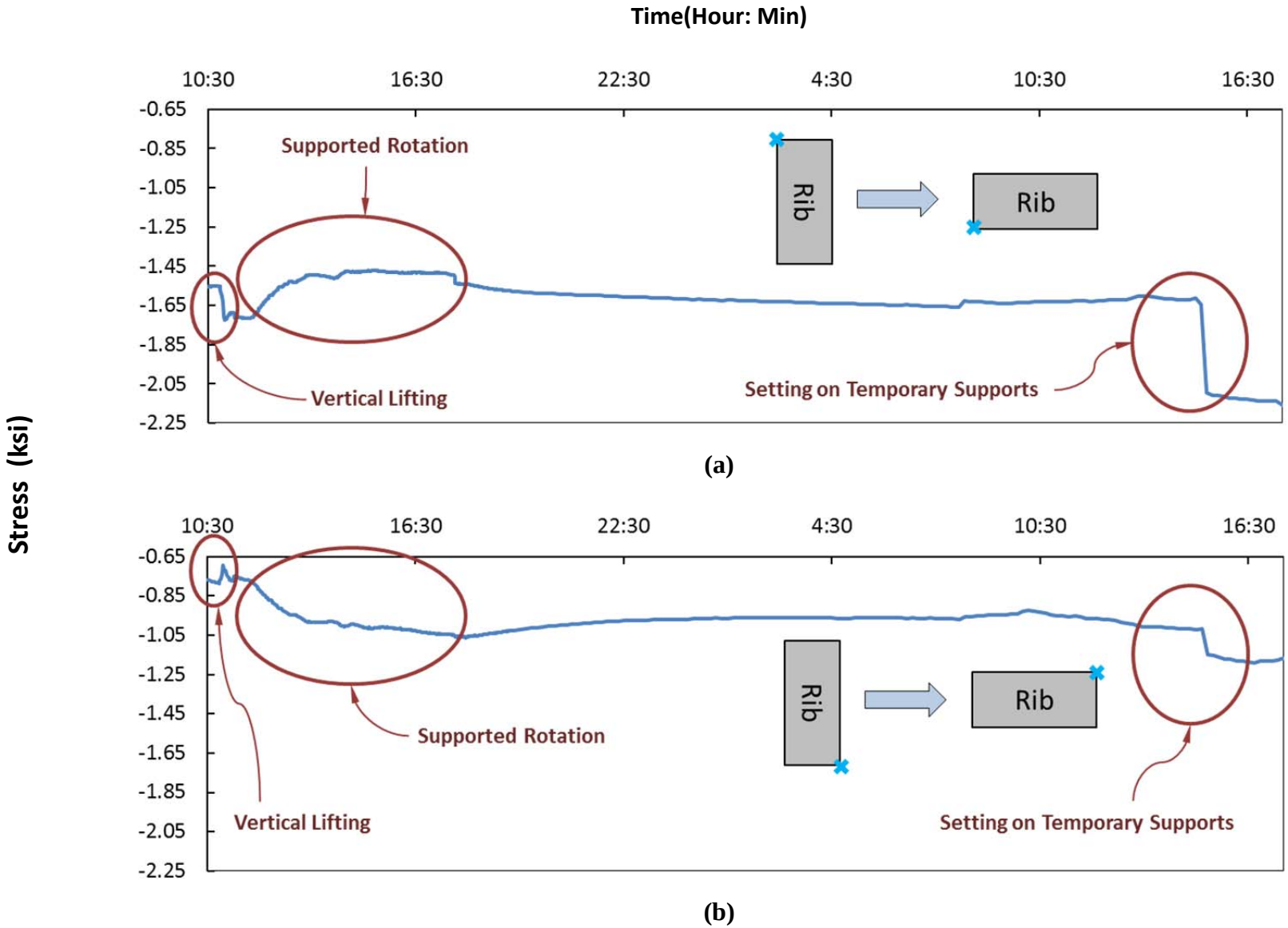

Figure 6.7- Stresses during rotation of Arch 2 at midspan-rib.
(a) Bottom left corner. (b) Top right corner.

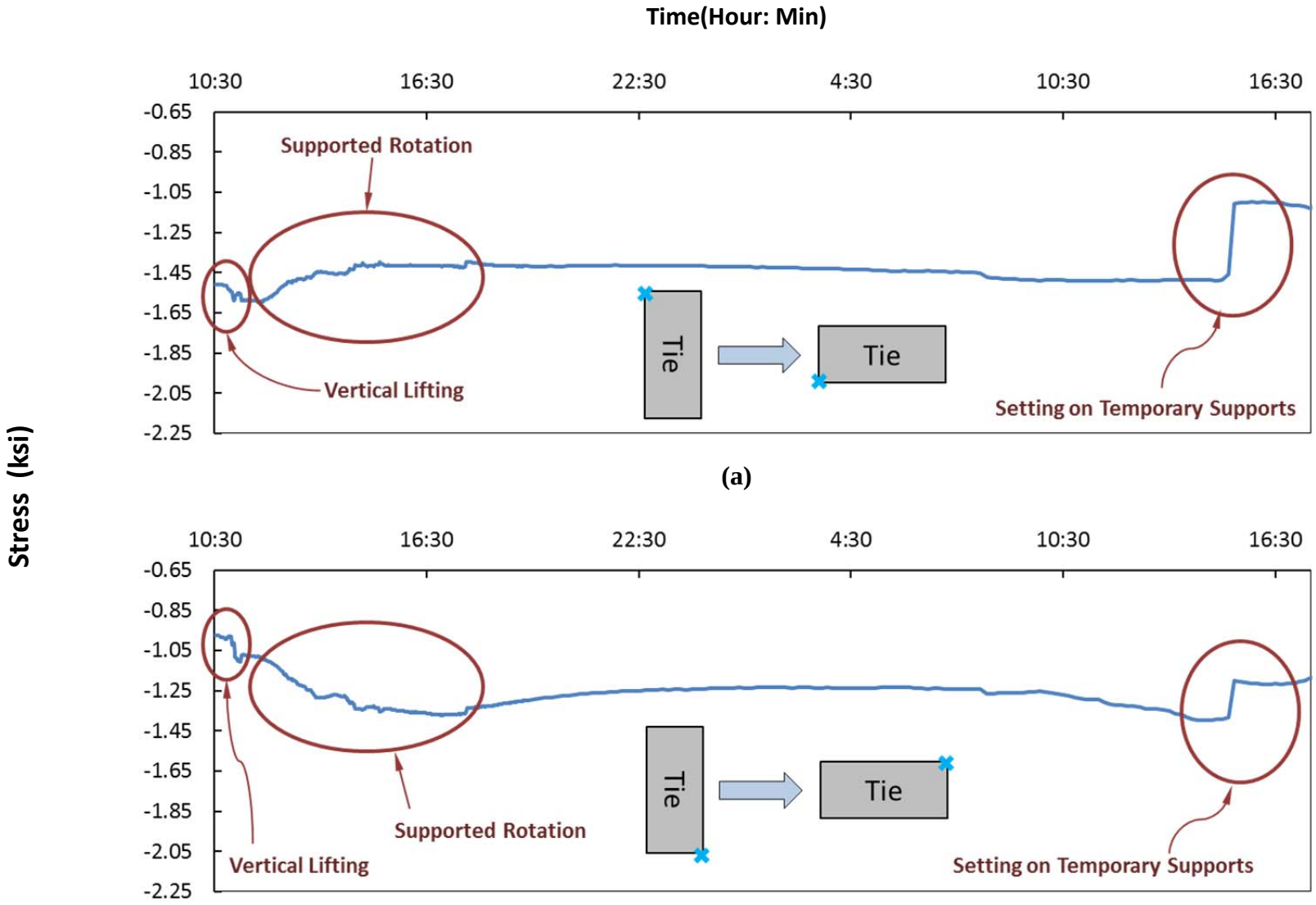

Figure 6.8-Stresses during rotation of Arch 2 at midspan-tie.
(a) Bottom left corner. (b) Top right corner.

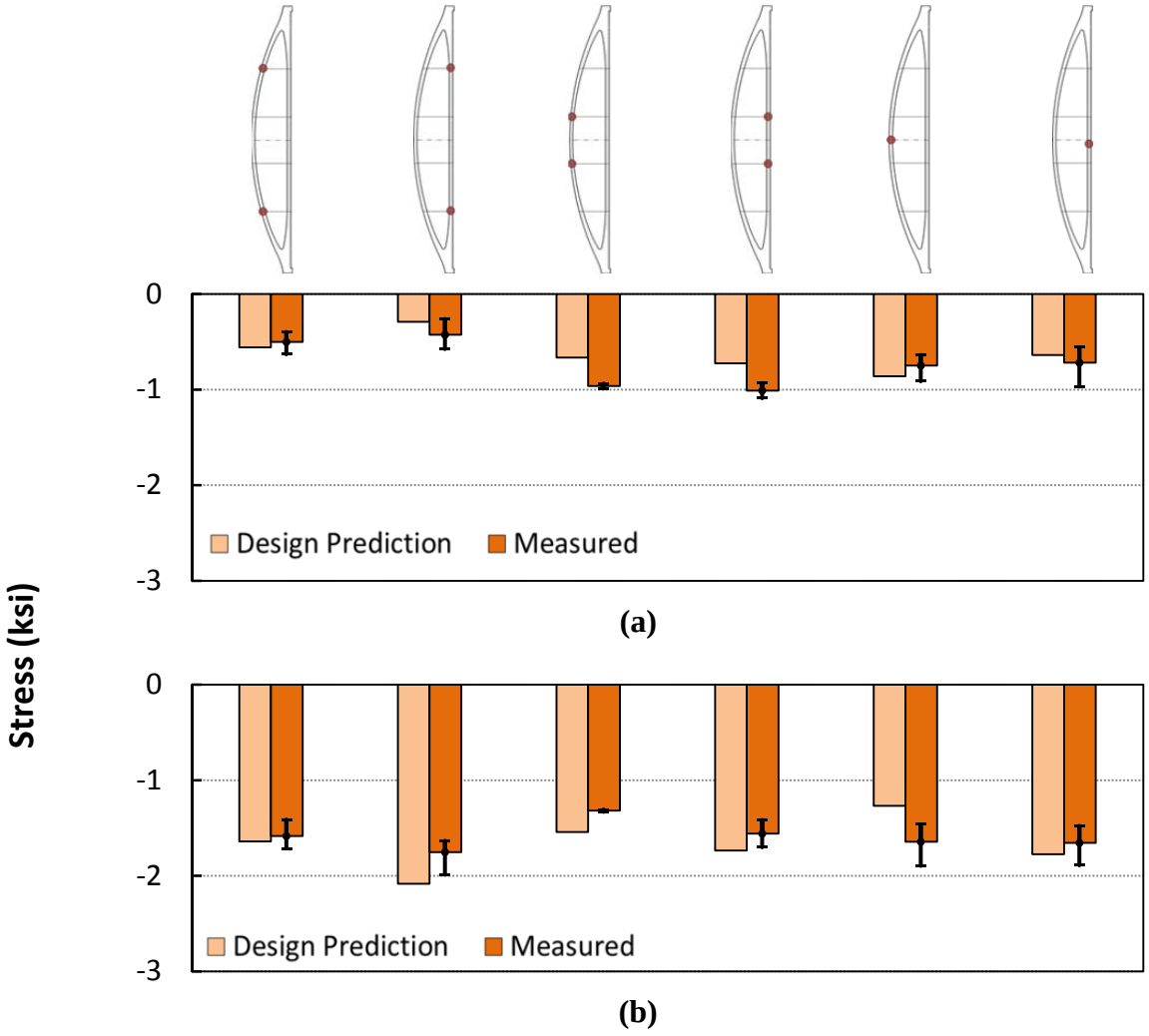

Figure 6.9- Critical stresses during supported rotation of the arches.
(a) Minimum compression. (b) Maximum compression.

Figure 6.9 shows the average maximum and minimum corner stresses observed in the arches during supported rotation. This figure shows that none of the arches experienced tension under this operation and therefore, the arches remained crack-free during rotation. The predicted stresses in Figure 6.9 are based on the calculations carried out by the construction engineering team, assuming a 50% dynamic allowance for the self-weight of the arch. The figure shows that the measured stresses were in reasonable agreement with the calculated results, and where a difference exists between measured and predicted stresses, the predicted response generally overestimated the risk of cracking. Although the rotation procedure was carried out relatively slowly, the 50% dynamic allowance appears to have contributed to obtaining more realistic stress levels. The range of maximum and minimum stresses in the arches is also relatively small, which shows consistency in performing the rotation operation on different arches.

Figure 6.10 shows the stresses in the arches after the arches were set on the temporary supports. As can be seen in this figure, the design predictions were in reasonable agreement with the measured stresses. However, the accuracy of estimated stresses is reduced as compared to Stage 1 PT stresses. The compressive stresses in the knuckle region following rotation were overestimated in design. In fact, several arches experienced tensile stresses at their knuckle region in the tie. However, the maximum tension observed in the arches was approximately 100 psi, which was relatively small. The design calculations also significantly underestimated the stresses at the bottom of the tie at midspan. The variability of stresses at the top of the tie at midspan was also very large. The range of stresses at this location among different arches was approximately 1.2ksi. The presence of hand-tightened hangers with unknown forces might have contributed to this large variability.

The large variability in the stresses did not pose any risks to the arches, as the compressive stresses were well below 50% of the compressive strength and the tensile stresses were well below the modulus of rupture.

6.3.3 Stage 2 PT

Figures 6.11 and 6.12 show the stress changes in Arch 2 during Stage 2 PT on the tie element. During Stage 2 PT, the arch had different boundary conditions than Stage 1 and included hand-tightened hangers, which connected the rib and the tie. However, as can be seen in the figures, the tie and the rib were still responding independently to the prestressing force. When Stage 2 PT was being carried out on the tie element, negligible stress changes could be detected in the rib.

The stresses at the end of Stage 2 PT on the tie and the rib are shown in Figure 6.13. While the agreement between predicted and measured stresses was generally improved after Stage 2 PT, the variability of midspan stresses in the tie was further increased. Since these stresses, which are induced by prestressing and self-weight, were sustained on the arches for an extended time, relatively large variability is expected in the time-dependent deformations in the arches. In some arches, tensile stresses were observed at the top of the knuckle in the rib. However, these tensile stresses were smaller than 100psi, well below the modulus of rupture of concrete.

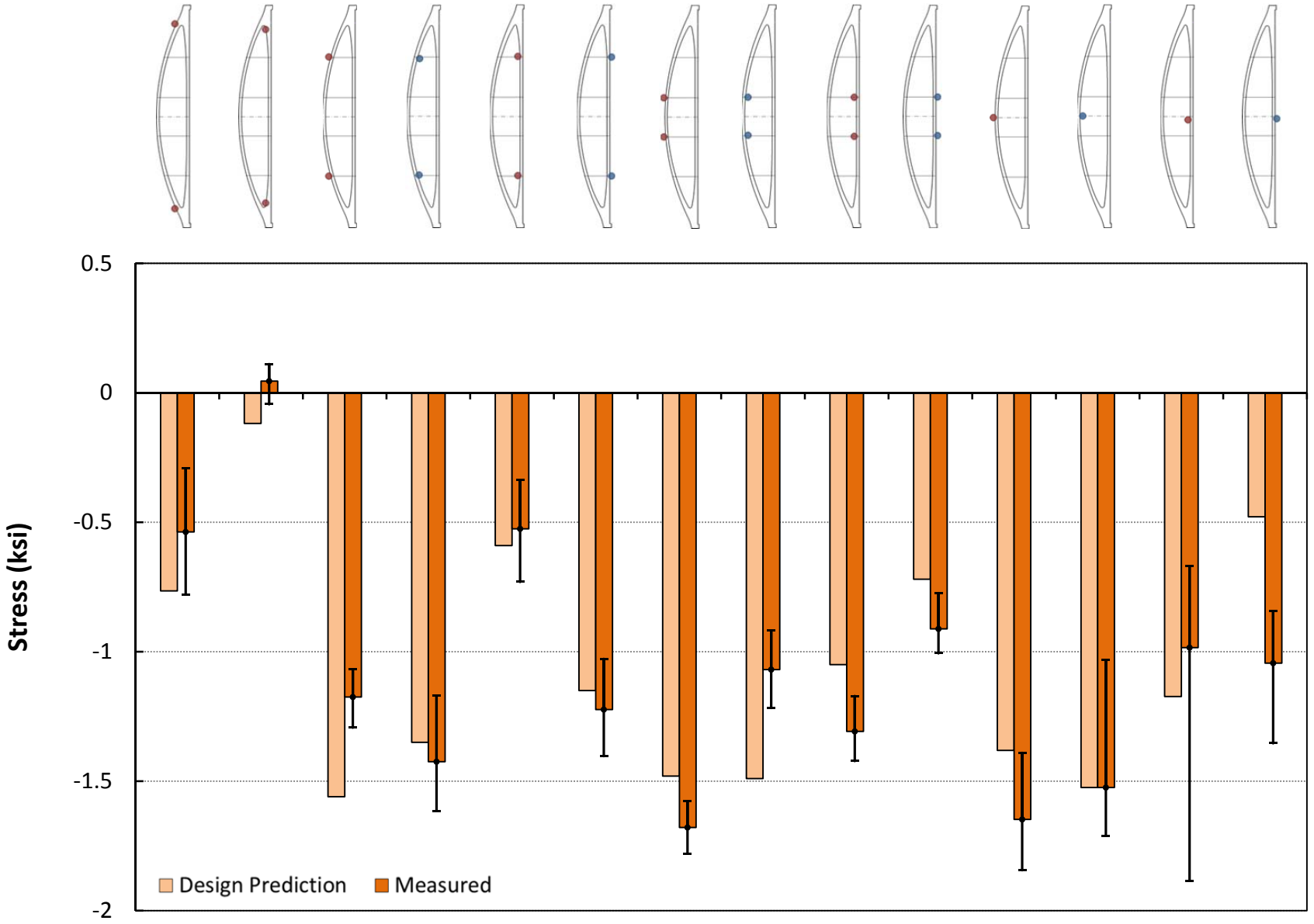

Figure 6.10- Arch stresses at the end of rotation.

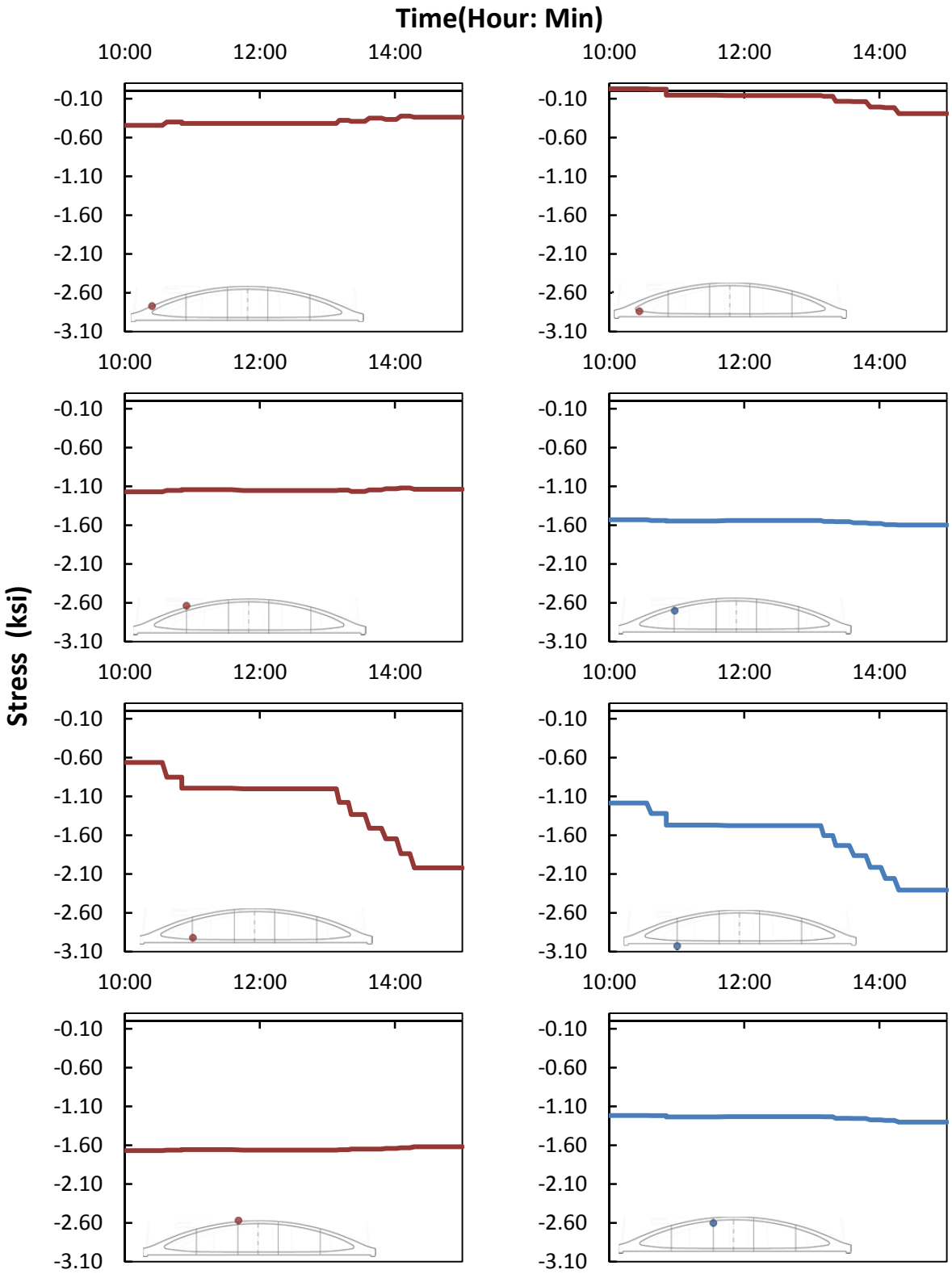

Figure 6.11- Stresses in Arch 2 during Stage 2 PT operations on the tie.

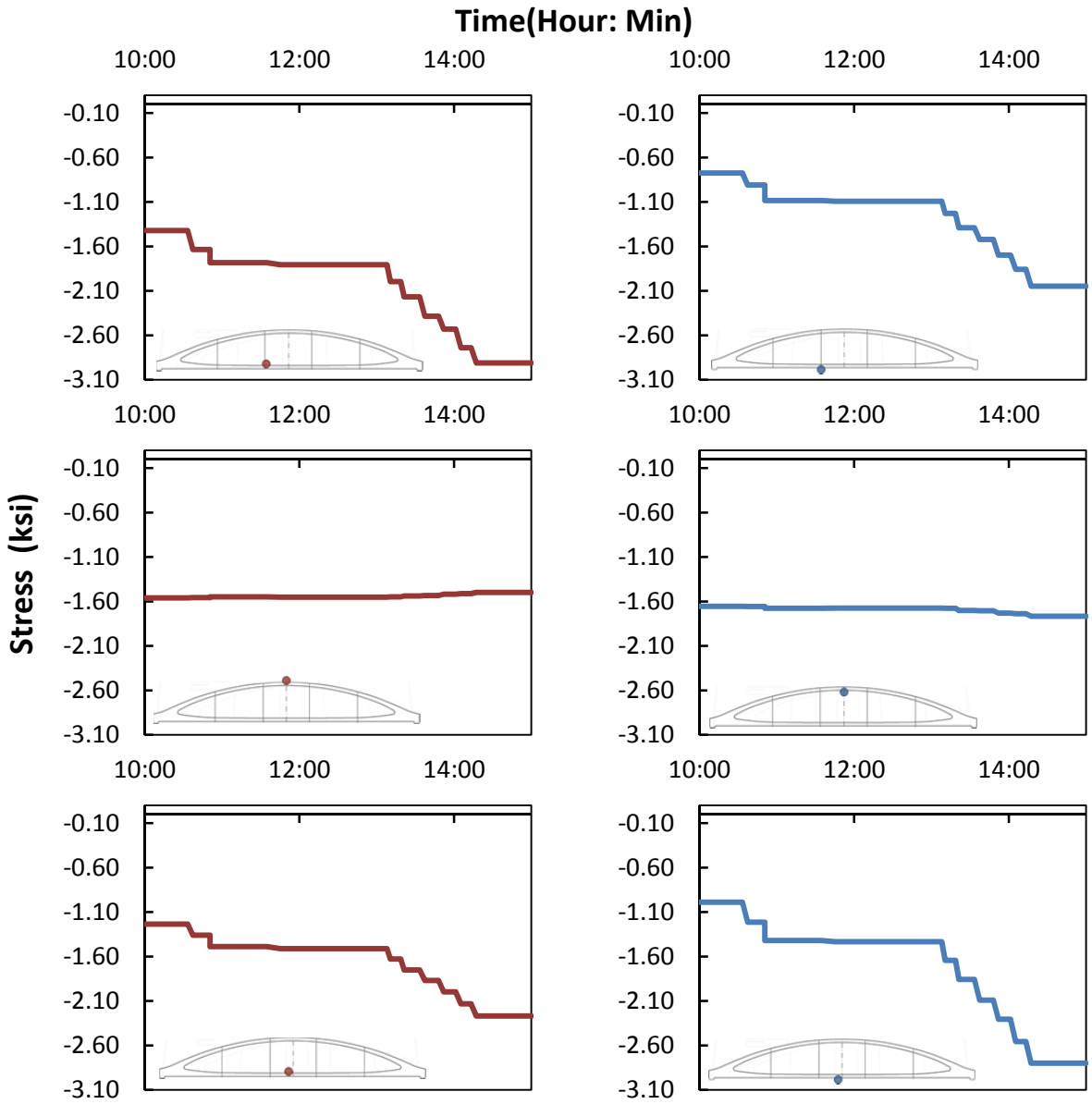

Figure 6.12- Stresses in Arch 2 during Stage 2 PT operations on the tie (continued).

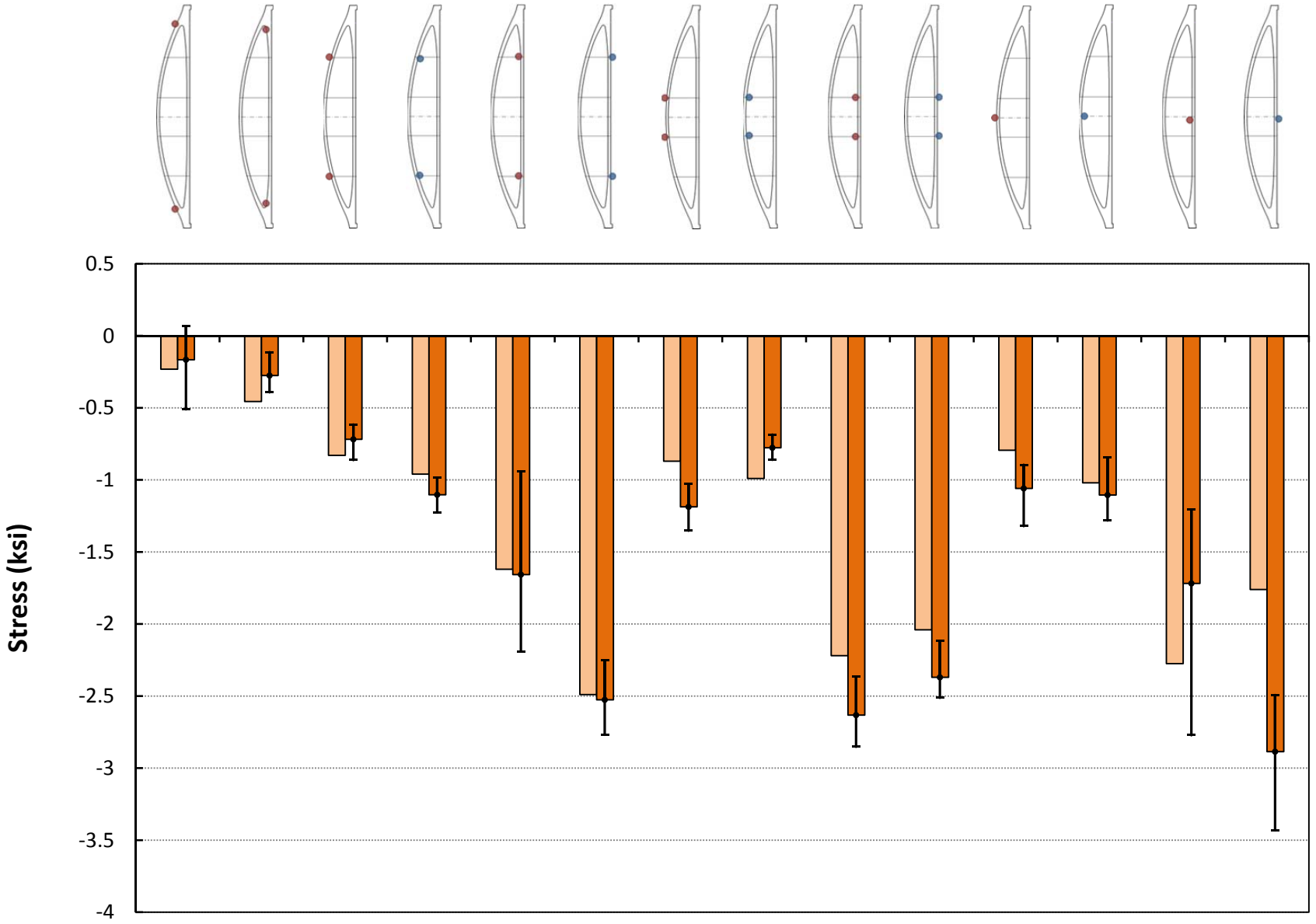

Figure 6.13- Arch stresses at the end of Stage 2 PT.

6.3.4 Sliding

Typical stress changes in Arch 2 during sliding operations are shown in Figure 6.14. In ideal conditions, the arches move as rigid bodies during sliding, without experiencing any loading. However, the two hydraulic rams that were pushing the arches were not perfectly synchronized. Moreover, the arch was not moving perfectly smoothly on the rails. As a result, some stress fluctuations are visible in the stress records, especially in the knuckle region. These stress changes were very small and short-lived. Therefore, stresses due to sliding operations were not taken into account in total stress calculations. However, sliding operations were carefully monitored to ensure that large stresses were not induced in the arches.

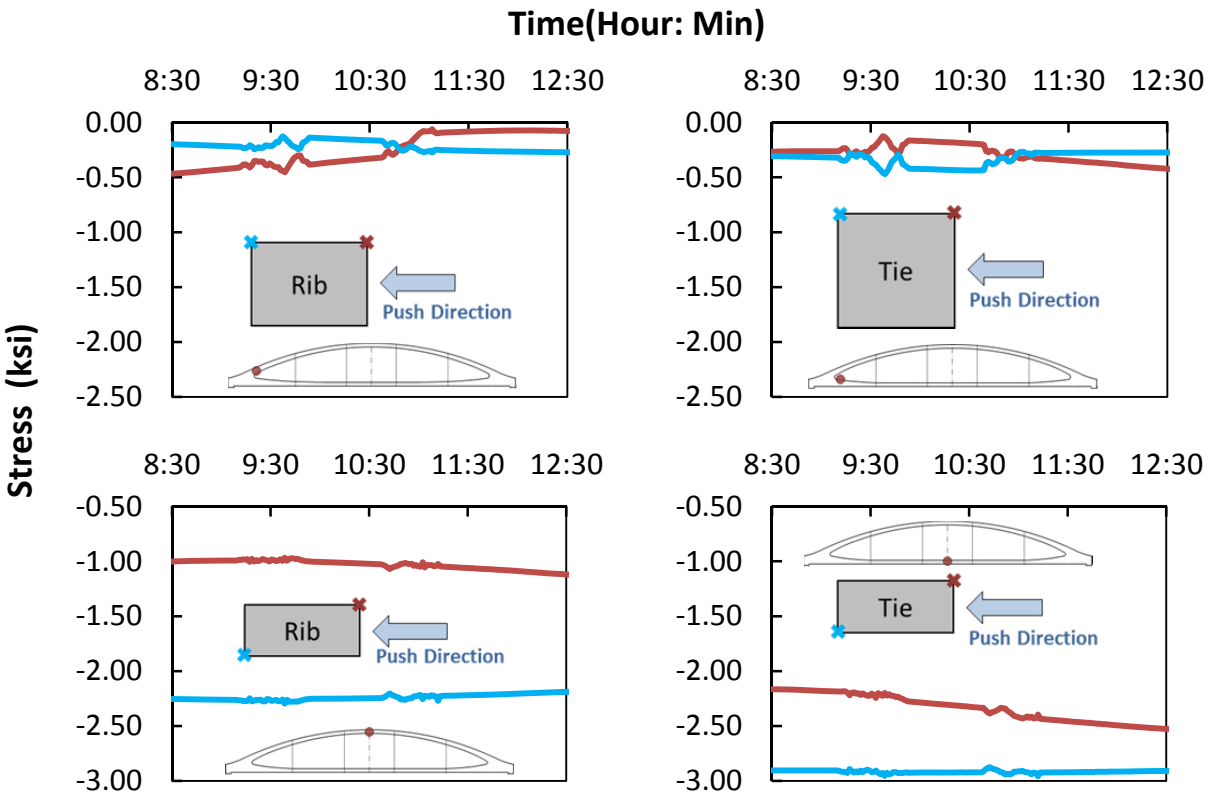

Figure 6.14- Typical stress changes in Arch 2 during sliding operations.

6.3.5 Upward Jacking

The upward jacking operation was the most critical stage for the knuckle region of the arches. The designers predicted that during upward jacking, tension would have been induced at the top of the rib in the knuckle region if the arches had not been temporarily strengthened.

Figures 6.15 and 6.16 show the stress changes during upward jacking operations on Arch 2. As shown in Figure 6.15, activating the hydraulic rams at the beginning of upward jacking reduces the compressive stresses at the top of the rib in the knuckle region. However, when the rams are deactivated after re-tightening of the hanger nuts, most of the compressive stresses are restored in this region.

Figure 6.17 shows the measured stresses in the arches when the hydraulic rams were activated but the hanger nuts were not yet re-tightened. As can be seen in this figure, the stresses in the knuckle region were in good agreement with the design predictions. Although some arches experienced tension during upward jacking, the tensile stresses were well below the modulus of rupture of the concrete. The variability in the stresses at the top of the tie at midspan is increased again in this stage, up to a stress difference of $1.8ksi$ between some arches. The stresses at the bottom of the tie were higher than design predictions but below 50% of the compressive strength of the concrete.

Arch stresses after re-tightening of the hanger nuts and removal of the hydraulic rams are shown in Figure 6.18. This figure shows that the difference between predicted and measured stresses is increased after removal of the rams. Some of the arches experience tensile stresses as large as $220psi$ in the rib. The maximum compressive stress at the bottom of the tie also reached a level of $3.77ksi$ in some arches.

Although the upward jacking operation was carried out in a way to reduce the variability of hanger stresses, removal of the sag from the hangers and re-tightening of the hanger nuts were carried out manually, depending on the judgment of construction personnel. Therefore, some variability was expected in the hanger stresses, resulting in different stresses in the arches. While the relatively large stresses noted above were not anticipated in design, the arches were still safe against cracking, as the maximum tensile stresses were well below the modulus of rupture.

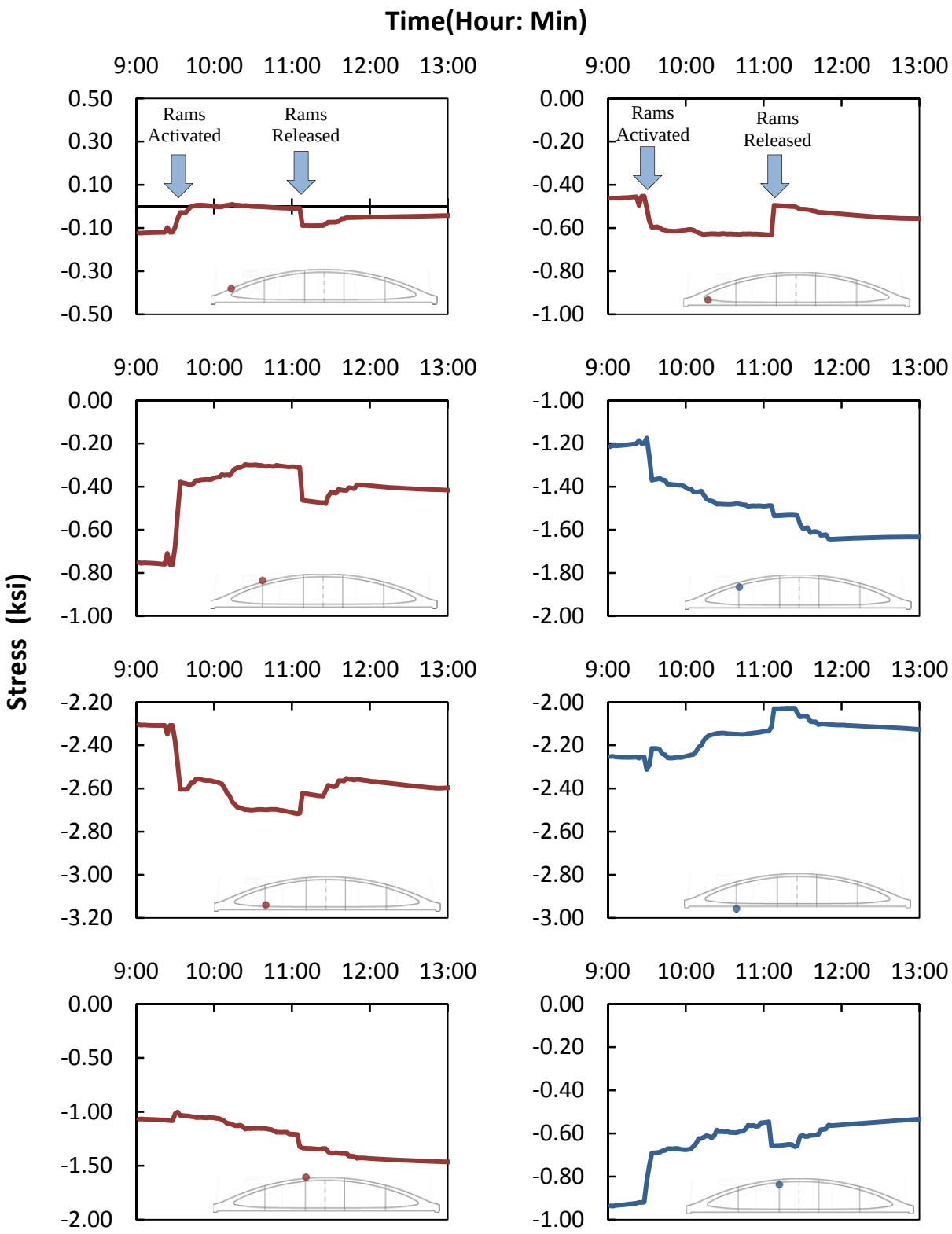

Figure 6.15- Stresses in Arch 2 during upward jacking operations.

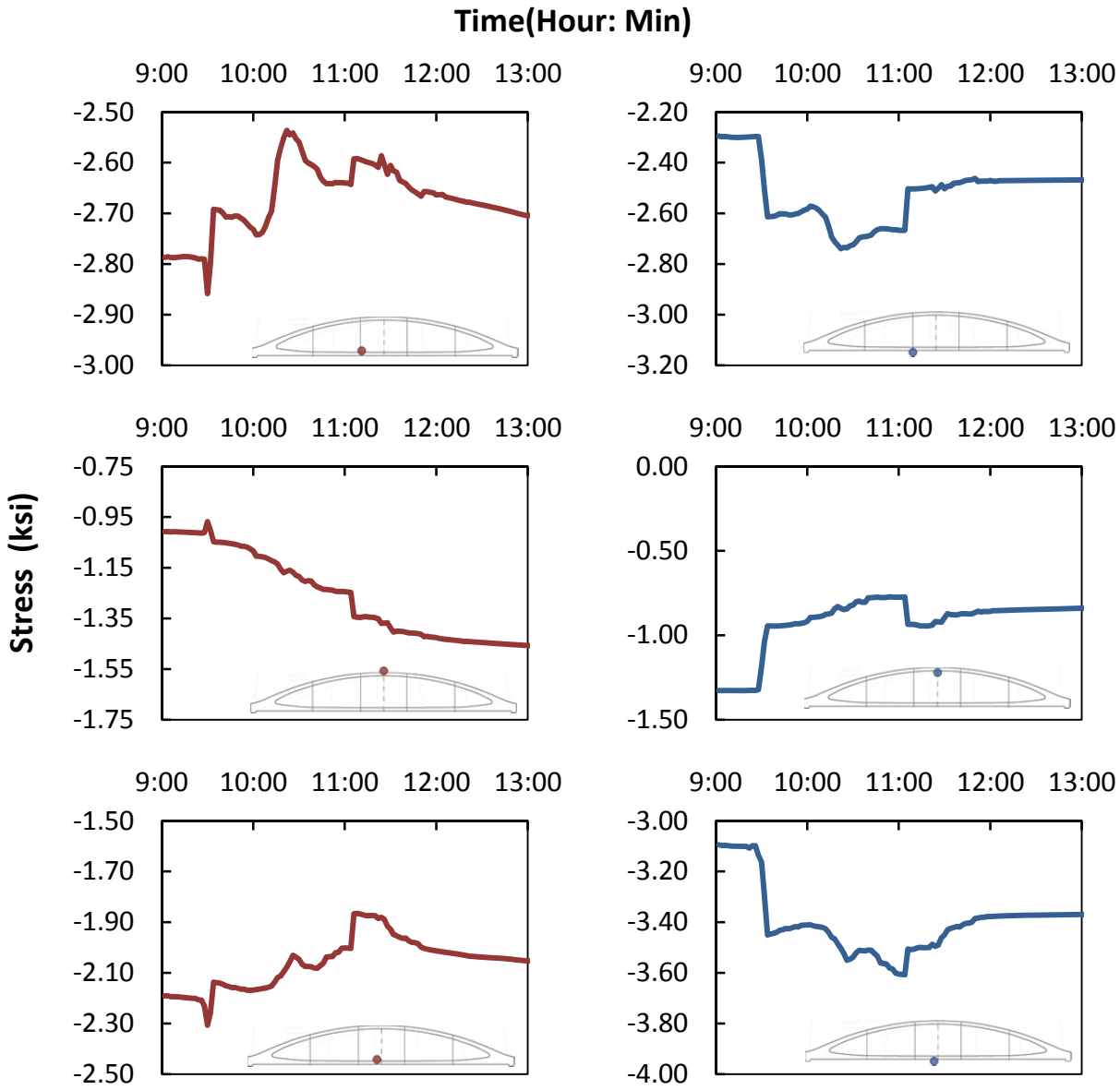

Figure 6.16- Stresses in Arch 2 during upward jacking operations (continued).

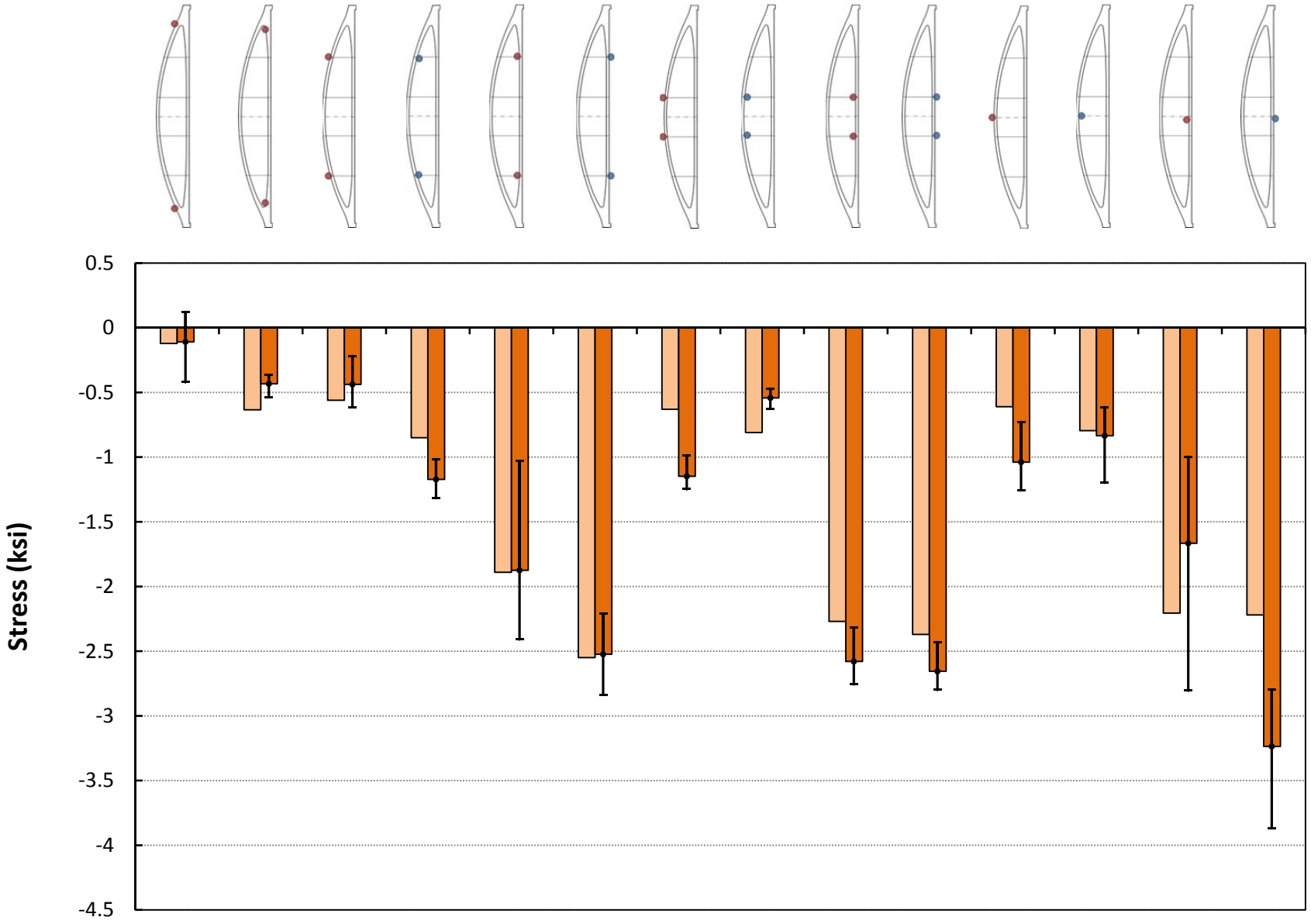

Figure 6.17- Arch stresses during upward jacking (rams active).

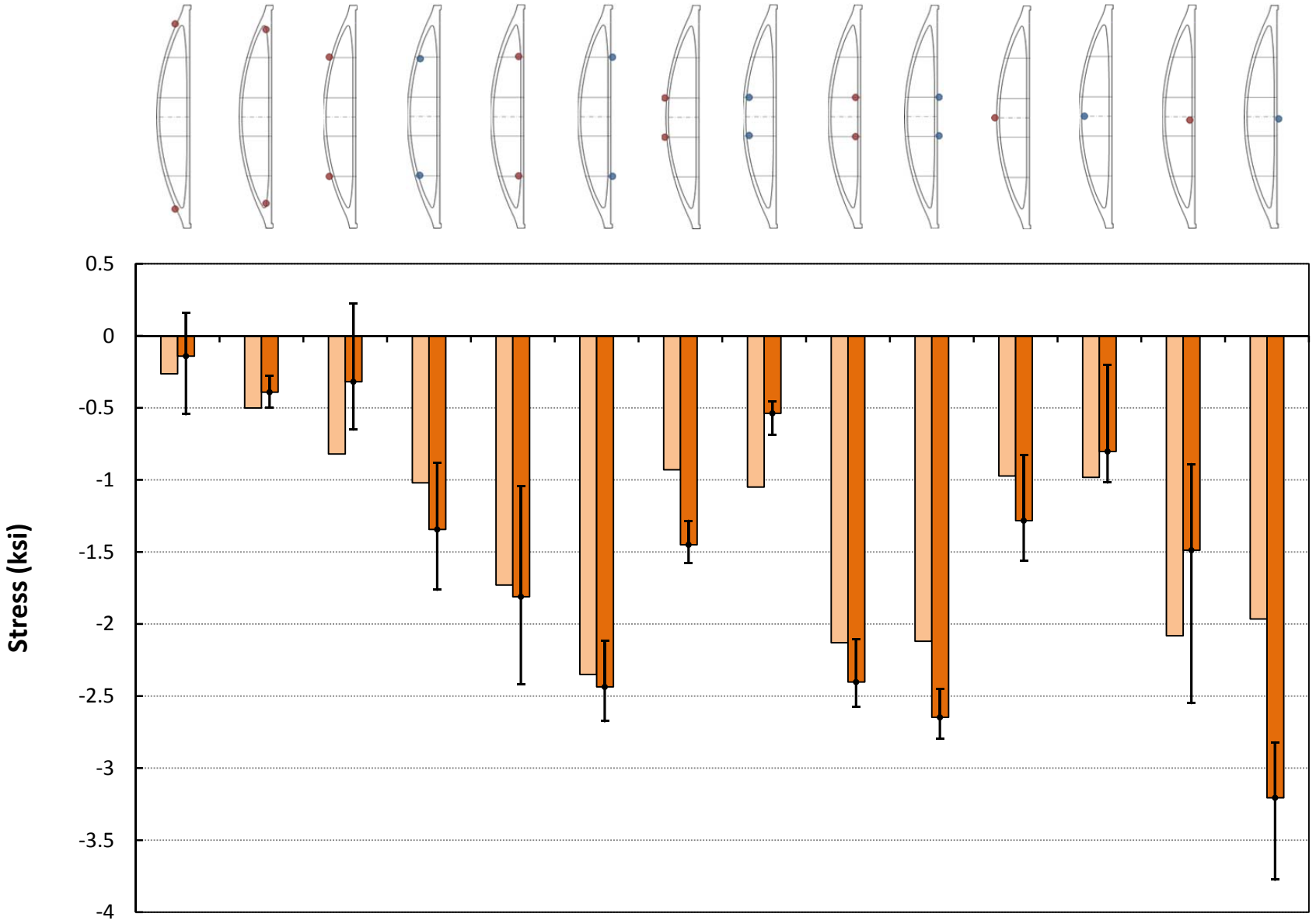

Figure 6.18- Arch stresses after upward jacking (after removal of the rams).

6.3.6 Arch Transportation

Figures 6.20 and 6.21 show the stresses in Arch 4 during transportation operations. As can be seen in these figures, most of the stress changes happen during setting of the arch on the SPMTs and on the bearings. The transport of the arch between the precast yard and the old bridge went smoothly with very small stress fluctuations that were smaller than 100 psi. However, the change in the support conditions, which was discussed in Section 2.2.2.1, reduced the compressive stresses in the rib, especially in the regions close to the knuckle.

The rib experienced negative bending when the arch was set on the SPMTs, which was due to different support conditions, as shown in Figure 6.19. The negative bending produced tension at the top of the rib, both at the knuckle and at the location of Lifting Frame 2. This change was particularly important in the knuckle region because following upward jacking operations, the remaining compressive stresses in this region were relatively small, and the arches were prone to cracking under tensile stresses.

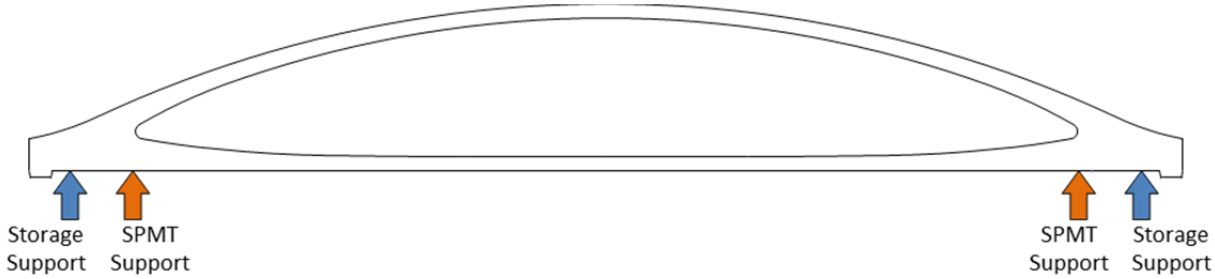

Figure 6.19- Change in the support conditions during arch transportation.

Apparently, the construction team had calculated the stresses in the arches during transportation and concluded that the arches would not be in distress. However, local cracking happened in Arch 2 at the top of the rib in the knuckle region, as shown in Figure 6.22. Arch 2 was moved out of the precast yard when setting of Arch 1 on bearings was still in progress. The researchers from UT were not informed of the beginning of transportation for Arch 2. Therefore, the initial stress changes due to setting on SPMTs were not monitored for this arch. However, comparing the strains before and after setting the arch on the SPMTs clearly shows that the arch experienced local cracking at the eastern knuckle. Based on the measured strains, the width of the local crack was approximately 0.0015”, and the crack was closed once the arch was set on bearings. As a result, this crack should not significantly affect the performance of the arch. For other arches, no stresses were observed that would indicate cracking during transportation.

Once the arches were set on bearings, the support conditions were changed again, and the rib experienced larger compressive stresses as compared to those before setting the arch on SPMTs.

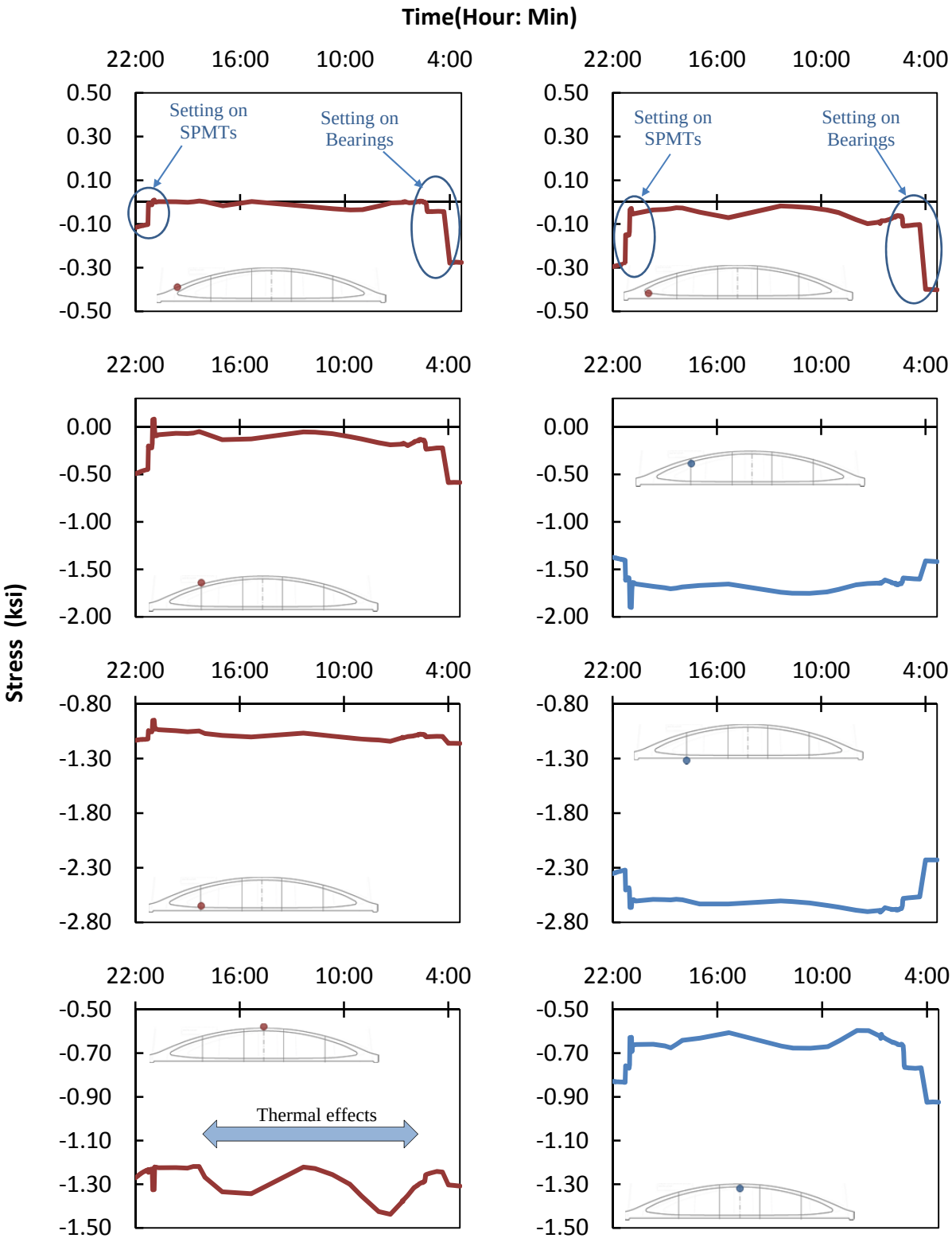

Figure 6.20- Stresses in Arch 4 during transportation.

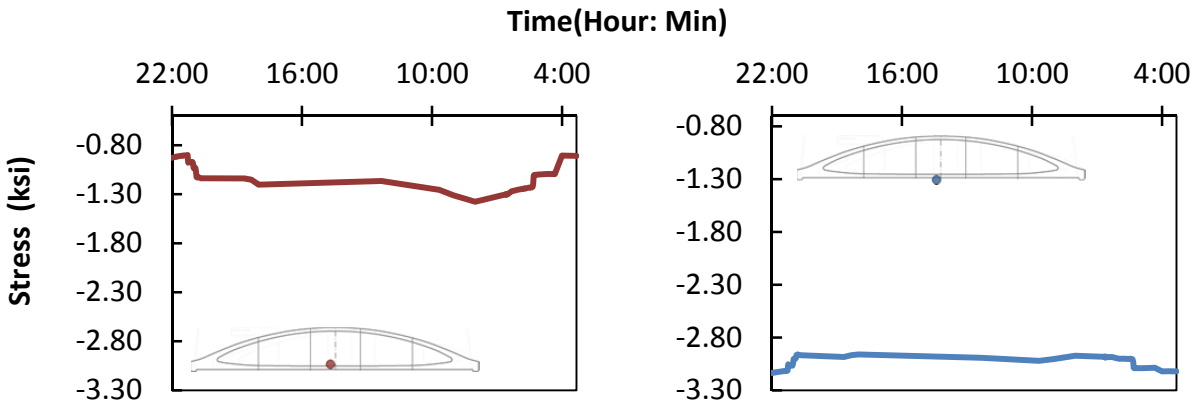

Figure 6.21- Stresses in Arch 4 during transportation (continued).

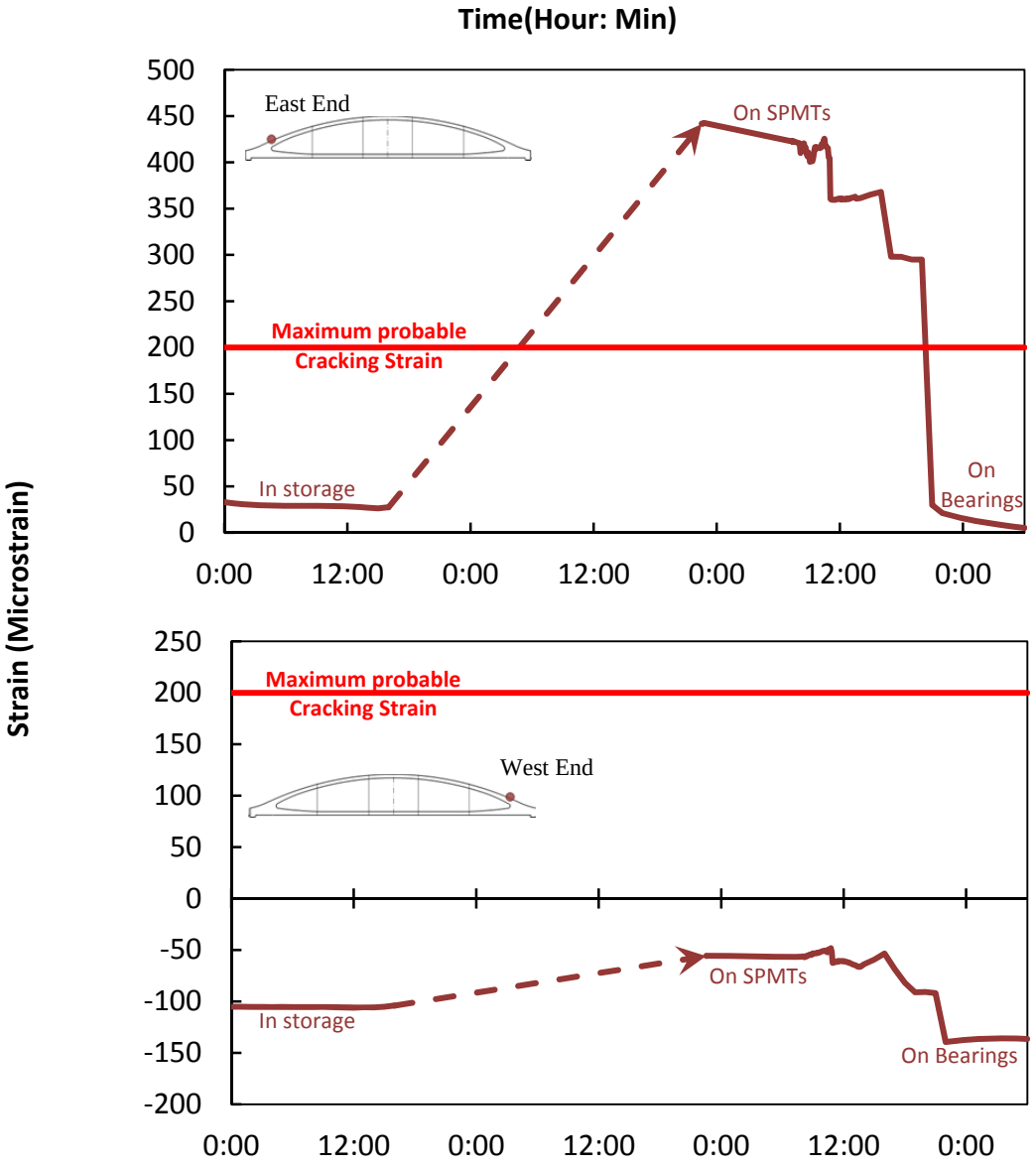

Figure 6.22-Strain changes in the knuckle region of Arch 2 during transportation.

6.3.7 Floor Beam Installation and Deck Construction

As mentioned in Chapter 4, only few of the arches were monitored during the floor beam installation and deck construction stages. The floor beam installation was monitored only on arches 2, 3, 4, 11, 12, and half of Arch 1. The topping slab cast was monitored only for arches 2 and 4 and half of Arch 1. The stresses in the arches following floor beam installation and topping slab cast are shown in Figure 6.23 and Figure 6.24, respectively.

The difference between predicted and measured stresses is intensified following deck construction. In the knuckle region, the design predicted larger compressive stresses than measured. However, the total compressive stress is still relatively large, providing a reasonable safety margin against cracking. The measurements also show larger bending in the rib than predicted in design. In terms of average stresses, the largest compression in the arches was approximately $2.4ksi$, which was measured at the bottom of the tie at midspan, and the smallest compression was $0.32ksi$, measured at the top of the knuckle region. The maximum and minimum stresses in all arches were $2.6ksi$ and $0.20ksi$, respectively.

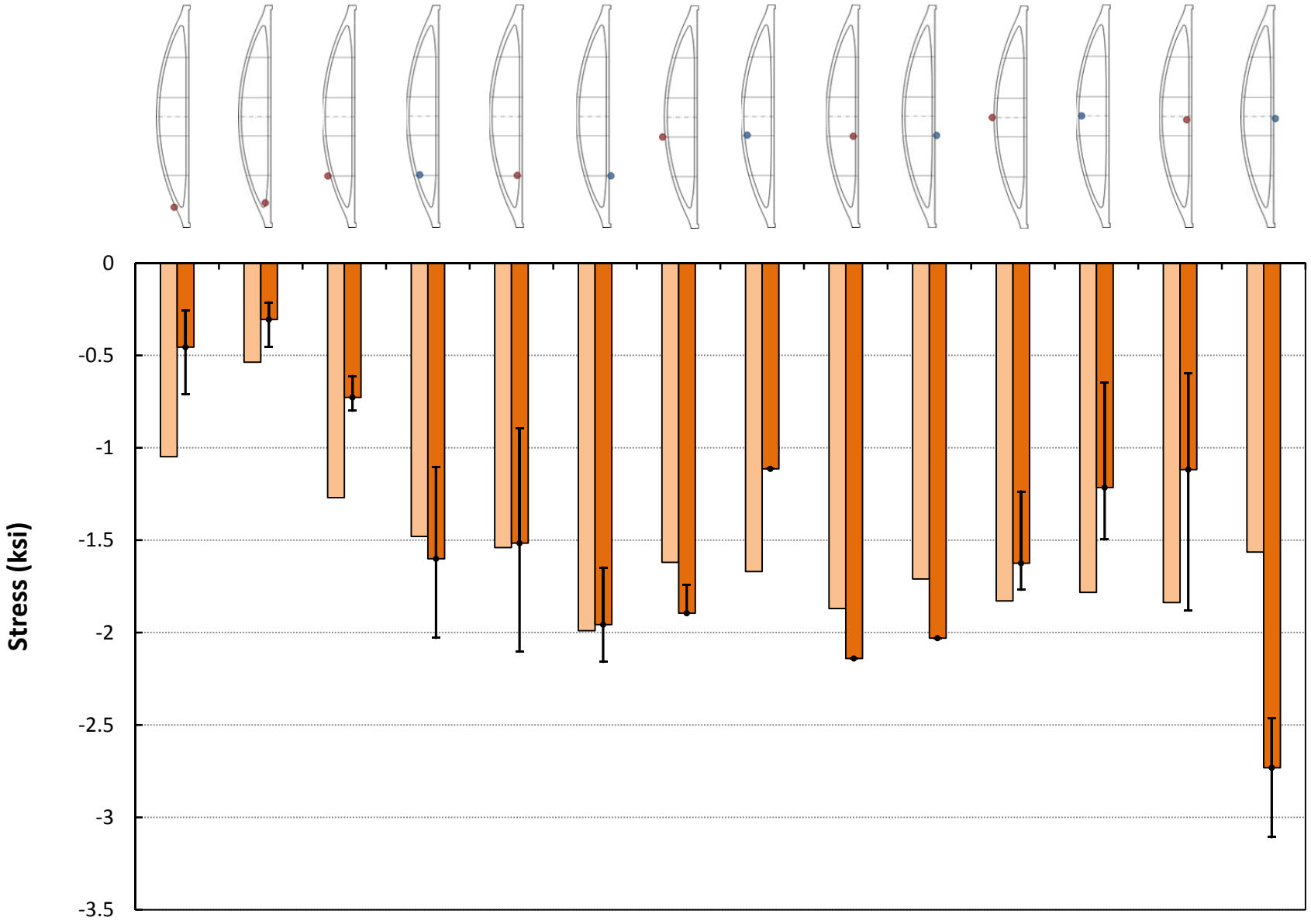

Figure 6.23- Arch stresses after floor beam installation (data from arches 2, 3, 4, 11, and 12).

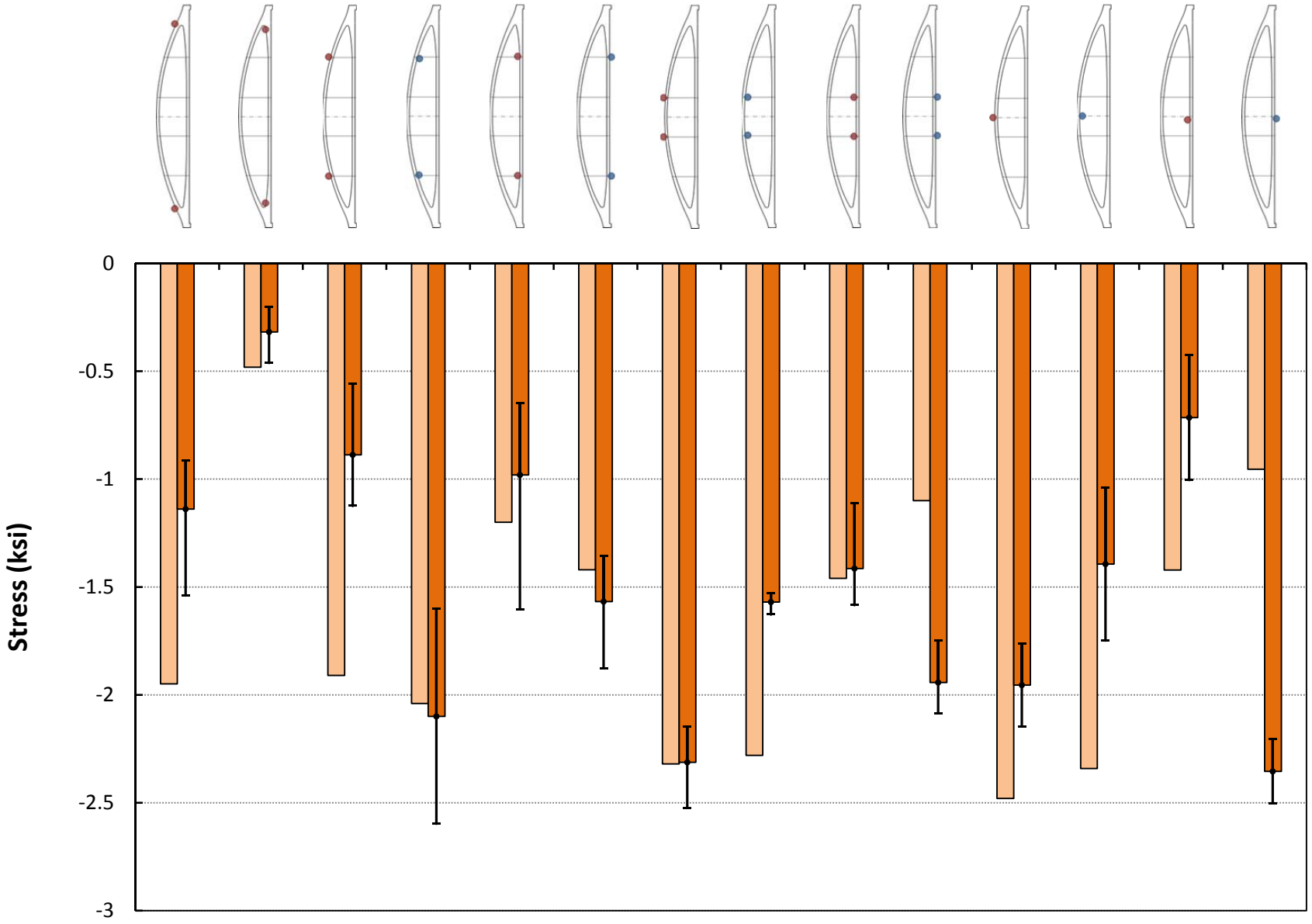

Figure 6.24- Arch stresses after casting the topping slab (data from arches 2 and 4, and half of Arch 1)

6.1 PRESTRESS LOSSES

As discussed in Chapter 5, the changes in prestressing force in the tendons were calculated based on the strain-related losses measured by the instrumentation and the relaxation losses that were calculated based on modified Magura equation.

Figure 6.25 shows the stresses in the PT tendons in Arch 2 following the end of post-tensioning operations. As can be seen in this figure, the prestress losses in Arch 2 were relatively small, all below $10ksi$. While some stress fluctuations happen in the tendons due to thermal changes, the changes in the average tendons stresses between upward jacking and transportation stages were minimal. During this storage period, the prestress loss in the tie tendons is governed by tendon relaxation. Since the stress in the rib tendons is below $0.55f_{pu}$, the relaxation losses are neglected in the rib tendons.

Also visible in Figure 6.25 are the effects of deck construction on the prestressing force in the tendons. As can be seen in this figure, with the start of deck construction, the prestress in the rib tendons decreases, while the prestress in the tie tendons increases. The main reason for this additional prestress loss in the rib and stress gain in the tie is the elastic deformations of the arches. Since the rib experiences more compression due to deck loading, the rib tendons are contracting, and hence, losing parts of their prestress. On the other hand, the tie tendons experience extension due to tensile forces acting on the tie, and therefore gain some prestress.

Figures 6.26 and 6.27 show the summary of tendon stresses in different arches. Since one of the VWGs was lost at the midspan of Arch 9 in the rib, the tendon stresses at the end of construction could not be calculated for this section of Arch 9 and are not shown in these figures. As can be seen in Figures 6.26 and 6.27, most of the prestress loss in the rib tendons happens after the start of deck construction. In the tie tendons, the stress gain after deck construction compensates most of the prestress loss. Therefore, the stress in the tendons at the end of construction is approximately equal to that at the time of upward jacking. There is also some variability in the PT stresses in the tendons, mostly due to different prestress losses before upward jacking.

While some variability is visible in the range of prestress losses among different arches, PT losses were generally small in the arches of the West 7th Street Bridge. This observation may be attributed to the very stiff network of hangers that prevent the rib and the tie from shortening due to time-dependent deformations of concrete.

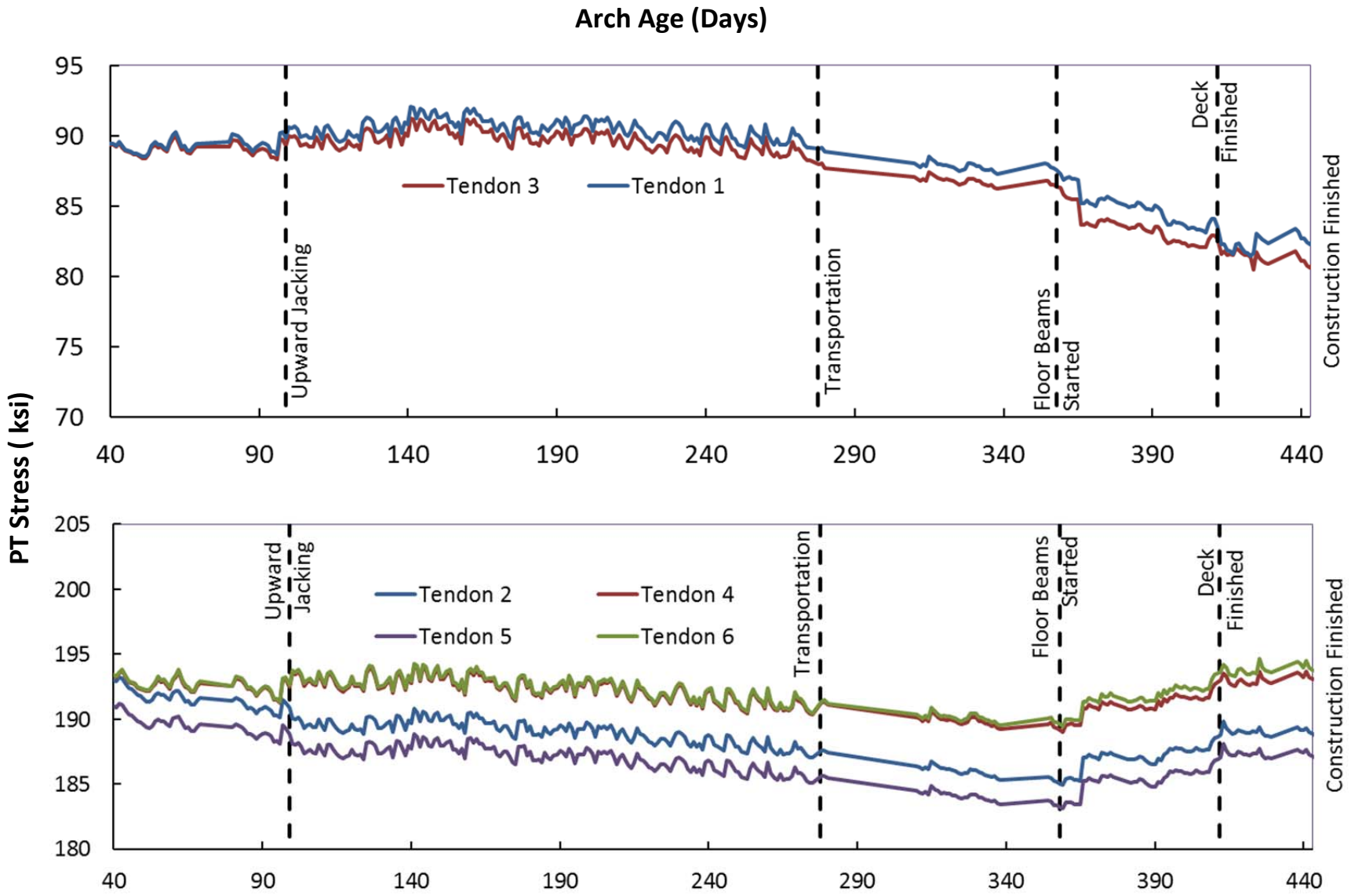

Figure 6.25- The stresses in PT tendons following Stage 2 PT.

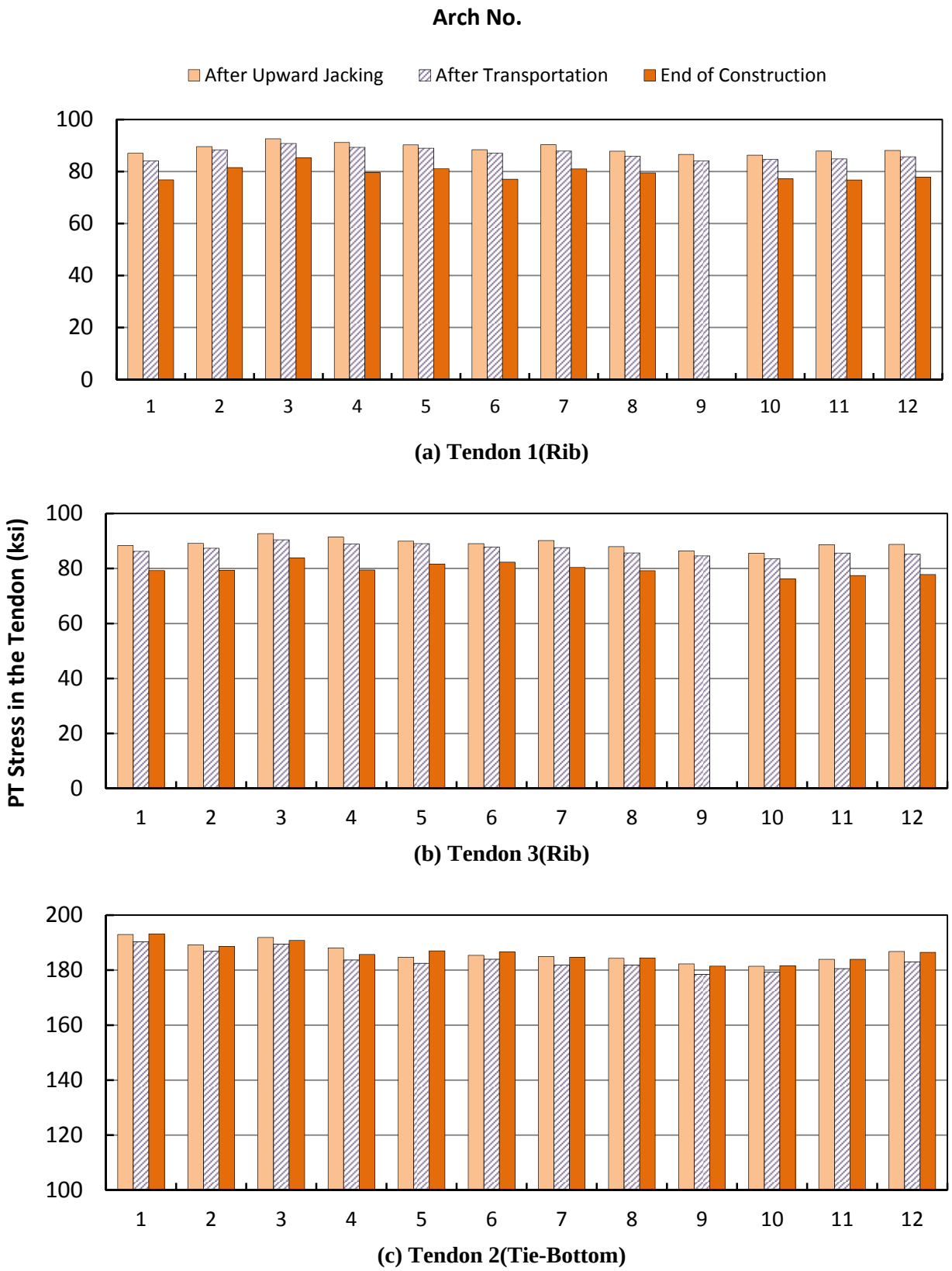

Figure 6.26- PT stresses in the arch tendons at different stages of construction.

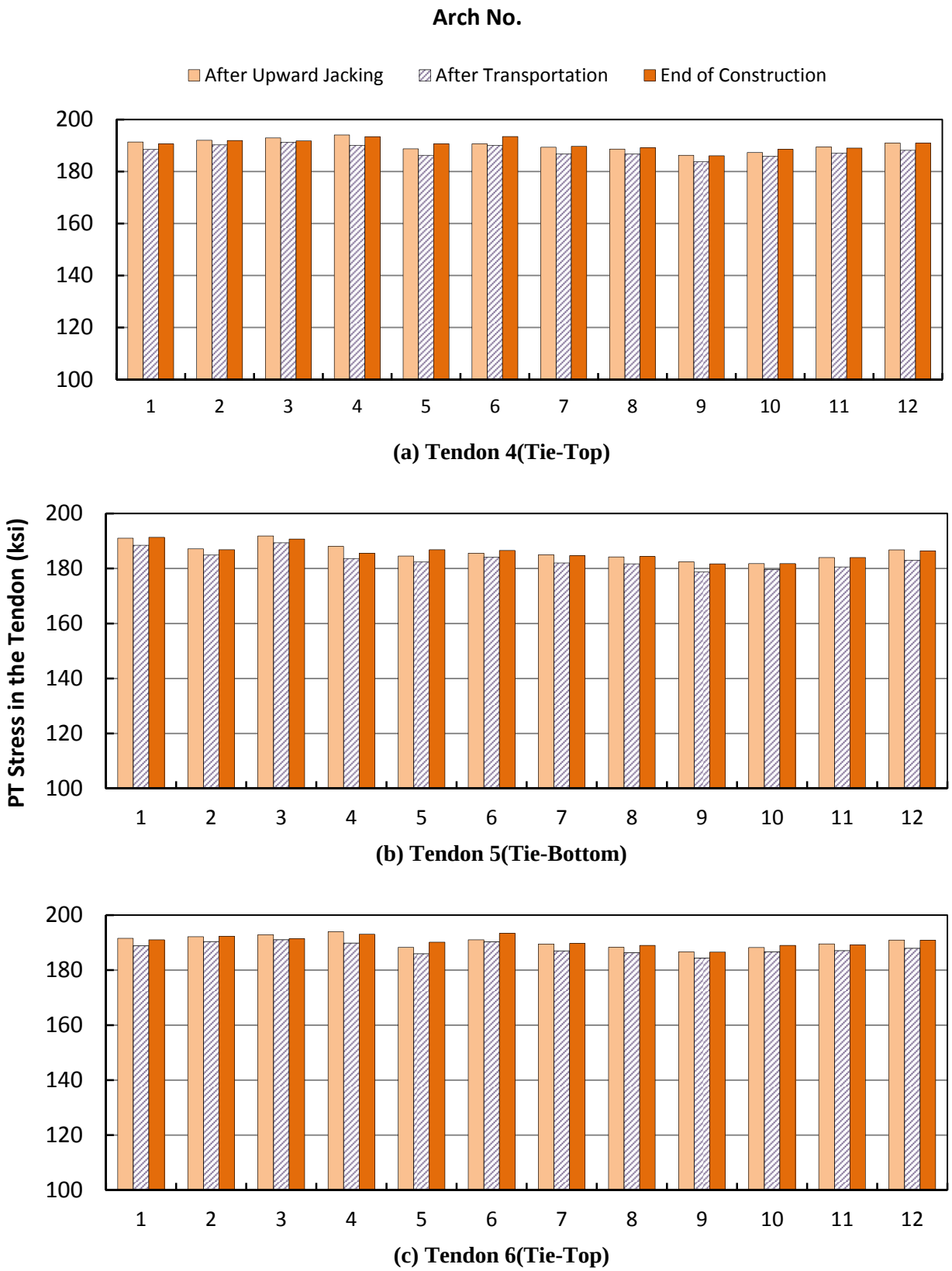

Figure 6.27- PT stresses in the arch tendons at different stages of construction (continued).

6.2 LIVE LOAD TEST RESULTS

Figures 6.28 to 6.33 show the stress changes in Arches 1 and 2 during the live load test, based on the positions that were introduced in Section 4.4. As can be seen in these figures, the maximum stress change observed in the arches during live load test was approximately $200psi$. Therefore, the arches provide a very stiff and strong load-carrying system.

The stresses shown in Figures 6.28 to 6.33 have provided valuable data for validating finite element models of the arches for further study.

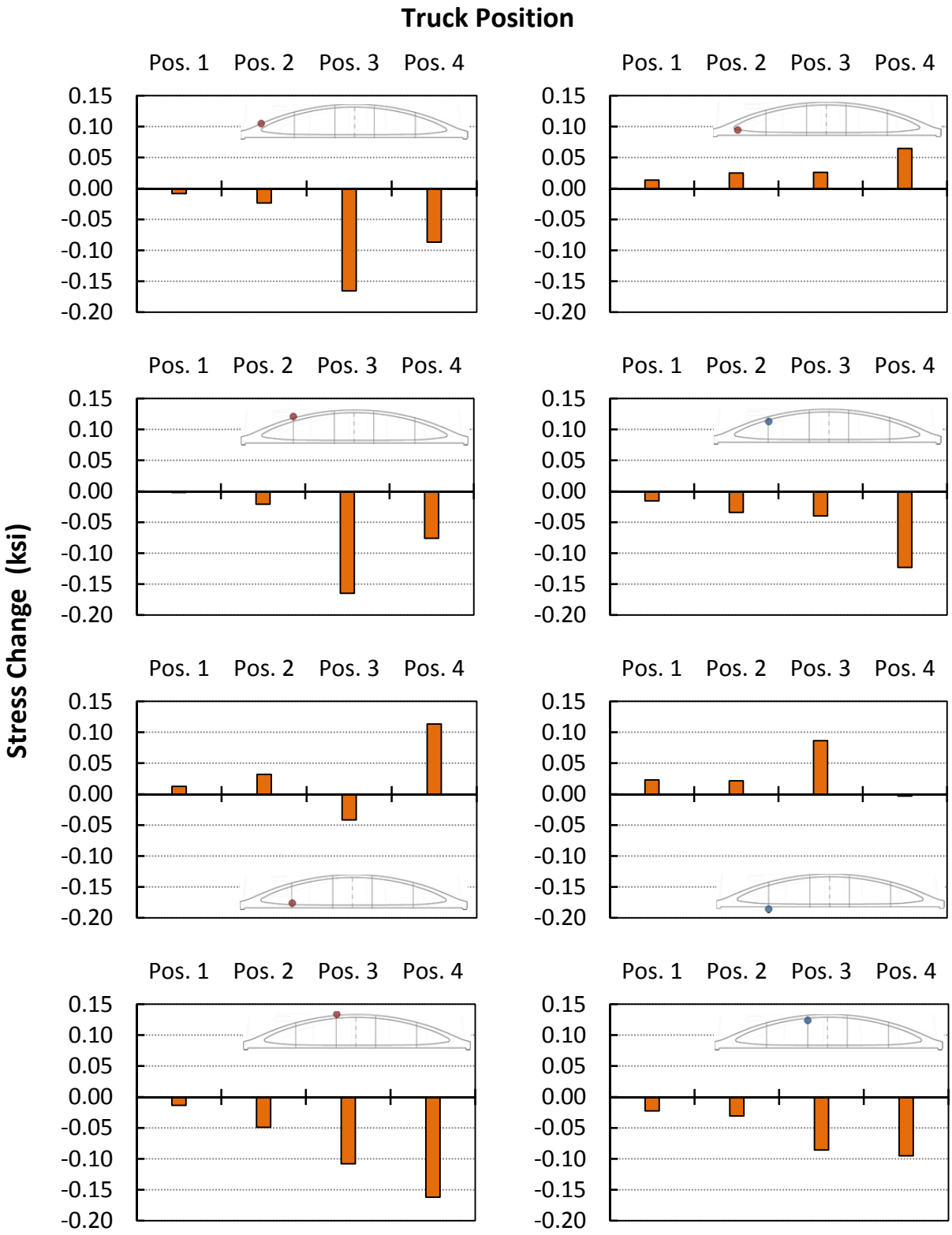

Figure 6.28- Stress changes in Arch 1 during live load test.
Since one VWG was lost in Lifting Frame 3 at the rib, no stresses are shown for that section.

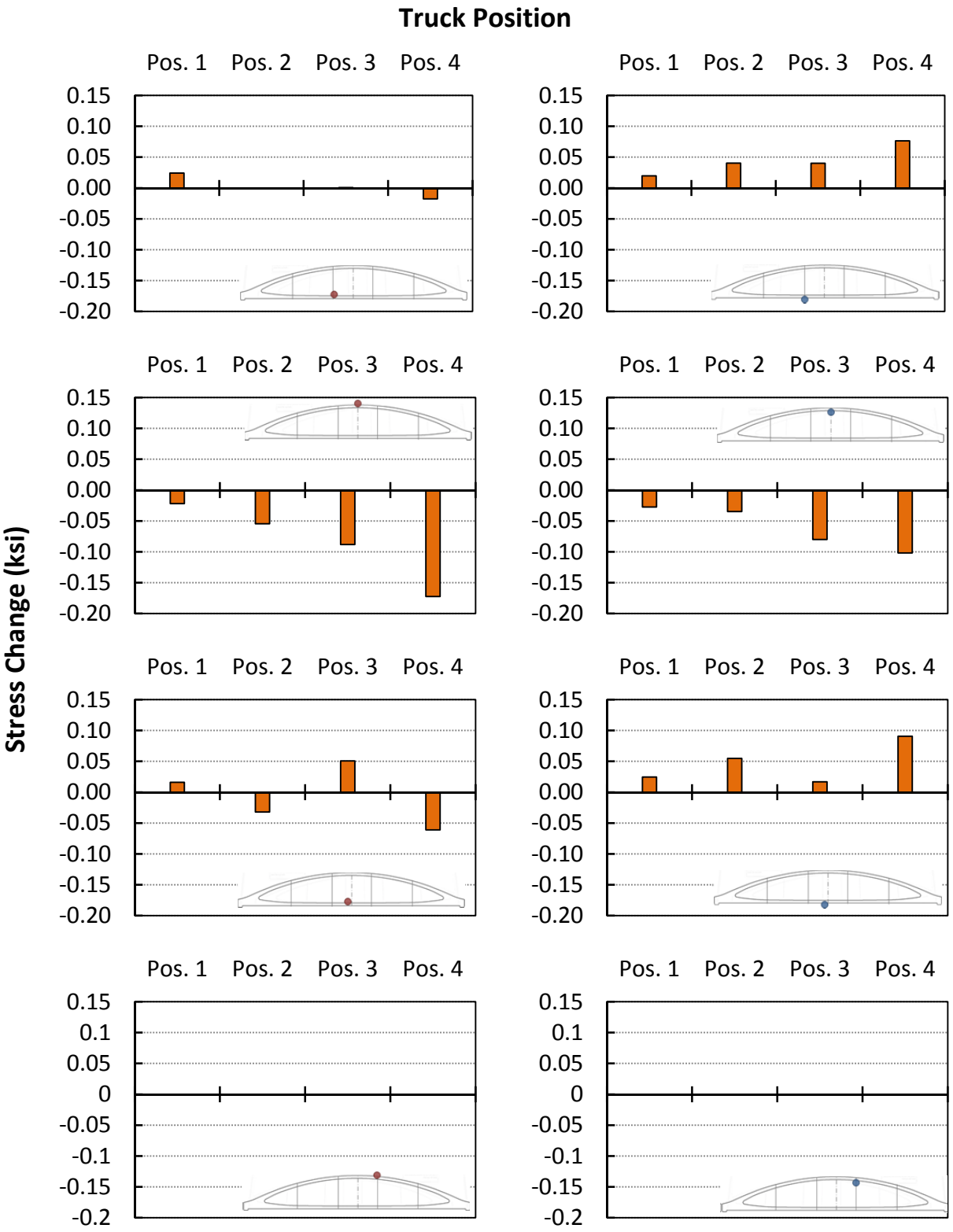

Figure 6.29- Stress changes in Arch 1 during live load test (continued).
Since one VWG was lost in Lifting Frame 4 at the rib, no stresses are shown for that section.

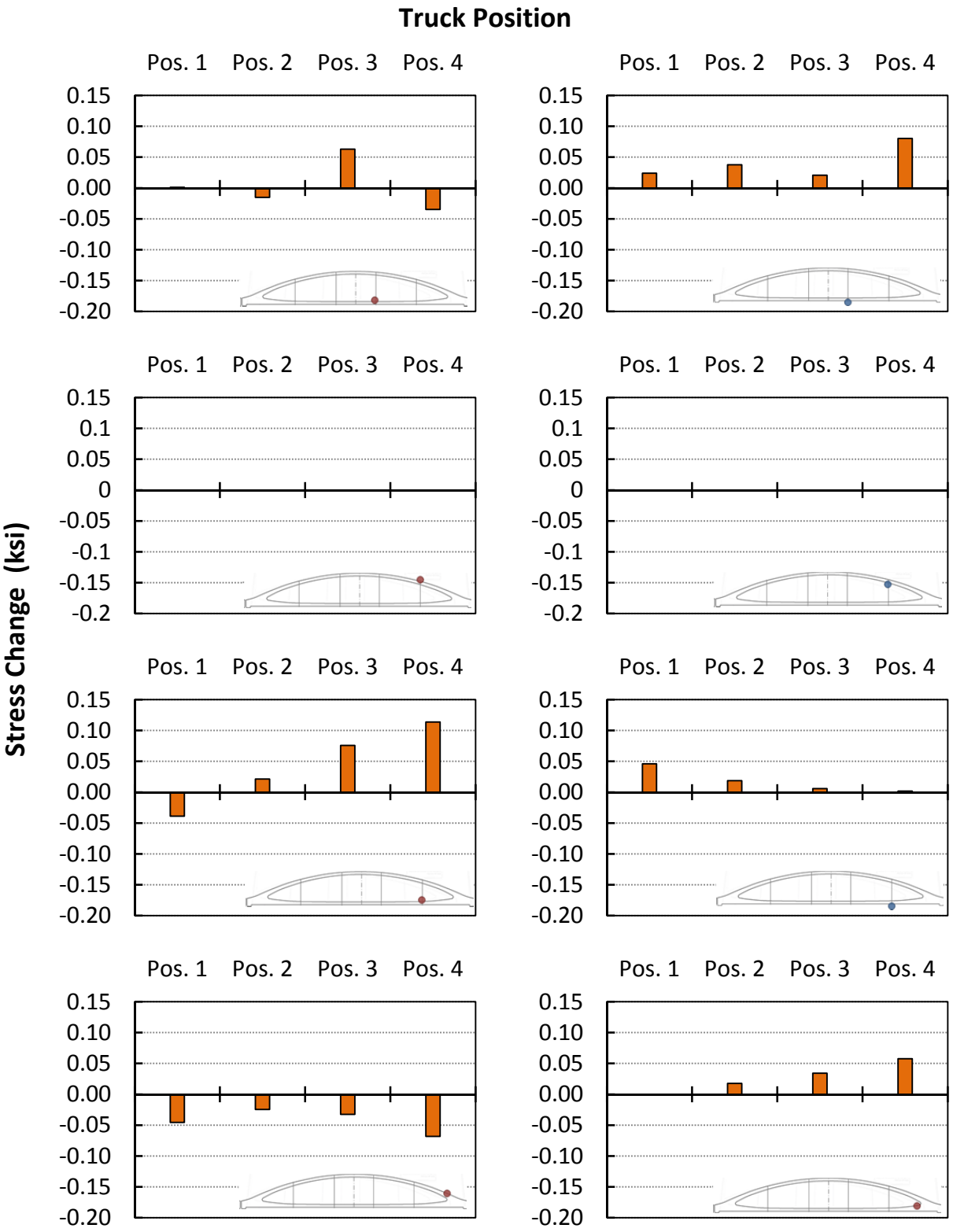

Figure 6.30- Stress changes in Arch 1 during live load test (continued).
Since one VWG was lost in Lifting Frame 5 at the rib, no stresses are shown for that section.

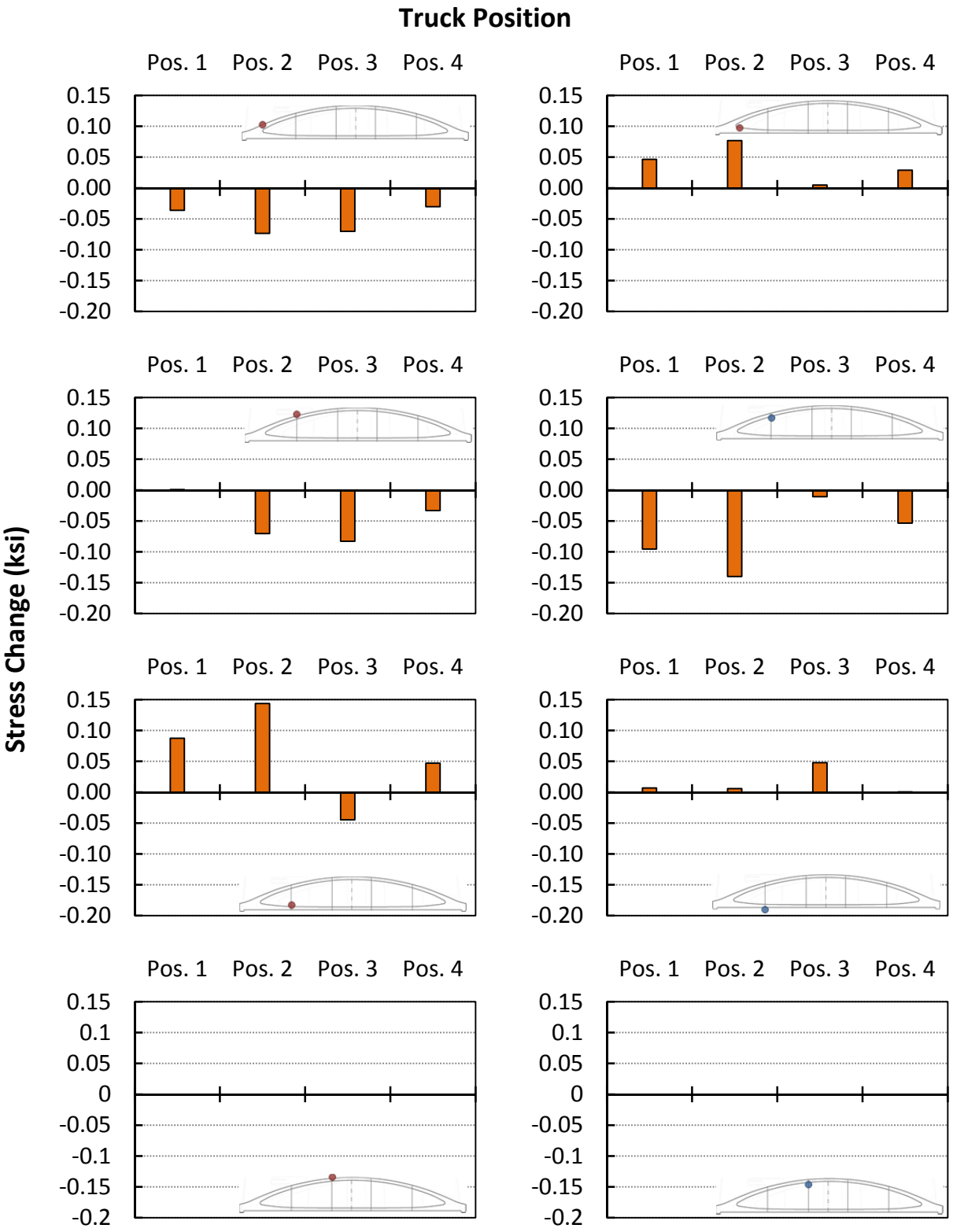

Figure 6.31- Stress changes in Arch 2 during live load test.
Since one VWG was lost in Lifting Frame 3 at the rib, no stresses are shown for that section.

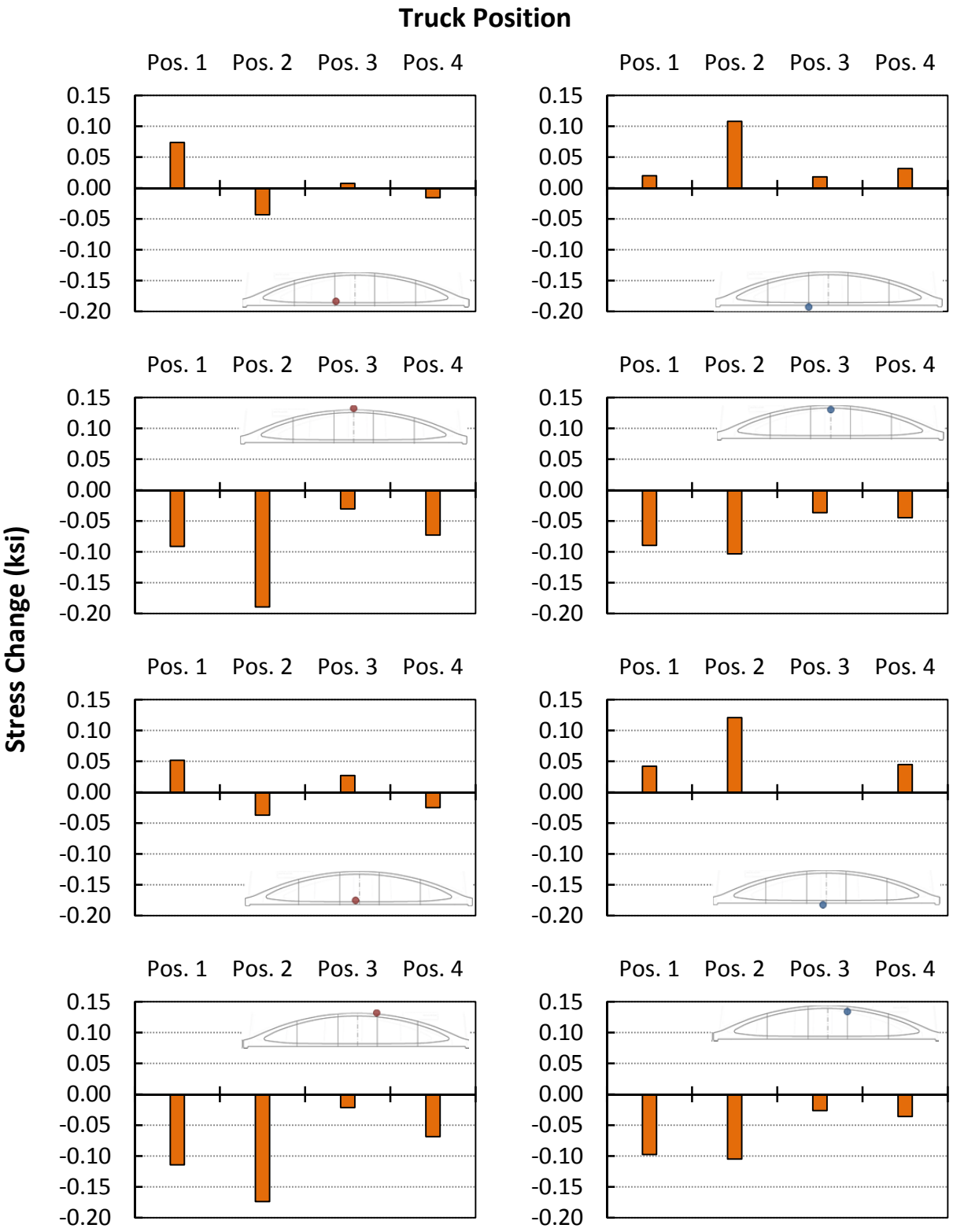

Figure 6.32- Stress changes in Arch 2 during live load test (continued).

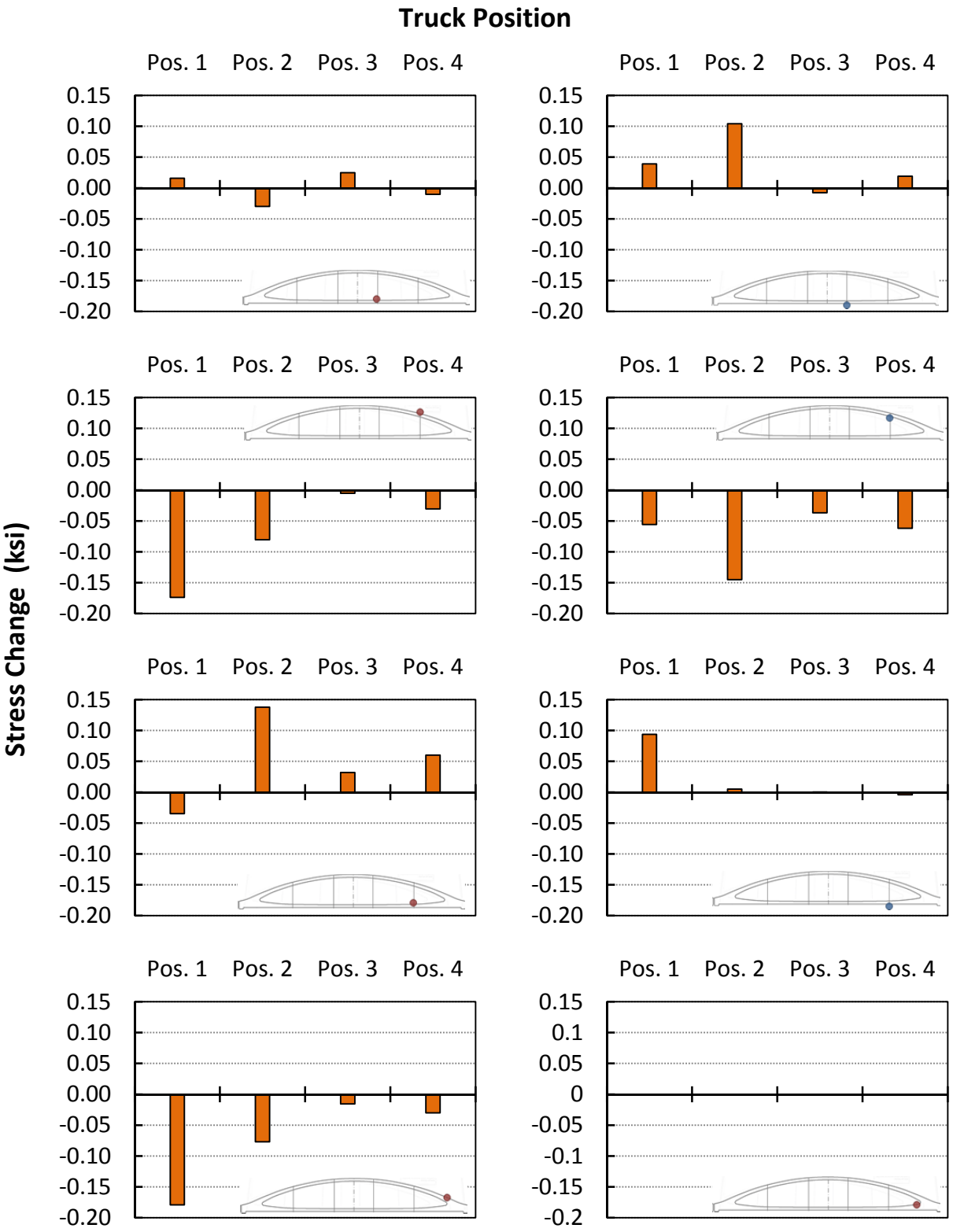

Figure 6.33- Stress changes in Arch 2 during live load test (continued).
Since one VWG was lost in the west knuckle at the tie, no stresses are shown for that section.

6.3 SUMMARY

This chapter provided an overview of the post-processed instrumentation results. Only representative graphs of stress changes in the arches were shown in this chapter. However, the researchers from UT carefully monitored a much wider variety of structural parameters during all construction operations in real time to make sure that the arches were not in distress during the construction. Due to the careful structural design of the arches and conservative construction design of the handling operations, the arches remained safe during all the construction operations on the casting yard. However, Arch 2 experienced local cracking in the knuckle region during transportation from the casting yard to the final location. The width of the generated crack was very small and the crack was soon closed due to the change in the support conditions of the arch. Therefore, no negative impact on the overall performance of Arch 2 is anticipated due to such local cracking.

As shown in several graphs throughout this chapter, the design calculations were generally successful in capturing the essence of structural behavior. However, in some sections, especially in the tie, notable differences were observed between predicted and measured stresses. Moreover, the variability of the stresses between different arches was relatively large in several sections in the tie. These inconsistencies may partly be attributed to the presence of hand-tightened hangers in the arches for an extended time. On the other hand, the tie element included a variety of embedded components and block-outs, which disrupt the flow of stresses. These components were not considered in the design models of the arches.

The prestress losses in the arches were also evaluated. While some variability was observed among different arches, the losses were generally small, mostly due to the stiff network of hangers that prevent the time-dependent shortening of the arch elements. The stresses during the live load testing of the bridge were also briefly introduced in this chapter.

A final summary of the findings of this study is presented in Chapter 7.

CHAPTER 7
Conclusion

This report provided an overview of the monitoring study that was carried out on the West 7th Street Bridge. This innovative bridge, completed in 2013 as a replacement for a century-old bridge, consists of 12 prestressed, precast network arches. The innovative construction method of the arches served to limit the time of street closure to 120 days and minimized the interruption to traffic.

Several post tensioning and handling operations were necessary, which could pose a cracking risk to the arches and endanger their stability in the finished bridge. Moreover, there were some uncertainties about the behavior of the arches due to their complex structural behavior. Therefore, this implementation project was initiated by TxDOT to ensure that the arches were not damaged during construction and to verify the design methodology for this innovative structure.

The arches were instrumented with 224 vibrating wire gages that were embedded in the arches prior to concrete placement. The gages were monitored during post-tensioning, handling, and transportation operations as well as deck construction. The collected data were post-processed to calculate the representative structural parameters, namely strains and stresses. In order to obtain better estimates of the mechanical properties of the concrete that was used in the arches, a material study was conducted in FSEL prior to the construction of the first arch. The results of this study were used in estimating the in-situ compressive strength and modulus of elasticity of the arches, which were critical in post-processing of the data.

Monitoring the stresses throughout the construction of the arches provided an improved understanding of the structure's behavior and ensured the safety of the arches against cracking. The instrumentation was used to assist the contractor with making decisions about modifying the construction procedure when needed. Moreover, the measured stresses in the structure were used to verify the design calculations and assess the validity of the assumptions made in the modeling of the structure. These comparisons will continue in the near future as the study of the arches continues.

The main conclusions that can be made about the arches of the West 7th Street Bridge to date are as follows:

- The instrumentation was successful in detecting the stresses in the arches due to different construction operations and in providing insight into the response of the arches.

- Design calculations were generally successful in capturing the essence of the structure's response during post-tensioning and handling operations. Due to careful structural design of the arches and conservative design of the handling operations, the arches were successfully constructed without experiencing excessive stresses. Isolated local cracking happened only in one of the arches during transportation from the casting yard to the bridge location. However, such cracking is not expected to have a significant effect on

the performance of the arch because the width of the crack was very small, and the crack was closed due to subsequent loading on the arch.

- The short-term construction stresses in the identical arches could be highly variable from one arch to another, particularly after the arches were rotated into the vertical orientation. Uncertainties due to presence of hand-tightened hangers may have contributed to such variability. In this project, the observed variability did not result in endangering the safety of the arches. However, reliable stress predictions for network arches must consider uncertainties due to unknown hanger forces, regardless of the level of sophistication used in modeling. A successful handling design would best be obtained by assuming multiple conditions of hanger forces and making sure that the structure will not undergo excessive stresses due to an unforeseen stiffness distribution.

- While implementing sophisticated finite element software resulted in accurate predictions of short-term stress changes in the structure, the accuracy of the predicted time-dependent stresses is highly dependent on the assumptions on the creep and shrinkage behavior of the concrete. In this project, relatively small prestress losses were recorded from the structure. This observation was mostly attributed to the presence of hangers, which restrain the time-dependent shortening of the rib and the tie. However, the prestress induced in the concrete might diminish over time due to stress relaxation and redistribution. Capturing the stress relaxation from the instrumentation output is not possible because relaxation happens without any change in strains. Accurate estimates of such time-dependent effects can be obtained through comprehensive time-dependent creep and shrinkage test data from the concrete mix and combining those data with the measured response of the structure. Such data were not available in this project. However, the researchers at UT are currently developing numerical procedures to evaluate the time-dependent stress changes in the arches of the West 7th Street Bridge using creep and shrinkage models that are calibrated based on the instrumentation outputs.

- Before finalizing the design of other structures that might be sensitive to cracking similar to these arches, a material study is highly recommended. The modulus of elasticity of the concrete and creep and shrinkage parameters will affect the stress calculations. Therefore, these parameters must be realistically estimated before design. Although such a study is often impractical in initial design calculations, it is possible to analyze the model with the updated parameters once the final mix is determined and make sure of the suitability of the design.

To the knowledge of the authors, the study presented herein is the first ever on the construction response of a concrete tied arch bridge of any type. Therefore, the data obtained in this study are a useful validation tool for future modeling of concrete tied arches.

APPENDIX A
As-Built Locations of the VWGs

A.1 INTRODUCTION

The locations of the VWGs that were embedded in the arches of the West 7th Street Bridge are presented in this appendix. For convenience, all of the directions and annotations in the figures of this appendix are based on the positions of the arches in the finished bridge.

A.2 THE INSTRUMENTED SECTIONS

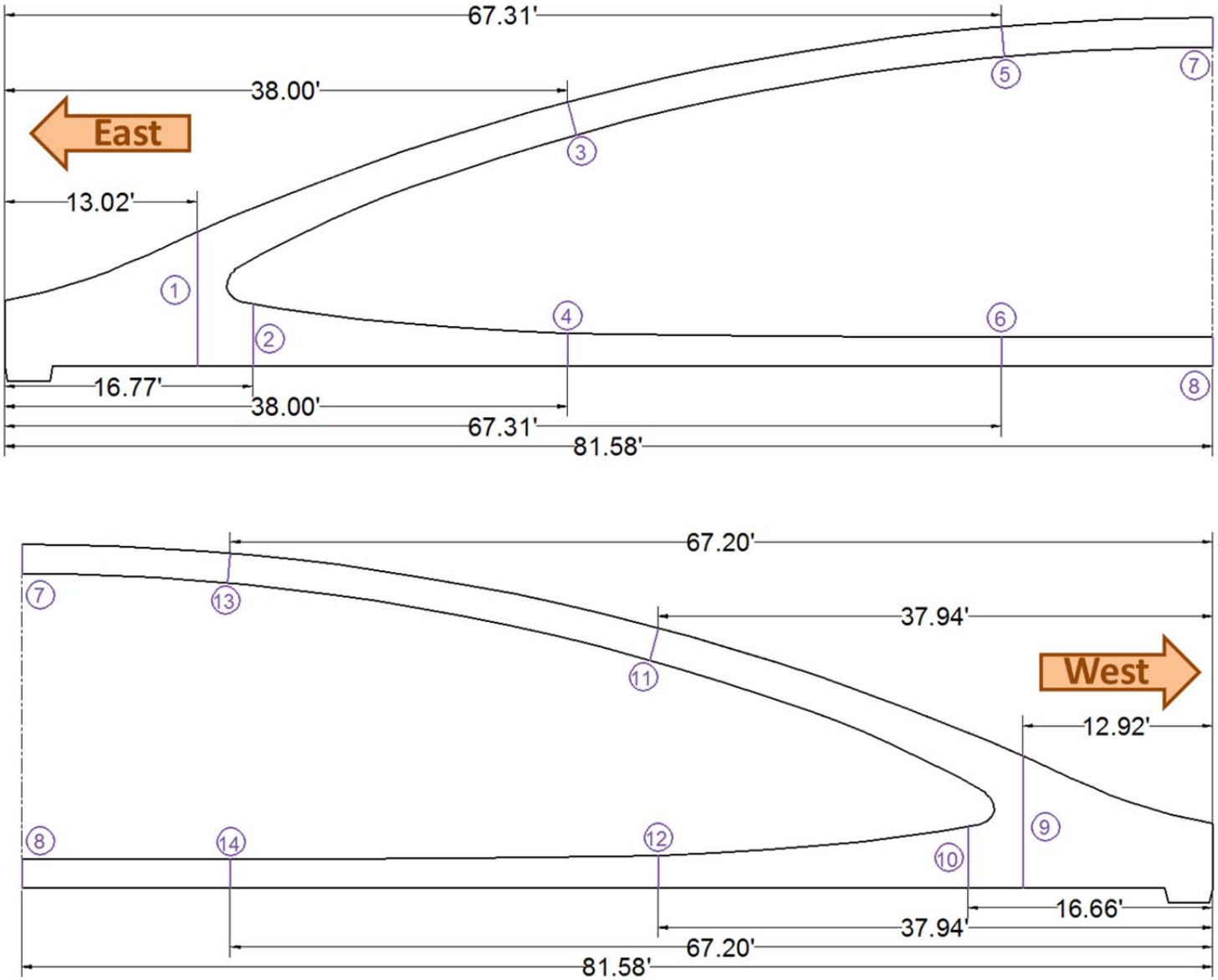

Figure A.1- The instrumented sections in Arch 1.

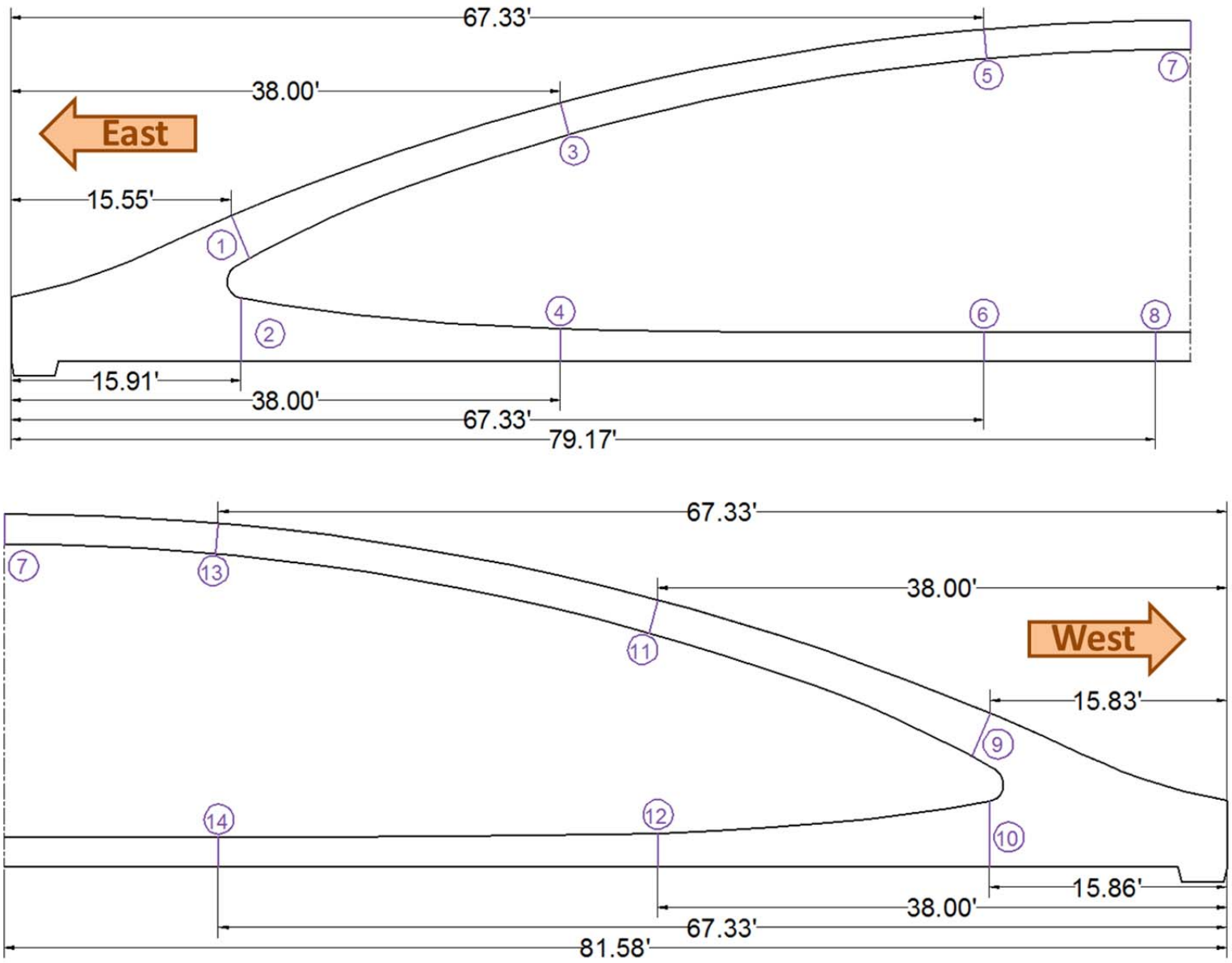

Figure A.2- The instrumented sections in Arch 2.

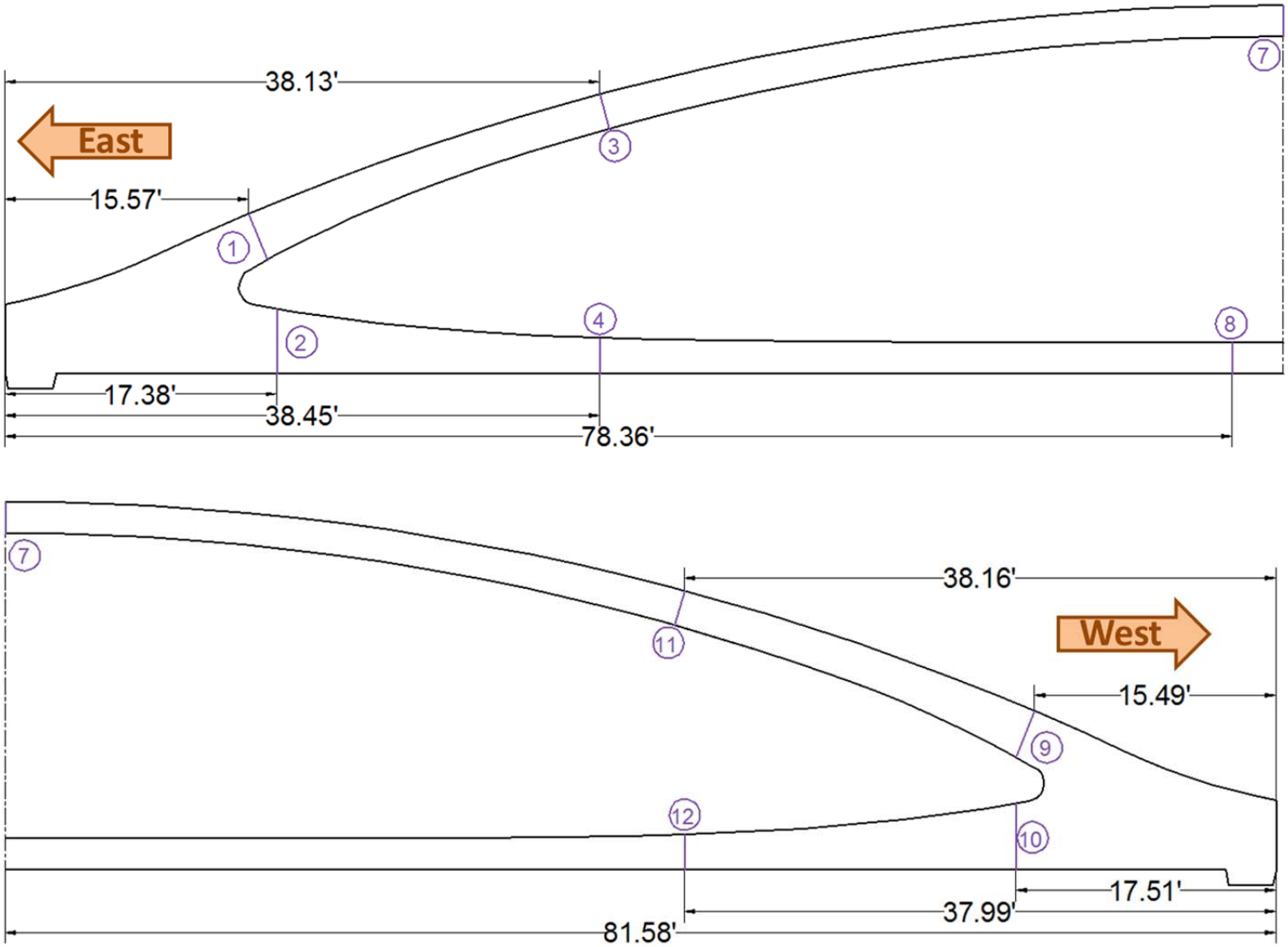

Figure A.3- The instrumented sections in Arch 3.

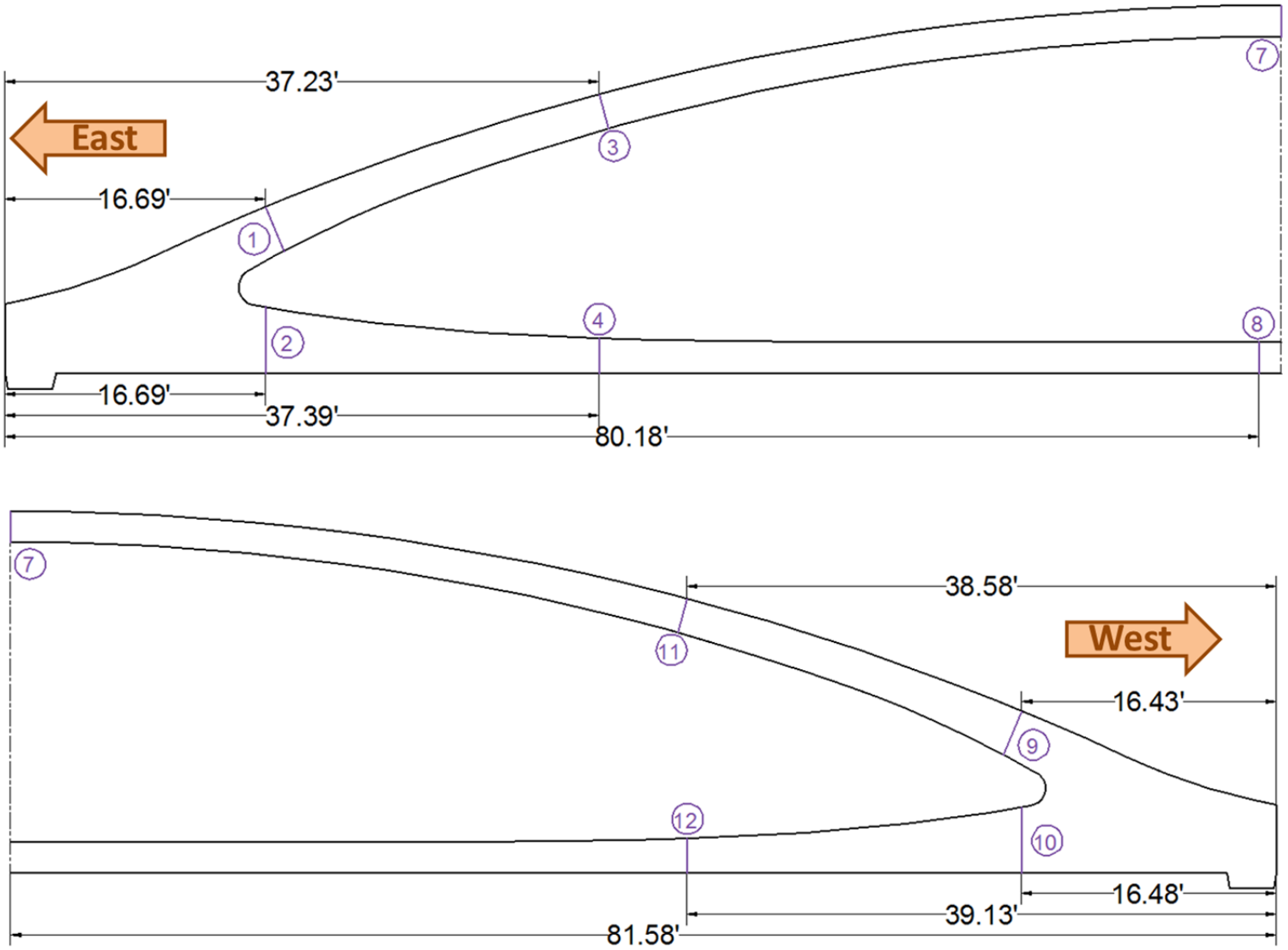

Figure A.4- The instrumented sections in Arch 4.

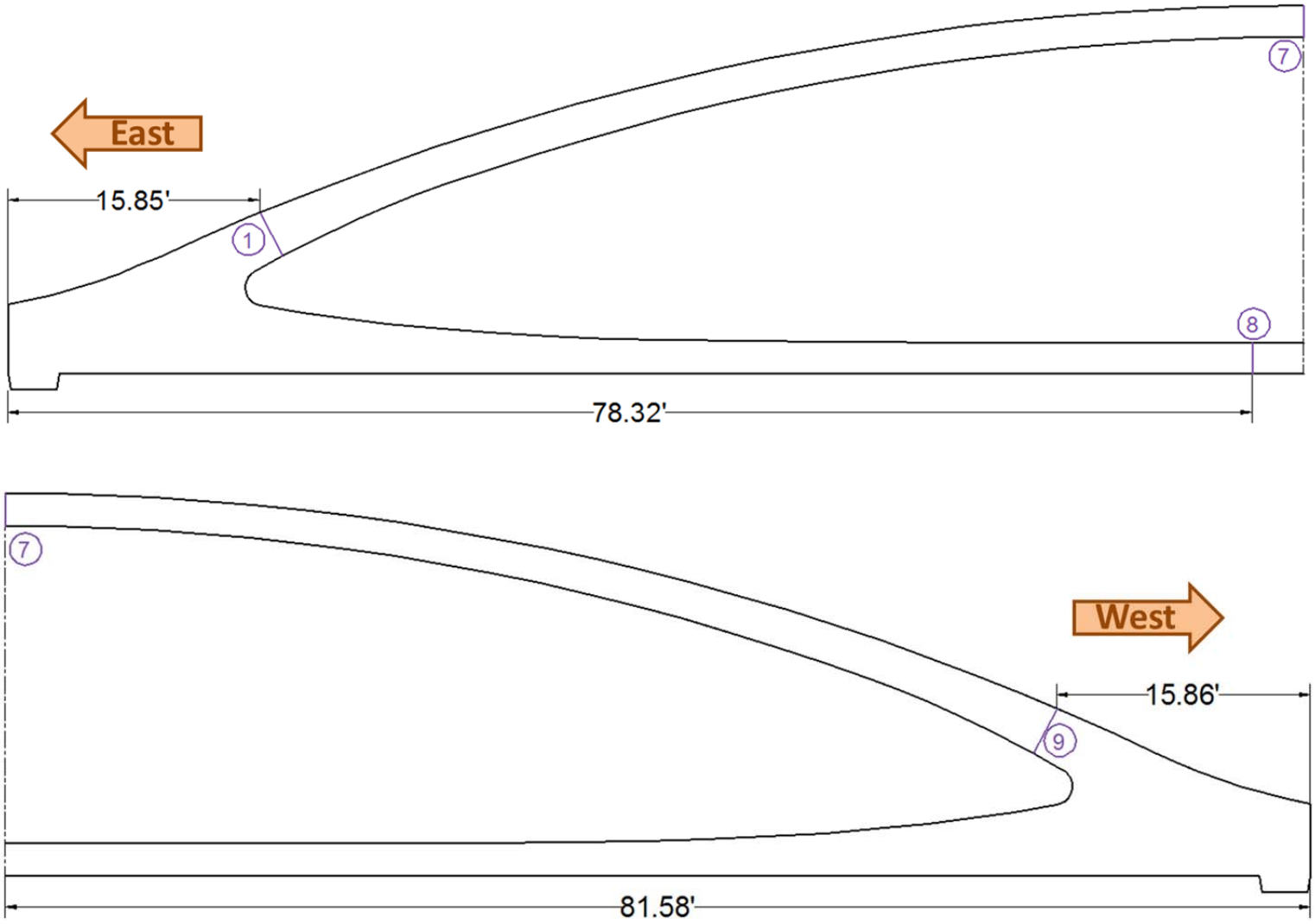

Figure A.5- The instrumented sections in Arch 5.

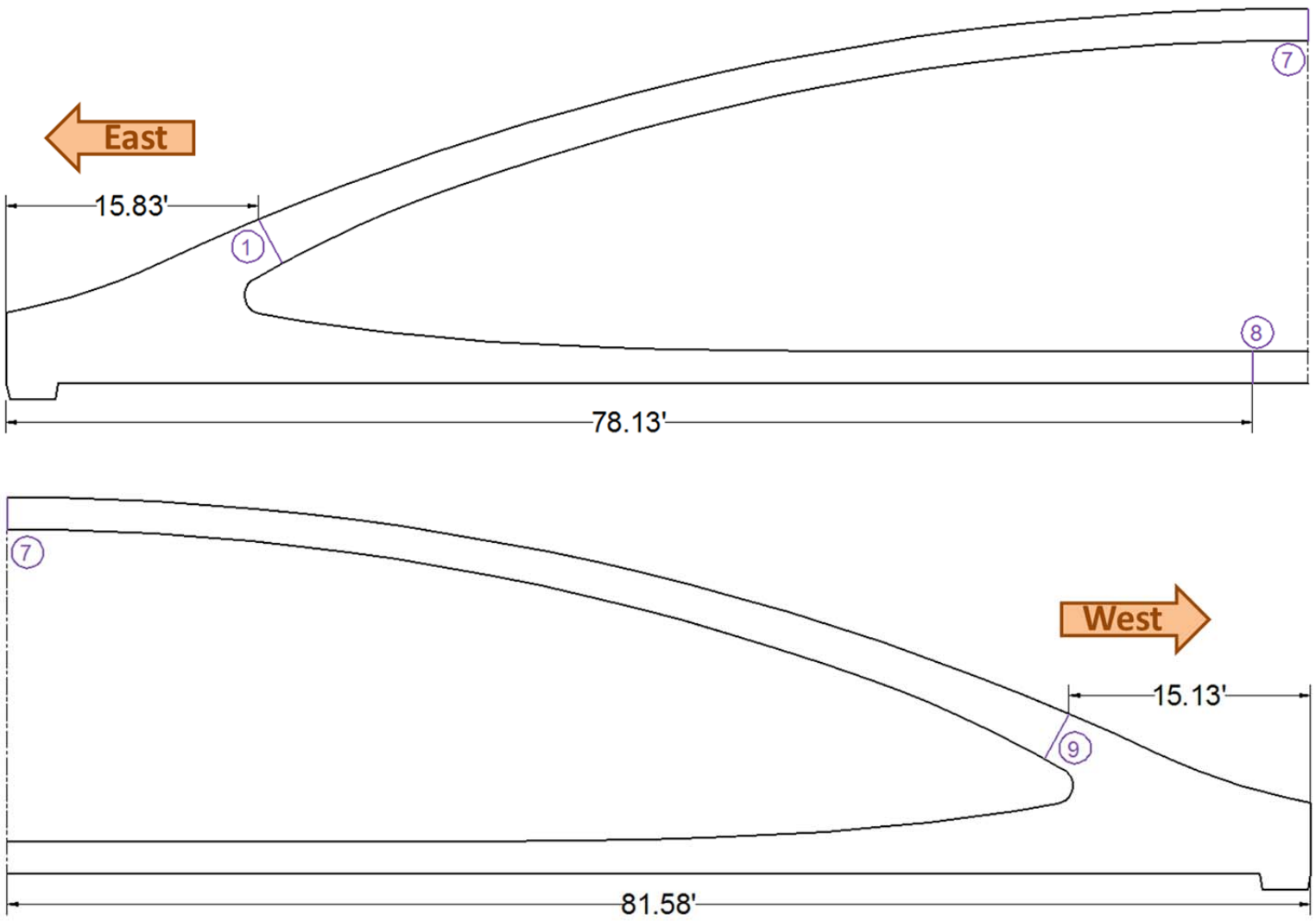

Figure A.6- The instrumented sections in Arch 6.

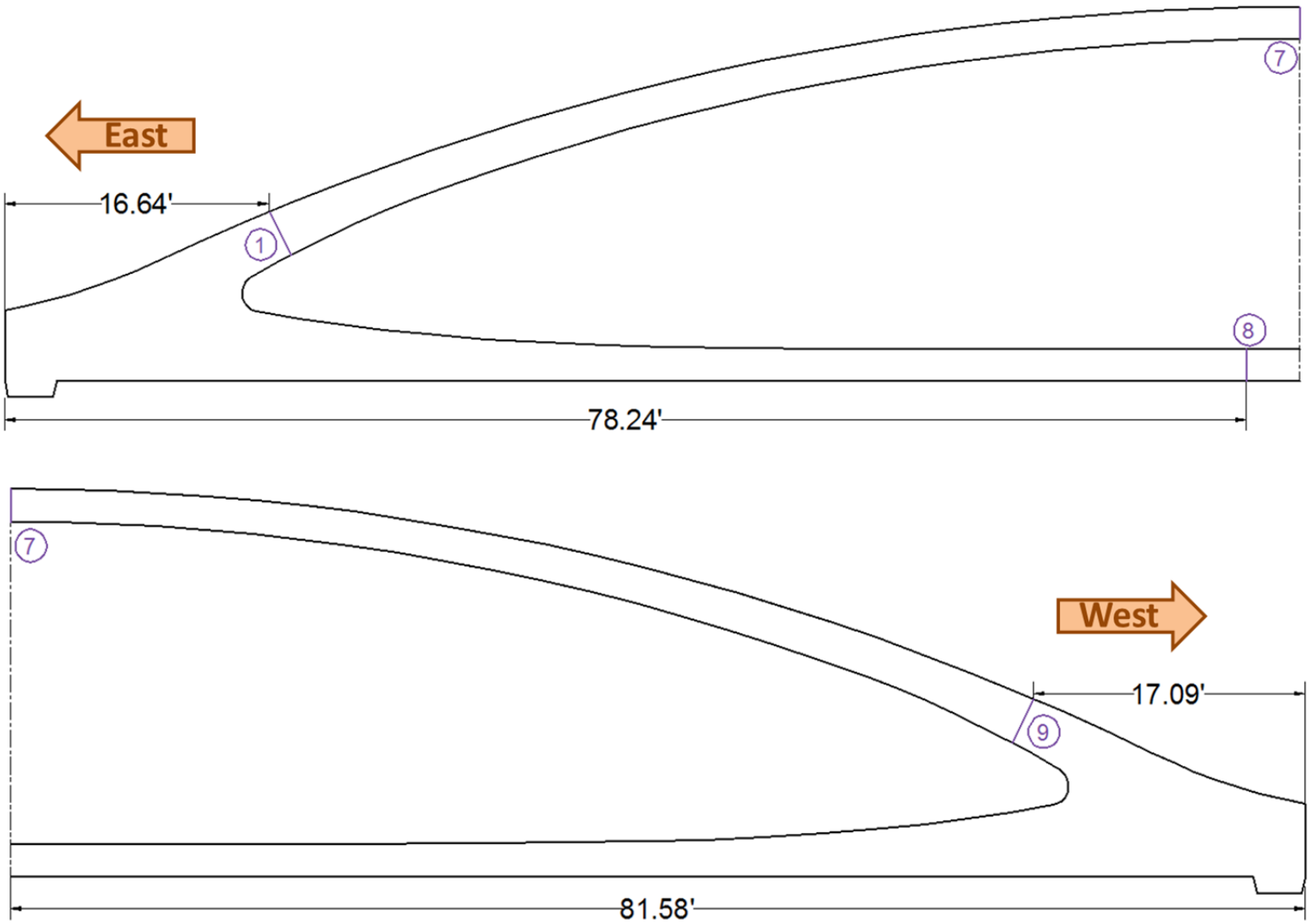

Figure A.7- The instrumented sections in Arch 7.

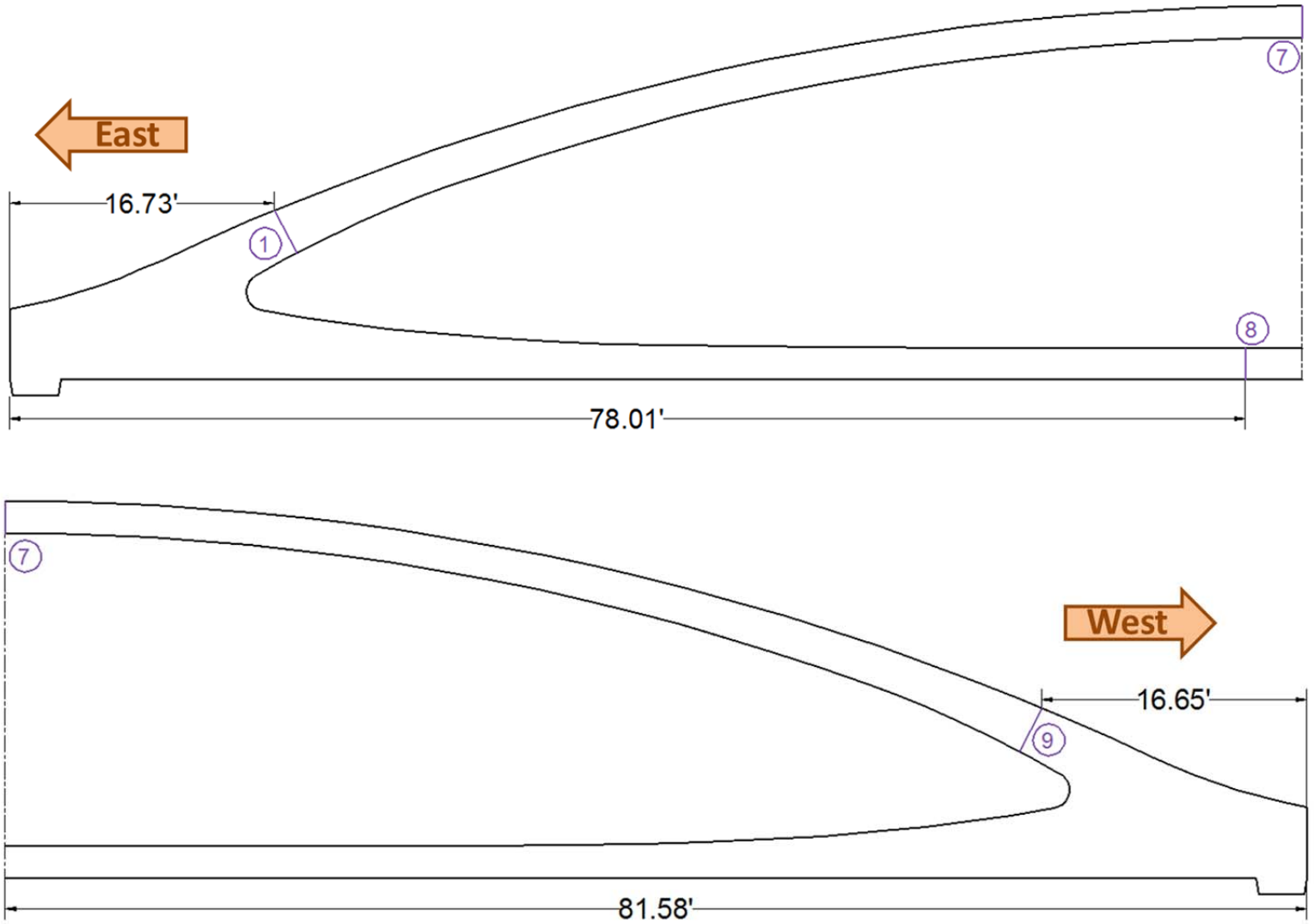

Figure A.8- The instrumented sections in Arch 8.

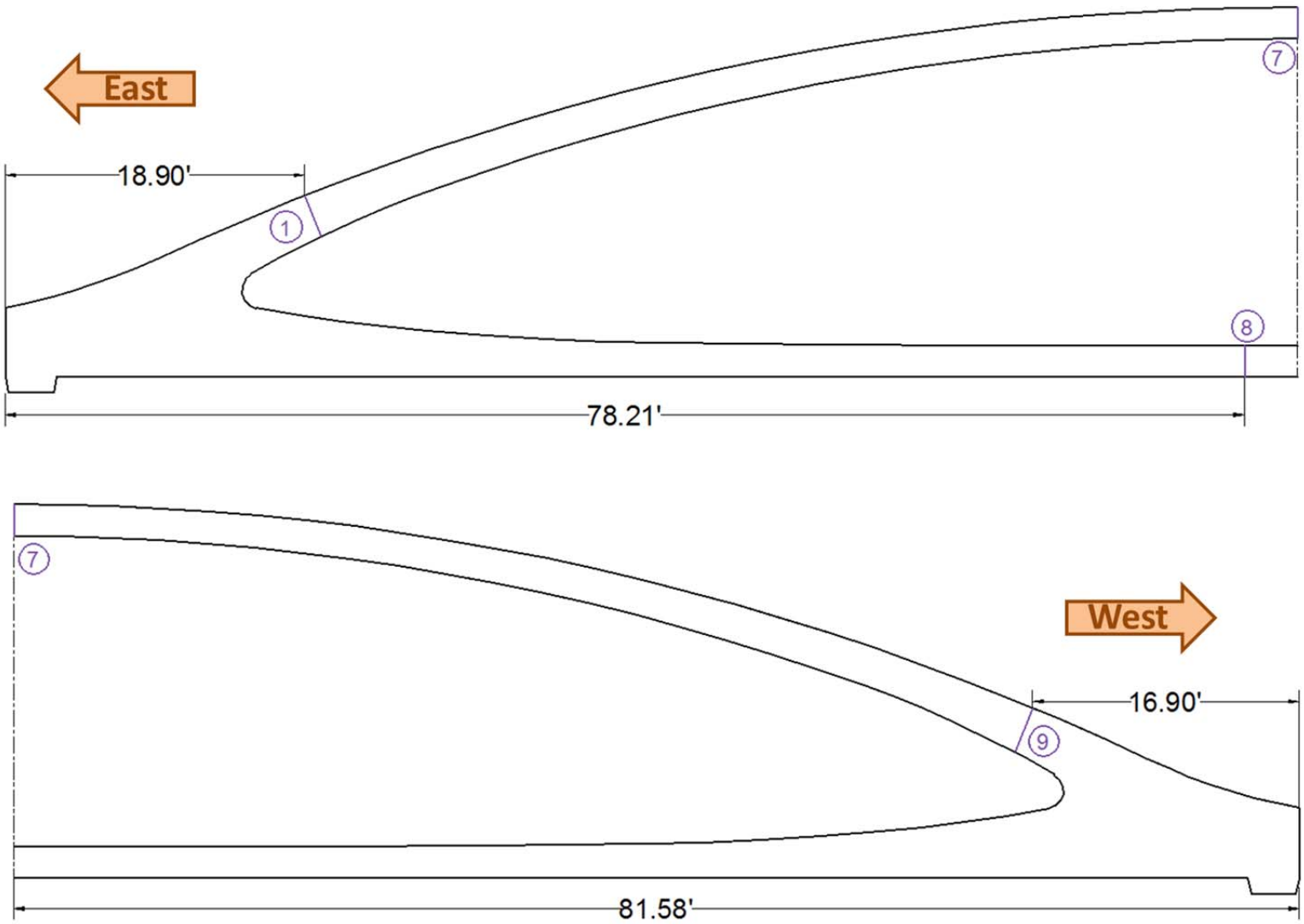

Figure A.9- The instrumented sections in Arch 9.

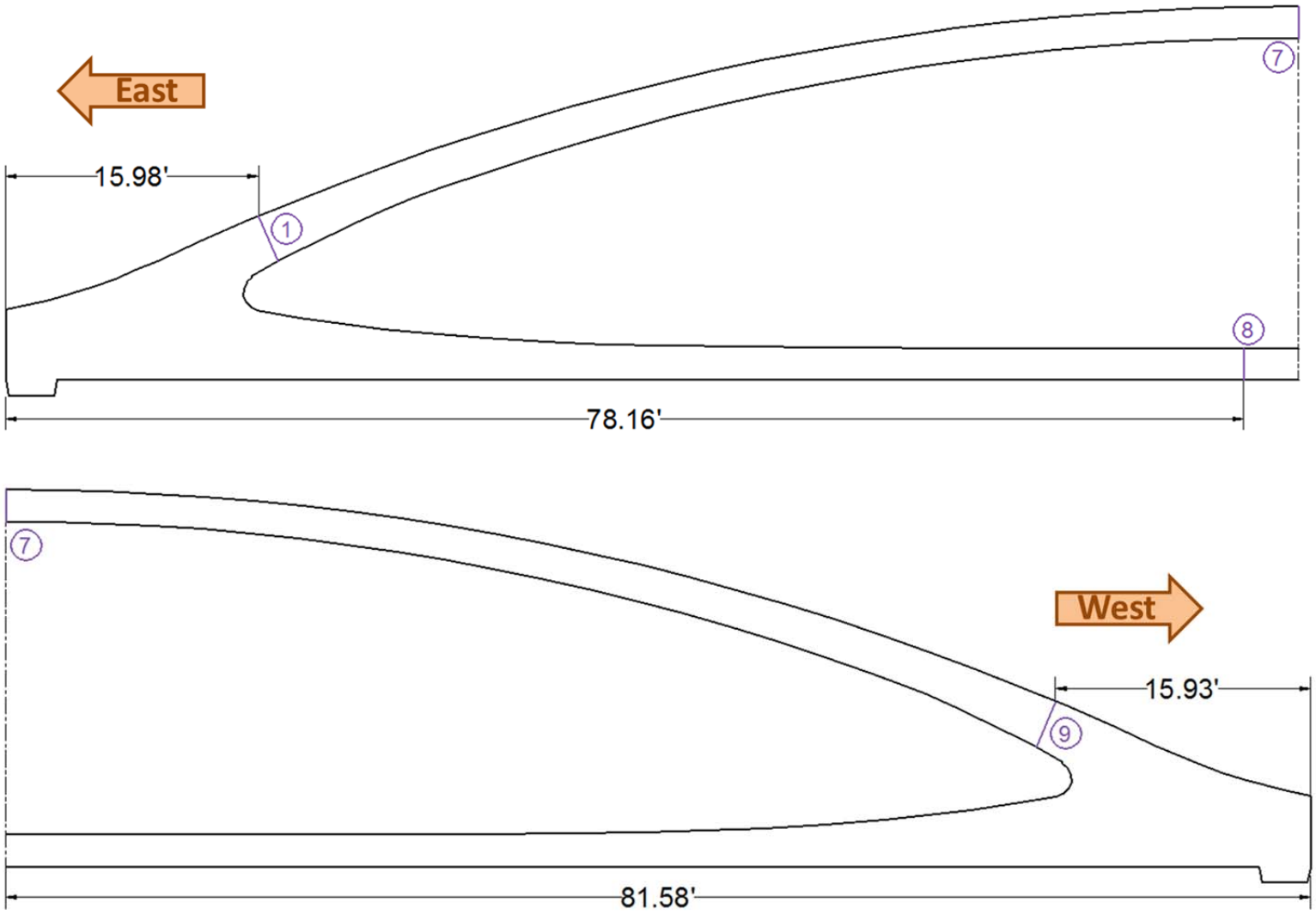

Figure A.10- The instrumented sections in Arch 10.

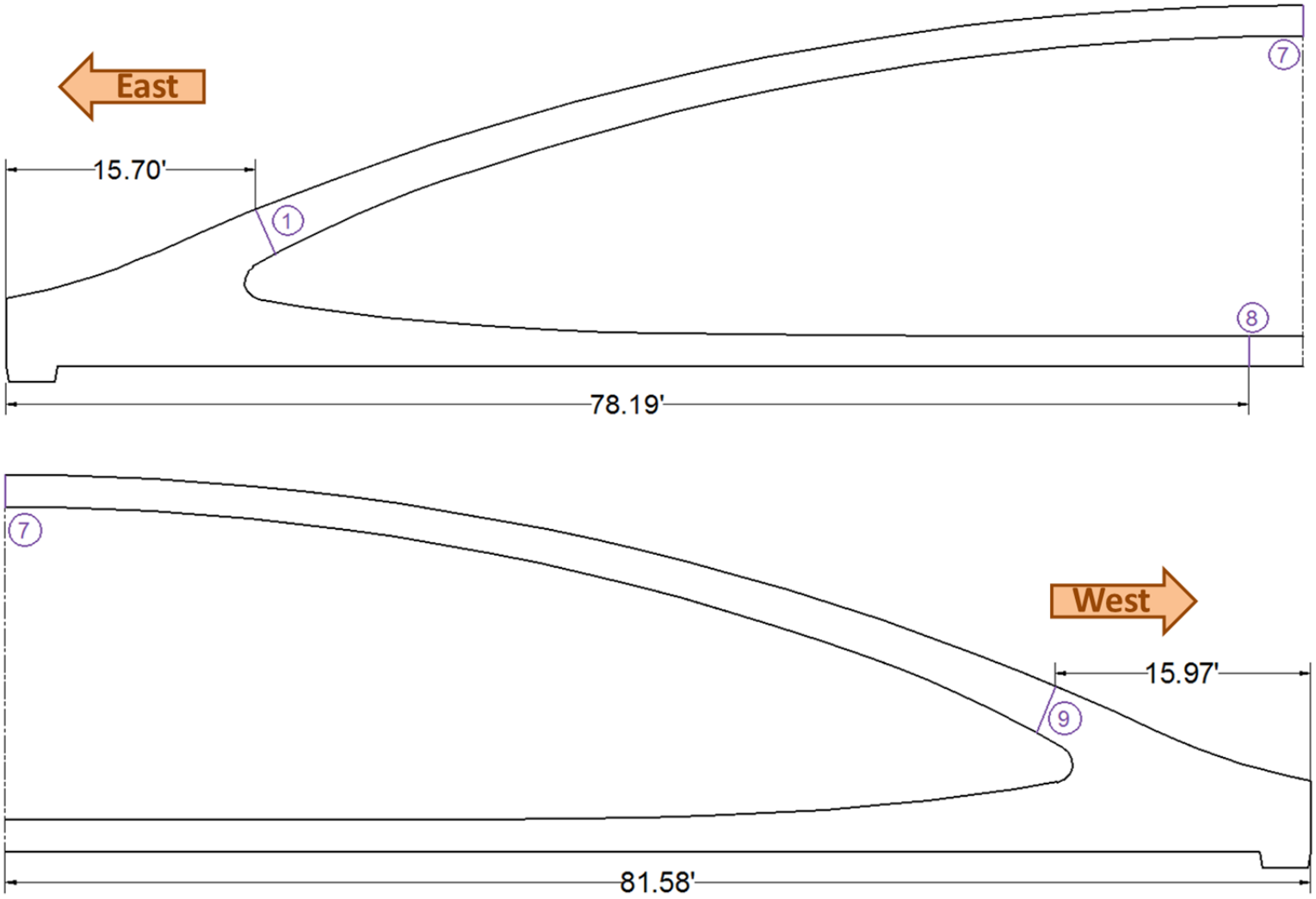

Figure A.11- The instrumented sections in Arch 11.

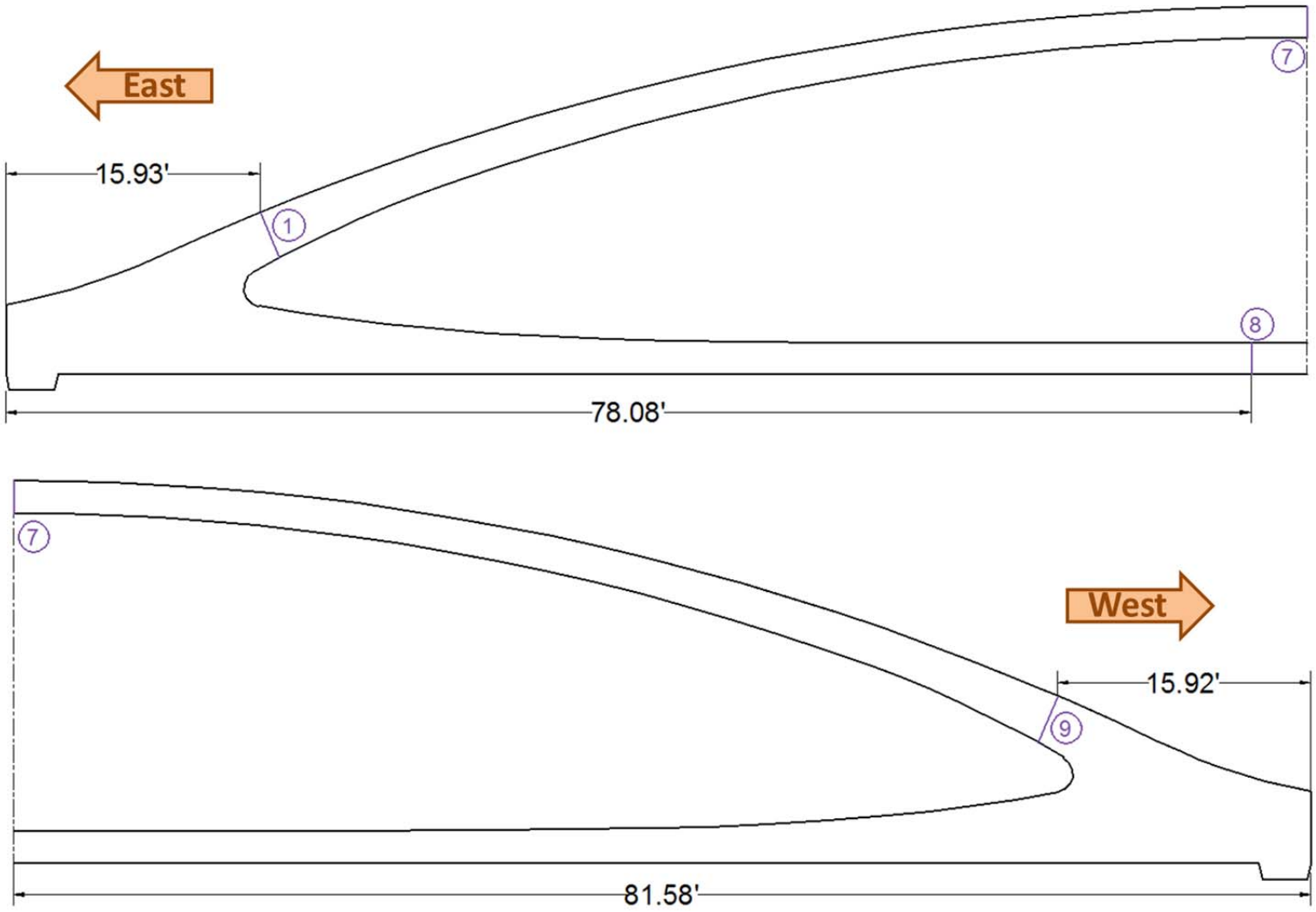

Figure A.12- The instrumented sections in Arch 12.

A.3 SECTIONAL LOCATIONS OF THE VWGS

The following tables provide the coordinates of the VWGs in each instrumented section of the arches. These coordinates are based on the coordinate system shown in Figure A.13.

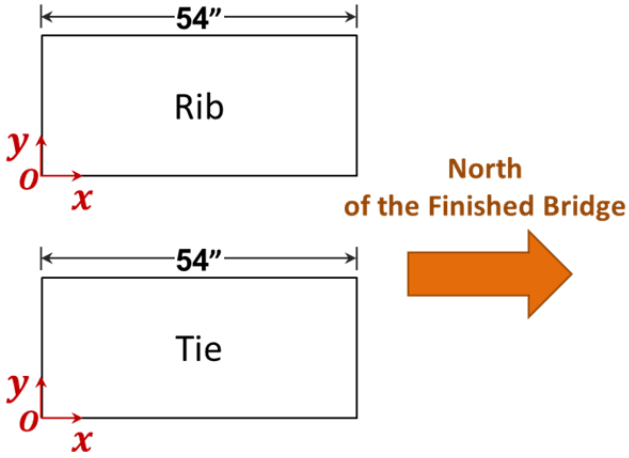

Figure A.13- The coordinate system for the locations of the VWGs.

Table A.1- Coordinates of the VWGs in Arch 1.

VWG No.	Section	x(in)	y(in)	VWG No.	Section	x(in)	y(in)
1	1	19.75	104.89	21	8	13.38	20.31
2	1	33.63	104.89	22	8	30.63	19.94
3	2	4.59	47.35	23	8	48.75	2.63
4	2	48.94	47.32	24	8	5.13	3.44
5	3	5.13	23.80	25	9	13.00	103.57
6	3	47.50	24.63	26	9	47.38	101.69
7	3	25.75	3.88	27	10	4.13	47.18
8	4	36.00	22.97	28	10	48.75	47.74
9	4	49.00	2.34	29	11	5.69	24.63
10	4	5.13	3.13	30	11	46.63	24.50
11	5	5.50	21.50	31	11	27.75	3.88
12	5	48.00	20.88	32	12	35.75	22.80
13	5	26.50	3.88	33	12	48.69	3.11
14	6	34.25	20.69	34	12	4.63	2.63
15	6	48.75	2.88	35	13	5.63	21.25
16	6	5.75	2.94	36	13	48.38	19.88
17	7	6.13	20.88	37	13	24.50	3.88
18	7	47.88	19.88	38	14	34.75	20.25
19	7	47.88	4.25	39	14	48.50	3.00
20	7	5.25	3.38	40	14	5.38	2.75

Table A.2- Coordinates of the VWGs in Arch 2.

VWG No.	Section	x(in)	y(in)	VWG No.	Section	x(in)	y(in)
1	1	34.75	33.75	21	8	48.50	20.88
2	1	6.75	33.64	22	8	5.94	20.50
3	2	48.69	48.75	23	8	5.13	2.63
4	2	6.25	48.75	24	8	48.50	2.69
5	3	48.88	24.13	25	9	42.38	33.50
6	3	20.63	23.88	26	9	6.88	32.63
7	3	28.63	3.63	27	10	49.25	48.85
8	4	19.50	23.34	28	10	11.50	49.79
9	4	6.00	2.59	29	11	47.25	24.00
10	4	48.44	2.03	30	11	20.75	24.25
11	5	48.63	21.13	31	11	29.00	3.50
12	5	5.88	21.75	32	12	38.75	23.97
13	5	27.38	3.88	33	12	5.63	2.34
14	6	18.75	20.00	34	12	49.06	2.84
15	6	5.81	2.44	35	13	47.13	21.50
16	6	48.44	2.63	36	13	6.13	22.00
17	7	47.63	22.00	37	13	25.75	4.38
18	7	6.13	21.63	38	14	37.50	19.75
19	7	6.00	5.50	39	14	5.94	3.00
20	7	48.75	4.75	40	14	48.44	2.00

Table A.3- Coordinates of the VWGs in Arch 3.

VWG No.	Section	x(in)	y(in)	VWG No.	Section	x(in)	y(in)
1	1	7.50	34.75	21	8	5.00	20.63
2	1	47.25	35.25	22	8	47.63	20.50
3	2	4.88	46.56	23	8	47.75	2.38
4	2	46.38	46.31	25	9	6.25	34.25
5	3	6.63	24.75	26	9	46.88	34.88
6	3	48.25	23.25	27	10	4.75	47.75
7	3	26.88	3.25	28	10	45.88	47.25
8	4	36.50	22.42	29	11	6.38	23.25
9	4	47.75	2.17	30	11	46.50	23.25
10	4	5.00	1.55	31	11	26.50	3.50
17	7	12.88	22.50	32	12	35.00	23.34
18	7	48.50	20.38	33	12	48.00	2.34
19	7	47.38	3.50	34	12	5.00	1.22
20	7	5.75	5.50				

Table A.4- Coordinates of the VWGs in Arch 4.

VWG No.	Section	x(in)	y(in)	VWG No.	Section	x(in)	y(in)
1	1	47.50	33.50	**21**	8	48.88	20.25
2	1	5.88	33.00	**22**	8	6.38	20.75
3	2	38.00	47.32	**23**	8	5.25	2.88
4	2	6.00	47.92	**24**	8	48.19	2.50
5	3	48.13	25.00	**25**	9	46.50	35.69
6	3	6.88	25.00	**26**	9	5.63	35.94
7	3	30.38	4.63	**27**	10	49.50	47.43
8	4	27.38	26.99	**28**	10	5.94	47.46
9	4	5.00	2.71	**29**	11	48.13	24.38
10	4	47.13	1.46	**30**	11	6.81	24.56
17	7	47.75	22.13	**31**	11	27.31	3.75
18	7	6.13	20.88	**32**	12	28.50	22.86
19	7	7.56	3.75	**33**	12	5.81	2.42
20	7	47.88	4.50	**34**	12	49.25	2.39

Table A.5- Coordinates of the VWGs in Arch 5.

VWG No.	Section	x(in)	y(in)
1	1	5.88	34.12
2	1	46.75	34.19
17	7	5.63	21.56
18	7	46.81	21.63
19	7	26.25	4.25
22	8	26.63	20.50
23	8	48.13	2.31
24	8	5.88	2.63
25	9	11.32	31.73
26	9	47.75	33.88

Table A.6- Coordinates of the VWGs in Arch 6.

VWG No.	Section	x(in)	y(in)
1	**1**	47.63	34.04
2	**1**	8.88	35.19
17	**7**	47.81	20.94
18	**7**	7.31	21.81
19	**7**	30.13	3.94
22	**8**	25.38	20.25
23	**8**	8.81	3.19
24	**8**	47.69	2.06
25	**9**	41.50	35.54
26	**9**	6.13	34.67

Table A.7- Coordinates of the VWGs in Arch 7.

VWG No.	Section	x(in)	y(in)
1	1	5.50	33.40
2	1	47.63	33.88
17	7	5.50	21.19
18	7	47.72	20.66
19	7	26.03	3.56
22	8	25.66	20.09
23	8	46.22	2.38
24	8	5.38	2.31
25	9	5.16	33.09
26	9	47.44	33.53

Table A.8- Coordinates of the VWGs in Arch 8.

VWG No.	Section	x(in)	y(in)
1	1	39.44	33.51
2	1	6.84	33.56
17	7	47.63	21.09
18	7	6.13	20.81
19	7	27.88	3.72
22	8	27.00	20.75
23	8	9.09	2.91
24	8	48.63	2.94
25	9	44.00	33.49
26	9	6.59	33.81

Table A.9- Coordinates of the VWGs in Arch 9.

VWG No.	Section	x(in)	y(in)
1	1	6.38	30.95
2	1	47.38	31.53
17	7	6.50	20.94
18	7	48.25	21.13
19	7	26.69	3.50
22	8	24.88	20.50
23	8	45.06	2.50
24	8	7.75	2.69
25	9	6.13	33.75
26	9	47.25	33.03

Table A.10- Coordinates of the VWGs in Arch 10.

VWG No.	Section	x(in)	y(in)
1	1	48.06	33.90
2	1	6.88	33.81
17	7	46.38	20.69
18	7	6.63	21.13
19	7	26.63	3.75
22	8	26.63	19.88
23	8	9.50	1.94
24	8	47.00	1.88
25	9	47.88	34.20
26	9	6.75	34.19

Table A.11- Coordinates of the VWGs in Arch 11.

VWG No.	Section	x(in)	y(in)
1	1	6.50	35.48
2	1	37.69	35.17
17	7	7.31	20.94
18	7	47.31	21.44
19	7	27.25	3.75
22	8	26.19	20.13
23	8	43.75	2.13
24	8	5.75	2.44
25	9	7.13	35.14
26	9	47.38	35.23

Table A.12- Coordinates of the VWGs in Arch 12.

VWG No.	Section	x(in)	y(in)
1	1	49.44	34.07
2	1	7.63	33.38
17	7	48.13	21.31
18	7	7.00	21.38
19	7	27.50	3.88
22	8	28.38	20.75
23	8	9.63	2.25
24	8	45.50	2.56
25	9	49.50	34.33
26	9	7.50	34.54